Nuclear Magnetic Resonance for the Characterisation of Hot-Melt Extruded Pharmaceutical Amorphous Solid Dispersions

Elena Pisa Chen

Department of Chemical Engineering and Biotechnology
University of Cambridge

This dissertation is submitted for the degree of
Doctor of Philosophy

Newnham College

March 2021

I would like to dedicate this thesis to my loving family and friends, who provide me with unconditional support and without whom none of this would be possible.

Declaration

The work presented in this dissertation was carried out in the Department of Chemical Engineering and Biotechnology, University of Cambridge, between October 2016 and March 2020. I hereby declare that except where specific reference is made in the text or Acknowledgements to the work of others, the contents of this dissertation are original and have not been submitted in whole or in part for consideration for any other degree or qualification in this, or any other university. This dissertation contains fewer than 65,000 words including appendices, bibliography, footnotes, tables and equations and has fewer than 150 figures.

Elena Pisa Chen
March 2021

Abstract

"Nuclear Magnetic Resonance for the Characterisation of Hot-Melt Extruded Pharmaceutical Amorphous Solid Dispersions"

Elena Pisa Chen

Low aqueous solubility of active pharmaceutical ingredients (APIs) presents one the greatest and most frequent challenges to formulation scientists. An estimated 75% of pharmaceutical compounds under development suffer from poor solubility. The formulation of drug/polymer amorphous solid dispersions (ASDs) is one of the most successful strategies for improving the oral bioavailability of poorly soluble APIs. Hot-melt extrusion (HME) is one method for preparing ASDs that is growing in importance in the pharmaceutical industry. HME involves the combination of an API and a polymer, which are heated and intensively mixed to yield a homogeneous product.

Despite the growth in the application of HME to drug development, there are still substantial gaps in our understanding regarding the dynamics of drug dissolution and dispersion in viscous polymers as well as physical stability (phase separation and API recrystallization). Computational models have been built in order to predict optimal processing conditions (e.g. temperature, residence time, drug loading), but they are limited by the lack of supporting data for key mass transport parameters. A key omission is the lack of experimental data on the API diffusion coefficient at conditions relevant to HME.

This dissertation reports the first measurements of API diffusion in pharmaceutical polymer melts at temperatures relevant to the HME process, by means of high-temperature PFG NMR. These measurements were performed in the absence of any solvents, for a range of drug loadings, temperatures, polymer systems and drug species. The mechanism of the diffusion process and its relationship to viscosity was explored with the Stokes-Einstein and Arrhenius models. Viscosity plots obtained from the rheology experiments uncovered the possibility of HME processing at significantly lower temperatures to reduce the risk of thermal degradation. Additional characterisation of extrudates prepared 30°C below the drug's melting point concluded that satisfactory ASDs were produced.

Furthermore, this dissertation includes ^{1}H solid-state NMR relaxometry measurements as an insight into physical state, phase separation and API/polymer interactions in extruded formulations. HME products were found to have formed successful ASDs, with no evidence

of crystalline drug remains or of phase separation. This was not the case for a physical mixture that had been heated up, but not actively mixed; meaning that extrusion is indeed required (and not just high temperatures) to achieve ASDs. Chemical shift changes suggested intermolecular associations between the drug and the polymer. These interactions were studied in greater detail through a range of novel solid-state and molten-state 2D NMR experiments. The results not only corroborated the existence of drug-polymer H-bonding, but also the presence of Van der Waals interactions between the two species.

Finally, several theoretical models were applied to predict solubility and dissolution rate of a drug in a polymer melt. This involved the calculation of the interaction parameter and the construction of a miscibility-solubility phase diagram. A simple static spherical particle dissolution model was fitted with the diffusion coefficient parameters measured in previous sections and the results were in agreement with experimentally obtained time-to-dissolution observations. This positive result highlighted the value of measuring the diffusion coefficient of drugs in polymer mixtures for predicting system behaviour and optimising process parameters.

Acknowledgements

I would like to acknowledge the role of both my academic supervisor Dr Mick Mantle (University of Cambridge), and my industrial supervisor Dr Les Hughes (AstraZeneca). They have been instrumental in providing me with invaluable guidance during the past four years; and I would like to thank them for introducing me and helping me understand and deal with the ups and downs of the world of NMR.

I would like to express my gratitude to Dr Stephen Wren (AstraZeneca) for his thought-provoking discussions and Dr Jonathan Booth (AstraZeneca) for his encouragement and his expertise in hot-melt extrusion and amorphous solid dispersions. I would also like to acknowledge Dr Gavin Reynolds (AstraZeneca) for performing the shear flow particle dissolution simulations.

I wish to thank Dr Jim McCabe (AstraZeneca), Dr Zoe Cotter (AstraZeneca) and Dr Helen Blade (AstraZeneca) for their assistance with thermal characterisation techniques. I would like to acknowledge Dr Simon Buttler (University of Cambridge), for sharing his know-how of rheology measurements and Dr Kevin Treacher (AstraZeneca) for his expertise in polymer and material science. I would also like to thank Dr Martin Kearns (AstraZeneca) for his help in the production of hot-melt extruded samples.

I would like to acknowledge that without AstraZeneca and EPSRC sponsorship, this research would not have been possible.

Finally, I would like to express my gratitude to the Magnetic Resonance Research Center and the Department of Chemical Engineering (University of Chemistry) and AstraZeneca (Macclesfield).

Dissemination of thesis

Publications:

Elena Pisa, Leslie P. Hughes, Stephen A.C. Wren, Jonathan Booth, James F. McCabe, David, T.E.Whittaker, & Mick D. Mantle. NMR and Thermal Studies for the Characterization of Mass Transport and Phase Separation in Paracetamol/Copovidone Hot-Melt Extrusion Formulations. *Molecular Pharmaceutics*, 17(6), 2021–2033, 2020.

Conference presentations:

"AstraZeneca PhD Day 2019", AstraZeneca, Macclesfield, (3rd April 2019).

"BRSG Magnetic Resonance: Challenges in Diagnosis and Drug Development", Science Centre, Anglia Ruskin University (4th July 2019).

Poster presentations:

"AstraZeneca PhD Day 2018", AstraZeneca, Macclesfield, UK (25th April 2018).

"EUROMAR (European Magnetic Resonance Meeting)", La Cité des Congrès, Nantes, France (1st-5th July 2018)

"AstraZeneca PhD Day 2019", AstraZeneca, Macclesfield, (3rd April 2019).

"SMASH (Small Molecule NMR Conference)", Porto, Portugal (22nd-25th September 2019).

Table of contents

List of figures

List of tables

Nomenclature

Roman Symbols

ΔC_p	Configurational heat capacity
ΔG_{mix}	Free energy of mixing
ΔH_{mix}	Enthalpy of mixing
ΔS_{mix}	Entropy of mixing
$\Delta\ C_p$	Configurational heat capacity
$\Delta\ G_{mix}$	Free energy of mixing
B_0	Static external magnetic field
B_1	Temporary field for spin excitation
B_{SL}	Spin-lock field
C_p	Heat capacity
C_p	Heat capacity
d_0	Variable delay of evolution time
D_{self}	Self-diffusion coefficient
d_{SE}	Spin echo delay
D_{SP}	Spin diffusion coefficient
D_{trans}	Transport diffusion coefficient
G'	Elastic modulus
G''	Viscous modulus
G^*	Complex modulus
m_0	Mass of solid drug
m_s	Mass of drug in solution
n_{part}	Number of drug particles in the system
R	Gas constant
R	Particle radius
S	Solubility
T_1	Spin-lattice relaxation constant
T_2	Spin-spin relaxation constant
T_2^*	Apparent spin-spin relaxation constant
t_c	Contact time
t_d	Detection time
T_g	Glass transition temperature
t_m	Mixing time
t_p	Length of B_1
T_R	Repetition time or recycle delay
$T_{1\rho}$	Spin-lattice relaxation constant in the rotating frame
T_m	Melting temperature
T_m^{mix}	Melting temperature of the mixture
T_m^{pure}	Melting temperature of the pure compound
V_{site}	Volume of lattice site
a.u.	Arbitrary units
CH_2	Methylene
CH_3	Methyl
CH	Methine

D_{SE}	Stokes-Einstein diffusion coefficient
D	Diffusion coefficient
E_A	Activation energy
G	Magnetic field gradient strength in imaging experiments
g	Pulsed field gradient strength in diffusion experiments
h	Planck's constant
I	Spin quantum number
k_{ml}	Mass loss rate constant
k	Boltzmann's constant
M_w	Molecular weight
M	Bulk magnetisation
r_g	Gyration radius
r	Particle radius
S	NMR signal
tanδ	Damping factor
T	Temperature

Greek Symbols

α	Nuclear low energy state
β	Nuclear high energy state
χ	Flory-Huggins interaction parameter
χ	Flory-Huggins interaction parameter
Δ	Observation time or spacing between the gradient pair in diffusion experiments
δ	Chemical shift symbol
δ	Length of the pulsed field gradient in diffusion experiments
δ	Solubility parameter
η^*	Complex viscosity
η	Shear viscosity
γ	Activity coefficient
γ	Gyromagnetic ratio
λ	Temperature coefficient
ν_{drug}	Molar volume of the drug
ω	Rotational rheology angular frequency
ω_0	Larmor precession frequency
ϕ	Phase shift
ϕ	Volume fraction
ρ	Density
τ_R	Period of rotating rotor
θ_m	Magic angle (54.74°)
θ	Spin excitation tip angle

Acronyms / Abbreviations

ADM	Adamantane
AFM	Atomic force microscopy
ALA	Alanine
APGSTE	Alternating pulsed gradient stimulated echo
API	Active pharmaceutical ingredient
ASD	Amorphous solid dispersion

BABA Back-to-back

BCS Biopharmaceutical classification system

COSY Correlation spectroscopy

CP Cross polarisation

CPMG Carr-Purcell-Meiboom-Gill

CSA Chemical shift anisotropy

d-HETCOR HETCOR with homonuclear FSLG decoupling

DQ Double quantum

DSC Differential scanning calorimetry

EB ethylbenzene

EG Ethylene glycol

FH Flory-Huggins

FID Free induction decay

FSLG Frequency-switched Lee-Goldburg

FT Fourier transform

FTIR Fourier-transform infrared spectroscopy

FWHM Full-width at half-maximum

GFA Glass forming ability

GLY Glycine

H-bond Hydrogen bond

HETCOR Heteronuclear correlation

HME Hot-melt extrusion

HPLC High-performance liquid chromatography

i.d. Internal diameter

LVR Linear viscoelastic region

MAS Magic angle spinning

mDSC Modulated differential scanning calorimetry

MQC Multiple quantum coherence

MRI Magnetic resonance imaging

NMR Nuclear magnetic resonance

NOESY Nuclear Overhauser effect spectroscopy

PFG Pulsed field gradient

PGSE Pulsed gradient spin echo

PGSTE Pulsed gradient stimulated echo

QbD Quality by design

r.f. Radio frequency

rmsd Root-mean-square displacement

RS Raman spectroscopy

SEM Scanning electron microscopy

SNR Signal-to-noise ratio

SPINAL-64 Small phase incremental alternation with 64 steps

SQ Single quantum

TEM Transmission electron microscopy

TGA Thermogravimetric analysis

TPPM Two-pulse phase modulation

VA Vinyl acetate

VP Vinyl pyrrolidone

XRD X-ray diffraction

Chapter 1

Introduction

Low aqueous solubility of active pharmaceutical ingredients (APIs) presents one of the greatest and most frequent challenges to formulation scientists [1–3] and it is becoming more prevalent with the use of high throughput screening in drug discovery and the targeting of hydrophobic receptors [4]. The formulation of drug/polymer amorphous solid dispersions (ASDs) *via* hot-melt extrusion (HME) is one of the most successful strategies for improving the oral bioavailability of poorly soluble APIs [5–7]. Despite the growth in the application of HME to drug development, there are still substantial gaps in our understanding regarding the dynamics of drug dissolution and dispersion in viscous polymers as well as the physical stability of the final formulations [8].

The aim of this chapter is to provide a brief overview of the challenges posed by poorly soluble drugs and the approaches to overcome them, and in particular of products formulated *via* HME, which is the focus of this thesis. The analytical techniques commonly employed to characterise products prepared by HME have been reviewed, with an emphasis on nuclear magnetic resonance (NMR), since it is the main technique used in this thesis. Mathematical models, both empirical and mechanistic, of drug dissolution and of the HME process are also introduced.

1.1 Outline of thesis chapters

Chapter 1 presents the motivation of the work, and a background into amorphous solid dispersions and hot-melt extrusion. In addition, a discussion on the use of NMR and MRI techniques in the characterisation of pharmaceutical formulations is provided.

Chapter 2 introduces basic NMR concepts, with a focus on the theory behind the experiments used throughout this thesis. These include: diffusometry, relaxometry, solid-state NMR and 2D NMR.

Chapter 3 reports quantitative measurements of the diffusion coefficient of molten paracetamol and in mixtures with copovidone at a range of industrially relevant temperatures and drug loadings. Additionally, a rheological study to examine the relationship between diffusion coefficient and viscosity is presented.

Chapter 4 discusses the use of solid state NMR spectroscopy and relaxometry and its application to a variety of paracetamol/copovidone systems. An extruded system is compared to a sample that was exposed to high temperature and demonstrates the need for active mixing to obtain homogeneous and amorphous preparations.

Chapter 5 examines intermolecular associations between paracetamol and copovidone in ASD formulations to identify the type of bonds present and the nuclei involved. Several noteworthy experimental techniques were used such as high-field fast-MAS multiple quantum coherence NMR or molten-state COSY NMR.

Chapter 6 applies NMR techniques validated in previous chapters on alternative formulations such as an industrially relevant drug. A design of experiments run investigates the effect of processing parameter on mass transport coefficients and sample micro-structure.

Chapter 7 describes a simple dissolution model that is fitted with parameters calculated in this thesis. The results from the model are validated experimentally. Additionally, a temperature-composition phase diagram is constructed for the paracetamol/copovidone system.

Chapter 8 summarises and discusses the key conclusions drawn from the experimental and numerical work performed in this thesis and explores the scope for future work.

1.2 Drug solubility issues and improvement techniques

The solid dosage oral formulation is the prevailing method for drug delivery; the main advantages being the ease of administration, high patient compliance and flexibility in formulation design [3]. The most important factor to ensure the desired therapeutic effect on a patient is adequate bioavailability. Bioavailability is the fraction of API that incorporates to the circulatory system, and it is controlled by two processes: solubility and permeability.

APIs are increasingly suffering from low solubility. It is estimated that 40% of currently marketed drugs and up to 75% of pharmaceutical chemical entities under development are poorly water-soluble [1]. Often, this means that in order to reach the blood concentration required for pharmacological response, high dosages are administered assuming that only a fraction will solubilise, resulting in waste and potential over-dosing risks.

Numerous strategies to enhance drug solubility have been investigated and they can be classified into three categories: physical modifications, chemical modifications, and the use of additives [6]. A summary is presented in the diagram below:

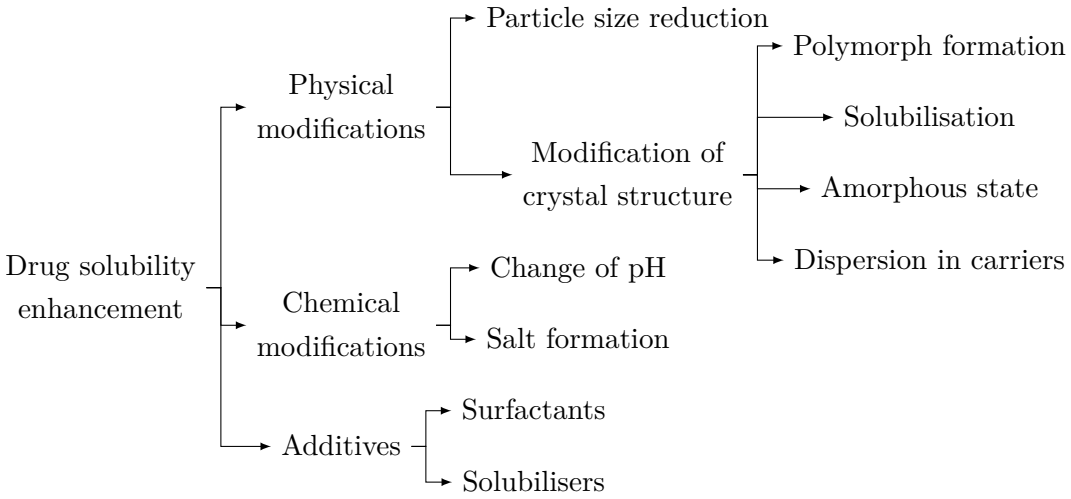

These approaches have been reviewed in detail by Savjani *et al.* and Williams *et al.* [3, 4]. An amorphous solid dispersion (ASD) takes advantage of the amorphous physical state of the drug and its dispersion in a water-soluble carrier, which acts as a stabilizer preventing recrystallization. Compounds in the amorphous state lack the long-range order of crystalline materials in the solid-state, and, consequently, exist at a higher energy than the corresponding crystalline forms. Therefore, the energy penalty to dissociate molecules is lower and this results in a higher solubility [9]. The formation of ASDs is one of the most promising strategies for drug solubility enhancement and some of the main advantages it poses over the approaches outlined in the diagram above are as follows:

- Solubilisation in a solvent results in a liquid dosage form, which is undesirable due to challenges in administration, commercialisation and storage.
- Particle size reduction limit is about $2-5\ \mu m$, which is usually not enough to significantly improve solubility.
- Chemical modifications are complex and compound-specific processes that transform the drug into a new chemical entity and thus require additional regulatory approval.

1.2.1 Biopharmaceutical Classification System (BCS)

As was outlined in the previous section, the most important considerations to ensure that the desired therapeutic effect of a drug is achieved are solubility and permeability. The BCS (Biopharmaceutics Classification System) was developed by Amidon *et al.* [10], and is now used by the US FDA as a framework to describe intestinal drug absorption. It is based on the aqueous solubility (property to dissolve in or make a homogeneous mixture with a solvent

- in this case the gastric juice) and intestinal permeability (ability to penetrate through a solid - in this case the intestinal membranes) characteristics of drugs. Efforts to enhance permeability have not been successful up to date [2].

The BCS definition of "good" solubility is when the highest strength dose is soluble in 250 ml of water at the full range of pH values that might be encountered in the gastrointestinal tract [4]. According to the BCS (Table 1.1), drugs that belong to classes *II* and *IV* display low bioavailability because they are poorly soluble in aqueous solutions. A wide variety of drugs belong to classes *II* and *IV*, such as acetaminophen (analgesic), azithromycin (antibiotic), cyclosporine (immunosuppressant), furosemide (diuretic), ibuprofen (anti-inflammatory), lorazepam (anxiolytic) or phenytoin (anti-convulsant), among many others [11].

Table 1.1 Biopharmaceutical Classification System

	High solubility	**Low solubility**
High permeability	Class *I*	Class *II*
Low permeability	Class *III*	Class *IV*

The European Pharmacopoeia has standardised dissolution testing for pharmaceutical solid dosage forms [12]. There are three conventional dissolution apparatus, from which a certain volume of the dissolution medium is collected at intervals for analysis:

- Paddle apparatus: covered cylindrical vessel with a vertical stirrer along the axis of the container that rotates smoothly.
- Basket apparatus: identical vessel as for the paddle apparatus, but the stirrer consists of a vertical shaft attached to a cylindrical basket, where the dosage form is introduced; the stirrer rotates smoothly.
- Flow-through apparatus: a pump forces the dissolution medium upwards through the flow-through cell, with a filter to prevent the escape of undissolved particles.

1.2.2 Amorphous solid dispersions (ASDs)

Formulation of poorly-soluble compounds for oral delivery presents a serious hurdle in pharmaceutical research and solid dispersions are deemed one of the most promising strategies to improve their oral bioavailability. A solid dispersion is a homogeneous mixture of two or more compounds - a drug and a carrier. Polymeric carriers have been the most successful for solid dispersions because of their ability to stabilise drugs in dispersion [6].

Solid dispersions were first proposed in 1961 by Sekiguchi and Obi as a means to increase drug solubility [13]. They prepared a drug/polymer eutectic mix (physical mixture, typically of very fine crystals, that melts and freezes at a single temperature) through co-melting and fast cooling. There are three different types of solid dispersions according to the molecular arrangement of drug molecules within the carrier (Figure 1.1): dispersed small crystalline

drug particles, amorphous drug particles in the polymer matrix and molecularly dispersed amorphous drug in the polymer (ASDs) [4].

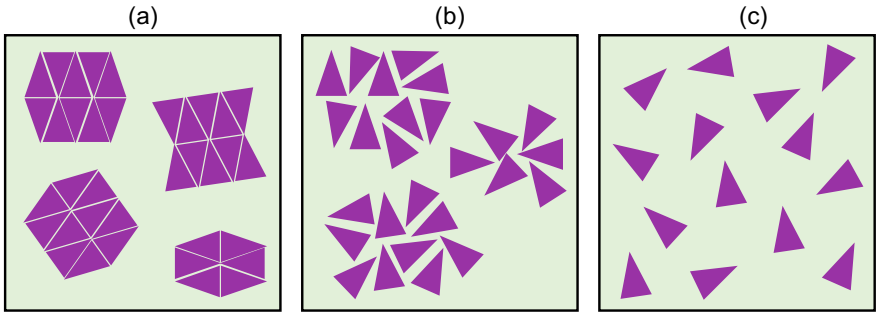

Fig. 1.1 Schematic of the three types of solid dispersions: a) dispersed crystalline drug particles, b) amorphous drug particles and c) molecularly dispersed drug (ASD) (modified from [4]).

A successful ASD is characterized by the presence of amorphous drug, which is dissolved in the polymer, such that the dispersion is homogeneous on a molecular level (Figure 1.1 c). The first to report the formulation of a pharmaceutical ASD were Chiou and Riegelman in 1969 [14]. Since then, there has been extensive research carried out on ASDs and this has been reviewed by Serajuddin *et al.*, Vasconcelos *et al.* and Williams *et al.* [4–6].

Up to several hundred-fold enhancement in dissolution has been reported for ASDs relative to the crystalline form of the drug [8, 15]. Three key features play a role in the increased drug solubility of ASDs: (i) maximised surface area available for dissolution, (ii) reduced intermolecular forces in the solid state, and (iii) increased strength of solute-solvent interactions in solution [4].

(i) Increased drug particle surface area

In the case of a molecular dispersion, the size of drug particles in the carrier is minimized, theoretically, to the size of a single molecule. This provides the maximum available surface area exposed to the solvent, which is a parameter that is directly proportional to dissolution rate according to the well-known Noyes-Whitney model (further details are presented in section 1.2.3). Moreover, the use of hydrophilic, highly water-soluble polymers as carriers also promotes rapid solvent penetration (increased wetting), which enhances dissolution.

(ii) Reduced drug-drug intermolecular interaction

In ASDs, the drug exists in the amorphous form. Amorphous solids lack the tight packaging and highly ordered lattice of crystalline solids. Intermolecular bond strength is strongly dependent on molecular distance, which is increased in the disordered amorphous physical state. Furthermore, it is common for the polymer in ASDs to establish ionic, hydrogen-bond or Van der Waals interactions with the drug. This also reduces drug-drug interactions since bonding sites get occupied with the polymer instead. The strength of intermolecular

drug-drug interactions in an ASD can therefore be greatly reduced compared to that in crystalline compounds, lowering solubilisation energy.

(iii) Increased solute-solvent interactions

Polymeric carriers can increase the aqueous solubility of the drug, so that an apparent supersaturation is achieved in the dissolution medium. The fact that the polymer is molecularly dispersed with the drug can slow crystal growth or altogether inhibit crystal nucleation by interfering with drug lattice assembly. This results in a greater concentration of drug in solution and increased drug-solvent interactions.

The main concern with ASDs is the generally poor predictability of the formulation due to lack of basic understanding of its properties. According to the review by Craig *et al.* there are several important areas of research [8]:

Solid state structure. The choice of polymeric carrier, as well as processing conditions, determine whether the drug is present as a molecular, a crystalline particulate or an amorphous particulate dispersion. Recently, calculations of the free energy of mixing and the Flory-Huggins interaction parameter have been employed to anticipate miscibility and solubility of a drug in a polymer (these models are explained in more detail in section 1.5.1).

Mechanism by which dissolution enhancement occurs. It is believed that the main contributing factors are as outlined above (maximised surface area, reduced intermolecular interactions and increased solvent interactions) but the specific mechanisms are not yet fully understood.

Stability of the ASDs. Typically, the drug/polymer solid solution is in a supersaturated state at storage conditions, which could trigger drug recrystallization. The glass forming ability (GFA) is the ease with which a compound will remain in the amorphous state without recrystallizing. This can provide an insight into the stability of a drug in an ASD [16]. According to their GFA, compounds can be classified into:

- Non-glass formers: drugs that re-crystallize in the first cooling cycle after melting.
- Unstable glass formers: compounds that remain amorphous during the cooling and re-crystallize in second heating cycle.
- Glass formers: compounds that remain amorphous upon cooling and reheating

Reproducibility of formulation properties. The final formulation is highly sensitive to manufacturing conditions and process parameters. Subtle changes in these could greatly influence the properties of the final formulation.

1.2.3 Solubility and the Noyes-Whitney equation

It has been established that solubility, i.e. the amount of solute that can dissolve in a certain volume of solvent, is an essential consideration in the design of solid dosage forms. The kinetics of the solubility process are expressed in terms of the dissolution rate. The dissolution rate is a measure of the pace at which a solute passes into solution and this is equally as important: after oral administration drug dissolution rate should exceed the rate of transit through the gastrointestinal system [4].

The most extensively used thin-film model for drug dissolution up to date is known as the Noyes-Whitney equation. Noyes and Whitney published experimental evidence in 1897 showing that the rate of solution of a solid substance is a diffusion process, which is proportional to the difference between the concentration of the saturated solution and that of the bulk solution [17]. Further contributions from Nernst and Brunner shaped the Noyes-Whitney equation into its final form [18]:

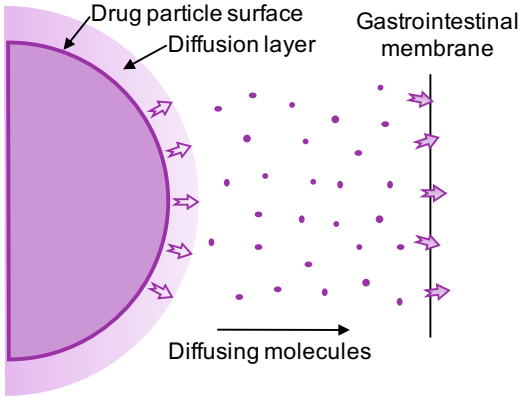

Fig. 1.2 Schematic of the Noyes-Whitney model for drug dissolution rate

$$\frac{dc}{dt} = \frac{AD}{h} \times (c_s - c) \tag{1.1}$$

In equation 1.1, $\frac{dc}{dt}$ is the dissolution rate, A is surface area available for dissolution, D is the diffusion coefficient of the solute, h is the thickness of the diffusion boundary layer (see Figure 1.2), c_s is the solute saturation concentration and c is the bulk concentration of drug at time t. Considering this model, several of the approaches presented in section 1.2.2 to increase drug solubility and dissolution rate can be interpreted [2]:

- Increasing surface area available for dissolution (A) by reducing particle size will directly influence dissolution rate. Alternatively, enhancing wetting characteristics will decrease diffusion boundary layer thickness (h).
- Polymeric carriers that can increase drug solubility to achieve stable supersaturation will effectively increase c_s, thus improving dissolution rate.

Thin-film systems are characterised by a diffusion boundary layer thickness (h) that is small compared to the root-mean-square diffusion length ($\sqrt{4Dt}$). There are several limitations to the Noyes-Whitney model stemming from the fact that it is a thin-film diffusion system [19]: (i) static diffusion layers do not exist in stirred fluids, (ii) h cannot be measured experimentally or obtained *a priori*, and (iii) in the absence of convection the diffusion equations have no steady state solutions. More complex models for which the diffusion layer

thickness could be determined (such as the rotating disc [20]) have been used to solve the Noyes-Whitney model.

1.2.4 Amorphous solid dispersions preparation methods

Preparing an ASD involves dispersing a poorly soluble drug in a water-soluble polymeric matrix. There are two main approaches to achieve ASDs: fusion and solvent evaporation methods [3].

The fusion approach generally consists on melting a drug/polymer physical mixture followed by rapid cooling. The heating, usually to the melting point of the drug to ensure molecular level mixing [21], encourages the drug to disperse in an amorphous physical state and the fast-rate cooling induces solidification before drug recrystallization can occur. This approach is simple and cost-effective, but the components are required to be thermostable. Hot-melt extrusion (HME) is a variant of the straightforward fusion method, in which mixing and homogenization at high temperature is encouraged by rotating screws. HME is the most widely used of the fusion manufacturing processes because the high viscosities of polymers usually require active mixing for preparation of a single-phase formulation.

Other effective and simple high viscosity mixing methods for polymers include rotating mixers and blade blenders. However, these usually require large quantities of material, which is not desirable for drug development due to high material costs. These approaches also do not allow for continuous manufacturing, as HME does, meaning that they are less efficient to run in the long term and could suffer from batch to batch inconsistencies.

Solvent evaporation entails the dissolution of the drug and carrier in a common solvent (typically ethanol or chloroform). The ASD is formed in dissolution and the polymer is then relied on to stabilize the drug in its amorphous state once the solvent is removed. A review on spray drying formulation of ASDs, from the effects of process parameters to scaling-up consideration was published by Singh *et al.* [22]. The way in which the solvent is evaporated (under vacuum, heating, rotary evaporator, spraying, nitrogen stream or slow evaporation at low temperature) gives rise to different variants of the solvent evaporation approach. Spray-drying is the most frequently employed alternative, and it involves spraying the drug/polymer solution into a stream of heated airflow. A review on spray-drying technology, formulation parameters and scaling up has been published by Patel *et al.* [23].

The primary benefit of spray-drying is that there is no risk of thermal degradation of the ASD components (when dried at low temperatures) . However, disadvantages include the use of large amounts of organic solvents, high processing cost, scalability issues, difficulties in completely removing the solvent and the selection of a common volatile solvent (drugs of interest are usually hydrophobic and polymers hydrophilic). It is essential that the solvent be completely removed from the ASD formulation since residual traces could carry toxicity hazards and also increases the likelihood of phase separation and crystallization. On the

other hand, HME is an extremely cost-effective, continuous manufacturing process, easy to scale up and requiring minimal downstream processing as the formulation can be shaped at the outlet of the extruder while heated and malleable.

There are other less frequently used but highly innovative approaches to prepare pharmaceutical ASDs. One such example is supercritical fluid impregnation, where supercritical (fluid state) CO_2 is introduced in a pressurized vessel containing the drug and carrier. The CO_2 swells the polymer matrix and promotes drug dissolution, penetration and mixing. Since CO_2 is a gas at room temperature, it is easily removed upon de-pressurisation. Although ASDs were successfully prepared through supercritical fluid impregnation, HME achieved stronger drug/polymer interactions and greater product homogeneity [24].

Comparative studies characterising different ASD manufacturing approaches have been published. Mahmah *et al.* performed thermal, microscopic and dissolution testing and found higher drug release rate in spray-dried formulations, but improved stability in HME products [25]. Another comprehensive study by Benes *et al.* reported extensive experimental testing and data interpretation was aided by computational analysis (principal component analysis and partial least squares regression analysis) [26]. No fundamental differences in drug surface area or dissolution profiles were observed for HME and spray-dried samples.

Regardless of the method employed, Verma *et al.* have proposed a systematic approach to design solid dispersions of poorly water-soluble drugs [27]. The approach consists of four phases:

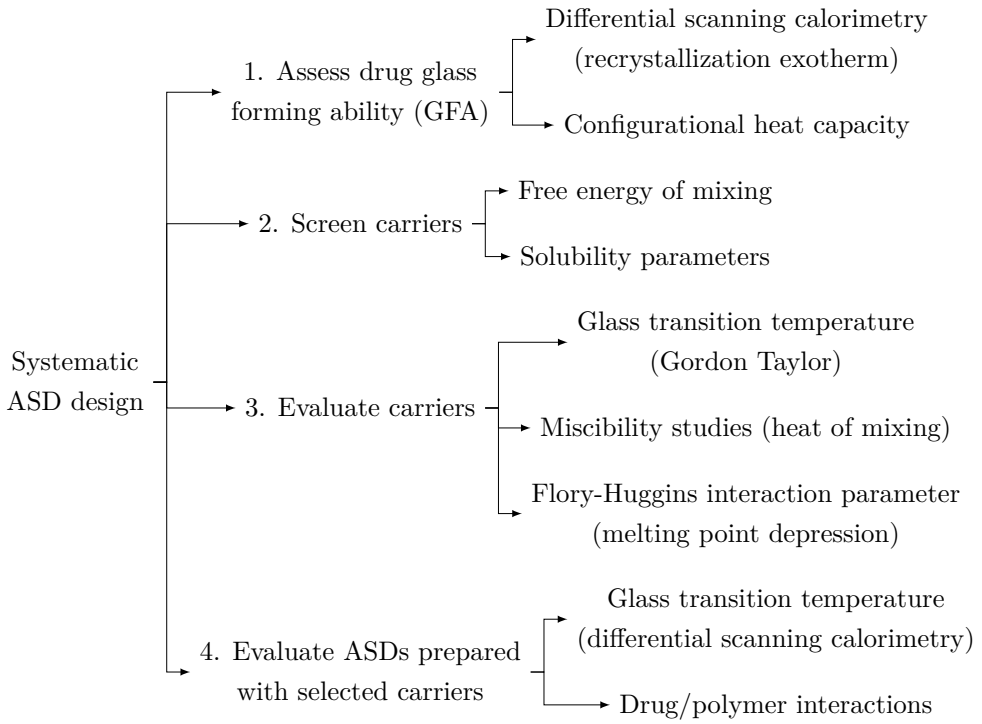

All the experimental and theoretical characterisation techniques mentioned above will be introduced at later stages in this thesis.

1.2.5 Investigations of amorphous solid dispersions

In the past decades, there has been extensive research conducted on ASDs, particularly on the amorphisation of crystalline drugs, the kinetics of recrystallisation, the conditions for physical stability and avoidance of phase separation, solid state micro-structural characterization and solubility and dissolution behaviour of the formulations. A comprehensive review on amorphisation, crystallisation, stabilisation, characterisation and solubilisation was published by Baghel *et al.* [28]. The bulk of the literature can be divided in two fields: physical stability of formulations and dissolution or drug release mechanisms.

Physical stability of ASDs

Phase stability is formally described as the susceptibility of a material to chemical and external pressures that result in changes in the interatomic distances giving rise to the change of relation between repulsive and attractive forces.

There are three indicators of physical stability that are frequently investigated: (i) the glass transition temperature, (ii) likelihood of recrystallisation and (iii) the theoretical limits of drug/polymer solubility and miscibility.

(i) Glass transition temperature

The glass transition temperature (T_g) marks the transition from a glassy (barely mobile) to a rubbery (somewhat flexible) state. ASDs are in a high-energy thermodynamically unstable state. Physical stability is more likely to be maintained, at least over short timescales, if the storage temperature is below the ASD's T_g [4].

The characteristic high viscosity of many polymers is associated with an elevated T_g. High-T_g polymers raise the apparent T_g of a drug in a solid dispersion. The T_g can be be determined experimentally using differential scanning calorimetry (DSC), or estimated theoretically using the Gordon-Taylor equation [29] from the individual component's weight fractions (w) and glass transition temperatures (T_g):

$$T_{g,mix} = \frac{w_{drug} \cdot T_{g,drug} + K \cdot w_{polymer} \cdot T_{g,polymer}}{w_{drug} + K \cdot w_{polymer}} \tag{1.2}$$

where parameter K can be approximated with the Simha-Boyer rule [30] from the densities (ρ) of the drug and the polymer:

$$K = \frac{\rho_{drug} \cdot T_{g,drug}}{\rho_{polymer} \cdot T_{g,polymer}} \tag{1.3}$$

(ii) Drug recrystallisation

The crystalline state is thermodynamically favoured over the amorphous, but an activation energy (for molecules to mobilise and align), has to be overcome to initiate nucleation and crystallisation. Experimentally, this energy is commonly estimated from the configurational heat capacity (ΔC_p). Heat capacity (C_p) is a basic thermal property, defined as the amount of heat that needs to be supplied to a certain mass to produce a unit change in its temperature. Heat capacity can be measured through DSC. The configurational heat capacity is the difference in heat capacity between the crystalline and the amorphous states:

$$\Delta C_p = C_p^{crystalline} - C_p^{amorphous} \tag{1.4}$$

It is generally assumed that dispersions in which no crystalline phase can be detected are amorphous [2]. The most straight forward way to probe for crystallinity is by the presence of a melting endotherm in DSC thermograms.

There are three main mechanisms through which polymeric ASDs hinder drug recrystallisation: drug-polymer intermolecular associations, inhibition of nucleation and reduced molecular mobility.

Drug-polymer intermolecular associations, such as ionic interactions, hydrogen bonding or Van der Waals forces, decrease the likelihood of recrystallisation by holding the drug molecules in place in the dispersion and limiting drug-drug molecular interactions. Traditionally, drug-polymer interactions are probed through FTIR (Fourier-transform infrared spectroscopy), a spectroscopic technique that operates in the infrared wavelength region. Positive deviations from Gordon-Taylor behaviour (where experimental T_g values are greater than estimated values) are also indicative of strong drug-polymer interactions [31–33].

Nucleation is the first step in the formation of a crystalline lattice. It entails the spontaneous self-assembly of a few molecules into a structure upon which additional molecules can attach to for a crystal to grow. The kinetics of nucleation are dependent on the activation energy for molecular diffusion and appropriate alignment to join the incipient lattice. The polymer chains in the ASD increase the activation energy for nucleation by: acting as a diluent and providing physical separation between drug molecules, reducing drug diffusivity and hindering their mobility, and accumulating at the nucleation interface to hinder or prevent further drug molecules from attaching.

A certain extent of molecular mobility is required for nucleation and crystallisation. Non- or unstable-glass formers (compounds with high crystallization tendencies) generally have lower molecular weights and fewer rotational bonds, which increases the probability of the drug exhibiting the appropriate orientation for crystallisation [34]. As mentioned above, polymers' high T_g decreases molecular mobility in ASDs, improving physical stability of amorphous drugs. There is a trade-off to be considered between a high-T_g polymer, which

reduces molecular mobility at storage temperatures, and a low-T_g polymer, which would allow processing at lower temperatures.

(iii) Drug/polymer solubility and miscibility

Solubility and miscibility of drugs in polymers have been widely studied, both theoretically and experimentally, in order to predict the behaviour and drug loading limits in ASDs. This has been done by constructing temperature-composition phase diagrams (Figure 1.3) consisting of three curves: solubility, miscibility and glass transition temperature [35–38]. The solubility curve defines the stable (A and B) and metastable (C and D) regions and the miscibility curve indicates the limit between the metastable and unstable (E and F) domains [39]. Regions B, D and F have enhanced stability over their A, C and E counterparts, respectively, because molecular motion is hindered as the temperature is below the system's T_g.

Drug-polymer miscibility describes the tendency of a liquid (molten or solubilised) drug to disperse in a polymer matrix; while solubility refers to the ability of a polymer to dissolve a solid or crystalline drug [40]. There are several qualitative and quantitative approaches to estimate drug/polymer solubility and miscibility.

Qualitative methods:

- Differential scanning calorimetry is predictive of drug-polymer miscibility when a single T_g is observed. Although this technique is considered the "gold standard", it has limitations: (i) T_g's of individual components have to differ at least by 10°C, and (ii) spatial resolution is 30 nm [41].
- Solubility parameter: the cohesive energy contribution of individual components can be determined using the relationship from Hansen (1967) [42]: $\delta^2 = \delta_d^2 + \delta_p^2 + \delta_h^2$. This takes into account the contribution from dispersion (δ_d), hydrogen bonding (δ_h), and polar (δ_p) forces. Low $\Delta\delta = \delta_{polymer} - \delta_{drug}$ is predictive of miscibility.

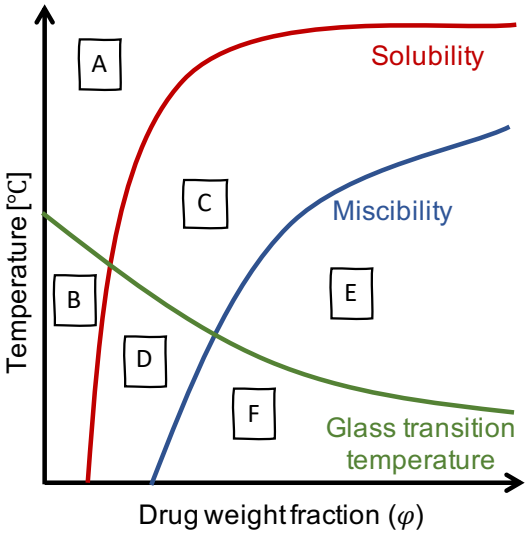

Fig. 1.3 Schematic of a traditional drug/polymer phase diagram.

- Microimaging techniques, such as Raman mapping or hot stage microscopy has been used to evaluate phase homogeneity of ASDs [43]. This method is limited by low spatial resolution (μm scale).

Quantitative methods:

- Flory-Huggins interaction parameter χ, describes the thermodynamic mixing of a drug-polymer system [44, 45]. χ can be calculated from the difference in solubility parameters between drug and polymer, or the melting point depression of the drug in the presence of the polymer. Negative χ suggests miscibility.
- X-ray diffraction (XRD). The XRD pattern of a crystalline material exhibits sharp peaks, while that of an amorphous compound shows a broad pattern. XRD combined with computational methods such as Pair Distribution Function calculations (PDFs) can be used to characterise nearest-neighbour interactions, from which drug-polymer miscibility can be inferred [46].
- In solid-state NMR, a single ^{1}H T_1 relaxation time for drug and polymer indicates miscibility in the 100 nm scale, and a single ^{1}H $T_{1\rho}$ relaxation time for both components estimates miscibility in the 5 nm scale [47, 48].
- High resolution imaging techniques such as atomic force microscopy (AFM) [43], scanning electron microscopy (SEM) [49] or transmission electron microscopy (TEM) [50] can be used to quantitate the growth rates of a drug crystal within polymers.

Dissolution of ASDs

Generally, the main objective for the formulation of ASDs is to improve solubility or dissolution rate of a drug. Therefore the dissolution behaviour of these preparations is studied, often using the standardised dissolution testing apparatus mentioned in section 1.2.1 coupled with UV/Vis spectrophotometers. Ultraviolet/visible spectroscopy is used for the determination of drug concentration in the dissolution medium. Combined with complementary analytical techniques, (i) polymer dissolution as well as (ii) drug release mechanisms have been investigated [51, 52, 43, 53].

(i) Polymer dissolution

Polymer dissolution is a complex phenomena. Several models have been proposed as dissolution behaviour is strongly dependent on the nature of the system (molecular weight, interactions between chains, physical state and solvent) [54–56]. Numerous techniques have been employed to gain a better understanding of polymer dissolution such as FTIR, NMR spectroscopy and imaging, optical and fluorescence microscopy, interferometry and gravimetry [57–61], among others.

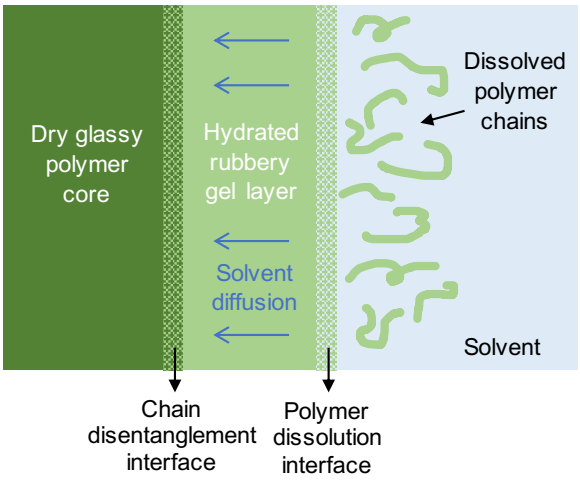

Fig. 1.4 Schematic of polymer dissolution.

Broadly, the dissolution of a polymer involves two transport processes: solvent diffusion and chain disentanglement. In the case of ASDs the carriers of choice are amorphous polymers. Their dissolution is characterised by the formation of a gel layer upon hydration and swelling (Figure 1.4). As the solvent penetrates, it mobilises the polymer chains and these transition from a dry glassy state to a rubbery material as chain disentanglement occurs. When the solvent concentration in the polymer exceeds a certain value, the unwound chains begin to truly dissolve. A comprehensive review of polymer dissolution can be found in [62].

(ii) Drug release mechanisms

Generally drug release rate is characterised through UV/Vis spectroscopy. This technique suffers from limitations, such as certain analytes not being UV-absorbing or that the lack of chemical sensitivity does not allow one to measure the dissolution rate of individual species in a complex formulation. NMR has proven to be an appropriate alternative and it will be discussed in more detail in section 1.4.1.

There are two main mechanisms of drug release from ASDs [63]: dissolution-controlled and diffusion-controlled. Dissolution-controlled processes exhibit a surge of drug supersaturation in the solution as the whole formulation solubilises rapidly. This may be followed by a sharp decline in drug concentration due to crystallisation if the polymer fails to inhibit drug nucleation. In diffusion-controlled dissolution the polymeric matrix is slow-dissolving and the drug has to diffuse out into the medium. Supersaturation is built up gradually and sustained as there is a continuous exchange of dissolved drug between the polymer matrix and bulk solution.

1.3 Hot-melt extrusion

Hot-melt extrusion (HME) was introduced in the 1930's for the plastic, rubber and food industries to mould heated viscous materials into any desired shape [21]. It was investigated for the first time as a manufacturing tool in the pharmaceutical industry by El-Egakey *et al.* in 1971 [64]. In this context, HME is typically performed using a twin-screw extruder, wherein a physical mixture of a drug and polymer are heated, at temperatures up to the melting point of the drug, and intensively mixed to yield a homogeneous product (Figure 1.5).

The assembly, as shown in Figure 1.5, is made up of a motor that drives the rotating screws, an extrusion barrel, and an end-plate die that shapes the product. The key input process parameters are screw speed, drug loading and temperature; and these will determine key characteristics of the process such as residence time or homogeneity of the formulation. Twin-screw extruders are generally preferred over single-screw because they reduce residence time (preventing thermal degradation) and exhibit greater mixing capabilities.

HME is a simple, robust, versatile, efficient, scalable and continuous process. Additionally, it has the ability to enhance the solubility of poorly soluble drugs. Particularly, compared to solvent evaporation approaches, HME is solvent-free and requires less downstream processing, as products can be easily moulded into marketable formulations (avoiding pulverisation and pressing into tablets). Solvent evaporation is less apt for scaling-up as the recovery costs of the evaporated organic solvents would be very high, and the removal of residual amounts of solvent is challenging. The main concerns with HME is that it would not be suitable for thermolabile compounds and that the viscoelastic properties of polymers need to fall within processable limits to be used as carriers. Detailed reviews on HME theory, technology and applications have been published by Maniruzzaman *et al.* [65] and Patil *et al.* [21].

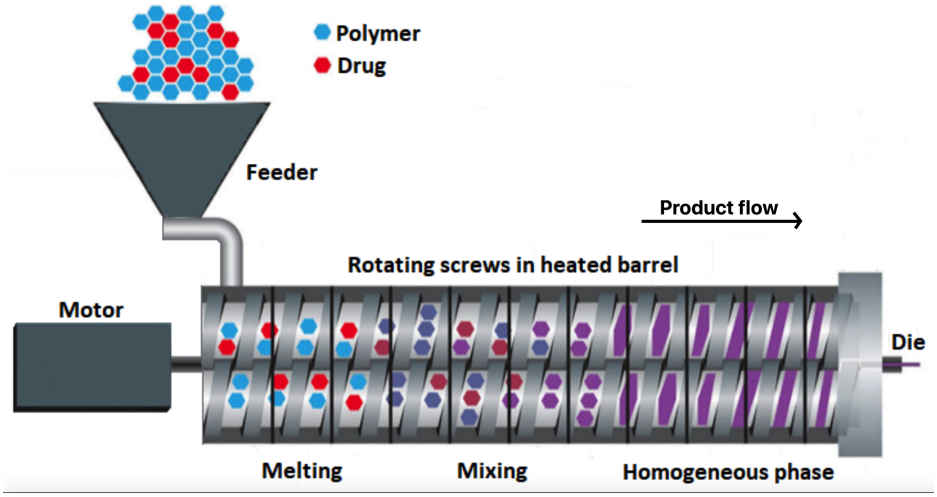

Fig. 1.5 Schematic of the HME process (adapted from [21])

Despite the growth in the application of HME to drug development, there are still substantial gaps in our understanding regarding drug solubility in polymers, product homogeneity, drug-polymer interactions and long-term stability of the formulation, among others. This is further hindered by the complexities involved in modelling (and thus predicting the outcome of) HME and the amount of computational power required for accurate system representations. Furthermore, there are numerous process parameters to be taken into account, such as screw speed, architecture, dimension and rotation; drug loading and particle size; and extruder degree of fill and residence time, to name a few. An encouraging fact, however, is that the number of pharmaceutical products formulated by HME has been rising in recent years (a table with the 11 commercially available formulations in 2014 was published by Li *et al.* [32]). The body of literature investigating pharmaceutical extrusion has also been growing and there are several companies that specialise in HME as a drug manufacturing technology, such as PharmaForm (BioDuro, San Diego, USA) and SOLIQS (Abbott, Maidenhead, UK).

1.3.1 Investigation of HME formulations

Most studies conducted up to the present day have been carried out on the extrusion products. Many analytical techniques have been applied for this purpose, such as: DSC, XRD, SEM, TGA (thermogravimetric analysis), FTIR, HPLC (high-performance liquid chromatography), RS (Raman spectroscopy), NMR and AFM. The literature review presented in this section has focused on three areas (dissolution enhancement, solid-state characterisation and prediction of formulation behaviour), as outlined in the diagram below:

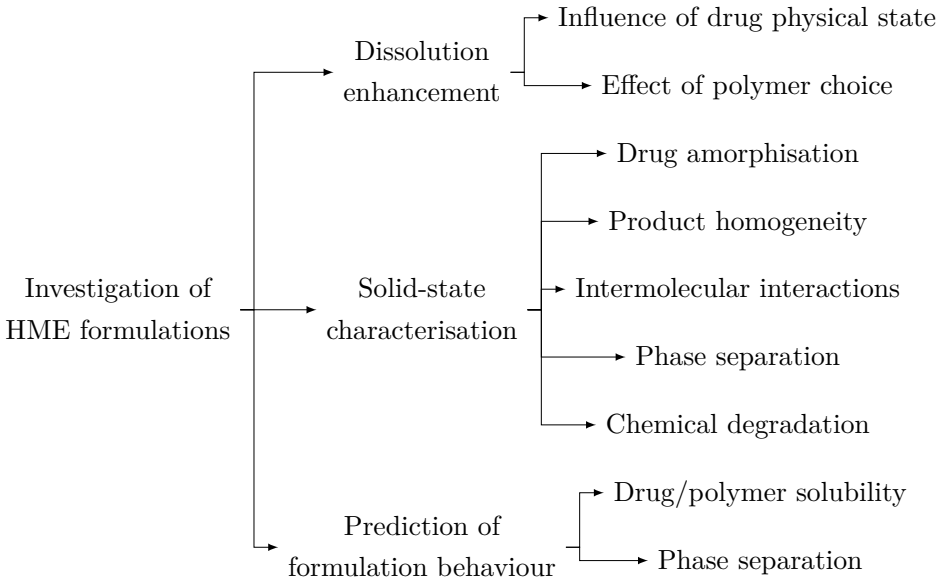

It is generally the case that the maximum dissolution rate enhancement is achieved when complete drug amorphisation is obtained. However, Pina *et al.* showed that, at least for a particular drug/polymer system, the dissolution behaviour of the polymer had a greater influence on the drug release rate than the absence or presence of crystalline drug particles in the formulation [66]. As Craig, reported in his review, there are two mechanisms for drug release: carrier-controlled and drug-controlled. Carrier-controlled drug release is only dependent on polymer behaviour, as the drug readily solubilises in the hydrated polymer layer; whereas in drug-controlled dissolution, the drug is released into the solvent as it was in the formulation [8]. It was reported by Ashour *et al.* that in drug-controlled dissolution, the apparent drug solubility is strongly dependent on the polymer of choice and the drug loading [15].

Solid-state characterisation has been the focus of many publications. XRD is the most widely used technique to probe for drug amorphisation (characterised by a broad signal) or detect the presence of residual crystals (narrow peaks) [43, 67]. Phase separation (homogeneity of drug distribution) has been generally investigated through DSC [68], but its limit of detection is 30 nm at most, so other approaches such as solid-state NMR, XRD and microscopy have been employed to achieve greater resolution [43, 46].

Extensive analysis of drug-polymer systems has been carried out to gain an understanding on the miscibility and solubility behaviour and thus predict phase stability of the formulation. Experimental as well as theoretical approaches have been used to estimate drug solubility in the polymer. Theoretical solubility parameters (introduced in section 1.2.5) were used by Maniruzzaman *et al.* in HME formulations to confirm drug-polymer miscibility [49]. On the other hand, Qi *et al.* employed SEM, DSC and NMR to predict phase separation on extrudates [69]. Sarode *et al.* studied phase separation and drug crystallization at different temperatures and humidity levels during storage, which could lead to chemical degradation, particularly in formulations with low T_g [70].

1.3.2 Analysis of extrusion process parameters

There is also a body of literature investigating the extrusion process itself, particularly with respect to making the optimal choice of processing parameters such as temperature, drug loading or screw rotation speed.

Li *et al.* modelled drug dissolution behaviour by calculating the free energy of mixing (ΔG_{mix}) as this provides an insight into the spontaneity of phase mixing (more on this model can be found in section 1.5.1) [71]. With this information, a temperature-composition phase diagram, like the one shown in Figure 1.3, was constructed to provide miscibility information for coordinates of interest. The phase diagram was corroborated experimentally by extruding at different drug loadings and temperatures and performing XRD and RS on the formulations. Li *et al.* also concluded that the shortage of thermodynamic forces for conditions corresponding to the metastable phase diagram region (between the solubility and miscibility curves) could be compensated for by increasing extrusion screw speed (which raises system entropy).

Alternatively, Van Renterghem *et al.* used viscosity measurements to estimate drug solubility in the polymer [72]. This was based on the plasticising effect (lowering of viscosity) that polymers generally experience when a miscible drug is dissolved in them. The decrease in viscosity is due to an increase in free volume as drug molecules separate polymer chains. On the other hand, when crystalline particles remain undissolved, they act as filler and increase the viscosity of the system.

In-line analysis of HME

In-line monitoring of the HME process is extremely challenging because the harsh environment within an extruder (high temperature, viscous medium and strong mechanical parts moving) makes it difficult to interface to analytical instruments. Among the investigations on extrusion process parameters, there are a few publications that have conducted in-line analysis of HME. For example where analytical techniques (Raman spectroscopy, near-infrared spectroscopy

and Terahertz-Raman) are coupled to the extrusion barrel to collect data during the HME process.

Raman spectroscopy was used by Saerens *et al.* and Van Renterghem *et al.* to investigate the influence of screw speed, drug loading and barrel temperature on crystalline drug dissolution and residence time distribution [73, 74]. Saerens *et al.* (2013) observed that for higher drug loadings (40 wt %) the physical state of the final product was achieved further down the barrel at lower temperatures and also at slower screw speeds. Van Renterghem *et al.* corroborated the aforementioned results, and also noticed that for processing temperatures below the melting point of the drug, increasing screw speed achieves lower residual crystalline drug fraction.

More recently, Bordos *et al.* made use of Terahertz-Raman (THzR) to determine drug solubility in polymer melts during HME [75]. Real-time measurements showed a decrease in the spectral components associated with the crystalline drug. This allowed, for the first time, for the construction of temperature-composition phase diagrams from experimental data.

1.4 Use of NMR and MRI techniques in the characterisation of pharmaceutical ASD formulations

Nuclear magnetic resonance (NMR) is well established as a powerful characterisation technique in pharmaceutical research, as its non-destructive, quantitative and chemically selective. Despite being expensive and time- and resource-intensive, NMR will remain prominent for structural and dynamic characterisation due to its versatility and capability [76]. The role of NMR in the investigation of ASDs can be broadly divided in five categories: high resolution spectroscopy, 2D correlation experiments, relaxometry, diffusometry and imaging.

1.4.1 Investigations of dissolution performance

The performance of many solid pharmaceutical dosage forms depends on their hydration and dissolution capabilities [77]. NMR has benefits over traditional dissolution testing (UV/Vis spectroscopy) due to much greater analyte selectivity and the ability to detect non-UV-absorbing species (*e.g.* sugars). Magnetic resonance imaging (MRI) can be used non-invasively to observe drug dissolution, polymer swelling and water penetration, concentration and diffusion.

Miller-Chou *et al.* reviewed polymer solubility behaviour [62]. They identified three spectroscopic NMR modalities that provide an insight into the dissolution dynamics of polymers:

- ^{1}H spectrum line width: narrowing of ^{1}H resonance signals is indicative of increased polymer mobility.

- Integrated ^{1}H signal: the area of polymer resonances as a function of time can be linked to the amount of polymer in dissolution.
- T_1 constant: the value of T_1 decreases when molecular motion becomes faster.

Additionally, MRI has been used to visualise polymer swelling and dissolution [78, 79]. Fyfe *et al.* determined polymer mobility and polymer distribution in swelling hydrogels [80]. Likewise, Narasimhan *et al.* studied molecular motion during polymer dissolution in water [81]. They showed that for a certain polymer, increasing molecular weight would result in a decrease in solvent penetration rate. Ashraf *et al.* and Hyde *et al.* visualised water penetration into polymer tablets using MRI. Ashraf *et al.* quantified the rate of penetration of the hydration front in slow-release capsule matrices [82]. For a specific system, they determined that the hydration rate was not a limiting step in the drug release process. Despite the spectral overlap between solvent and polymer, Hyde *et al.* achieved quantitative measurements of the concentration profiles for the solvent and polymer with T_1-weighted one-dimensional MRI [83]. This technique was able to resolve the two species due to their distinctive T_1 behaviours.

The main draw-back of MRI is that, to achieve high resolution, experiments are long. Chen *et al.* devised an ultra-fast MRI experiment (RARE - rapid acquisition with relaxation enhancement) to visualise polymer dissolution in water [84]. The achievable spatial resolution was high (469 μm) while experimental time was minimised (less than 3 minutes).

More recently, Coombes *et al.* and Tres *et al.* have integrated flow-through UV/Vis cells with NMR to simultaneously measure dissolution rates of different species in complex formulations [85, 52]. Coombes *et al.* determined the release profiles of three drug substances and lactose from a single tablet through in-line acquisition of ^{1}H spectra [85]. This was possible due to water suppression techniques. Similarly, Tres *et al.* measured the dissolution rates of both the polymer and API in an ASD from the ^{1}H spectra of the dissolution medium. Interestingly, they observed that, at low drug loading, the dissolution performance was governed by the high solubility of the polymer, whereas for the high drug loading formulations it was dominated by the properties of the drug. Tres *et al.* also showed that, while the dissolution profile of the polymer reached a plateau, the drug concentration in solution declined after reaching a maximum, as super-saturation was not maintained so the drug recrystallised and precipitated [52].

1.4.2 Mass transport and diffusivity studies in polymers

A key parameter underpinning tablet hydration, dissolution rate and release profile characteristics is the diffusion coefficient, D [m^2/s]. The term diffusion coefficient alludes to two mass transport phenomena: the self-diffusion of molecules in a homogeneously mixed medium (D_{self}) and the transport diffusion of molecules across a concentration gradient (D_{trans}). A more comprehensive review of diffusion in liquid systems can be found in [86]. Through pulsed-field gradient (PFG) NMR techniques, it is possible to measure the self-diffusion

coefficient of solvents, excipients and drugs in pharmaceutical formulations. Mathias *et al.* compared the mass transport characteristics of a hydrophilic and a hydrophobic drug, of similar size, in a hydrogel using ^{1}H PFG-NMR [87]. The hydrophilic drug had a larger D and the diffusion of the hydrophobic drug was more restricted, as it was held by the swollen polymer layer for longer.

MRI pulse sequences can be preceded by a PFG programme to obtain a diffusion-weighted MRI. The result is a map of diffusion coefficients. Similarly, T_1- and T_2-maps can be acquired. These techniques have been widely used to study the spatial distribution of diffusion coefficients, as well as T_1 and T_2 values to gain a deeper understanding on solvent penetration, polymer swelling dynamics, and drug release kinetics.

Diffusion-weighted MRI (D-MRI) has been extensively used to study polymer hydration through solvent mobility [88]. Using water concentration and D-MRI 1D profiles, Narasimhan *et al.* observed that the diffusivity of water gradually decreased from the solvent interface towards the core [81]. Also, D values within the dissolving polymer increased as dissolution time progressed while those at the polymer-solvent interface remained constant. This evidenced the disentanglement phenomenon: polymer chains become more flexible and polymer-polymer interactions decrease as solvent penetrates. Weisenberger *et al.* Rajabi-Siahboomi *et al.* and Kojima *et al.* obtained similar results by combining D-MRI with T_1- and T_2-MRI [89–91]. Weisenberger *et al.* noted that not only does D decreases towards the core, but also T_1 and T_2 values, despite solvent concentration being constant throughout the hydrated region [89]. This indicated that solvent motions decreased towards the centre, presumably because polymer chains were effectively fixed to the dry region. Furthermore, Kojima *et al.* noted that the D and T_2 values of water in polymer were much lower than those of bulk water, indicating that the hydrating water is in a highly restricted environment, likely interacting with the polymer [91].

D- and relaxation-weighted images have also revealed further insights on drug/polymer tablet dissolution behaviour [92–94]. Madhu *et al.* identified four regions in a dissolving tablet system: unhydrated tablet core, hydrated tablet core, gel layer and bulk solvent [92]. The D and T_2 profiles acquired by Kojima *et al.* revealed a positive correlation between drug release rate and water T_2 in the gel layer [93]. This suggests that water mobility measurements could be adopted as an indicator of drug release dynamics. Baumgartner *et al.* studied polymeric tablets for controlled drug release [94]. In these systems, it was the swollen gel layer that restricted drug mass transport into the solvent. MRI revealed hydrated layer thickness and T_1- and T_2-map determination allowed to quantify polymer concentration and free and polymer-bound water fractions.

Mass transport in polymers can be categorised in terms of the rate of solvent diffusion relative to the rate of relaxation and mobilisation of the polymer chains [95]:

- Case I: diffusion rate controls liquid ingress (Fickian diffusion)
- Case II: polymer chain relaxation is rate-controlling

- Anomalous diffusion: both rates are of similar magnitude

Several studies have used MRI to analyse diffusion in polymers and assess which mass transport mechanism best described the systems under consideration. Tritt-Goc *et al.* investigated the effect of solvent pH on transport behaviour in a polymer through MRI and T_2-maps [96]. Time-dependence of the diffusion front evolution and water penetration and distribution analysis revealed case II diffusion for pH 2 and case I diffusion for pH 6. Obradovic *et al.* combined the use of terahertz (THz) time-domain reflectance spectroscopy with MRI to measure solvent penetration in polymers [97]. Plots of hydration front position versus evolution time indicated case I behaviour.

1.4.3 Characterisation of the solid state structure of ASDs

There are three major solid-state NMR (ssNMR) approaches that have been employed for the characterisation of ASD formulations [98]:

(i) High resolution MAS spectroscopy, *e.g.* ^{13}C CP-MAS (cross polarization magic angle spinning): for the identification and quantification of different solid forms of API. Resonance linewidths are affected by changes in structural properties. Amorphous compounds exhibit broader linewidths due to the increased number of molecular orientations present in unordered solids. High resolution MAS spectroscopy can also determine the presence of impurities and degradation products from the emergence of additional peaks in the spectrum as well as intermolecular associations from chemical shift changes.

(ii) 2D correlation spectroscopy, *e.g.* ^{1}H-^{13}C HETCOR (heteronuclear correlation): for the determination of the structural properties of APIs such as molecular conformations, polymorphism and intramolecular interactions. It can also uncover physical and chemical interactions between drug and polymer. Cross-peaks in correlation spectroscopy reveal spatial proximity or chemical connectivity between the probed nuclei.

(iii) Relaxation times, *e.g.* T_1 and $T_{1\rho}$: for insight into phase separation, physical stability and average estimates of the dimensions of drug and polymer domains. ^{1}H T_1 and $T_{1\rho}$ are affected by spin diffusion and tend to average. The degree of averaging serves as an indicator of the heterogeneity of the sample at the nanometre level. Identical values of ^{1}H T_1 (and/or $T_{1\rho}$) are indicative of an intimately mixed ASD.

The use of high resolution MAS spectroscopy and 2D correlation experiments in the investigation of drug/polymer interactions will be discussed in more detail in section 1.4.4. High resolution spectroscopy for the elucidation of crystalline or amorphous drug physical structure has been widely integrated as part of the routine characterisation of ASDs. Broader drug resonances were observed in ASD samples than in physical mixtures in which the drug was crystalline [51, 47]. Apperley *et al.* (2005) used real-time ^{1}H and ^{13}C band-shape measurements to follow temperature-dependent drug recrystallisation [99].

There are numerous examples of ^{1}H T_1 and $T_{1\rho}$ measurements to assess phase separation and miscibility in the literature [100, 51, 47, 101]. Aso *et al.* observed that the ^{1}H $T_{1\rho}$ of one of the drug/polymer systems under study (nifedipine–PVP) was described by a mono-exponential curve, which suggested miscibility [100]. The other system (nifedipine–PHPA) was described by a bi-exponential equation, indicating that the drug and polymer were immiscible. Song *et al.* detected no drug/polymer phase separation (single ^{1}H T_1 and $T_{1\rho}$ for both species) in the felodipine/copovidone ASDs even after storage for two months at 40°C and 75% relative humidity [51]. Yuan *et al.* obtained the same ^{1}H T_1 for polymer (PVP) and drug (nifedipine) in all the ASDs studied except for the 95% drug loading, and a single ^{1}H $T_{1\rho}$ was identified for all except the 95% and 90% drug loaded ASDs [47]. They used the formula for the length-scale of spin diffusion to estimate the drug domain sizes in the formulations: samples with a unique T_1 were miscible giving domain sizes between 20-50 nm and those with the same $T_{1\rho}$ were determined to have domain sizes smaller than 2-5 nm.

Most recently, Yin *et al.* used ssNMR ^{1}H T_1 and $T_{1\rho}$ to assess *in-situ* thermal mixing of a drug in a polymer [101]. The temperature in the magnet was stepped up from 115°C to 140°C while ^{1}H T_1 measurements were performed. As temperature increased, the T_1 of the drug and the polymer became closer, indicating higher degree of molecular miscibility.

1.4.4 Analysis of drug/polymer interactions in ASDs

It is well established in the literature that drug-polymer interactions can increase the stability of a drug in an ASDs with respect to thermal degradation, drug recrystallization on storage and maintaining supersaturation during dissolution [32, 102]. Strong drug-polymer bonds favour the chemical potential depression and enhance the solubility and miscibility of the drug and polymer. The main types of interactions, in decreasing order of bond energy, are ionic, hydrogen bond, dipole-dipole and Van der Waals.

Traditional approaches to probe for intermolecular associations include FTIR and Raman spectroscopy. These are revealed as a red shift of the spectral band (movement to lower wave number) and/or band broadening. However, as mentioned in section 1.4.3, intermolecular bonds in solid-state ASD formulations can also be investigated by NMR either through high resolution MAS spectroscopy or 2D correlation experiments.

The chemical shift of API and polymer resonances can be affected by changes in structural properties (local magnetic fields or shielding components) induced by the establishing of interactions between them [98]. Usually, solid-state ^{13}C high resolution spectra are required to detect these changes, which can be smaller than 1 ppm, but solution-state ^{1}H NMR resonance line widths can also provide indirect information on drug-polymer interactions. Peak width is proportional to T_2, so that shorter T_2 results in peak broadening. Faster T_2 relaxation can be attributed to decreased rotational mobility; consequently peak broadening could be attributed to strong interactions.

There are numerous examples in the literature of one-dimensional high-resolution (solid-state and solution-state) NMR spectra from which chemical shift differences are used to investigate drug-polymer interactions in ASDs, particularly hydrogen bonds were hypothesised [103, 104, 51, 47, 105, 102, 106, 101]. Generally, chemical shift differences range from 1 to 5 ppm and these occurred toward higher resonant frequencies due to deshielding of the nuclei (^{1}H, ^{13}C and ^{15}N are the most commonly studied). Yuan *et al.* deconvoluted the isotopically labelled carboxylic acid carbon of the drug (the most likely moiety to bind to the polymer) into four peaks at different chemical shifts [105]. These were a result of different drug interaction patterns: drug-drug dimers, drug-drug chains, drug-polymer associations and free drug (Figure 1.6a). Interestingly, drug-drug interactions were gradually disrupted with increasing polymer content, until at 50 wt% they were almost undetectable (Figure 1.6a-d). Recently, Yin *et al.* observed evidence of drug-polymer hydrogen bonding in ^{13}C and ^{15}N spectra at temperatures lower than melting [101].

A 2D correlation experiment is visualised as an intensity plot in which each signal is a function of two frequencies. The position of the peak indicates the presence of magnetic moment coupling (*e.g.* scalar or J-coupling) between the corresponding nuclei. Certain experiments probe for through-space interactions (NOESY, HETCOR) [107] and other sequences explore through-bond interactions (COSY) [108].

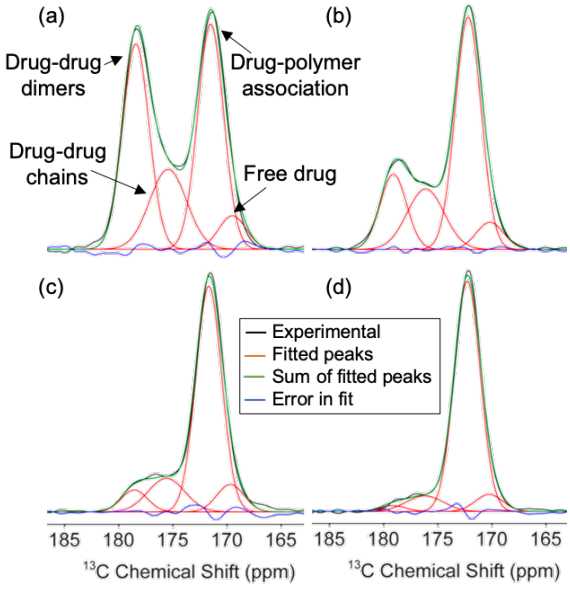

Fig. 1.6 ^{13}C spectra of carboxylic acid in indomethacin/copovidone ASDs at (a) 90 wt%, (b) 80 wt%, (c) 70 wt% and (d) 60 wt% drug loading (modified from [105]).

Solid- and solution-state 2D NMR correlation experiments have been employed to gain a deeper understanding on drug-polymer interactions, structural characteristics and bond strengths [109–112, 43, 106]. Pham *et al.* (2010) performed 2D solid-state analysis on ASDs. Results from heteronuclear correlation (^{1}H-^{13}C) and double quantum coherence (^{1}H-^{1}H) experiments showed that at longer contact times, there was increasing evidence of dipolar coupling. They concluded that a large percentage of molecules must have been in intimate contact to produce the observed results, proving molecular-level interactions between drug and polymer in ASDs [111]. Fule *et al.* and Liu *et al.* conducted solution-state 2D correlation experiments (COSY and NOESY) on drug/polymer mixtures in solution; evidence of ^{1}H-^{1}H coupling was observed between drug and polymer [43, 106].

The diagram below summarises the main NMR and MRI techniques used for ASD characterisation:

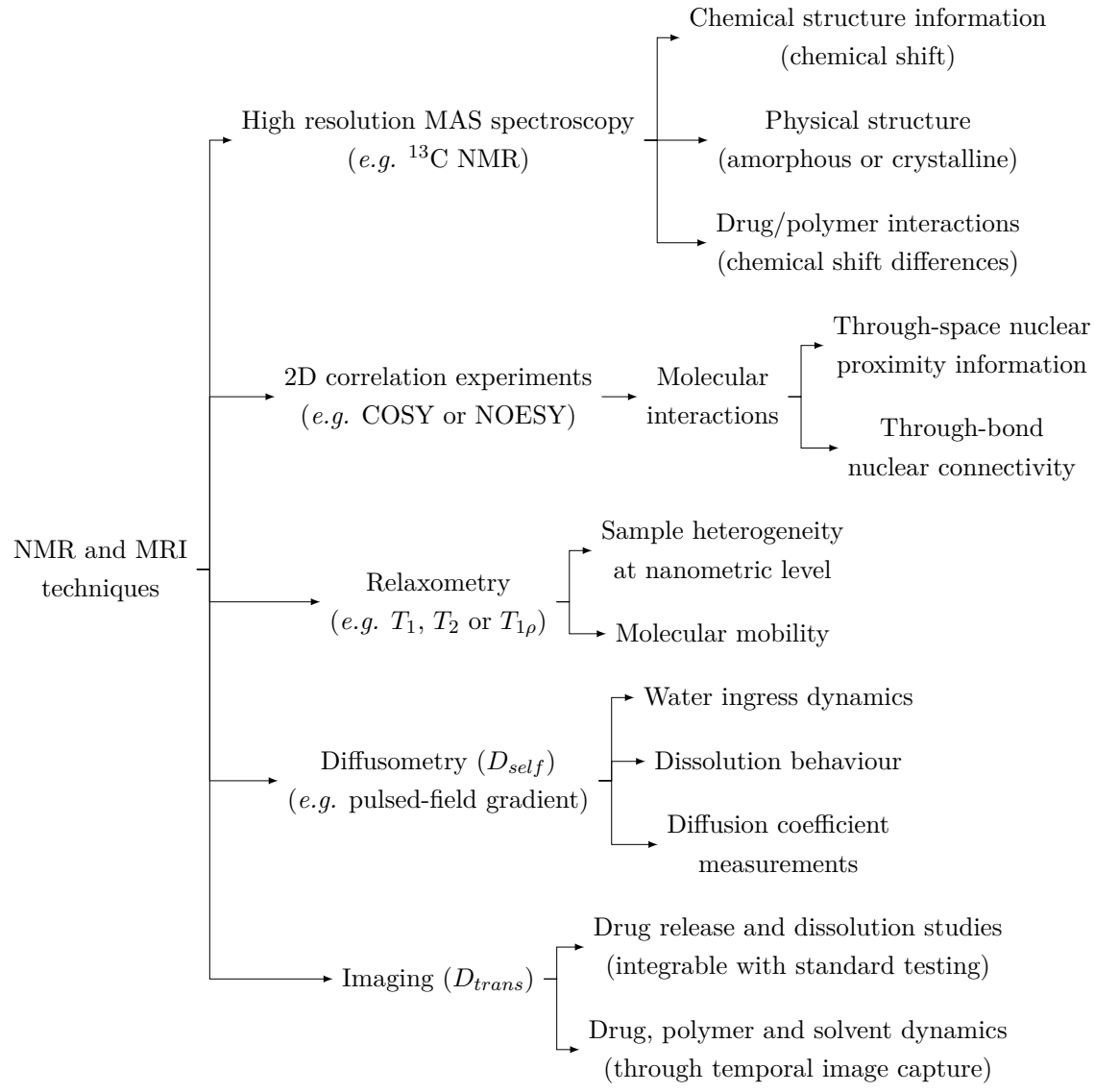

1.5 Modelling the formation and stability of ASDs

Mathematical and computational models are being increasingly implemented in drug development and manufacturing as an efficient approach to understand systems and predict process output. Moreover, regulatory bodies encourage the implementation of techniques that allow quality by design (QbD) of pharmaceutical manufacturing processes [21]. QbD implies gaining knowledge on the processes instead of following a trial-and-error approach until a satisfactory end product is obtained. In the context of ASDs, mathematical and computational models generally aim to estimate drug solubility and miscibility in polymers to avoid phase separation and ensure stability. Similarly, in the context of HME, several

mathematical and computational models have been proposed, frequently to predict optimal processing conditions (*e.g.* temperature, residence time or drug loading). Some focus on the mass transport of drug/polymer in the extruder to predict residence time distributions and others investigate single particle dissolution and interactions to determine the drug particle dissolution time. These models are simplifications of the actual HME process, due to the mechanical complexities and the large number of variables and parameters to consider, but they still require high computational power.

1.5.1 Models for ASD formulation stability

Physical instability in ASDs is likely when there is heterogeneous mixing, where drug-polymer miscibility is poor and where drug loading exceeds the drug/polymer miscibility limit [4]. Miscibility denotes the dissolution of a liquid solute in a liquid solvent and it depends on cohesive (drug-drug and polymer-polymer) and adhesive (drug-polymer) interactions. For drug/polymer miscibility to be favoured, the free energy of mixing (ΔG_{mix}) should be negative:

$$\Delta G_{mix} = \Delta H_{mix} - T\Delta S_{mix} \tag{1.5}$$

Traditionally, DSC is employed to probe for miscibility, where a single T_g is considered satisfactory evidence of drug-polymer miscibility. However, this measurement is not necessarily representative of miscibility at storage (lower temperature) conditions. A mathematical expression for a temperature-dependent miscibility function can be obtained by combining equation 1.5 with the Flory-Huggins theory of mixing or solubility parameters (introduced in section 1.2.5). A more in-depth discussion will be presented in chapter 8. Examples of this application can be found in Marsac *et al.*, Maniruzzaman *et al.* and Calahan *et al.* [113, 104, 48], among others.

1.5.2 Computational models of HME

Mathematical and computational modelling of the HME process has been conducted in the past decades to determine optimal operating parameters and to aid in the development of sensors and controllers. The complexity in formulating an accurate model for HME lies in the number of process parameters and operational variables such as screw rotation speed, barrel temperature, drug loading, filling ratio, residence time and screw elements. Based on a review by Grimard *et al.* HME models can be categorized into five types [114]:

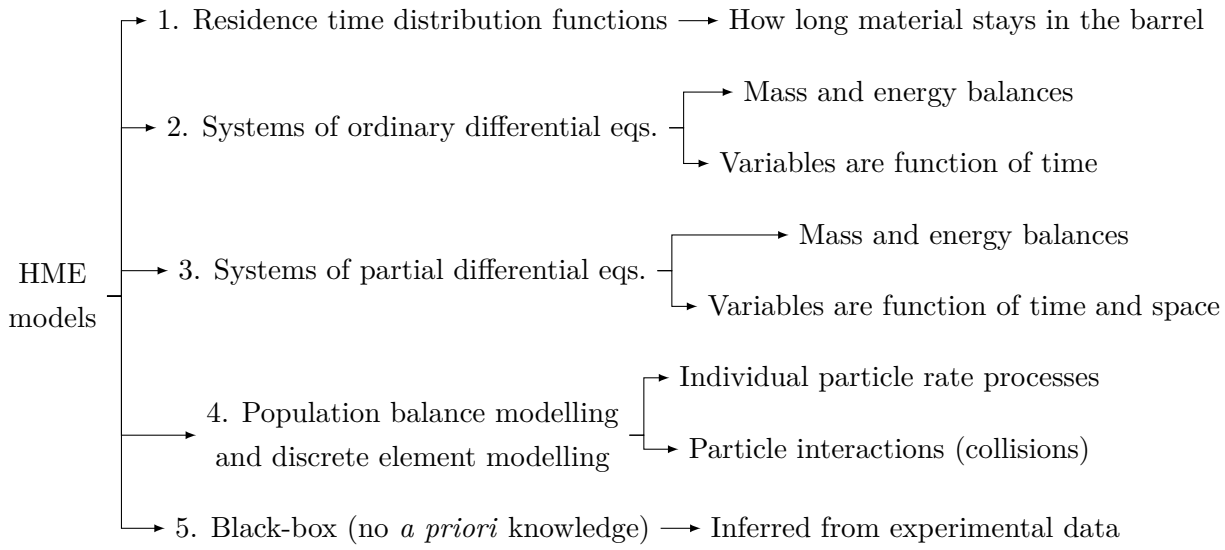

Eitzlmayr *et al.* mathematically characterised the correlation between the axial pressure gradient in the extrusion barrel with the material throughput in one-dimension for a completely filled screw section [115]. This model was further developed by Eitzlmayr *et al.*to account for heat and mass transfer [116]. A system of ordinary differential equations were solved to yield a 1D profile of the filling ratio, pressure, and temperature, and predict residence time distributions. Although the full complexity of HME was not captured in this simplified 1D model, as further experimental and computational work would have been necessary to verify empirical fitting parameters, the model was successful at predicting mixing performance and optimising screw architecture.

Derksen *et al.* built a simplified HME model: spherical drug particles suspended in a viscous matrix subjected to laminar shear flow [117]. They solved the convection-diffusion equations to obtain an estimation of the time to dissolution as a function of shear rate, drug loading, diffusion coefficient and solubility. Schittny *et al.* also explored the links between the formation of ASDs and HME process parameters, but built a more complex model by taking into account extruder and screw geometry [118]. They combined calculations of time to dissolution of solid drug particles in a molten polymer with a model of mean residence time of material in the extruder. With a few exceptions, experimental data supported the validity of the model. These models are considered in more detail in chapter 8.

1.6 Aims and scope of thesis

The primary aim of this thesis is to assess and develop NMR based diffusion techniques to quantify the self diffusion coefficient of drug molecules in polymer melts at temperatures relevant to the hot-melt extrusion process. For this end, a model system of paracetamol and

copovidone will be used. The significance of measuring the mass transport parameter will be explored by using it in drug particle dissolution models to yield system behaviour predictions. The aim is that more advanced versions of these models will eventually be used in industrial settings to anticipate the characteristics of extruded product formulations and accelerate the innovation process.

Additionally, a variety of techniques from the NMR-toolbox will be employed to further characterise amorphous solid dispersions. This will include an analysis of the micro-structure and phase separation behaviour of formulations and an innovative study of drug-polymer intermolecular interactions. Both of these play a crucial role in the investigations of physical stability and suitability of extruded products.

Finally, the techniques developed for the paracetamol/copovidone model ASD system, will be applied to a variety of other systems. These will include a more industrially relevant API (nifedipine), a comparison of three commonly used pharmaceutical polymers (PVP, PVA and copovidone), and HME samples from a design of experiments run in which key process parameters such as temperature, drug loading and screw rotation speed are considered.

Chapter 2

Analytical techniques

2.1 Nuclear magnetic resonance (NMR)

Nuclear magnetic resonance (NMR) was first studied and described in hydrogen molecular beams by the Nobel Laureate Isidor Rabi (1934) [119], and in liquids and solids by physicists Felix Bloch [120] and Edward Mills Purcell [121] in 1946. The NMR phenomenon is based on the absorption and emission of radio frequency (r.f.) electromagnetic radiation from specific atomic nuclei when placed in an external magnetic field. This work led to the development of NMR spectroscopy and the diverse toolbox that is used nowadays to characterise molecular structures, behaviours and dynamics. In this chapter, the fundamental basics of NMR, including several pulse sequences relevant for this thesis are introduced, however the complete and detailed theory of NMR can be found in standard texts, such as the ones by Malcom Levitt and James Keeler [122, 123].

2.1.1 Principles of NMR

The nuclear spin is an intrinsic quantum mechanical property that is characterised by a spin quantum number (I). I represents the number of unpaired nucleons (protons and neutrons) and it can be zero or an integral multiple of $\frac{1}{2}$. Only nuclei with odd number of protons and/or neutrons will be NMR active. The hydrogen atom (^{1}H) is of particular interest because it has a spin number of $\frac{1}{2}$ and is naturally abundant. Other common elements such as carbon (^{12}C) or oxygen (^{16}O) have a spin number of zero, so they are NMR inactive.

In the absence of an external magnetic field, a nucleus displays $(2I + 1)$ degenerate states (meaning that they are all at the same energy level). However, when exposed to an external magnetic field ($\mathbf{B_0}$), the degenerate states unfold to occupy $(2I + 1)$ energy levels. This is known as Zeeman splitting and, in the case of the ^{1}H nucleus, a high (β) and a low (α) energy state can be associated with $I = \frac{-1}{2}$ and $I = \frac{1}{2}$, respectively (Figure 2.1a). This can be considered as the magnetic moments of the nuclei aligning with (α-state) or against (β-state) $\mathbf{B_0}$. The transition between the α and β states is possible through the absorption/emission

of electromagnetic energy packages:

$$\Delta E = \bar{h} \cdot \gamma \cdot B_0 \tag{2.1}$$

where $\bar{h}$ is Planck's constant ($1.055{\cdot}10^{-34}$ J·s), γ is a nuclei-specific constant known as the gyromagnetic ratio (*e.g.* 42.56 MHz/T for ^{1}H) and $\mathbf{B_0}$ is the external magnetic field vector.

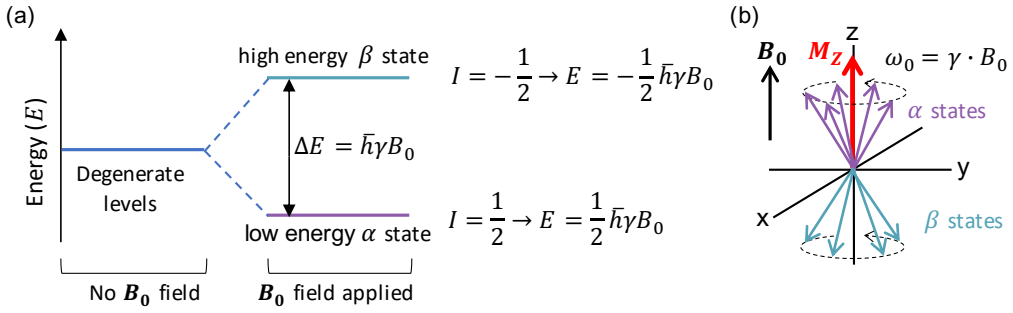

Fig. 2.1 Schematic of (a) an energy diagram depicting the Zeeman splitting effect for the ^{1}H nucleus and (b) a spin system (some in the α and others in the β state) precessing at ω_0 in the presence of an external magnetic field $\mathbf{B_0}$, where M_z denotes the total magnetisation vector.

When a large ensemble of spins is considered, the presence of an external magnetic field influences them to align in its direction; however, random thermal motion opposes this arrangement. The populations of α (N_α) and β (N_β) states follow a Boltzmann distribution:

$$\frac{N_\beta}{N_\alpha} = exp\left(-\frac{\bar{h} \cdot \gamma \cdot B_0}{k \cdot T}\right) \tag{2.2}$$

where B_0 is the external magnetic field magnitude, k is Boltzmann's constant ($1.38 \cdot 10^{-23}$ J/K) and T is the temperature in Kelvin units. Due to the difference in N_α and N_β, the sum of the magnetic moments of all the spins in the system, or the bulk magnetisation ($\mathbf{M}$), will be parallel to $\mathbf{B_0}$. This is known as the Bloch vector model [120], which characterises the magnetisation vector of the entire spin system in terms of the external magnetic field as:

$$\frac{d\mathbf{M}}{dt} = \gamma \cdot \mathbf{M} \times \mathbf{B_0} \tag{2.3}$$

Equation 2.3, describes that the magnetic field exerts a torque that causes $\mathbf{M}$ to rotate (or precess) about the axis of $\mathbf{B_0}$ (Figure 2.1b). The precession angular frequency (ω_0), also known as the Larmor frequency, is derived from equation 2.1 as:

$$\omega_0 = \gamma \cdot B_0 \tag{2.4}$$

This is also the frequency of the electromagnetic radiation emitted when a transition from the β to the α state occurs.

Spin excitation and free induction decay (FID)

At equilibrium, in a magnetic field applied in the z-direction the total magnetisation along $\mathbf{B_0}$ is $M_z = M_0$. In the transverse (x-y) plane $M_{xy} = 0$ because the distribution of the x- and y-components of the equilibrium magnetisation is random (*i.e.* there is no coherence). M_z, however, cannot be detected directly, so the system has to be perturbed (*i.e.* excited) to relocate M_0 to the transverse plane. The excitation required is supplied through a temporary $\mathbf{B_1}$ magnetic field in the form of an r.f. pulse perpendicular to $\mathbf{B_0}$.

For clearer visualisation, the system is considered in the rotating frame at the Larmor frequency about $\mathbf{B_0}$ (*i.e.* the x- and y-axes are rotating about the z-axis, forming the x'-y' plane), Figure 2.2a. If the $\mathbf{B_1}$ r.f. pulse is supplied in the same rotating frame (resonance condition), M_0 will effectively be tilted towards the transverse plane at a 'tip' angle (θ) dependent on r.f. pulse magnitude (B_1) and length (t_p):

$$\theta = \gamma \cdot B_1 \cdot t_p \tag{2.5}$$

The most common pulses are: (i) for excitation ($\theta = 90°$), which tilts the entirety of M_0 to the transverse plane, yielding maximum signal; and (ii) for inversion ($\theta = 180°$), which inverts M_0 to the negative z-axis. Henceforth, the rotating frame (x'-y') will be considered in the context of magnetization vectors.

Once the magnetization has been rotated to the transverse plane ($\mathbf{M_{xy}} = \mathbf{M_0}$), the precession of $\mathbf{M_{xy}}$ is detected by an r.f. coil surrounding the sample. The measured signal (S) decreases in intensity as $\mathbf{M_{xy}}$ spontaneously returns to its equilibrium state at $\mathbf{M_z}$ (Figure 2.2b). This is a process of 'relaxation' and will be explored in the following section. The signal acquired after an excitation pulse is known as a free induction decay (FID, Figure 2.2c).

The FID is a time-domain sinusoidal function that can be expressed as:

$$S(t) \propto M_0 \cdot exp(i \cdot \omega_0 \cdot t) \tag{2.6}$$

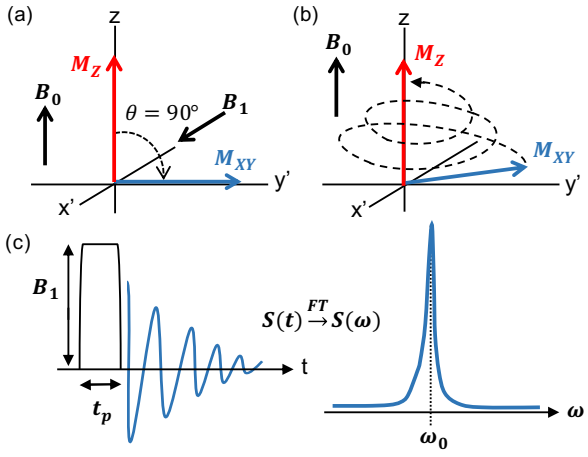

Fig. 2.2 Schematic of (a) $M_z = M_0$ relocated to the x'-y' plane; (b) relaxation of the magnetisation to equilibrium; and (c) free induction decay (FID) signal detected in NMR experiments and its frequency-domain counterpart.

if relaxation effects are ignored.

Interpretation of the FID acquired from a sample is highly complex, as it is generally comprised of a superposition of several periodic signals corresponding to distinct nuclear environments, as well as noise. Local magnetic environments (*e.g.* moving electrons) act to shield/deshield nuclei from $\mathbf{B_0}$, resulting in different effective magnetic fields experienced by the spins. The time-domain signal is converted to a frequency-domain signal, $S(\omega)$, *via* a Fourier Transform (FT) for explicit interpretation (Figure 2.2c):

$$S(t) \xrightarrow{\text{FT}} S(\omega) = \int_{-\infty}^{\infty} S(t) \cdot exp(i \cdot 2\pi \cdot \omega \cdot t) dt \tag{2.7}$$

Frequency units, however, do not provide unambiguous classification of NMR signals because precession frequencies depend on external field strength. For that reason, the unequivocal chemical shift (δ) variable is used, with units of ppm:

$$\delta = \frac{\omega_0 - \omega_{ref}}{\omega_{ref}} \cdot 10^6 \tag{2.8}$$

where ω_{ref} is the Larmor frequency of a reference compound. For solution-state ^{1}H and ^{13}C NMR, tetramethylsilane (TMS) is accepted as the internal standard for calibrating the chemical shift scale. Chemical groups have characteristic chemical shifts that can be used to identify compounds, and this is the foundation of NMR spectroscopy.

Relaxation processes

Relaxation is the mechanism by which magnetization returns to equilibrium. This is a spontaneous process driven by random thermal motion and exchanges with the environment (lattice). In this section, the T_1 and T_2 relaxation constants are described based on the Bloch equation (extended form of equation 2.3, which did not account for relaxation effects).

Spin-lattice, longitudinal or T_1 relaxation is the recovery of magnetisation along the z-axis due to energy exchange between the nuclear spins and their surroundings (lattice).

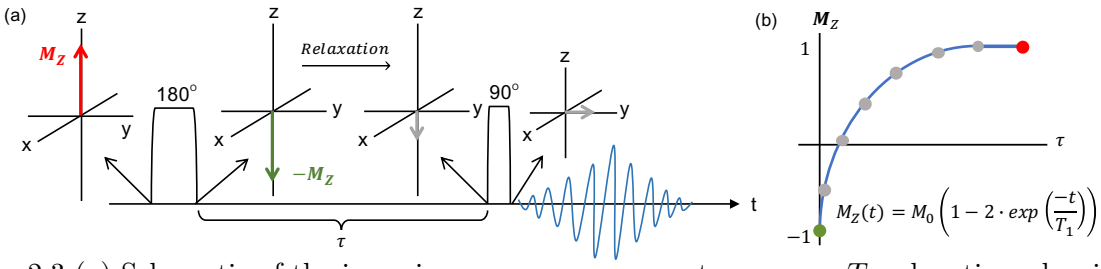

Fig. 2.3 (a) Schematic of the inversion recovery sequence to measure T_1 relaxation, showing the evolution of magnetisation throughout the pulse sequence. (b) Typical inversion recovery plot for a range of delays (τ).

The most common approach to measure T_1 is through the inversion-recovery pulse sequence [124] (Figure 2.3a). M_z is inverted with a 180° pulse, followed by a variable delay (τ) during which the magnetisation begins to recover. Then a 90° pulse is applied, allowing the signal to be recorded. The T_1 constant provides a guideline for selecting appropriate repetition time (T_R), which is the delay allowed between experiments, and it is described as follows (Figure 2.3b):

$$\frac{dM_z}{dt} = -\frac{M_z - M_0}{T_1} \rightarrow M_z(t) = M_0 \left[1 - 2 \cdot exp\left(\frac{-t}{T_1}\right)\right] \tag{2.9}$$

Spin-spin, transverse or T_2 relaxation characterises the loss of phase coherence in the plane perpendicular to $\mathbf{B_0}$. There are two factors that contribute to transverse magnetisation decay: (i) an irreversible component caused by molecular interactions (T_2) and (ii) a reversible component produced by inhomogeneities in $\mathbf{B_0}$ (T_{2,B_0}). The combined effect of these two factors gives rise to the apparent transverse relaxation time (T_2^*):

$$\frac{1}{T_2^*} = \frac{1}{T_2} + \frac{1}{T_{2,B_0}} \tag{2.10}$$

The peaks' full-width at half-maximum (FWHM) in a spectrum are proportional to $\frac{1}{\pi T_2^*}$.

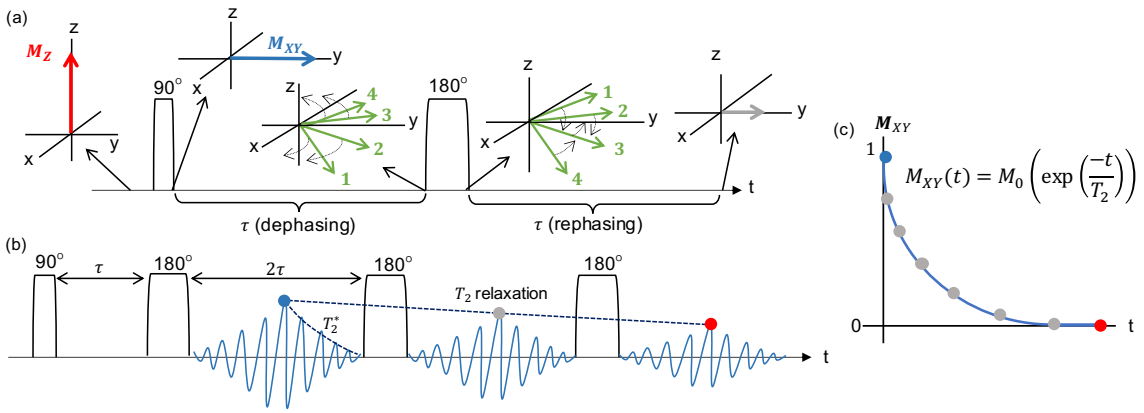

Fig. 2.4 (a) Schematic of the spin-echo sequence to measure T_2 relaxation, showing the evolution of magnetisation throughout the experiment. Schematic of (b) the CPMG sequence, depicting the difference between T_2 and T_2^* relaxations; and (c) a typical CPMG plot for a range of (180°) refocusing pulses.

T_2 relaxation can be measured through the Carr-Purcell-Meiboom-Gill (CPMG) sequence [125], which is based on the spin-echo experiment. The spin-echo sequence (Figure 2.4a) compensates for the reversible spin dephasing effects caused by field inhomogeneities, which are constant throughout the experiment, to reveal the 'pure' T_2 processes, which are random. After a 90° pulse, the magnetisation dephases due to molecular and inhomogeneous field effects, at a rate defined by T_2^*. A 180° pulse is then applied to refocus the phases of the

dephasing spins, causing them to rephase, until the only loss of coherence is that due to the irreversible T_2 effects.

In the CPMG sequence a spin-echo is followed by a train of equally spaced 180° pulses (Figure 2.4b). By repeating this sequence with varying numbers of refocusing pulses, the T_2 relaxation can be found according to the following equation (Figure 2.4c):

$$\frac{dM_{xy}}{dt} = -\frac{M_{xy}}{T_2} \rightarrow M_{xy}(t) = M_0 \left[exp\left(\frac{-t}{T_2}\right)\right] \tag{2.11}$$

2.1.2 Diffusometry: Pulsed-field gradient (PFG) NMR

Diffusion is the passive movement of particles suspended in a medium. If it is driven by a chemical gradient generated by differences in concentration of species, it is known as transport diffusion (D_{trans}). Diffusion can also be used to describe the Brownian (random) motion of molecules suspended in a fluid. This is the case for self-diffusion D_{self}, which can be measured with PFG NMR techniques as will be described in this section.

Magnetic field gradients

As mentioned before (and shown in equation 2.4), the Larmor frequency is dependent on the magnetic field strength (B_0). Applying a linear magnetic gradient ($\mathbf{g}$), in any given direction ($\mathbf{r}$), results in a spatial dependence of spin Larmor frequency ($\omega(\mathbf{r})$):

$$\omega(\mathbf{r}) = \gamma(B_0 + \mathbf{g} \cdot \mathbf{r}) \tag{2.12}$$

Once the gradient is removed, the spins return to their original precession frequency, but with a relative phase shift, ϕ, which is a function of the gradient applied and the time over which it was applied (δ):

$$\phi(\mathbf{r}) = \gamma \cdot \delta \cdot \mathbf{g} \cdot \mathbf{r} \tag{2.13}$$

δ is typically in the order of a few milliseconds, and for this reason the technique is called pulsed field gradient (PFG) NMR.

In the case that the spins remain in their initial positions, application of a second gradient, identical to the first but of opposite polarity ($-\mathbf{g}$), results in all of the spins being rephased. Neglecting relaxation effects, the initial magnetisation $\mathbf{M_{xy}}$ is recovered. In the case that the spins evolve (diffuse) for a time (Δ), the second magnetic gradient experienced by the individual spins will not be of the same magnitude but inverse polarity to the first one, which will result in incomplete recovery of the spin phases. The net phase shift after the second gradient will be a function of the spins' initial ($\mathbf{r_i}$) and final ($\mathbf{r_f}$) positions:

$$\phi(\mathbf{r}) = \gamma \cdot \delta \cdot \mathbf{g} \cdot (\mathbf{r_i} - \mathbf{r_f}) \tag{2.14}$$

In a system undergoing Brownian diffusion, the spins will have moved randomly, so the $\mathbf{M_{xy}}$ magnetisation will remain in the same orientation, but have a lower magnitude than before the gradients were applied. The relationship between the diffusion coefficient (D) and the intensity of the signal measured ($S(\mathbf{g})$) is known as the Stejskal-Tanner equation [126]:

$$S(g) = S(0) \cdot exp\left[-D \cdot (\gamma \cdot \delta \cdot g)^2 \cdot \left(\Delta - \frac{\delta}{3}\right)\right] \tag{2.15}$$

where $S(0)$ is the signal intensity in the absence of gradients, $\mathbf{g}$ is the gradient strength and δ its duration, and Δ is the observation time between the two gradients. The term $\frac{\delta}{3}$ accounts for diffusion during the application of the gradients. It should be noted that relaxation occurs during the measurement and that is why, in practice, the NMR signal is acquired for different values of gradient strength ($\mathbf{g}$) while maintaining δ and Δ the same.

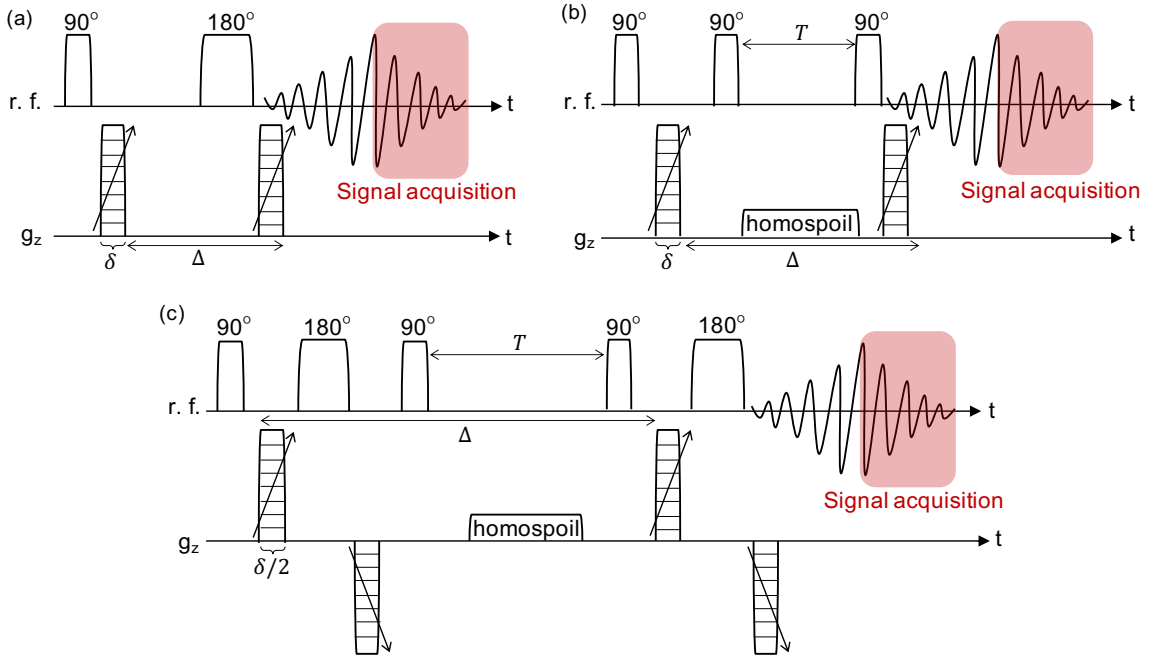

Fig. 2.5 Schematic of (a) the pulsed-gradient spin-echo (PGSE), (b) the pulsed-gradient stimulated-echo (PGSTE), and (c) the alternating pulsed-gradient stimulated-echo (APGSTE); where Δ and δ are the pulse interval and duration respectively and T is the storage period.

PGSE

The pulsed-gradient spin-echo (PGSE) sequence [126] is one of the most basic NMR techniques for measuring diffusion coefficients and it is based on the spin-echo experiment presented in the previous section (Figure 2.4a). As shown in Figure 2.5a, in the PGSE sequence the magnetic field gradients are applied with the same polarity and magnitude. The second gradient comes after a refocusing 180° pulse, which has the same effect as applying a gradient of opposite polarity. The sequence is repeated after a recycle time (T_R) with increasing

gradient strengths and the intensity of the measured signal is fitted to the Stejskal-Tanner equation (equation 2.15) to obtain a diffusion coefficient (D).

The main issue with the PGSE sequence is that signal attenuation will occur due to T_2 relaxation (as in the spin-echo sequence) during Δ. In systems with short T_2 values or slow diffusing particles that require long observation times, there will be no spin coherence by the time of acquisition

PGSTE

The pulsed-gradient stimulated-echo (PGSTE) sequence [127] is an alternative to the PGSE. As shown in Figure 2.5b, the PGSTE experiment is comprised of three sequential 90° pulses. The first one rotates magnetisation to the transverse plane, the second one rotates it to the negative z-axis. In this state, the spins no longer dephase according to T_2, but undergo only T_1 relaxation (of particular interest for systems in which $T_1 \gg T_2$). Consequently, longer observation times (Δ) can be used, which is necessary for slow-diffusing particles, such as those suspended in viscous media. During this 'storage' period (T) a spoiler gradient (homospoil) is applied to dephase any magnetisation that remains in the transverse plane due to pulse imperfections, which gives rise to unwanted spin-echoes.

APGSTE

A further improvement is the use of bipolar gradients in the alternating pulsed-gradient stimulated-echo (APGSTE) sequence [128]. As shown in Figure 2.5c, the APGSTE is based on the PGSTE experiment, but includes two refocusing pulses between the magnetic gradients of opposite polarity.

The APGSTE improves NMR diffusion measurements in heterogeneous systems, particularly when components have different magnetic susceptibilities. This usually generates local background gradients, which may cause excessive signal attenuation and a systematic error in the diffusion measurements. The 180° pulse recovers the dephasing effects of the local background gradients, under the assumption that the diffusing molecules experience a constant internal gradient during the experiment.

It should be noted that a modified Stejskal-Tanner equation is required to calculate the diffusion coefficient from APGSTE data:

$$S(g) = S(0) \cdot exp\left[-D \cdot (\gamma \cdot \delta \cdot g)^2 \cdot \left(\Delta - \frac{\delta}{3} - \frac{\tau}{2}\right)\right] \tag{2.16}$$

where τ is the time between each of the gradient pulses in a pair of opposing gradients. If τ, which is dependent on the length of the 180° pulse, were insignificant, then equation 2.16 would tend to the traditional Stejskal-Tanner equation (equation 2.15).

2.1.3 NMR profiles: 1D imaging

An NMR profile is a one-dimensional image, or intensity plot that spatially maps the concentration of a certain nucleus along the desired axis (Figure 2.6a). 1D spatial resolution is achieved through a magnetic field gradient, in a similar way as it is used to quantify spin mobility (diffusion). An imaging gradient along the z-direction causes spins to precess at different frequencies (equation 2.12). The signal ($dS(t)$) obtained from a slice in the sample (dV) when a gradient $\mathbf{G}$ is applied in direction $\mathbf{r}$ (neglecting relaxation effects and considering it in the rotating frame) is proportional to:

$$dS(\mathbf{G},t) \propto \rho(\mathbf{r}) \cdot exp(i \cdot \gamma \cdot \mathbf{G} \cdot \mathbf{r} \cdot t) dV \tag{2.17}$$

$$S(\mathbf{G},t) \propto \int\int\int \rho(\mathbf{r}) \cdot exp(i \cdot \gamma \cdot \mathbf{G} \cdot \mathbf{r} \cdot t) d\mathbf{r} \tag{2.18}$$

where $\rho(\mathbf{r})$ is the spin density in the considered voxel. By defining a reciprocal term (or k-space) [129]:

$$\mathbf{k} = \frac{\gamma \cdot \mathbf{G} \cdot t}{2\pi} \tag{2.19}$$

equation 2.18 can be simplified. Signal intensity ($S(\mathbf{k})$) and spin density ($\rho(\mathbf{r})$) become a Fourier transform pair:

$$S(\mathbf{k}) \propto \int\int\int \rho(\mathbf{r}) \cdot exp(i \cdot 2\pi \cdot \mathbf{k} \cdot \mathbf{r}) d\mathbf{r} \tag{2.20}$$

$$\rho(\mathbf{r}) \propto \int\int\int S(\mathbf{k}) \cdot exp(-i \cdot 2\pi \cdot \mathbf{k} \cdot \mathbf{r}) d\mathbf{k} \tag{2.21}$$

This implies that an acquired time-domain signal ($S(\mathbf{k})$) can be Fourier transformed to yield a spin density ($\rho(\mathbf{r})$) map or image.

The pulse sequence for such an experiment is shown in Figure 2.6b: the initial excitation pulse is followed by a gradient that phase-encodes the positions of the spins along the chosen direction. The spins acquire relative phase differences when the gradient is removed. The 180° pulse then refocuses the magnetisation in the transverse plane and a second gradient (applied in the same direction as the first, but for twice as long) rephases the signal. With respect to k-space definition, the first gradient sweeps from the center of k-space to the positive edge, the 180° pulse moves the spins to the negative edge and the second gradient (twice as long as the first) reads one whole line of k-space ($S(\mathbf{k})$) while signal is acquired (Figure 2.6c). Resolution in additional Cartesian coordinates to obtain 2D and 3D signal intensity images can be obtained by applying field gradients along these axes to frequency-encode the spatial location of spin-packets.

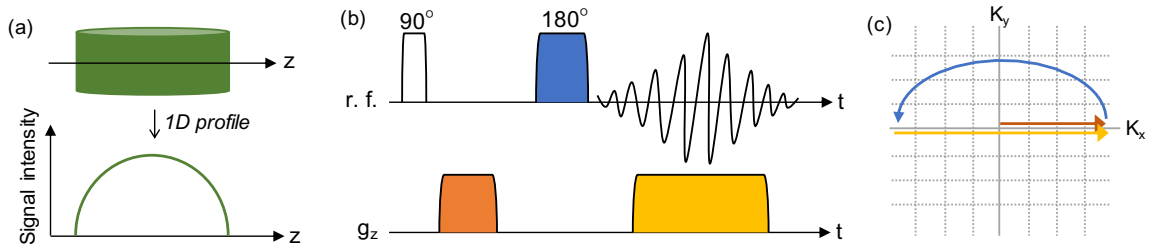

Fig. 2.6 (a) Diagram illustrating the 1D profile from a cylindrical sample when a gradient is applied, (b) schematic of the pulse sequence to acquire 1D profiles (along the z-axis), and (c) a Cartesian representation of k-space color-coded to match the pulses shown in (b). Each of the intersections in (c) represents a different k-space coordinate.

2.1.4 Solid-state NMR for miscibility studies

Solid-state NMR (ssNMR) is an independent field within the magnetic resonance toolbox. In the context of this thesis, and for the sake of brevity, this section will focus on the basic principles of ssNMR and its uses in the context of miscibility and phase separation studies [76, 98, 130].

The local magnetic field experienced by a nucleus (and thus its resonant frequency) is dependent on the external field (B_0) and a shielding factor, determined by the distribution of surrounding electrons and the orientation of the molecular fragment the nucleus belongs to with respect to B_0. Unlike in liquids, molecular tumbling is absent in solids; consequently, for a powder sample in which all orientations are statistically possible, a certain nucleus in a molecule will precess at a range of frequencies, which results in severe broadening (lack of resolution) of resonances. This is known as chemical shift anisotropy (CSA). In liquids, the continuous molecular tumbling averages out the orientation-dependent contributions to its frequency spectrum.

The line-broadening phenomenon in solids is further exacerbated by all the orientation-dependent nuclear spin couplings. A coupling interaction between two nuclei occurs when a spin can exist in different energy levels depending on the state of a neighbouring spin. There are three types:

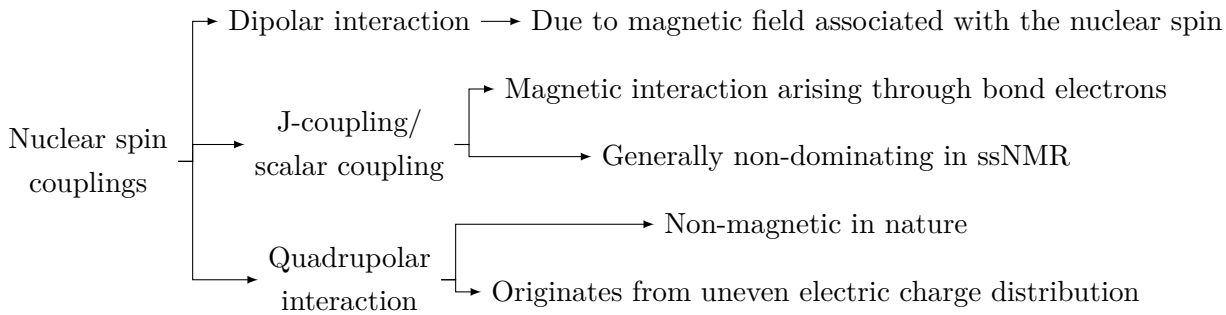

Andrew *et al.* (1958) and Lowe (1959) were the first to describe that spinning a solid sample at high speeds (∼kHz) at a specific angle with respect to B_0 (θ_m=54.74°) averages out the orientation-dependence of spin interactions outlined above [131, 132]. This is known as magic angle spinning (MAS) and if the rotating frequency was infinitely high, all anisotropy would be averaged. In practice, the highest MAS frequency routinely achievable is ∼70 kHz, which averages J-couplings and quadrupolar interactions. However, it usually results in a limited improvement for strong dipolar couplings, particularly in nuclei with high gyromagnetic ratio, as is the proton. Another characteristic of MAS spectra is the appearance of spinning side-bands at integer multiples of the spinning frequency [133].

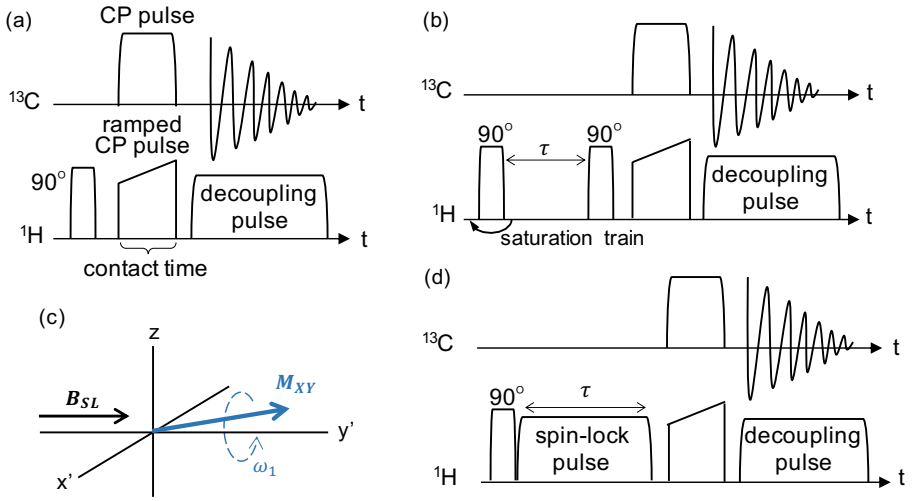

Fig. 2.7 Schematic of (a) cross-polarization (CP), (b) saturation recovery for ^{1}H T_1 *via* ^{13}C detection, and (d) ^{1}H $T_{1\rho}$ *via* ^{13}C detection pulse sequences for solid-state NMR. (c) Diagram illustrating the magnetisation vector during the application of a spin-lock pulse.

High resolution proton studies are hampered by the excessive line broadening effects due to the strong nature of the ^{1}H–^{1}H dipolar couplings, which even at high MAS rates and with the use of decoupling techniques are only partially reduced. For this reason, it is more common to acquire spectra from less abundant nuclei, such as ^{13}C. In this case, heteronuclear decoupling to remove ^{1}H–^{13}C dipolar coupling (such as SPINAL-64 [134, 135]) is highly effective, but the ^{13}C nucleus is so rare (1% natural abundance) that the sensitivity of the measurement is very low. Therefore, cross-polarization (CP) is applied before heteronuclear decoupling. CP is a pulse sequence (Figure 2.7a) that exploits the dipolar coupling between an abundant and a rare (or low-γ) nucleus. It not only increases sensitivity through magnetisation transfer of coupled spins, but it also reduces experiment time (T_R) due to the shorter T_1 relaxation of abundant (a) spins compared to that of dilute (d) nuclei (usually up to three orders of magnitude). For magnetisation transfer to be efficient, both nuclei need to be irradiated

fulfilling the Hartmann-Hahn condition [136]:

$$\gamma_a \cdot B_{1a} = \gamma_d \cdot B_{1d} \tag{2.22}$$

This condition ensures the ^{1}H and ^{13}C spin systems are in thermal contact, which enables the flow of energy. As shown in Figure 2.7a, the CP contact pulse is ramped. This was proposed by Metz *et al.* as it improved the performance of the conventional CP sequence, particularly for ^{1}H–^{13}C CP [137].

Relaxation measurements in ssNMR carry information on nuclear dynamics and nanometric-level structural conformation. In solution-state NMR T_1 and T_2 are usually of the same magnitude, but in solid-state T_2 is generally three to seven orders of magnitude shorter than T_1. There is another relaxation constant that is relevant in solids: the spin-lattice relaxation time in the rotating frame, or $T_{1\rho}$. It is defined as the decay of signal when magnetisation is held aligned to an axis in the transverse plane by a spin-lock pulse, B_{SL}, (refer to Figure 2.7c). T_1 is sensitive to rapid molecular motions in the MHz scale and $T_{1\rho}$ to slower molecular motions in the kHz regimen. Statistically identical values of ^{1}H T_1 and $T_{1\rho}$ is an indication of an intimately mixed system in the 10-100 nm and 1-10 nm scale, respectively.

For abundant nuclei such as ^{1}H, T_1 and $T_{1\rho}$ are strongly affected by spin diffusion, which is defined as the spontaneous transfer of magnetization between neighbouring spins. The characteristic length scale (L) of spin diffusion is:

$$L = \sqrt{6 \cdot D_{SP} \cdot t} \tag{2.23}$$

where D_{SP} is the spin diffusion coefficient of the system and depends on the distance between neighbouring protons and t is the time constant associated with the diffusion process.

If the sample is an intimate mixture of two or more compounds, spin diffusion effects result in the measured relaxometry constants being closer together to one another (due to averaging) than the intrinsic ones. The degree of averaging is associated with the heterogeneity of the sample at the nanometric scale. Since ^{1}H spectral resolution is low in ssNMR, T_1 and $T_{1\rho}$ are measured *via* ^{13}C MAS-CP with dipolar decoupling (pulse sequences shown in Figure 2.7b and d).

Saturation recovery [138] is used in ssNMR instead of the inversion recovery sequence introduced in the previous section because there is no need for T_R to be $5\times T_1$, which significantly reduces experimental time, especially in crystalline solids that have long spin-lattice relaxation constants. In this pulse sequence, a train of 90° saturation pulses transfer all magnetisation to the transverse plane and dephase the spins so that there is no coherence and thus the initial $M_{xy} = 0$. The system is allowed to evolved for an increasing delay, τ, during which magnetisation begins to relax in the longitudinal direction. When a second 90° pulse is applied, the component of the total magnetisation that had relaxed towards the

z-axis is tipped to the transverse plane and recorded (Figure 2.7b). For the shorter delays, little signal is acquired, whereas for the longer ones almost the total magnetisation is recorded according to the expression:

$$M_z(t) = M_0 \left[1 - exp\left(\frac{-t}{T_1}\right)\right] \tag{2.24}$$

Similarly, the decay of magnetisation along the spin-lock field (applied for a variable length of time, τ) is described as follows:

$$M_{SL}(t) = M_0 \left[exp\left(\frac{-t}{T_{1\rho}}\right)\right] \tag{2.25}$$

2.1.5 2D NMR for molecular interactions

This section briefly describes the basic principles of two-dimensional NMR and introduces the pulse sequences used for the results presented in chapter 5. In two-dimensional NMR spectroscopy (2D NMR) signal intensity is plotted as a function of two frequencies, usually as a contour plot. The presence of cross-peaks between two resonances indicates a correlation between homonuclear or heteronuclear spin pairs originating from scalar or dipolar coupling. The intensity of the signal observed reflects the extent of nuclear proximities, which will be through-bond or through-space depending on the NMR experiment used for acquisition.

^{1}H–^{1}H COSY

Correlation spectroscopy (COSY) was the first 2D NMR experiment proposed [108]. COSY is a homonuclear experiment that produces two types of signals (Figure 2.8): diagonal-peaks (at the same frequency coordinates), which are centred at every resonance in the corresponding 1D spectra; and cross-peaks, which indicate that the nuclei pairs are coupled through scalar interactions (through-bond).

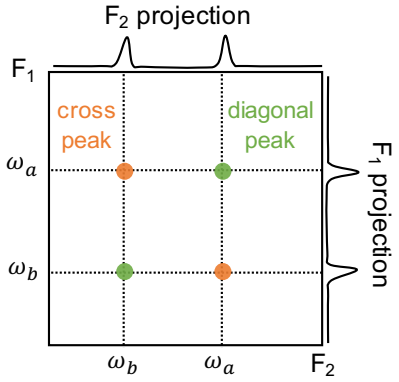

Fig. 2.8 Interpretation of peaks in a hypothetical 2D COSY spectrum consisting of two protons that are coupled together

The pulse sequence for a COSY experiment is shown in Figure 2.9a. The first pulse creates transverse magnetisation along the y' axis that is labelled by chemical shift and coupling. This magnetisation is allowed to evolve during d_0 (variable delay). After the second 90° pulse, the magnetisation along y' is tipped to the z-axis and is undetectable, only the component in the x' direction evolves and is detected. During t_d (detection time), the transverse magnetisation contains components from the nuclei under observation as well as the frequency

of the coupling. This sequence is repeated for increasing values of d_0 and the FID is recorded as a function of t_d to create the 2D plot.

In COSY spectra, all resonances give rise to diagonal-peaks and some may generate cross-peaks as well. The appearance of a cross-peak between two frequencies (ω_a and ω_b) implies that part of a signal that was present during d_0 with a frequency of ω_a was transferred through a scalar interaction to another signal that precessed at ω_b during t_d (Figure 2.8). The rest of the signal precessing at ω_a in d_0 that remains unaffected during t_d leads to the diagonal-peak. The COSY pulse sequence has two possible spin coherence transfer pathways [123]. Traditionally, phase cycling is used to select one of the coherence pathways and avoid them interfering with each other; however, it results in very lengthy experiment times. An alternative for coherence pathway selection is applying pulsed field gradients, which significantly reduces data acquisition time.

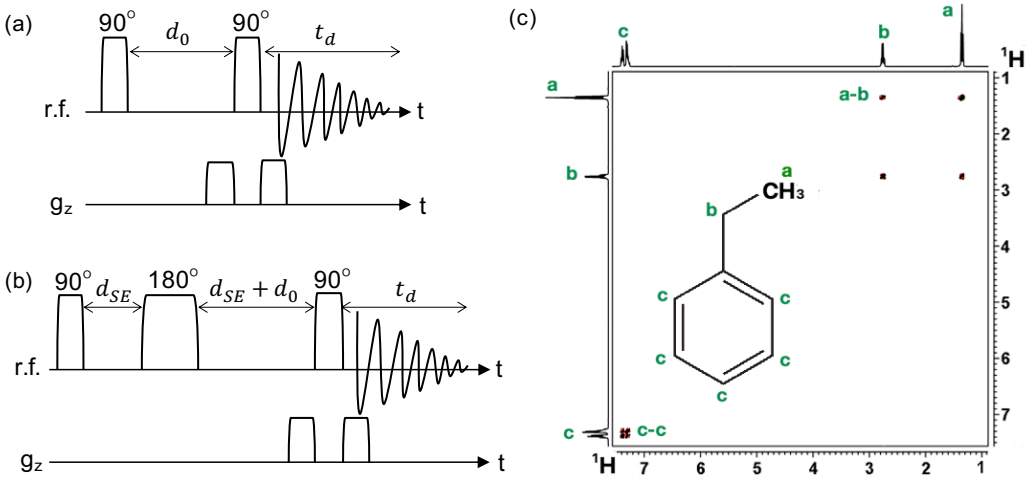

Fig. 2.9 Schematic of (a) COSY, and (b) SE-COSY 2D NMR pulse sequences, where d_0 is the variable delay, t_d the detection time and d_{SE} the spin-echo delay. (c) Example ^{1}H–^{1}H COSY spectrum of ethylbenzene (the chemical structure with protons labelled *a*-*c*, adapted from http://chem.ch.huji.ac.il/nmr/techniques/2d/2d.html).

The conventional COSY experiment can be modified to include a spin-echo pulse sequence (Figure 2.9b). Increasing the spin-echo delay (d_{SE}) results in a stronger T_2-weighting effect of the COSY spectrum. In this way, the signals from the protons that have the shortest T_2 constants are removed from the 2D contour plot.

Figure 2.9c shows the 2D ^{1}H–^{1}H COSY spectrum of a model compound, ethylbenzene (EB). The structure of EB has three resolvable proton environments: methyl (*a*), methylene (*b*) and aromatics (*c*). Outside the diagonal peaks, the cross-correlations detected correspond to the methylene-methyl protons (*a*-*b*) and the aromatic-aromatic ones (*c*-*c*). These signals indicate through-bond coupling.

^{1}H–^{1}H NOESY

NOESY stands for nuclear Overhauser enhanced spectroscopy. The nuclear Overhauser effect (NOE) is the transfer of magnetisation between populations of spins *via* cross-relaxation. NOESY is a 2D experiment that detects dipolar interactions between neighbouring protons undergoing spin-lattice relaxation to probe average distance between coupled nuclei.

The basis of NOESY is closely related to COSY and the result is a 2D plot with a diagonal-peak centred at each resonance and cross-peaks indicating through-space interactions (refer to explanation for Figure 2.8). The pulse sequence for a NOESY experiment is shown in Figure 2.10a. The excited magnetisation is labelled with the chemical shift during the variable delay d_0. The second 90° pulse rotates magnetisation into the negative z-axis. This magnetisation causes an NOE on spatially close nuclei during t_m: the M_z of a nucleus A will oscillate at ω_A in d_0, and the NOE magnetisation at the chemical shift of a nearby nucleus B will also oscillate at ω_A. The interaction is detected with the third 90° pulse.

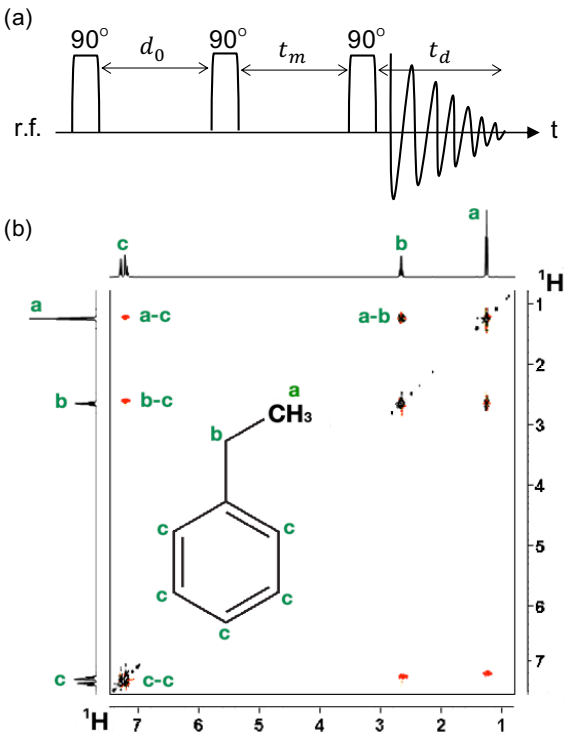

Fig. 2.10 (a) Schematic of a NOESY pulse sequence where where d_0 is the variable delay, t_m is the mixing time and t_d the detection time. (b) Example ^{1}H–^{1}H NOESY spectrum of ethylbenzene, the protons in the chemical structure are labelled *a*-*c* (adapted from http://chem.ch.huji.ac.i).

Figure 2.10b shows the 2D ^{1}H–^{1}H NOESY spectrum of EB. The same cross-correlations as in the COSY experiment were detected (*a*-*b* and *c*-*c*). Two additional through-space correlations are visible from the NOESY plot: the methyl and the methylene protons coupled with the aromatic ones (*a*-*c* and *b*-*c*, respectively).

^{13}C–^{1}H HETCOR

^{13}C–^{1}H heteronuclear correlation (HETCOR) experiments highlight carbon nuclei with directly attached or nearby protons (depending on cross-polarization time). The pulse sequence used for this work is the ^{13}C–^{1}H CP-MAS HETCOR with FSLG (frequency-

switched Lee-Goldburg) and TPPM (two-pulse phase modulation) decoupling, as shown in Figure 2.11a [107].

After a pulse of $(90° + \theta_m)$, where θ_m is the magic angle, the ^{1}H magnetisation is aligned at the magic angle during d_0 and forced to precess about it using 2π pulses to average ^{1}H–^{1}H dipolar coupling (FSLG proton homonuclear decoupling). After d_0, any magnetisation perpendicular to θ_m is transferred to the transverse plane through a θ_m pulse. Heteronuclear CP is then applied to transfer ^{1}H magnetisation to ^{13}C, since the natural abundance of ^{13}C is less than 1%. For short contact times, t_c, the correlation map exhibits ^{1}H–^{13}C pairs that are most strongly dipolar coupled; whereas for increasingly longer t_c, additional correlation cross-peaks appear, resulting from longer range couplings and ^{1}H spin diffusion. The ^{13}C signal is recorded during t_d using TPPM to decouple the protons from the carbons to improve ^{13}C signal resolution.

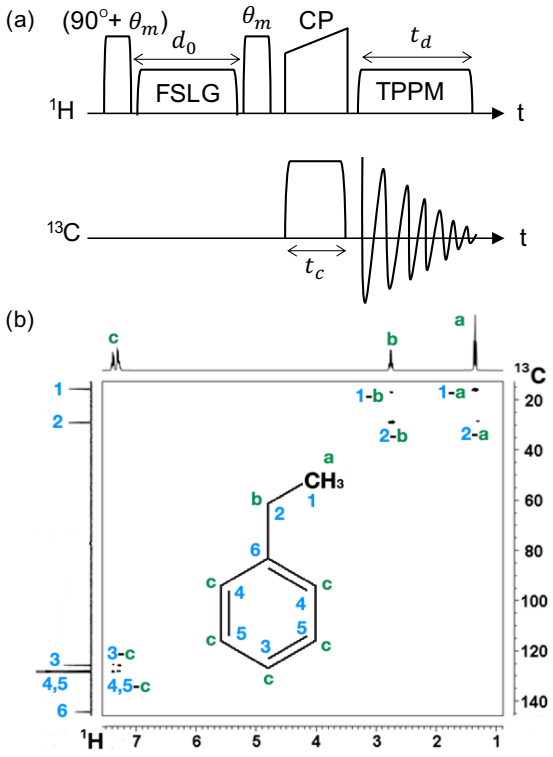

Fig. 2.11 (a) Schematic of a ^{13}C–^{1}H HETCOR with FSLG and TPPM decoupling pulse sequence where θ_m is the magic angle, d_0 is the variable delay, t_c is the contact time and t_d the detection time. (b) Example ^{13}C–^{1}H HETCOR spectrum of ethylbenzene, the protons and carbons in the chemical structure are labelled *a-c* and *1-6* respectively (adapted from http://chem.ch.huji.ac.i).

Figure 2.11b shows the 2D ^{13}C–^{1}H HETCOR spectrum of EB. In the horizontal dimension, the same three proton environments (*a*, *b* and *c*) identified in Figures **??** and 2.10 are observable. In the vertical ^{13}C dimension there are six resonances: *1* corresponds to the methyl carbon, *2* to the methylene one, and *3-6* to the aromatic carbons. Through-space correlations are detected between the methyl and methylene carbons to both their corresponding protons (*1-a*, *1-b*, *2-a* and *2-b*). Additionally, the aromatic carbons *3*, *4* and *5* display nuclear proximity to the aromatic protons (*c*). There is no observed coupling between carbon *6* to any proton.

^{1}H–^{1}H MQC (DQ/SQ)

In a one-spin system there are two possible states (α and β). The transition between one to the other involves only one quantum, which is why it is known as a single-quantum transition (Figure 2.12a). In a two-spin system in which the spins are coupled through some interaction (such as dipolar) there are four possible states (Figure 2.12b). Several transitions can occur involving none, one or two quanta (zero-, single-, or double-quantum transitions). The evolution of quantum transitions is also known as coherence transfer pathways.

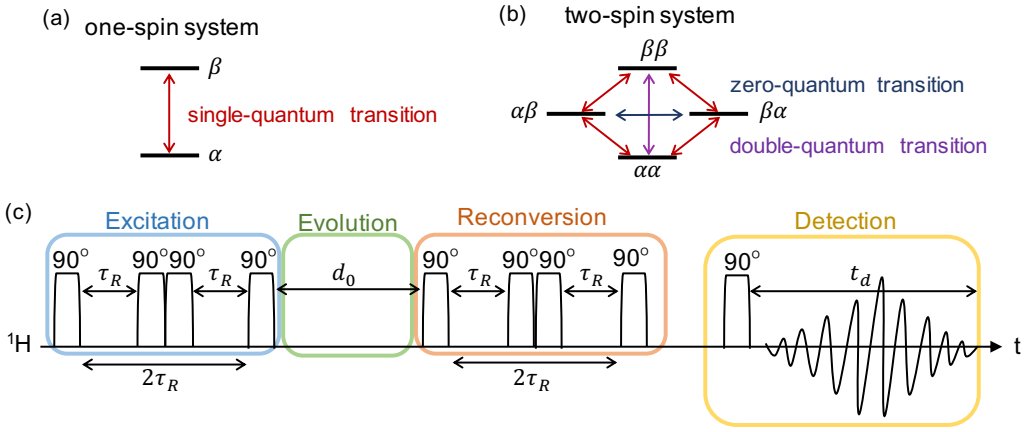

Fig. 2.12 (a), (b) Illustration of zero-, single- and double-quantum transitions in a one- and a two-spin system, respectively. (c) Schematic of a ^{1}H–^{1}H MQC SQ/DQ experiment, where τ_R is the period of the rotating rotor, d_0 is the variable delay and t_d the detection time.

Multiple quantum coherence (MQC) 2D NMR experiments can correlate single quantum (SQ) and double quantum (DQ) coherence in dipolar coupled spins. Althugh pulse sequence architecture is usually complex, they follow a basic scheme of four stages: excitation, evolution, reconversion and detection (Figure 2.12c). The first stage is designed to excite the desired MQC pathway, as could be ^{1}H DQ coherence. The MQC system is then allowed to evolve for a variable delay d_0 under the influence of local and external magnetic fields. However, MQ coherences are not directly measurable so they have to be transferred to the SQ modes for detection (reconversion stage). Finally, the magnetisation has to be tipped from the $\mathbf{B_0}$ axis to the transverse plane for signal acquisition. The delay between the reconversion and detection stages serves to dephase spurious (interfering) transverse magnetisation.

^{1}H–^{1}H MQC DQ/SQ correlation can be acquired with the BABA pulse sequence (Figure 2.12c) [139, 140]. BABA stands for *back-to-back*, since the rotor synchronisation is achieved by setting the r.f. pulses back-to-back. Rotor synchronisation is required to recover dipolar coupling when spinning at very high frequencies, which is why the spacing between pulses in the excitation and reconversion stages is dependent on rotor spinning frequency (through τ_R). At such high MAS rates, high resolution spectral lines can be accomplished, but dipole-dipole couplings are greatly averaged. The advantages of DQ/SQ experiments is

that double-quantum coherence selects spin pairs and the spectrum from isolated spins is suppressed. Furthermore, there is no interference for the typically high-intensity diagonal components.

Figure 2.13 shows the 2D ^{1}H–^{1}H BABA spectrum of alanine (ALA). The structure of ALA has three resolvable proton environments: methyl (a), methine (b) and amine (c). In DQ/SQ experiments like this one, peaks in the diagonal indicate self-correlation. The methyl and amine groups in ALA display diagonal peaks (a-a and c-c, respectively) because they involve more than one proton. No self-correlation is observed for methine, as there is only one proton in this group. Interpretation of cross-peaks is made in the following way: two resonances are considered to be coupled when a signal is detected at both of their corresponding chemical shifts in the SQ dimension and their position along the DQ dimension is the sum of said chemical shifts. In Figure 2.13 there are three sets of cross-peaks observable. The first one is between the methyl and methine protons (a-b); their chemical shifts are 1.5 ppm and 4 ppm respectively and the position of these signals in the DQ dimension is at 5.5 ppm ($1.5 + 4 = 5.5$). The second one is between methyl and amine resonances at 1.5 ppm and 9 ppm in the SQ axis, positioned at 10.5 ppm in the DQ axis (a-c). Finally, a coupling between methine and amine protons (b-c) is exhibited by the signals at 4 ppm and 9 ppm along the SQ axis, at 13 ppm in the DQ dimension.

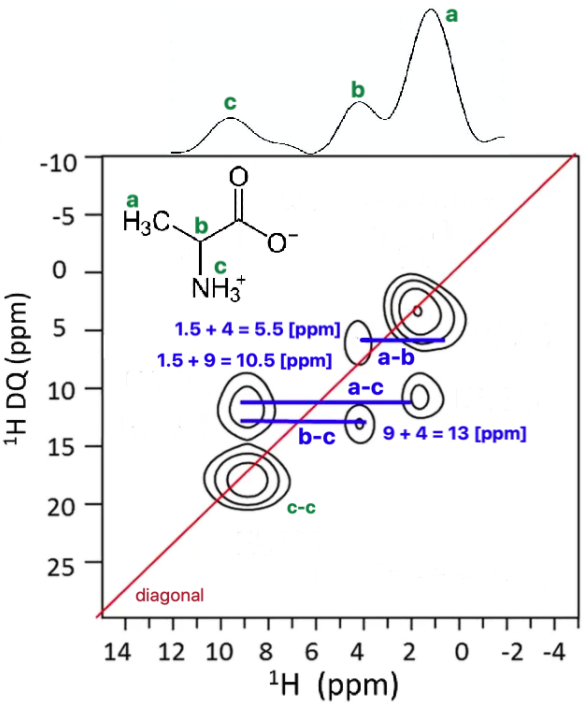

Fig. 2.13 Example ^{1}H–^{1}H MQC SQ/DQ BABA example spectrum of alanine, the protons in the chemical structure are labelled a-c (adapted from [141]).

2.2 Differential scanning calorimetry (DSC)

Differential scanning calorimetry (DSC) is a widespread thermoanalytical technique to measure the temperatures and heat flows associated with physical and chemical transitions in materials as a function of temperature and time. It was developed by Watson and O'Neill in 1962 [142]. A schematic of the cross-section of a typical DSC instrument is shown in Figure 2.14a. A sample (contained in an aluminium pan) and a reference (an identical, but empty pan) sit on carefully calibrated discs. DSC measures the difference in heat flow rate, in Watts

(W), between the sample and the reference as they are heated, cooled or held isothermally. Nitrogen purge is used to maintain an inert atmosphere.

There are two main types of DSC experiments. Standard DSC is a relatively fast technique that allows quantitative analysis of transitions (*e.g.* glass transition, crystallisation, melting or degradation, Figure 2.14b). Its main limitation is in the interpretation of results for mixture systems, since the DSC thermograms display the average heat flow from overlapping processes. Sensitivity can be improved by increasing sample size and heating rate, but this results in lower resolution. In modulated DSC (mDSC) the sample and the reference are exposed to a linear heating or cooling ramp, which has a superimposed sinusoidal temperature modulation. Experiments are longer, but it allows to separate the total heat flow (obtained in standard DSC) into reversing (heat capacity-related) and non-reversing (kinetic) components, which enhances sensitivity, resolution and accuracy. The reversing heat flow component provides the best data for glass transition and melting events.

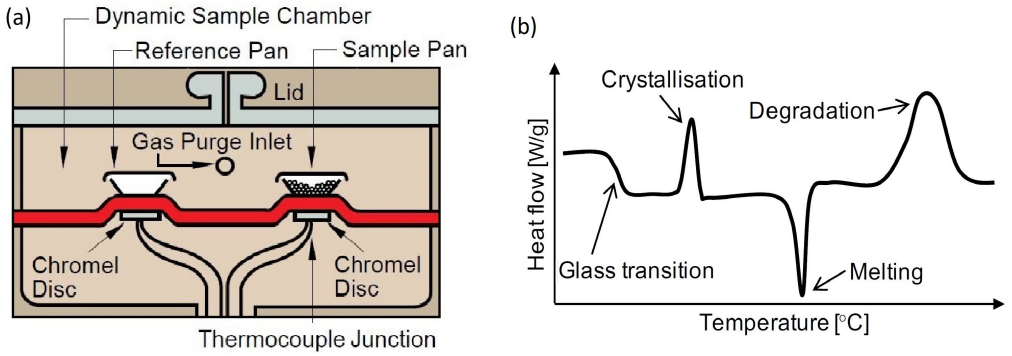

Fig. 2.14 Schematic of (a) a DSC instrument, adapted from TA Instruments documentation (http://www.tainstruments.com/pdf/literature/DSC_2910.pdf) and (b) DSC thermogram showing some common thermal transitions.

The glass transition temperature (T_g) is one of the most important thermophysical properties of amorphous materials. It can be compared with the melting point of a crystalline compound since it indicates the transition from hard, brittle, glassy material to soft and rubbery. It is not a discrete event, but a range of temperatures over which the molecular mobility increases significantly. The convention is to report a single temperature, defined as the midpoint of the temperature range bounded by the tangents to the two baselines of the heat flow curve.

2.3 Thermogravimetric analysis (TGA)

Thermogravimetric analysis (TGA) is a technique in which the mass of a material is monitored as a function of temperature and time as the sample is heated, cooled or held isothermally. The sample is contained in a TGA pan (platinum basket that has been previously tared), which is placed in a furnace while supported by a precision balance, Figure 2.15a. TGA

measures the percentage change in sample mass during the experiment for quantitative analysis of events such as solvent loss, oxidation, decomposition or sublimation, Figure 2.15b. Nitrogen purge is used to maintain an inert atmosphere. TGA has several applications, such as evaluating thermal stability or purity of a substance.

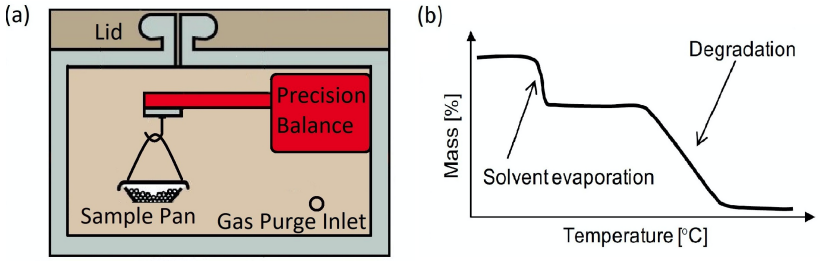

Fig. 2.15 Schematic of TGA (a) instrument and (b) thermogram showing some common events.

2.4 Rheology

Rheology is the study of flow and deformation of matter in response to applied forces or stresses [143]. The physical property that characterises the resistance to deformation of a material is the viscosity, quantified in Pa·s. It reflects the internal frictional force between adjacent layers of liquid as they shear or move with respect to one another. Rheological properties are measured on a rheometer, such as the parallel plate rheometer illustrated in Figure 2.16. The bottom plate applies a strain on the sample through continuous rotation or rotational oscillation. A transducer attached to the top plate converts the torque or stress transmitted by the material into an electrical signal for interpretation. The mathematical definition of pure viscosity (or shear viscosity), η, is:

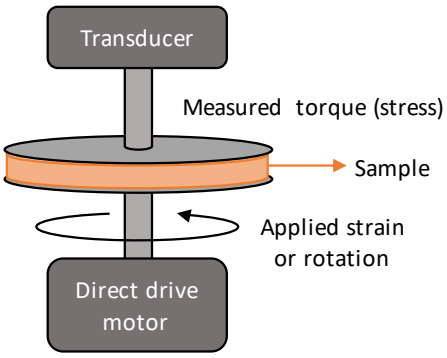

Fig. 2.16 Schematic of parallel plate rotational rheometer for the determination of the complex viscosity, η^*, of a sample.

$$\eta = \frac{shear\ stress\ [Pa]}{shear\ rate\ [s^{-1}]} \tag{2.26}$$

In rotational rheology tests, the complex (or frequency-dependent) viscosity, η^*, is determined from two additional parameters: G' and G''. The storage or elastic modulus (G') is a measure of the energy stored in a material in which a deformation is imposed. This energy allows the material to recover its initial shape after the stress has been applied. The loss or viscous modulus (G'') is the energy dissipated upon deformation. This energy is unrecoverable and results in permanent deformation. The ratio of loss to storage modulus is known as the damping factor ($tan\delta$) and indicates viscous-dominant behaviours for values

greater than one and elastic-dominant performance for values smaller than one:

$$tan\delta = \frac{G''}{G'} \tag{2.27}$$

The overall resistance to rotational deformation, whether viscous or elastic, is characterised by the complex modulus (G^*):

$$G^* = G' + iG'' \tag{2.28}$$

From the complex modulus definition in equation 2.28, the complex viscosity can be calculated for a specific angular velocity of the rheometer's bottom plate:

$$\eta^* = \frac{G^*}{\omega} \tag{2.29}$$

Chapter 3

High-temperature PFG NMR diffusion studies of paracetamol

3.1 Introduction

There is a growing body of literature exploring pharmaceutical HME, however, there are still substantial gaps in our understanding regarding the dynamics of drug dissolution and dispersion in viscous polymers. Computational models have been built in order to predict optimal processing conditions (*e.g.* temperature, residence time or drug loading), but they are limited by the lack of supporting data for key mass transport parameters. A common omission is the lack of experimental data on the API diffusion coefficient at conditions relevant to HME [117], and currently molecular diffusivities are extracted from complex and time-consuming molecular dynamic simulations [118].

Diffusion coefficient measurements are not straightforward and there is no standard or universally applicable method. As outlined in section 1.4.2, PFG-NMR has been extensively used to observe and measure self-diffusion coefficients in drug/polymer pharmaceutical systems as it is non-invasive, non-destructive, quantitative and chemically selective. Diffusion-weighted NMR imaging has been performed on pharmaceutical polymers of interest for controlled-release applications to study the rate of hydration or solvent diffusion into polymeric gels and tablets [89, 90, 88, 92, 81, 93, 84]. However, all of these examples are either non-quantitative (mass transport was observed but a diffusion coefficient was not calculated) or were quantitative in measuring the diffusion coefficient of a solvent in a polymer, but not of an API. There are a few reports of API diffusion measurements in polymers, but these are either mediated by a solvent (hydrogels) [87] or in polymers with very low glass transition temperatures (23°C) [144].

PFG-NMR studies on molten polymers above 100°C have been conducted by Liu *et al.* and Stepisnik *et al.* to characterise mobility regimes [145, 146]. No publications were found that explored the application of PFG-NMR at temperatures higher than 150°C other than

to measure the diffusion of ions (^{7}Li, ^{19}F, ^{23}Na, ^{27}Al and ^{39}K) in molten salts, where a specifically designed laser heating apparatus was used to reach temperatures of up to 1200°C [147–150].

In all of the pharmaceutical studies referenced above the focus was on the mass transport of water into polymer tablets or solvent-mediated drug release. Recently, Moseson *et al.* visualized the solubilisation of drug particles in polymer melts (with no solvents present) [151]. Through elemental composition analysis (SEM with an energy dispersive X-ray detector) of carbon, oxygen, chlorine and nitrogen at 130°C, the system was visualised to be diffusion-based. There was no direct measurement of the drug diffusion coefficient in the polymer melt and it was speculated that this could be estimated through the Stokes-Einstein model.

Gupta *et al.* has published several studies on the importance of viscoelastic properties of polymers for the understanding of HME [152]. Gupta *et al.* suggested that rheological analysis provides more appropriate characterisation of polymer behaviour than the more widely used DSC technique, due to mass effects. Rheological thermomechanical analysis considers chain disentanglement and mobility phenomena that results in the characteristically broad glass transition and melting events in polymers. These transitions are influenced by the amount of material; and DSC experiments samples are of a few milligrams, while rheology uses 0.5-1 g. In a subsequent publication, Gupta *et al.* argued that the most relevant rheological property in the context of polymer HME is the complex viscosity [153]. This is due to the decrease in complex viscosity exhibited by polymers at increasing shear rates (this characteristic is known as shear thinning), which is representative of the high shear environment in the extrusion barrel due to screw rotation and friction with the wall. They also reported that the optimal system viscosity range for extrusion is 1,000-10,000 Pa·s.

Rheological characterization has been used in the context of HME to assess API solubility in pharmaceutical polymers at high temperatures [154, 155]. It has also been recently employed for thermal assessments of API/polymer solid dispersions prepared by different methods (physical mixtures, cryo-milled and extrudates) and as a predictive tool for processability and for the selection of optimal processing temperature [156, 157, 72]. In this study, I used rheological analysis to further interpret observations from high-temperature diffusion NMR experiments and to improve our understanding of paracetamol/copovidone systems.

To the best of my knowledge there is no quantitative data on API mass transport in polymer melts in the literature and the work presented in this chapter reports the first observations of API diffusion in pharmaceutical polymers at temperatures relevant to the HME process, by means of high-temperature PFG-NMR. The relationship between diffusivity and viscosity is also explored with the Stokes-Einstein and Arrhenius models.

3.2 Materials and methods

3.2.1 Materials and sample preparation

API/polymer systems were studied using paracetamol (mean particle diameter ~300 μm, Mallinckrodt) and copovidone (Kollidon VA 64®, M_w 45,000-70,000 and 20-200 μm chain length [158], BASF), supplied by AstraZeneca. Copovidone is a copolymer of 1-vinyl-2-pyrrolidone (VP) and vinyl acetate (VA) in mass ratio 6:4.

Hot-melt extrudate was prepared using a Haake Minilab II twin-screw extruder (Thermo Fisher Scientific, Waltham, MA) configured with co-rotating screws in the Alford facility in AstraZeneca, Macclesfield (Figure 3.1). Extrusion was performed at 170°C and a screw speed of 40 rpm by manually feeding 10 g of a 30 wt% paracetamol/copovidone physical mixture, prepared using a Turbula blender for 5 min at 23 rpm. Once cooled, extrudates were collected and ground to powder with a mortar and pestle.

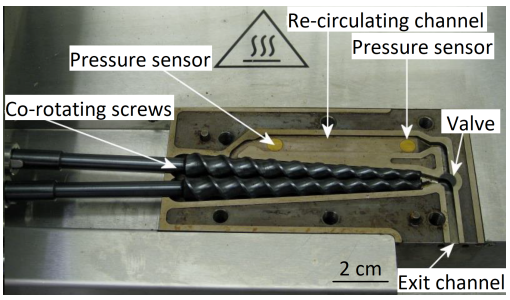

Fig. 3.1 Haake Minilab II twin-screw extruder (Thermo Fisher Scientific) configured with co-rotating screws.

Non-HME physical mixtures of paracetamol and copovidone at 20:80, 30:70, 40:60, 50:50 and 70:30 weight ratios were prepared by weighing and blending the two powders with a mortar and pestle.

All samples for NMR studies were vacuum dried at room temperature for 10 min to remove moisture and sealed with paraffin film prior to analysis.

3.2.2 NMR spectroscopy and diffusometry

All ^{1}H NMR experiments were performed on a 7.07 T Bruker Biospin DMX 300 MHz spectrometer (BrukerBiospin, Billerica, USA) operating at a ^{1}H frequency of 300.23 MHz through the ParaVision 4.0 software. A Bruker Biospin DIFF-30 probe was equipped with an extended variable temperature range ^{1}H/^{19}F 5 mm internal diameter (i.d.) r.f. coil (the 90° pulse length was 8 μs). All NMR measurements were made on 100 mg of sample and over a range of temperatures from room temperature to 180°C.

Diffusion measurements were performed using a single z-axis shielded gradient system capable of producing a maximum gradient of 12 T/m. These experiments were based on the PGSTE sequence for paracetamol and the APGSTE pulse programme for paracetamol/copovidone mixtures (schematics of the pulse sequences are shown in Figure 2.5). APGSTE was used for the heterogeneous systems because it minimises effects of background gradients due to differences in magnetic susceptibility. The recycle delay (T_R) was three

times the measured longitudinal relaxation (T_1) of the system at each temperature. For the paracetamol/copovidone systems, the T_R used were: 6 s at 150°C, 5 s at 160°C and 3 s at 170°C. Diffusion coefficients (D) were calculated by fitting the normalised peak integrals (from the spectra recorded at different gradient strengths) to the Stejskal-Tanner equation (equation 2.15). The key experimental parameters are listed in Table 3.1. Curve fitting was performed on MATLAB_R2017b.

Table 3.1 Values of experimental parameters for the PGSTE and APGSTE experiments: pulsed field gradient strength range (**g**), duration (δ), interval (Δ) and number of scans (ns), and stabilization delay (SD).

	g [G/cm]	δ **[ms]**	Δ **[ms]**	**ns** [−]	**SD [ms]**
Paracetamol (PGSTE)	10-300	1	50	16	1
Parac/copov (APGSTE)	10-1,000	1.5-5	30	32	1.5

Prior to recording spectra at high temperatures, the temperature performance of the PFG probe was calibrated at 10°C intervals in the 100-180°C range for an airflow of 670 L/h. The results of the temperature calibration are presented in section 3.3.1.

3.2.3 Differential scanning calorimetry

Thermal analysis was conducted with a Q2000 (TA Instruments, New Castle, DE, USA) differential scanning calorimeter. Approximately 3-7 mg of sample was sealed in a standard aluminium pan and heated from 20°C to 200°C at a rate of 4°C/min, with a modulation amplitude of ±1°C and period of 60 s, and cooled back to 20°C at 10°C/min. Two controlled sequential heat-cool cycles were performed on all samples under a nitrogen stream of 50 mL/min. Melting and crystallisation temperatures were determined as the inflection points of the corresponding peaks in the normalised heat flow thermogram. The data was processed and plotted using TRIOS software (TA Instruments).

3.2.4 Parallel-plate rotational rheology

An ARES G2 rheometer (TA Instruments, New Castle, DE, USA) with parallel plate geometry (diameter 25 mm) was used for rheological evaluation. Zero gap calibration was performed at the test temperature. Powder samples were loaded on the heated bottom plate until a uniform disc of approximately 1 mm height was formed. A 3 min delay was allowed for thermal equilibration before tests. Dynamic strain sweeps ($\omega = 10\ rad/s$, $strain = 0.01\% - 100\%$) were conducted at 150°C and 170°C and from these, a strain of 10% was selected for subsequent tests to ensure operation within the linear viscoelastic region (LVR). The LVR is the range of frequencies and strains for which the structural integrity of the sample is maintained. Frequency sweeps at 150°C and 170°C were conducted at angular frequencies from 0.1 to 100 rad/s. For temperature ramps the samples were heated from 140°C to 180°C,

at rate of 2°C/min, 10% strain and 10 rad/s. The gap distance was kept constant using the expansion coefficient tool (2.3 $\mu m/°C$ for the apparatus used), which accounts for the thermal expansion of the metallic parallel plates at increasing temperatures. All tests were conducted under nitrogen to avoid sample oxidation. Storage modulus (G'), loss modulus (G''), complex viscosity (η^*) and damping factor ($tan\delta$) plots were generated using the TRIOS software (TA Instruments).

3.3 Results and discussion

3.3.1 High temperature calibration of the PFG probe

For high temperature experiments, a heating system that introduces hot air into the magnet at 670 L/h was incorporated to the PFG probe. A thermocouple to measure the temperature inside the magnet was located 5 cm below the r.f. coil so as not to disrupt the magnetic field and cause artefacts. In order to calibrate the temperature in the middle of the r.f. coil (optimal sample position), a sealed glass-bulb (Wilmad) with ethylene glycol (EG) was used (Figure 3.2a). The chemical shift of the hydroxyl (OH–) proton in EG is temperature dependent and shifts to lower frequencies at increasing temperatures [159]. This is a result of the higher thermal energy disrupting the hydrogen bonds in which the OH– groups are involved, which leads to greater shielding. The relationship between temperature (T) and chemical shift difference ($\Delta\delta$) between the hydroxyl and the methyl groups of EG is defined by [160]:

$$T[°C] = 191.9 - 100.3 \times \Delta\delta \tag{3.1}$$

The ^{1}H spectrum of EG was recorded every 10°C in the range 100˘180°C (Figure 3.2b) with a simple pulse-and-acquire experiment (refer to Figure 2.2c for the schematic of this pulse sequence). A linear calibration curve between the sample (T_{sample}) and thermocouple ($T_{thermocouple}$) temperature was produced (Figure 3.2c) and the relationship between the two was found to be:

$$T_{sample}[°C] = 0.78 \times T_{thermocouple}[°C] + 7.8 \tag{3.2}$$

Axial temperature gradients along the ∼20 mm span of the r.f. coil were studied by centring the EG bulb at 4 mm, 10 mm and 16 mm (Figure 3.2d) and acquiring a ^{1}H spectrum at 120°C, 150°C and 175°C. The standard deviation of the measurements was of the same order as the differences in temperature in the three axial positions at all temperatures studied, so it was concluded that if there was an axial temperature gradient, it was negligible over the 20 mm active region of the r.f. coil (data not shown).

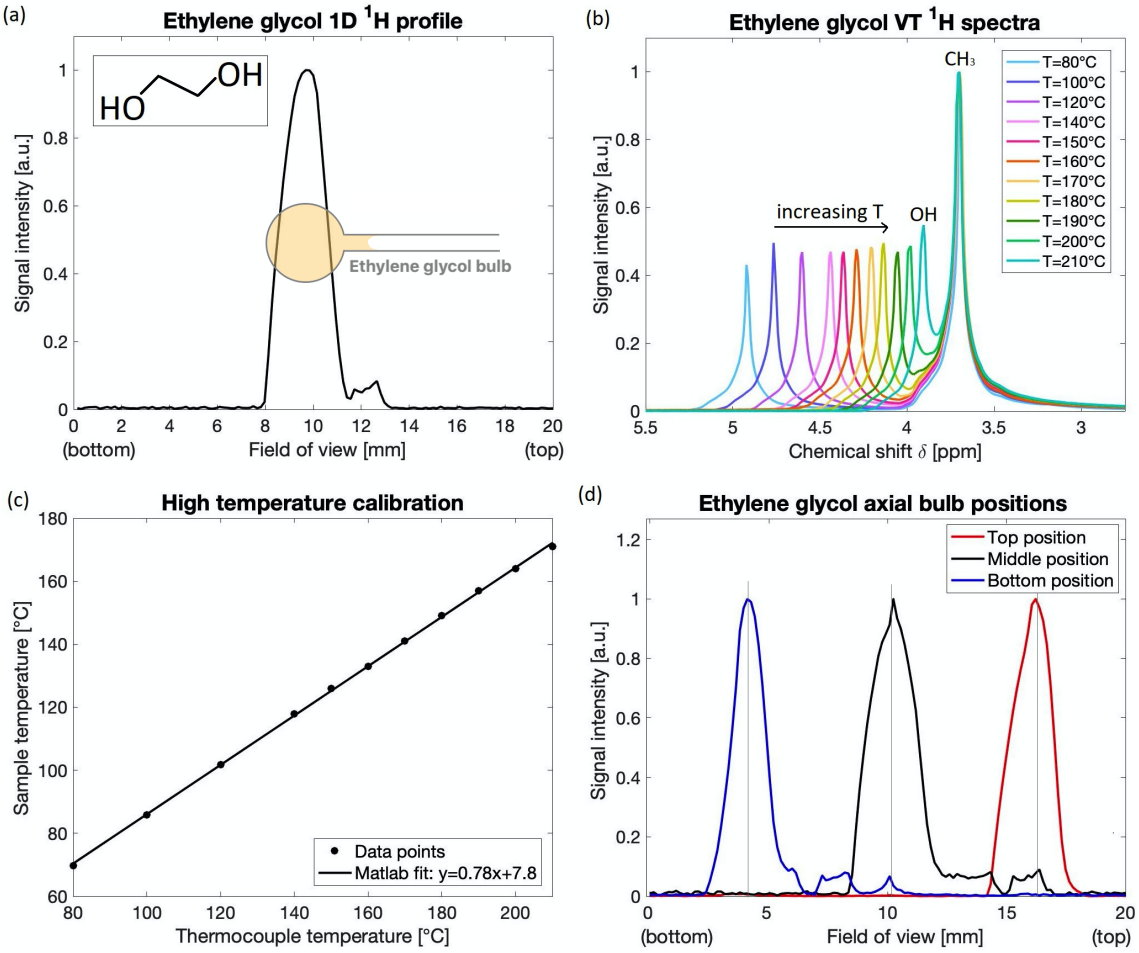

Fig. 3.2 (a) 1D profile of the EG bulb positioned in the middle of the r.f. coil with an overlaid schematic of the glass bulb (inset: chemical structure of EG); (b) ^{1}H spectra of EG at a range of temperatures between 80-210°C, where the temperature-dependent resonance corresponds to the OH– proton; and (c) calibration curve to characterise the relationship between the temperatures of the thermocouple and the sample. (d) 1D profiles of the EG bulb positioned at three axial positions centred at 4, 10 and 16 mm.

3.3.2 High temperature characterisation of materials

^{1}H NMR spectroscopy

The ^{1}H NMR spectra of copovidone and paracetamol are shown in Figure 3.3. The proton resonances of molten paracetamol, by holding it above its melting point were assigned by comparison with the literature [161, 162] (chemical structure and nuclei labelling in Figure 3.3a). Assignments of the copovidone spectrum (chemical structure and proton labels in Figure 3.3b) when dissolved in deuterated acetone (Figure 3.3d), were based on previously reported chemical shifts of similar molecules [163–165]. The spectrum of molten copovidone at 170°C (Figure 3.3c) shows a single broad resonance. The large peak width is a consequence of the short T_2 of copovidone (Table A.1), which in turn is due to its high viscosity and hindered molecular tumbling. Molten paracetamol resonances are generally well resolved, with the exception of the OH– and NH– protons (*1* and *6* in Figure 3.3a), which overlap at 170°C. Since the chemical shifts of OH– and NH– protons are temperature dependent, both resonances were resolvable as the temperature was lowered to 130°C (Figure 3.3c inset).

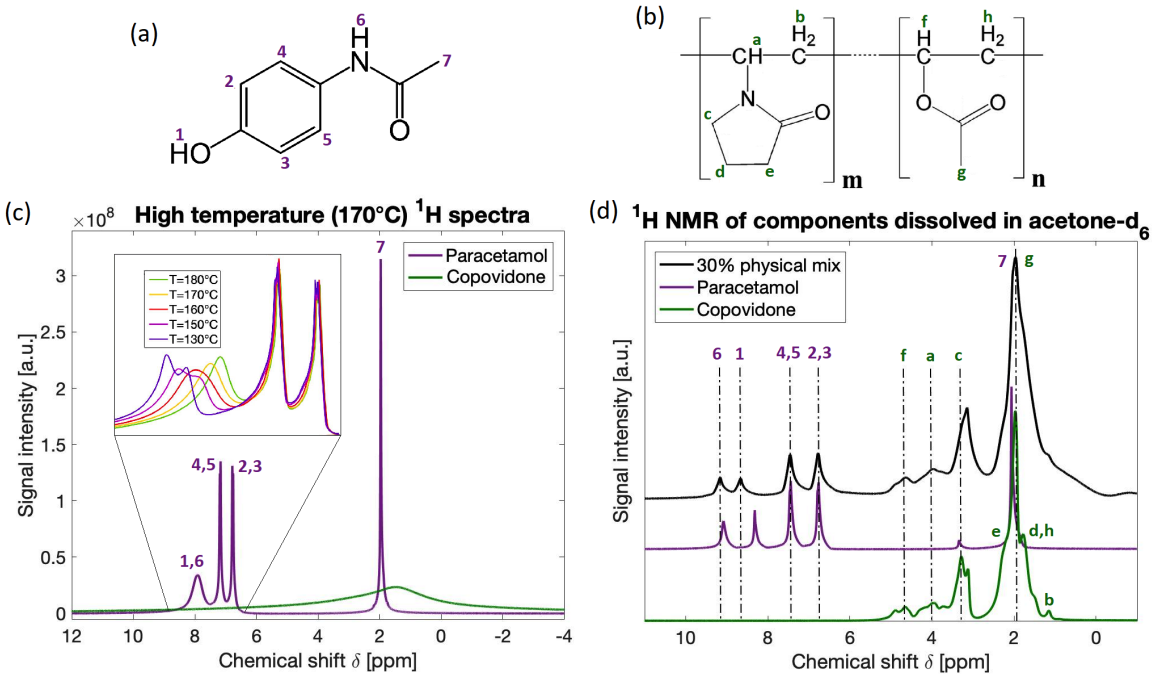

Fig. 3.3 Chemical structures of (a) paracetamol and (b) copovidone (Kollidon VA 64) with protons labelled (*1-7* for paracetamol and *a-g* for copovidone). (c) Overlaid ^{1}H spectra of molten paracetamol and copovidone at 170°C. (d) Stacked ^{1}H spectra of a 30 wt% paracetamol/copovidone physical mix, paracetamol and copovidone dissolved in deuterated acetone (resonance assignments refer to the molecular structures).

To further characterise the temperature dependence of the OH/NH protons in paracetamol and in the 30 wt% physical mixture, the ^{1}H spectra was acquired at a range of temperatures in the 120-170°C range. The position of the hydroxyl peak (or OH/NH when they overlapped

in the spectrum) was plotted as a function of temperature (Figure 3.4). For comparison, the chemical shifts of EG's hydroxyl proton (Figure 3.2b) are shown in the same graph. The data points fitted well to a linear function [166], the slope of which is known as the temperature coefficient (λ [ppm/°C]). The temperature coefficients of the three compared samples are similar: $\lambda_{PAR} = -0.0064$, $\lambda_{mix} = -0.0079$ and $\lambda_{EG} = -0.0101$ ppm/°C. It should be noted that the chemical shift of the OH– and NH– peaks in the ^{1}H spectrum of paracetamol when dissolved in deuterated acetone (Figure 3.3d) is significantly different than in the molten state, when held above its melting point (Figure 3.3c). This is an effect both of temperature and hydrogen bonding activity with the solvent.

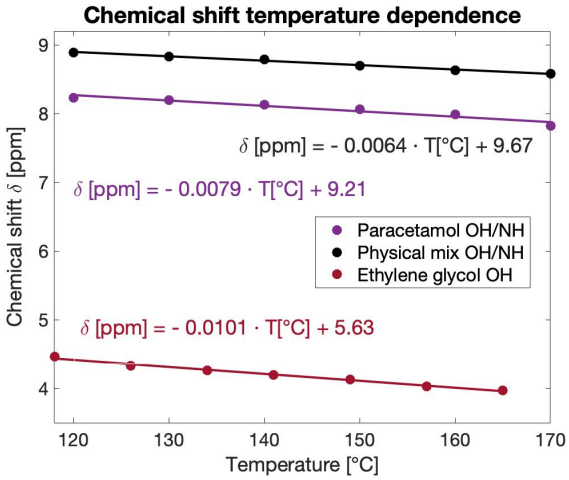

Fig. 3.4 Chemical shift temperature dependence of the OH/NH protons in paracetamol, a 30 wt% paracetamol/copovidone physical mix and ethylene glycol.

DSC

To better understand the high temperature behaviour of paracetamol, a DSC experiment where the sample was subjected to two consecutive heat-cool cycles from room temperature to 200°C was performed. For comparison, a similar heating cycle was carried out in the NMR magnet and the ^{1}H spectra of paracetamol was acquired at several temperatures.

In the first heating ramp, DSC shows no events other than the melting of polymorph I at 170°C (Figure 3.5a, blue trace). In agreement, no NMR signal was observed for paracetamol as it was heated from 20°C to 160°C. At 165°C two peaks are present (one for the aliphatic and another for the aromatic protons), but these are broad and weak due to the slow molecular tumbling rate. At 170°C (melting temperature) these become sharp and resolved intro four distinct peaks (Figure 3.5b).

The four distinct NMR peaks remained sharp as the paracetamol was cooled down (Figure 3.5c) to 80°C. This is indicative of the paracetamol remaining in a super-cooler state in which a high molecular tumbling rate was maintained. Below 80°C, thermal energy was too low for

molecular tumbling and the sample yielded no signal. Similarly, the first DSC cooling stage exhibits no thermal events (Figure 3.5a, green trace).

Upon reheating, the thermogram shows a large exothermic transition at 80°C followed by a smaller one at 132°C (Figure 3.5a, red trace). These have been assigned to the crystallisation to polymorph form III and a solid-solid transition to form II, respectively, in accordance with the literature [167]. As the heating is continued, another melting event is observed, but this time at 163°C, since it corresponds to the melting point of paracetamol's form II. These observations are supported by the NMR data (Figure 3.5d), in which the signal disappears at 80°C (due to crystallisation) and then reappears at 160°C. It should be noted that the spectra at 160°C and 170°C in Figure 3.5d are distorted because the NMR tube broke during the experiment. This would have been caused by the thermal expansion as form III transitions to form II [168]. No thermal events are present in either of the cooling processes because paracetamol is a class II drug in regard to its glass-forming ability, meaning that it remains amorphous as its melt is cooled down and it crystallises upon reheating [169].

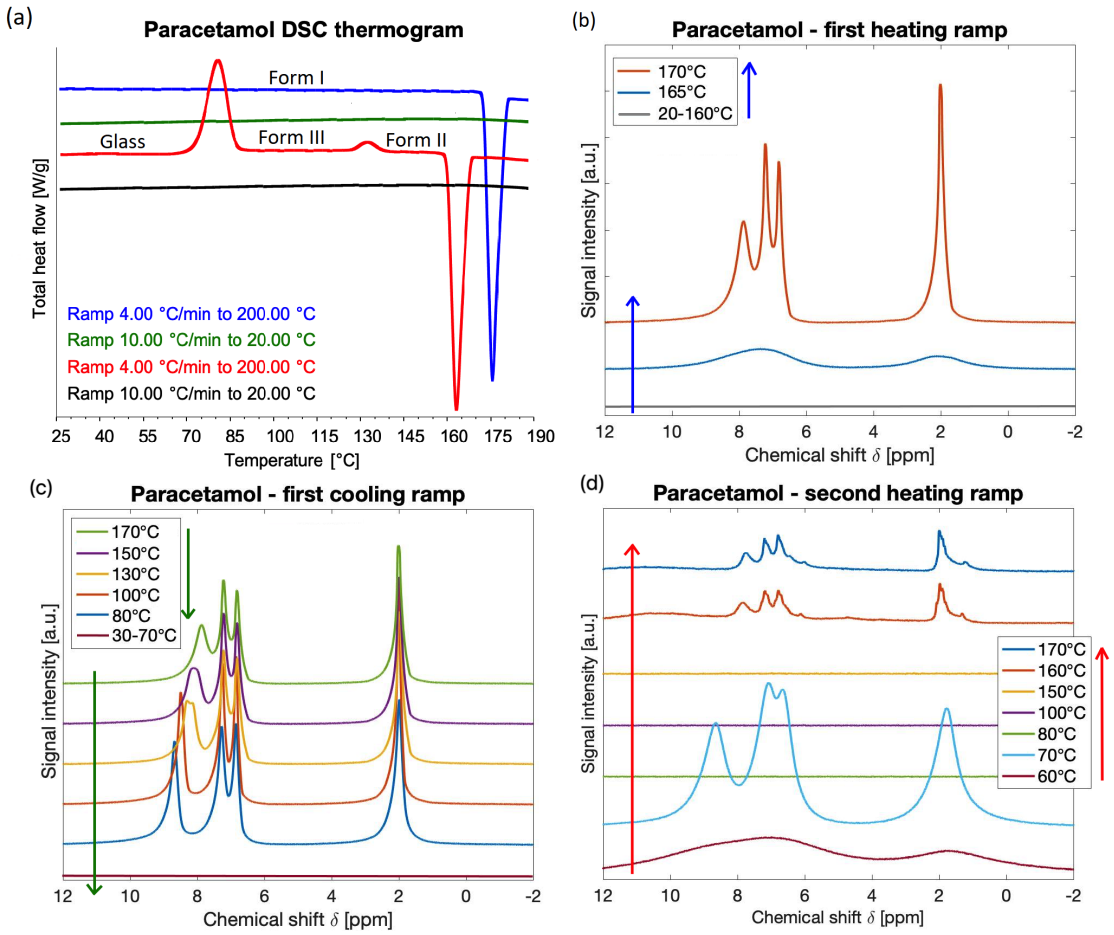

Fig. 3.5 (a) High temperature characterisation of paracetamol using DSC consisting of two consecutive heat-cool cycles. ^{1}H NMR spectra of paracetamol corresponding to (b) the first heating ramp, (c) the first cooling stage, and (d) the second heating ramp.

3.3.3 Determination of the microscopic self-diffusion coefficient of paracetamol and paracetamol/copovidone blends

Figure 3.6a shows the PGSTE diffusion-weighted spectra for pure paracetamol at 170°C, and Figure 3.6b its corresponding Stejskal-Tanner plot. The gradient of the line of best fit yields a molecular self-diffusivity of molten paracetamol of $1.9{\cdot}10^{-10}$ ($\pm 0.2{\cdot}10^{-10}$) m^2/s. This is three times slower than the value obtained by Ribeiro *et al.* (2012) for $0.001 - 0.05$ M paracetamol in aqueous solutions at room temperature, $0.66 - 0.62{\cdot}10^{-9}$ m^2/s [170]. The diffusion coefficient obtained is similar to that of the measured diffusivity of small drugs in hydrogels by Mathias *et al.* (2010), which where in the range of $3.3 - 6.8{\cdot}10^{-10}$ m^2/s [87].

The diffusion-weighted ^{1}H spectra of an extrudate sample (Figure 3.7a) are chemically similar to that of pure molten paracetamol except for the lower overall spectral resolution (due to slower molecular tumbling of the paracetamol molecules in copovidone, as is evident from the T_2 relaxation values in Table A.1). Additional peaks that resonate between $3 - 5$ ppm and at 1 ppm are attributed to the ^{1}H resonances of copovidone. The peaks due to the polymer have the appearance of those already shown in Figure 3.3d and suggest that, for the copovidone/paracetamol system at 160°C, copovidone is dissolving in paracetamol (and *vice versa*). The fact that paracetamol's NMR signal can be detected as low as 120°C (data shown in page 113, chapter 6) means that there has been a significant depression of its melting point in the presence of copovidone, which is indicative of high miscibility between paracetamol and copovidone [154].

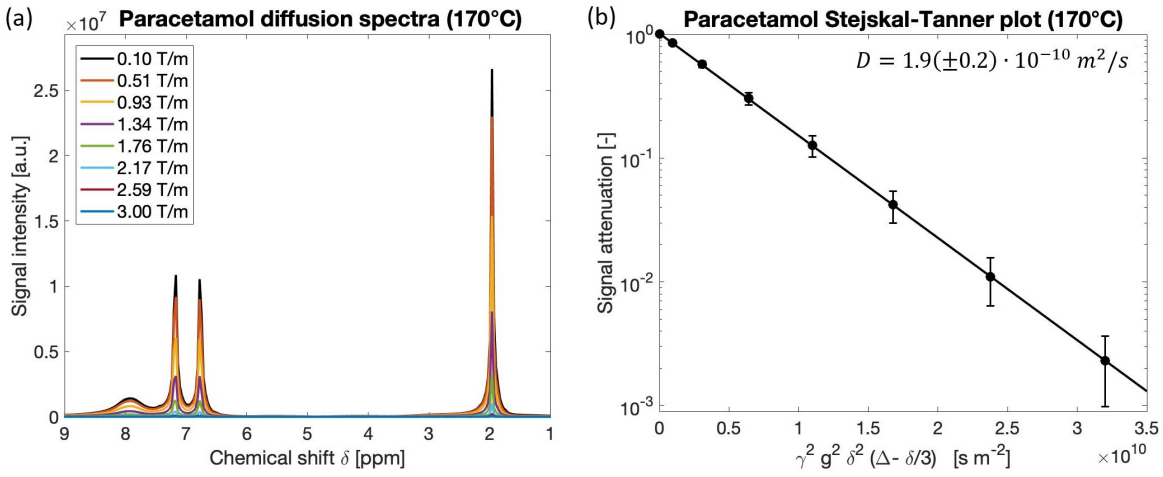

Fig. 3.6 (a) Diffusion-weighted spectra for different pulsed-field gradient strengths and (b) corresponding signal attenuation plot fitted to the Stejskal-Tanner equation for molten paracetamol at 170°C. The standard deviation from three independent measurements is indicated in parenthesis. Error bars indicate the standard deviation at each data point.

The diffusivity of copovidone could not be measured because the transverse relaxation time (T_2) of the polymer was determined to be less than 2 ms in the 140˘170°C range (see

Table A.1), and the minimum achievable echo time for the PGSTE experiment was 2.94 ms. The lack of mobility in high molecular weight polymers that leads to rapid T_2 relaxation has been previously known to prevent the use of some pulse sequences [145]. Even though the diffusivity of pure copovidone could not be determined, its signal is detected in APGSTE experiments when mixed with paracetamol. This behaviour can be explained by paracetamol molecules diffusing between and separating (*i.e.* plasticising) the polymer chains (further evidence for this is found in the viscosity measurements presented in the following section). Copovidone then becomes more mobile resulting in an increase in its T_2 constant making the polymer ^{1}H signal observable in the diffusion-weighted spectra of physical mixtures and extrusion samples containing paracetamol and copovidone.

Figure 3.7b shows that paracetamol's aromatic and aliphatic resonances seem to not be attenuating at the same rate, which is counter-intuitive since the whole molecule should be diffusing at the same speed. Data from the aliphatic peak in Figure 3.7b (green symbol) exhibits an initial decay that tails off well above noise level due to the very slow diffusion associated with the polymer. The aromatic peak, on the other hand, attenuates linearly to noise level with a gradient that can be attributed to the "true" diffusion of paracetamol (Figure 3.7b, purple symbol). The initial linear decays of aliphatic and aromatic resonances are different because the aliphatic curve is comprised of a weighted average of contributions from both the polymer and paracetamol. This is due to the spectral overlap of copovidone groups *d*, *e* and *f* (Figure 3.3b) with the aliphatic peak of paracetamol (*7* in Figure 3.3a) in the 2 ppm region. Due to this overlap, diffusion data was calculated from the signal of paracetamol's aromatic resonances only.

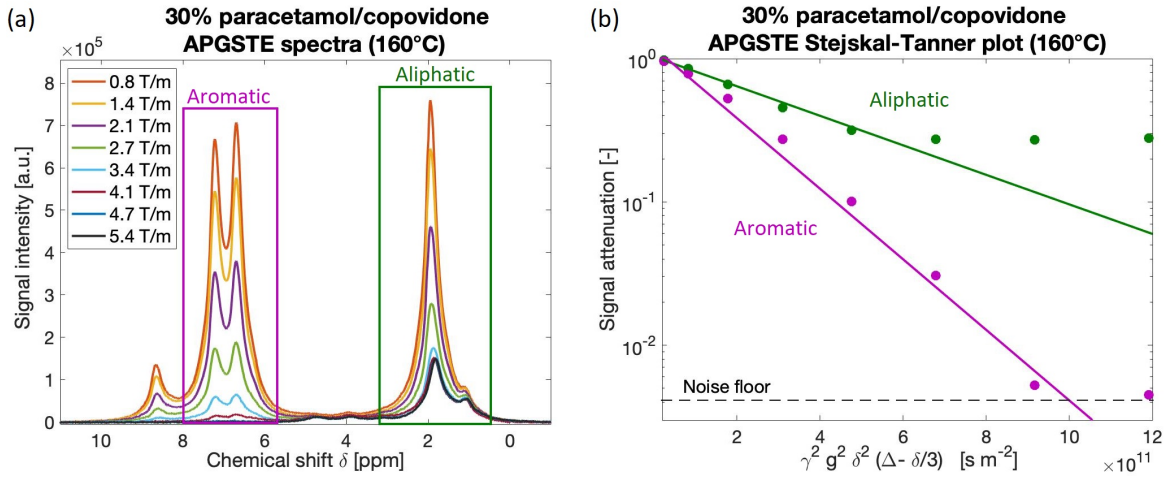

Fig. 3.7 (a) Diffusion-weighted spectra for different pulsed-field gradient strengths and (b) corresponding signal attenuation plot fitted to the Stejskal-Tanner equation for 30 wt% paracetamol/copovidone extrudate at 160°C. The fits correspond to the paracetamol-only aromatic region (purple) and aliphatic paracetamol/copovidone protons (green). Integration regions to provide plot (b) were calculated form the purple and green boxes in (a).

Table 3.2 summarises paracetamol's diffusion coefficients in physical mixtures and extrudate samples of different drug loadings at several temperatures. Paracetamol's self-diffusivity (at 170°C) is included for comparison. Samples were prepared in triplicate to determine sample-to-sample variation in the diffusivity measurement, but this was found to be of the same order as the standard deviation errors quoted in Table 3.2. The fact that the diffusion of paracetamol is over twenty times slower at 170°C in 30 % polymer mixtures than when in a pure molten state suggests that the diffusion of paracetamol is controlled by copovidone (viscosity effects and molecular interactions will be discussed in the following section).

Figure 3.8a shows that there is a small but statistically significant increase in diffusion coefficient over the 20°C range studied ($150-170$°C) for all samples, with a greater difference being observed in the samples with higher drug loadings ($40-70\%$). There is a positive correlation between diffusivity and temperature. Figure 3.8b depicts diffusion data against drug loading, and it exhibits a positive correlation of diffusivity with paracetamol content, which can be explained by the increased plasticisation of copovidone. However, there is a significantly greater increase in the diffusion coefficient between 30% and 40% paracetamol content than between any of the other drug loadings. This could be an indication that the solubility limit of paracetamol in copovidone is close to 30-40 wt% and thus there are dispersed drug-rich domains that contribute with faster diffusivity values. Bordos *et al.* identified the solid solution capacity of paracetamol in copovidone as 40 wt% and the solubility at 150°C as 45-60 wt% [75]. The solubility was determined as the extrusion temperature for which no crystalline paracetamol was detected, but this does not rule out the presence of amorphous drug-rich domains.

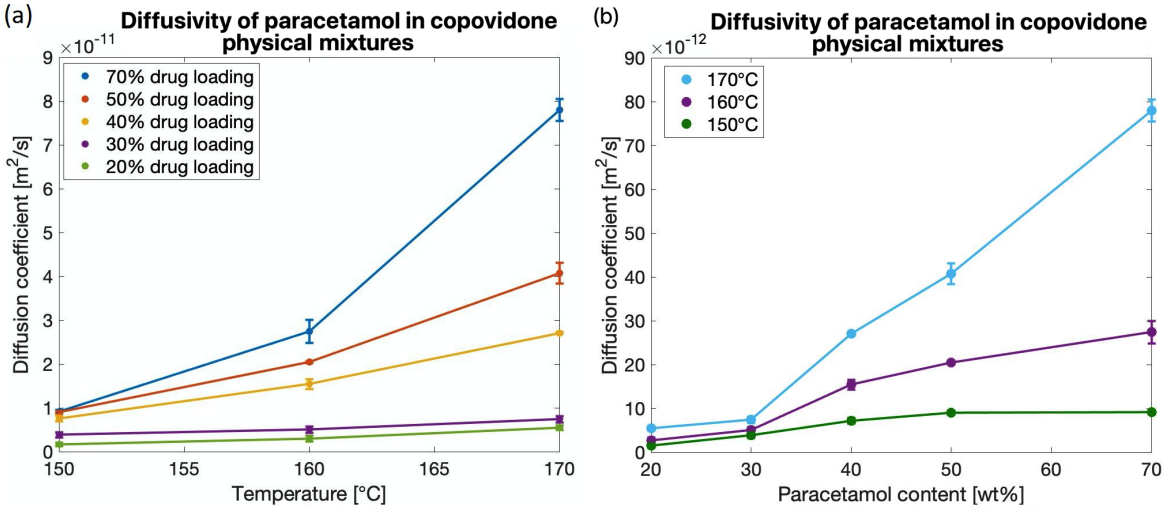

Fig. 3.8 Visual representation of part of the data in Table 3.2. (a) Diffusion coefficients of paracetamol in physical mixtures with copovidone *vs* temperature (error bars represent the standard deviation from three measurements) and (b) diffusion coefficients in physical mixtures with copovidone *vs* drug loading.

The difference in diffusion coefficient in the 30% paracetamol/copovidone mix and the 30% extrudate is very small statistically (Table 3.2) due to the associated variation (standard deviation from three repeat measurements). It is apparent, however, that the physically mixed sample exhibits consistently faster diffusivity. This can be explained by the presence of small paracetamol-rich domains in the physical mixture. No active mixing is applied on this sample, unlike the extrudate, relying only on passive mass transport (diffusion) to achieve homogenisation. Due to the very slow diffusion coefficients, it would be reasonable to assume that drug-rich domains will exist during measurements, particularly if this drug loading was close to the solubility limit. According to Einstein's discrete formula to predict the average distance travelled, root-mean-square displacement ($rmsd$), by a randomly diffusing particle in a one-dimensional system is [171]:

$$rmsd = \sqrt{2 \cdot D \cdot t} \tag{3.3}$$

According to equation 3.3, the average molten paracetamol molecule at 170°C ($D = 6{\cdot}10^{-12}$ m^2/s) will travel 0.2 mm in 1 hour. The fact that the viscosity of the 30% extruded sample is almost an order of magnitude smaller than that of the 30% physical mix, as will be discussed in the next section, supports this hypothesis. The presence of small drug-rich domains, arising due to insufficient mixing in the physical mixtures would suggest that the diffusion coefficients measured are slightly over-estimating the diffusivity of paracetamol in paracetamol/copovidone ASDs.

Table 3.2 Diffusion coefficients of paracetamol with copovidone in extrudates and physical mixtures with different drug loadings at 150-170°C. The self diffusion coefficient of paracetamol measured at 170°C is also included for comparison.

	$D \times 10^{-12} m^2/s$		
Paracetamol content	150 °C	160 °C	170 °C
20% physical mix	1.56 (±0.35)[a]	2.69 (±0.70)	5.47 (±0.54)
30% extrudate	2.18 (±0.64)	4.23 (±1.6)	6.09 (±1.0)
30% physical mix	3.85 (±0.59)	5.04 (±0.71)	7.40 (±0.73)
40% physical mix	7.16 (±0.68)	15.4 (±1.1)	27.1 (±0.21)
50% physical mix	8.96 (±0.31)	20.4 (±0.14)	40.7 (±2.4)
70% physical mix	9.17 (±0.32)	27.4 (±2.6)	78.0 (±2.5)
Paracetamol	–	–	190.0 (±20.0)

[a] The numbers in parenthesis indicate the standard deviation of three repeat measurements.

3.3.4 Rheological characterisation

Figure 3.9a shows the complex viscosities of pure copovidone, a paracetamol/copovidone physical mixture and an extrudate at 150°C for a range of angular frequencies ($0.1 - 100$ rad/s). The dashed vertical line at 4.2 rad/s has been included to indicate the angular

frequency that corresponds to 40 rpm (rotational speed of the twin screws used in this study's small-scale extruder), although it should be noted that shear rate cannot be directly related to angular frequency. In any extrusion barrel system, there will be a distribution of shear rates dependent on screw diameter, screw speed and gap between moving surfaces [172]. For the HME system used in this work (10 mm screw diameter at its widest point, 40 rpm screw speed and 0.5 mm gap between rotating screws and extrusion barrel) the upper limit of shear rate expected is approximately 40 s^{-1}. In large-scale extruders, however, shear rates reach values of hundreds and even low thousands (in the high shear regions, as are the tips of the mixing elements) [173]. This could mean that the diffusion values measured under static conditions would not be relevant at high shear rates, but it would depend on the shear thinning characteristics of the sample.

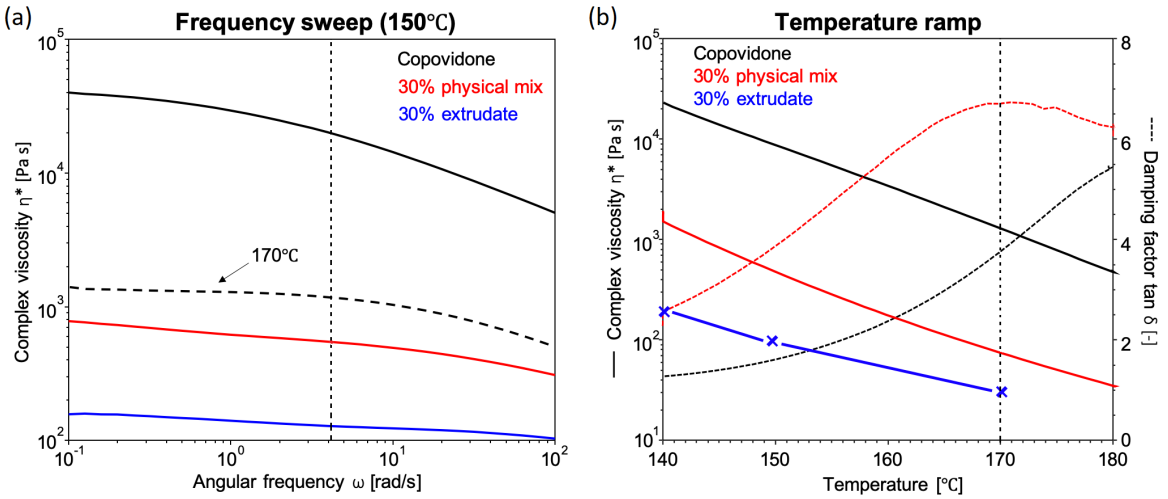

Fig. 3.9 (a) Complex viscosities from a frequency sweep at 150°C (vertical dashed line at 4.2 rad/s) and (b) complex viscosity (solid) and damping factor (dotted) from a temperature ramp of copovidone (black), and paracetamol/copovidone physical mixture (red) and extrudate (blue). In (a) the dotted black trace corresponds to the frequency sweep of copovidone at 170°C. In the temperature ramp, extrudate data was only obtained at 140°C, 150°C and 170°C as indicated by the blue × symbols.

The comparative shear thinning study of different pharmaceutical polymers by Gupta *et al.* concluded that copovidone's viscosity has a significantly lower angular frequency dependence than the other polymers studied [153]. The complex viscosities of the two paracetamol/copovidone systems shown in Figure 3.9a exhibit an even weaker dependence on angular frequency than copovidone. This suggests that the difference between the zero-shear-rate viscosity and the viscosity at 4.2 rad/s is small and thus the diffusion coefficients measured in the previous section are representative of HME in the Minilab extruder under the conditions used. A frequency sweep was also performed for the three samples at 170°C and the same conclusions were drawn (copovidone's frequency sweep at 170°C is shown in

Figure 3.9a, black dotted trace). The shear rate dependence of diffusivity *via* viscosity is explored at the end of this section through the Stokes-Einstein equation.

Figure 3.9a also shows that the physical mixture has a much lower viscosity than copovidone, which supports the argument that the incorporation of paracetamol results in a significant plasticising effect in this polymer. This is not surprising, since API molecules are known to increase the mobility of polymer chains by creating space between them and reducing intermolecular chain interactions [49]. The plasticising effect of drugs on polymers is favourable for HME because it enables processing at lower temperatures [174]. Compared to the physical mixture, the extrudate exhibits a viscosity four times lower (at 150°C). This difference can be explained by chain separation being more efficient in the extrudate as the paracetamol molecules are more homogeneously dispersed [156]. This is to be expected since, as will be discussed in the next chapter, extrudate systems achieve amorphous dispersions on the nanometre scale, whereas molten physical mixtures do not. Furthermore, due to potential for incomplete dissolution of paracetamol into the polymer over the time-scale of the rheology test, any undissolved paracetamol particles could be acting as a filler, which could contribute to an increase in apparent viscosity of the physical mixture [175].

The depression of paracetamol's melting point in copovidone presents the opportunity to extrude physical mixtures and form ASDs at temperatures lower than pure paracetamol's melting point. In practical terms, processability limitations can be assessed by the viscosity of the system. The processable viscosity range in the HME process was estimated by Gupta *et al.* as 1,000 Pa·s to 10,000 Pa·s [152]. The upper limit of this range was established as the viscosity at which 80% of the maximum torque was reached. This varies with equipment: the maximum torque in the melt extruder from Gupta *et al.* was 12 N·m and the Haake Minilab extruder used in this study could only reach 5.5 N·m. The lower limit of the processable range, however, was selected under the rationale that below 1,000 Pa·s, the benefits of extrusion would not be maximised because the material would be free flowing and it would not provide a good mixing medium, which could result in the API degrading as it settled at the bottom of the barrel.

Figure 3.9b shows the complex viscosity (solid lines) and damping factor (dotted lines) temperature ramps for copovidone and the paracetamol/copovidone physical mixture. The rheometer settings allowed compensation for the thermal expansion of the parallel plates (which was known to be 2.3 μm/°C for the apparatus used) in order to keep the distance between the plates constant. However, the viscosity of the extrudate system dropped so low that, if a variable-temperature experiment was performed, the sample leaked from the rheometer plates even at a constant plate gap. Consequently, only three individual measurements (at 140°C, 150°C and 170°C) were taken for comparison with the other samples. With reference to Figure 3.9b, the viscosity of the 30% paracetamol/copovidone physical mixture is below 1,000 Pa·s for temperatures over 144°C, which suggests that lowering the processing temperature of this system under 170°C is not only possible (with

respect to rheological behaviour and processability), but would be necessary to operate at the optimal conditions. This would especially be the case for larger scale extruders where shear rates and residence times are greater than for the small-scale extruder used in this study.

The maximum in the damping factor (Figure 3.9b) has been used as an indication that the API in pharmaceutical polymer mixtures is no longer in a crystalline state. The study by Yang *et al.* in which a 50 wt% physical mixture of nifedipine/copovidone exhibited the transition maximum 13°C below the melting point of crystalline nifedipine, proposed that this thermal event could be correlated with crystalline nifedipine dissolution [157]. The damping factor for the system under consideration peaks around 170°C (dashed vertical line), which coincides with the melting point of crystalline paracetamol. The rheology temperature ramp experiment, however, is not representative of the HME process, so perhaps processing at lower temperatures could still yield extrudates with no crystalline paracetamol.

As mentioned previously, to prove the link between viscosity and diffusivity, the Stokes-Einstein (SE) relationship was explored. The SE equation [171] correlates the diffusion coefficient of infinitely dilute spherical particles undergoing Brownian motion with the viscosity of the fluid they are suspended in:

$$D_{SE} = \frac{k \cdot T}{6 \cdot \pi \cdot r \cdot \eta} \tag{3.4}$$

where D_{SE} is the SE diffusion coefficient, k is Boltzmann's constant (k=1.38·10^{-23} J/K), r is the diffusing-particle's radius, T is the temperature in Kelvin and η is the bulk viscosity. If the data collected in the previous sections for the 30% extrudate system at 170°C (T=443 K): D=2.2·10^{-12} m^2/s and η=35 Pa·s, was used in equation 3.4, the predicted molecular radius (r) would be 1.5 pm. This value is two orders of magnitude smaller than the molecular radius of benzene [176], raising the question of the validity of the SE equation for this system.

There are several reasons why the SE equation is not applicable to the 30% paracetamol/copovidone extruded system. Firstly, the SE model is only predictive of systems in which the particles undergoing diffusion are significantly larger than the solvent molecules [177]. Liu *et al.* reported that for nano-particles in polymer melts, in which the diffusing-particle radius (r) is smaller than the polymer's gyration radius (r_g), the SE becomes invalid [178] (Figure 3.10a). The gyration radius of a polymer chain is a characteristic length scale, which is defined as the average distance from the monomers to the centre of mass of the polymer chain. The radius of a paracetamol molecule is approximately 0.3 nm [179] and the gyration radius of PVP-based polymers usually lies between $1-80$ nm, according to several studies [180–183]. The fact that the g_r of the polymer (acting as the solvent) is larger than the molecular radius of paracetamol (solute) means that the local viscosity (nano-viscosity) experienced by the solute molecules is smaller than the measured macro-viscosity of the bulk medium. This results in an underestimation of the diffusion coefficient by the SE equation.

Secondly, the SE model assumes infinite dilution and non-interacting solute-solvent systems. At significant diffusing-particle volume fractions and for interacting drug/polymer systems, particle-particle and particle-polymer interactions hinder mobility and result in further underestimation of the diffusion coefficient by the SE equation. For a highly dilute system and considering r_{par}=0.3 nm, $\eta_{copov,150°C}$=8,735 Pa·s and $\eta_{copov,170°C}$=1,290 Pa·s, the SE model predicts the diffusion coefficient of paracetamol to be $D_{par,150°C}$=1.2·10^{-16} m^2/s and $D_{par,170°C}$=8.4·10^{-16} m^2/s. These are four orders of magnitude smaller than the direct measurements presented in this chapter, and result from the gross underestimation due to the two factors explained above.

The relative solute/solvent size argument would be the fundamental reason why the SE equation is not valid for small (drug) molecules in polymer melts. Moreover, practical drug loads necessary to develop a viable ASD product will be well above infinite dilution with respect to the drug concentration, and interactions between drug and polymer are not a given but are typical in ASDs. Therefore, the SE equation is not a good predictor of the diffusion coefficient of drug molecules in drug/polymer melts and there is a need to measure this mass transport parameter experimentally in order to understand and model system dynamics.

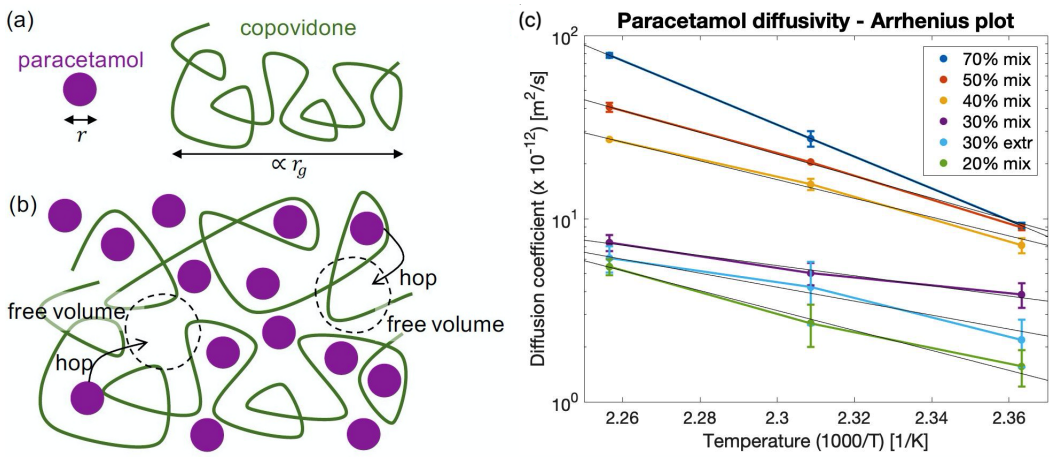

Fig. 3.10 Schematic of (a) paracetamol radius and copovidone gyration radius and of (b) the Arrhenius diffusion mechanism. (c) Diffusion data (presented in Table 3.2) fitted to the Arrhenius model (equation 3.5) for paracetamol/copovidone physical mixtures and an extrudate (error bars are the standard deviation of three measurements); the coloured traces represent the experimental data and the black lines the fit to the Arrhenius model.

Alternatively, the Arrhenius equation [184] has been used to describe the diffusion hopping mechanism (Figure 3.10b) [185, 186]. This equation correlates a rate constant (as the diffusivity) with temperature and an activation energy required to move to a neighbouring location of free volume:

$$D = D_0 \cdot exp\left(\frac{-E_A}{R \cdot T}\right) \tag{3.5}$$

where E_A is the activation energy of the diffusion process and D_0 is an amplitude parameter that represents the diffusivity as $T \to \infty$. All systems considered in this study fitted equation 3.5 very well (Figure 3.10c), with R-squared values greater than 0.956 (Table 3.3), although it should be noted that there were only three data points available to fit the model.

The Arrhenius law has been used before to mathematically characterise the high temperature diffusion of ions in molten salts [148, 150]. The Arrhenius equation has also been employed to model the diffusion of drug release from polymeric matrices during dissolution and predict diffusion coefficients [187]. Lucero-Acuña *et al.* modelled controlled drug release parameters such as temperature-dependency of drug release, time to achieve 50% of release and effective diffusion coefficient constant using mathematical expressions of the Arrhenius equation form. In that case, the interpretation of E_A was of the energy needed to overcome drug-drug and drug-polymer interactions and allow molecular diffusion. The activation energy obtained by Lucero-Acuña for the diffusion of nano-particles in a polymer, mediated by a liquid buffer, was 41.5 kJ/mol, which is of a similar magnitude as the values obtained in this study (Table 3.3). In this context, a higher activation energy would be indicative of stronger drug-polymer interactions and so of a greater barrier to diffusion. It would be expected that the 30% paracetamol/copovidone extrudate sample would exhibit a higher E_A than the physical mixture, because the formation of drug-polymer interactions has been encouraged by the molecular dispersion achieved *via* HME. This is in fact the case, as an activation energy for diffusion of 73 kJ/mol was calculated for the 30% extrudate, whereas that of its corresponding physical mixture was 53 kJ/mol.

Table 3.3 The equation used in Matlab to fit the diffusion data from Table 3.2 to the Arrhenius model (equation 3.5) was: $y = a \cdot exp(b \cdot x)$. The table below presents the results from the fits, where a and b are the fitting coefficients and R^2 is the adjusted R-squared value of the fit. E_A is the calculated activation energy for diffusion; $E_A = -1000 \cdot b \cdot R$, by comparison of the fitting model with the Arrhenius equation ($x = 1000/T$).

Paracetamol content	a	b	R^2	E_A [kJ/mol]
20% physical mix	$1.05{\cdot}10^{13}$	-12.54	0.991	104
30% extrudate	$2.51{\cdot}10^{9}$	-8.78	0.956	73
30% physical mix	$1.34{\cdot}10^{7}$	-6.39	0.978	53
40% physical mix	$9.79{\cdot}10^{12}$	-11.79	0.992	98
50% physical mix	$1.19{\cdot}10^{15}$	-13.74	0.998	114
70% physical mix	$3.71{\cdot}10^{21}$	-20.08	1.000	167

3.4 Conclusion

The work included in this chapter reports the first direct, non-invasive measurements of API diffusion in polymer melts. These were carried out at temperatures relevant to extrusion processes ($150 - 170$°C) of a paracetamol/copovidone system, providing a new way to gain

fundamental information about HME (and other high temperature processes where mass transport is critical). In a 30% paracetamol/copovidone extruded sample, the diffusion coefficient at 170°C is $6.1(\pm 1.0)\cdot 10^{-12}$ m^2/s, which is over twenty-five times slower than the self-diffusion coefficient of paracetamol in the molten state ($1.9(\pm 0.2)\cdot 10^{-10}$ m^2/s). This indicates that the diffusion of paracetamol is greatly influenced by copovidone.

The diffusion coefficients were measured at several paracetamol loadings (20-70 wt%) and temperatures ($150 - 170$°C) and their values ranged from $1.56\cdot 10^{-12}$ m^2/s for 20 wt% paracetamol at 150°C to $78.0\cdot 10^{-12}$ m^2/s for 70 wt% at 170°C. A sudden increase in the diffusion coefficient was observed between 30% and 40% drug loaded samples at the three considered temperatures. This was associated with the presence of small drug-rich domains (exhibiting faster diffusion coefficients) as the solubility limit of paracetamol and copovidone was approached ($\sim$ 40 wt%). The presence of paracetamol-rich regions in the higher drug loading physical mixtures would suggest that the diffusion coefficients measured are slightly overestimating the diffusivity in paracetamol/copovidone ASDs, but these measurements are still relevant for API/polymer mixing during extrusion.

Following rheological characterisation, the mass transport behaviour of the 30% paracetamol/copovidone system was compared to the Stokes-Einstein equation. However, it was found that it was not applicable as the size of a paracetamol molecule is smaller than the characteristic length scale (gyration radius) of copovidone resulting in a nano-viscosity experienced by the drug molecules that does not correspond to the measured macro-viscosity. Additionally, the large particle volume fraction and the probable drug-polymer interactions act to interfere with Brownian diffusion. Both of these factors result in an overestimation of the diffusion coefficient by the Stokes-Einstein model. Since this model is not a good predictor of the diffusion coefficient of drug molecules in drug/polymer systems, there is a need to measure this mass transport parameter experimentally. Alternatively, the data was successfully fitted to the Arrhenius equation, in which the activation energy can be interpreted as the energy needed to overcome drug-drug and drug-polymer interactions to allow molecular diffusion.

Chapter 4

Solid-state NMR studies of phase separation in paracetamol/ copovidone formulations

4.1 Introduction

A key area of concern regarding ASDs is their post-processing stability, particularly that the API remains in an amorphous state (no recrystallisation) and that no API/polymer phase separation occurs (miscible mixture). These features are indicative of a molecular-level dispersion and provide maximum stabilisation of the amorphous API. ^{13}C solid-state NMR (through CP-MAS techniques) conveys information on the physical state of the API: narrow line-widths are characteristic of crystalline materials, while broad line-widths are indicative of an amorphous state (due to the increased number of molecular orientations in unordered, amorphous solids) [111, 76, 156]. CP-MAS spectra also provide information on chemical interactions, which are known to play a crucial role in maintaining the physical stability of ASDs [106]. They manifest as a change in the chemical shift of the resonances involved in the interaction. Typical interactions in API/polymer systems are hydrogen bonds (H-bonds), which cause a deviation to higher chemical shifts due to delocalisation of electrons [188, 103, 111, 101].

DSC has been traditionally used to assess API/polymer miscibility in solid dispersions through observation of the number of glass transition temperature (T_g) events [69, 189, 156, 26]. A single T_g with an intermediate value between that of the polymer and the API is regarded as indicative of the formation of an ASD. The limit of detection of this technique is approximately 30 nm, but a more important limitation is that other thermal events may overlap with the T_g, concealing this transition [100, 111]. Experimental evaluation of the T_g of an API/polymer system can also provide information on molecular interactions. A positive deviation of the

measured T_g from the theoretical prediction by Gordon-Taylor's equation (further details presented in section 4.3.4) indicates strong API-polymer interactions [190, 68, 155, 27, 106].

As an alternative to DSC, there is ample evidence in the literature of ^{1}H CP-MAS T_1 (spin-lattice relaxation constant in the laboratory frame of reference) and $T_{1\rho}$ (spin-lattice relaxation constant in the rotating frame) measurements being used to obtain micro-structural information in pharmaceutical ASDs [100, 47, 48, 191]. If the API and the polymer are homogeneously mixed, the rates of relaxation will average out through spin diffusion mechanisms (spontaneous magnetisation exchange between neighbouring spins). Magnetisation transfer through this mechanism can span long distances (hundreds of nanometres) because protons are abundant and strongly coupled in the solid state. Consequently, the measured relaxation times for both species will equal the weighted average of the values of the individual components. The characteristic length scale (L) of spin diffusion, or diffusing path length is:

$$L = \sqrt{6 \cdot D_{SP} \cdot t} \tag{4.1}$$

where D_{SP} is the spin diffusion coefficient of the polymer and depends on the distance between neighbouring protons, and t is the relaxation time. D_{SP} is generally approximated to 10^{-16} m^2/s for organic polymers [192]. If drug domain sizes (Δx) are larger than L, different relaxation time constants will be measured for drug and polymer resonances. Therefore, if relaxation time constants are the same for both species, domain sizes are smaller than the diffusive path length associated with that time value (*e.g.* $\Delta x < \sqrt{6 \cdot D_{SP} \cdot T_1}$). In order to obtain chemical resolution and be able to differentiate between resonances of the two species, ^{1}H relaxation was measured indirectly through ^{13}C observation (for improved spectral resolution), following the method of Yuan *et al.* (2014) [47].

Dempah *et al.* conducted ^{1}H CP-MAS T_1 and $T_{1\rho}$ measurements on samples with markedly different particle sizes and concluded that smaller particles exhibited shorter relaxation times, to the extent that mixtures containing two particle sizes of the same compound could be deconvoluted based on their ^{1}H relaxation behaviour and their relative populations estimated [191]. More examples on the use of ^{1}H T_1 and $T_{1\rho}$ relaxometry on ASDs can be found in chapter 1 (section 1.4.3). The work presented in this chapter includes ^{1}H CP-MAS T_1 and $T_{1\rho}$ *via* ^{13}C measurements as an insight into physical state, phase separation and API/polymer interactions in ASD formulations.

4.2 Materials and methods

4.2.1 Materials and sample preparation

The materials and preparation methods followed were the same as those outlined in chapter 3 (section 3.2.1). The samples used for the work presented in this chapter are as follows:

- Physical mixtures: 30 wt% paracetamol/copovidone

- Extrudates: 20 wt%, 30 wt% and 40 wt% paracetamol/copovidone

4.2.2 Solid-state NMR spectroscopy and relaxometry

Solid-state NMR characterisation was performed in a Bruker Avance spectrometer (Bruker-Biospin, Billerica, USA) operating at a frequency of 400.23 MHz and 100.64 MHz for the ^{1}H and ^{13}C nucleus, respectively, using a 4 mm DB-MAS probe. Spectroscopy experiments were based on the magic angle spinning (MAS) ramped-cross polarization (CP) pulse sequences [137] under a spinning frequency of 9 kHz. Contact and decoupling pulses were optimised with adamantane and glycine (refer to section 4.3.1).

Samples were packed in 4 mm diameter Zirconia rotors and sealed with Kel-F caps. ^{13}C CP-MAS spectra were obtained with 2 ms contact time, 120 W proton decoupling power and the SPINAL-64 decoupling programme. The length of the 90° pulse was 2.5 μs for ^{1}H and 1.7 μs for ^{13}C. A ^{1}H saturation recovery sequence *via* ^{13}C detection was implemented with 32 pulses in the saturation train and the following list of delays: [1, 2, 3, 5, 7, 10, 15, 20, 30] all in seconds. The ^{1}H $T_{1\rho}$ sequence *via* ^{13}C detection had a 120 W spin-locking field and was repeated with the following spin-locking pulse lengths: [1, 2, 5, 7.5, 10, 15, 20, 25, 30, 40, 50, 60, 70, 80, 90, 100] in milliseconds. T_1 and $T_{1\rho}$ values were calculated from fitting the peak areas from the different delays and pulse spin-lock pulse lengths, respectively, to the exponential functions introduced in section 2.1.4 (equations 2.24 and 2.25). The number of scans acquired for CP-MAS ^{13}C spectra were 256, while for relaxometry experiments 512 averages were performed. The recycle delays used for the different samples and experiments are listed in Table 4.1. Curve fitting was performed on MATLAB_R2017b.

Table 4.1 Recycle delay experimental values for CP-MAS experiments, where *PAR* stands for crystalline paracetamol, *COP* for copovidone, *Extr* for extrudate, *PM* for physical mixture and *mPM* for molten physical mixture.

	PAR	***COP***	***Extr***	***PM***	***mPM***	***Relaxometry***
T_R **[s]**	60	5	5	30	7.5	5

4.2.3 Modulated differential scanning calorimetry

Thermal analysis was conducted with a Q2000 (TA Instruments, New Castle, DE, USA) differential scanning calorimeter. Approximately 3-7 mg of sample was sealed in a standard aluminium pan and heated from 20°C to 200°C at a rate of 4°C/min, with a modulation amplitude of ±1°C and period of 60 s, and cooled back to 20°C at 10°C/min. Two controlled sequential heat-cool cycles were performed on all samples under a nitrogen stream of 50 mL/min. Glass transition temperatures were assigned to the stationary point of the normalised reversing heat flow data. Similarly, melting temperatures were determined as the inflection point of the endotherms. The thermogram data was processed and plotted using TRIOS software (TA Instruments).

4.3 Results and discussion

4.3.1 Calibration of the CP-MAS pulse sequence parameters

Prior to conducting CP-MAS solid-state experiments, key pulse sequence parameters (^{1}H and ^{13}C 90° pulses, high-power decoupling power and cross-polarization contact pulse and decoupling pulse lengths) were calibrated on reference samples.

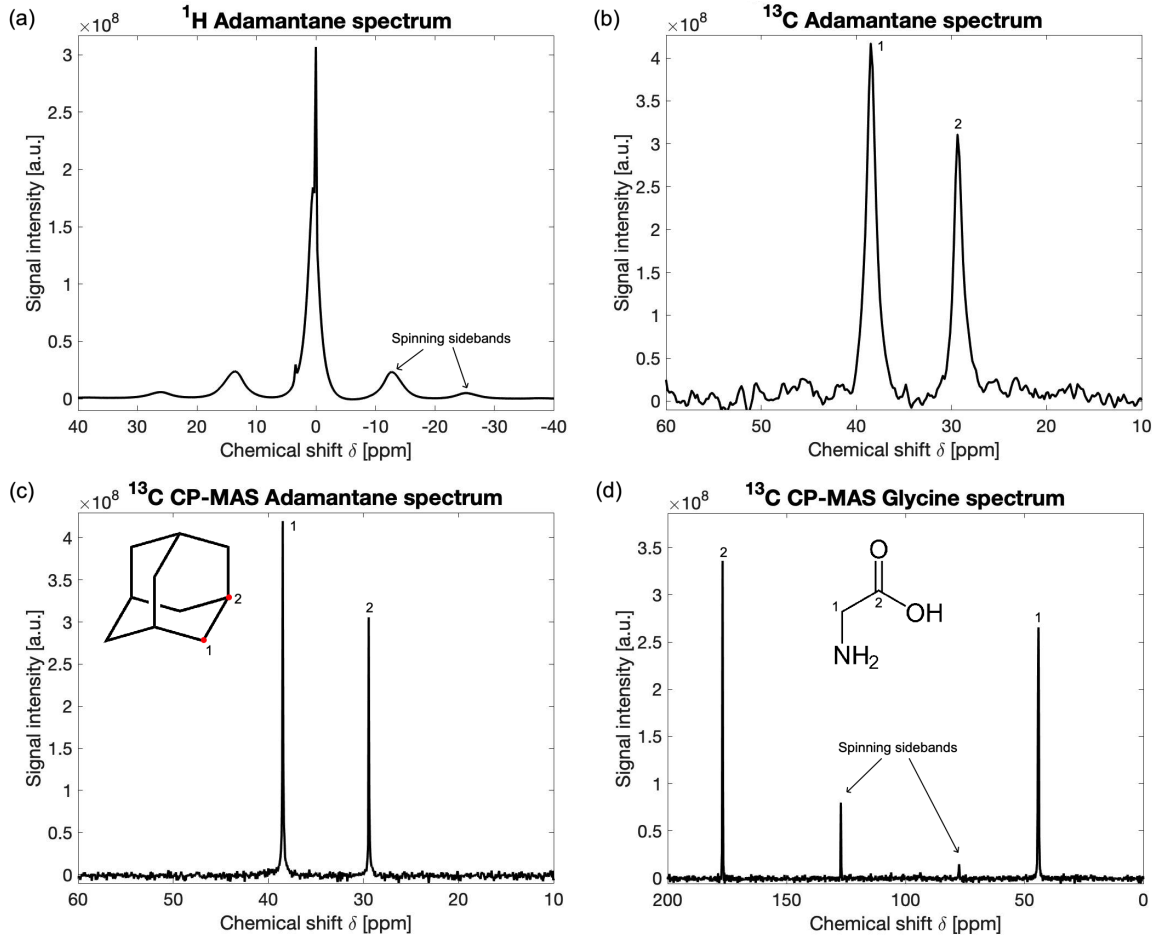

Fig. 4.1 (a) ^{1}H spectrum of adamantane; ^{13}C spectra of adamantane (b) without and (c) with high power decoupling cross polarisation (inset: chemical structure of adamantane). (d) ^{13}C CP-MAS spectrum of glycine (inset: chemical structure of glycine).

Adamantane (ADM) is a crystalline compound with chemical formula $C_{10}H_{16}$ (chemical structure is shown in Figure 4.1c, inset). ADM is used as a ^{1}H and ^{13}C 90° pulse calibration standard because: (i) the proton signal is easily detectable as, even at low MAS spinning rates, proton homonuclear dipolar interactions significantly average and (ii) ^{13}C signal-to-noise ratio (SNR) is high and few scan averages are required to obtain a high resolution spectrum [193]. The ^{1}H and ^{13}C spectra of ADM are shown in Figure 4.1a and b, respectively. These spectra

were used to calibrate the ^{1}H and ^{13}C 90° pulses, which were 2.5 μs and 1.7 μs respectively, for 150 W magnitude.

To improve ^{13}C sensitivity, high power heteronuclear (proton-carbon) decoupling can be implemented through a decoupling pulse. The optimal amplitude of this pulse was found to be 120 W. ADM also serves as a chemical shift calibration standard, as peak *2* (refer to Figure 4.1c) is known to be centred at 29.46 ppm [194]. The cross-polarisation sequence further increases signal intensity (Figure 4.1c).

Glycine (GLY) is the simplest amino acid, and its structure is shown in Figure 4.1d inset. GLY is used to calibrate the CP pulse (contact pulse during which polarisation is transferred from the protons to the carbons) instead of ADM because it is more representative of solid samples of interest [193]. The optimised contact pulse length and power is selected as the parameter combination that maximises the intensity of peak *1* (refer to Figure 4.1d). These were found to be 2 ms and 50 W, respectively.

4.3.2 ^{13}C CP-MAS spectra of paracetamol/copovidone physical mixtures and extrudates

^{13}C CP-MAS NMR spectra of pure copovidone and crystalline paracetamol were acquired and are shown in Figure 4.2c. Assignment of paracetamol and copovidone ^{13}C resonances (with reference to the labelling in Figures 4.2a and b) have been made by comparison with the literature [195, 157]. In agreement with DSC results from section 3.3.2, as-received paracetamol's crystalline spectrum corresponds to polymorph form I [168].

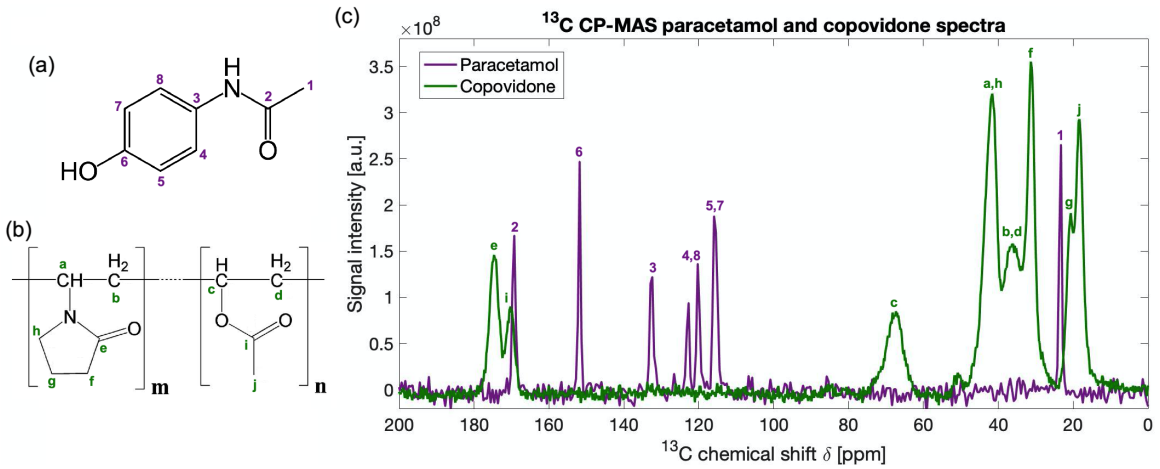

Fig. 4.2 Chemical structures of (a) paracetamol and (b) copovidone, with carbon atoms labelled (*1-8* for paracetamol and *a-j* for copovidone). (c) Overlaid ^{13}C CP-MAS spectra of solid-state paracetamol and copovidone.

^{13}C NMR spectroscopy has been used to distinguish between crystalline and amorphous API because amorphous materials exhibit characteristically broad peaks, in contrast with

crystalline compounds, which produce sharp resonances [51, 47, 76]. The line-broadening is caused by the lack of structural isotropy in amorphous compounds, as different molecular orientations will result in different resonant frequencies and thus a loss of resolution. Figure 4.3a shows the ^{13}C high resolution spectra of a 30 wt% paracetamol/copovidone physical mixture. The paracetamol resonances (*1-8*) are noticeably sharper than the copovidone ones (*a-j*), because paracetamol is in a crystalline physical state while copovidone is amorphous. The ^{13}C spectra of three extruded samples at 20%, 30% and 40% drug loading are displayed in Figure 4.3b. In contrast to Figure 4.3a, all resonances appear broad indicating that both paracetamol and copovidone are in an amorphous state.

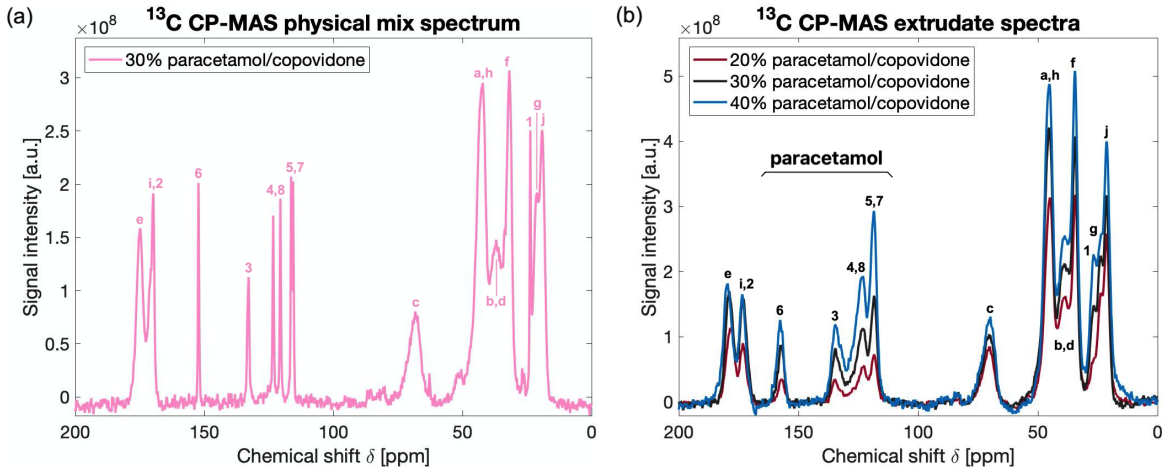

Fig. 4.3 ^{13}C CP-MAS spectra of paracetamol/copovidone systems: (a) 30% physical mix, and (b) 20%, 30% and 40% extrudates. Resonance assignments refer to the molecular structures shown in Figure 4.2a and b.

Closer examination of Figure 4.3b reveals that the intensities of the resonances that correspond to paracetamol increase with drug loading, as expected. However, the intensity of the copovidone peaks also strengthens with paracetamol content. This could be due to increased CP (proton to carbon magnetisation transfer) efficiency. The CP efficiency to a dilute nucleus, as is ^{13}C, is dependent on the proximity of the abundant nuclei (^{1}H) [76]. Paracetamol/copovidone extrudates have been characterised as a homogeneous and intimate dispersion of the drug particles. This was evidenced by a decrease in viscosity in extrudates when compared to physical mixtures in chapter 3 (section 3.3.4) and will be further backed up by the results from the CP-MAS relaxometry experiments presented in the following section. As a result of the homogeneous dispersion, the small paracetamol molecules are in closer contact with the copovidone chains than the polymer-polymer chain spacing. This means that, while the system remains miscible and homogeneous, increasing drug loading increases CP efficiency from the ^{1}H in paracetamol to the ^{13}C in copovidone and thus increases the signal from copovidone resonances.

Figure 4.4 is a comparison of the spectra of three different 30 wt% paracetamol/copovidone systems: (1) extruded, (2) physically mixed and (3) a physical mixture that was heated to 170°C and held isothermally for 10 min and then let to cool down before acquisition at room temperature. For the extruded sample, trace (1), all peaks are broad, indicating that paracetamol was rendered amorphous *via* HME. In trace (2), as expected for a physical mixture, the paracetamol resonances (Figure 4.4 purple box) are sharp and well resolved, as in the spectrum of crystalline paracetamol shown in Figure 4.2c, purple line. In the 30% molten mix, trace (3), paracetamol is present both in crystalline and amorphous states as can be observed by the presence of overlapping broad and narrow resonances.

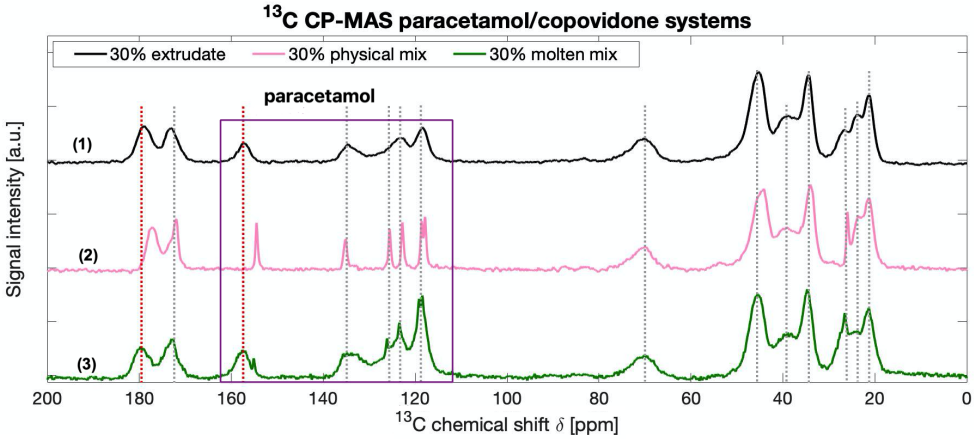

Fig. 4.4 ^{13}C CP-MAS spectra of 30 wt% drug loading paracetamol/copovidone extruded sample (1), physical mixture (2) and a physical mixture that was molten at 170°C (3). The purple box surrounds the paracetamol-only region of the spectra. The red vertical dashed lines mark the resonances that exhibit a change in chemical shift between the extrudate and physical mixture systems.

Interestingly, in traces (1) and (3) of Figure 4.4, the copovidone peak at the highest chemical shift is centred at 179 ppm (Figure 4.4, red dashed line), whereas for trace (2) that resonance is at 177 pm (while the position of all other copovidone resonances is essentially identical in the three traces). This peak is assigned to the carbonyl group of the vinyl-pyrrolidone (VP) monomer (carbon *e* in Figure 4.2b), which is the most likely to interact with other molecules (more so than the carbonyl of the vynil-acetate group) [106]. Likewise, if the position of paracetamol peaks is compared in the three traces, there is only one resonance that differs: the peak that corresponds to the carbon from the phenolic group (carbon *6* in Figure 4.2a) shifts from 155 ppm in trace (2) to 157 ppm in trace (1), Figure 4.4, red dashed line. In trace (3), both resonances (at 155 ppm and 157 ppm) are present. The chemical shift of the carbonyl in the VP monomer of copovidone and the phenol in paracetamol occurs to higher chemical shift values, that is downfield. This is consistent with HME having induced hydrogen-bonding in the paracetamol/copovidone systems because this type of interaction will decrease the electron density around the carbons closest to the acceptor and donor atoms,

resulting in deshielding [188]. Such features have also been reported by Watanabe *et al.* in ASD formulations of PVP polymer with indomethacin [103]. It is also well established in the literature that drug-polymer H-bonding can increase the stability of ASDs with respect to drug recrystallisation on storage and maintaining supersaturation during dissolution [32, 102].

4.3.3 ^{1}H T_1 and $T_{1\rho}$ measurements for phase separation studies

Additional information regarding phase separation of samples was obtained through CP-MAS ^{1}H relaxometry by measurement of T_1 and $T_{1\rho}$ parameters *via* ^{13}C observation. The four ^{13}C peaks used for paracetamol ^{1}H T_1 and $T_{1\rho}$ calculations were the ones resolvable in the 105-165 ppm region, as there is no copovidone signal in that frequency range (Figure 4.2b). Four copovidone-specific resonances, centred at 34 ppm, 45 ppm, 70 ppm and 178 ppm were selected for calculating copovidone's relaxation constants. The saturation recovery T_1 plots for the 30 wt% physical mixture and extrudate are shown in Figure 4.5a and b.

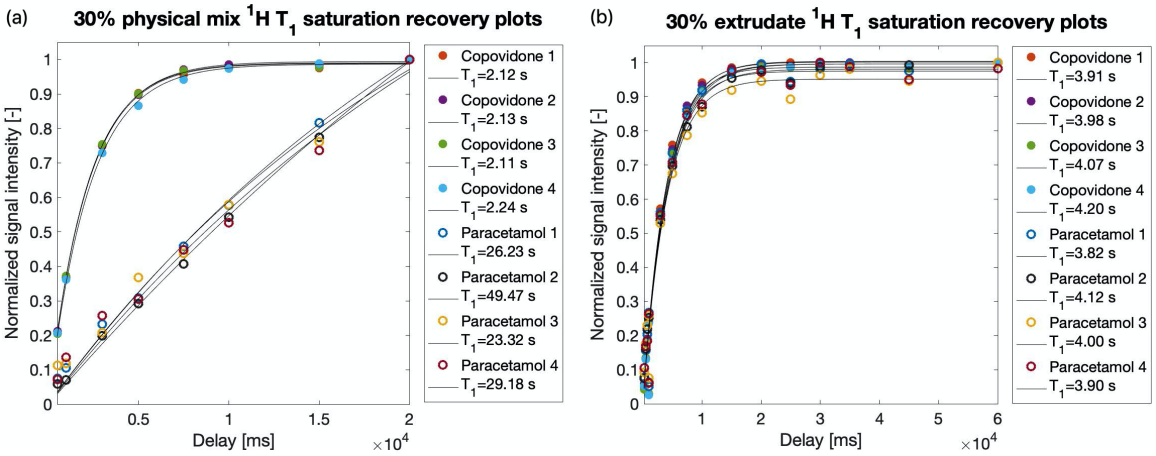

Fig. 4.5 T_1 saturation recovery plots for four resolved copovidone and paracetamol resonances in (a) a 30% physical mixture and (b) a 30% extrudate.

For each species (paracetamol and copovidone), a ^{1}H T_1 and $T_{1\rho}$ value was calculated as the average from the four individual peaks. The absolute difference between copovidone's and paracetamol's T_1 and $T_{1\rho}$ constants are shown for five different paracetamol/copovidone systems are shown in Figure 4.6a. Error bars represent the standard deviation of the relaxation values for each species. The dashed line at zero represents the position at which the T_1 or $T_{1\rho}$ is identical for paracetamol and copovidone (because the difference between the two is zero). The difference in T_1 and $T_{1\rho}$ was so large in the physical mixture sample between paracetamol and copovidone resonances that the data was scaled down by a factor of 10 and 200, respectively, for representation purposes. The reason for comparing the absolute differences in relaxation instead of the relaxation constants' values is that these are highly sensitive to moisture content [47].

Figure 4.6a shows that there is no statistical difference between T_1 or $T_{1\rho}$ of paracetamol and copovidone in any of the extrudate systems at any of the drug loadings considered (20-40 wt%). This indicates that there is no phase separation and, using equation 4.1, that the paracetamol domain size in these systems is smaller than the diffusive path length corresponding to the smallest time constant ($T_{1\rho}$): Δx<3.8 nm. In the 30% physical mix case, both relaxation constants are considerably different for paracetamol and copovidone. As expected, the results reveal phase separation with paracetamol domain sizes larger than 130 nm. These results can also be observed in Figure 4.5a and b, where paracetamol exhibits a much longer T_1 than copovidone in the physical mixtures, but their values are identical in the extrudate sample.

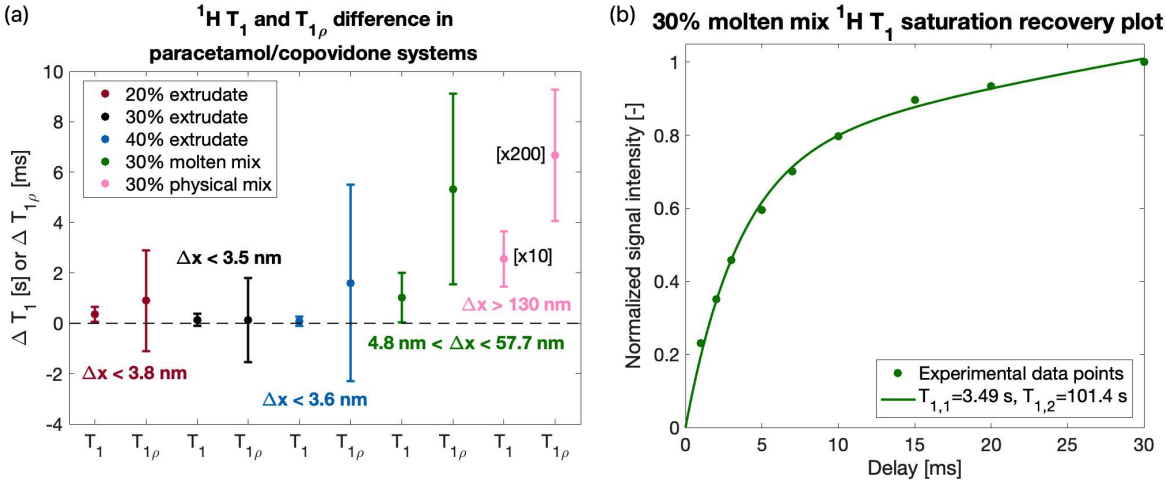

Fig. 4.6 (a) ^{1}H T_1 and $T_{1\rho}$ difference between average paracetamol and copovidone relaxation values obtained *via* ^{13}C resolved resonances for 20%, 30% and 40% extrudates, a 30% physical mixture and a 30% molten physical mixture. (b) Deconvolution of ^{1}H T_1 data for the 30% molten mix system.

In agreement with the observations made from Figure 4.4 trace (3), the results for the molten mix system lie in between the extrudate and the physical mixture samples. While no significant difference was detected for paracetamol and copovidone in T_1, the opposite was true for $T_{1\rho}$. According to equation 4.1, paracetamol domain sizes in this system are estimated as larger than 5 nm, but smaller than 58 nm. By integrating over the paracetamol peaks in the 105-165 ppm region and fitting a two-component exponential, it is possible to deconvolute the relaxation into two rates [191]. For T_1 two relaxation rates were obtained: 3.5 s corresponding to molecularly dispersed paracetamol, and 101.4 s from the crystalline paracetamol [195] (Figure 4.6b). This means that a physical mixture that has been heated to 170°C does not have the same microscopic structure as one that has been through the HME process. It is also further evidence that a multi-phase system with paracetamol-rich domains was formed upon heating, which backs up the hypothesis presented in section 3.3.4 regarding incomplete intimate mixing in molten physical mixtures.

4.3.4 Glass transition temperature assessment by mDSC

The normalised reversing heat flow thermograms of copovidone, paracetamol, a paracetamol/copovidone physical mixture and extrudate can be found in Figure 4.7a (a section of the thermogram for paracetamol is shown as an inset). The measured T_g of copovidone ($T_{g,copov}$=108.5°C) is consistent with literature values [196], as is the T_g of paracetamol ($T_{g,par}$=23.7°C) [197].

In Figure 4.7a, the 30% drug loaded physical mixture exhibits a T_g (105.0°C) that corresponds to the copovidone in the system. The melting peak at 168°C has an early onset that overlaps with the baseline at the end of the glass transition event. Despite the overlap of events, the apparent start of the endotherm is at 120°C (vertical dotted line), which agrees with the melting point depression observations in NMR experiments (data shown in chapter 7). Marsac *et al.* revealed that strong API/poymer interactions result in large melting point depression and are indicative of miscible systems [154]. Paracetamol and copovidone can thus be considered to be miscible according to DSC characterisation.

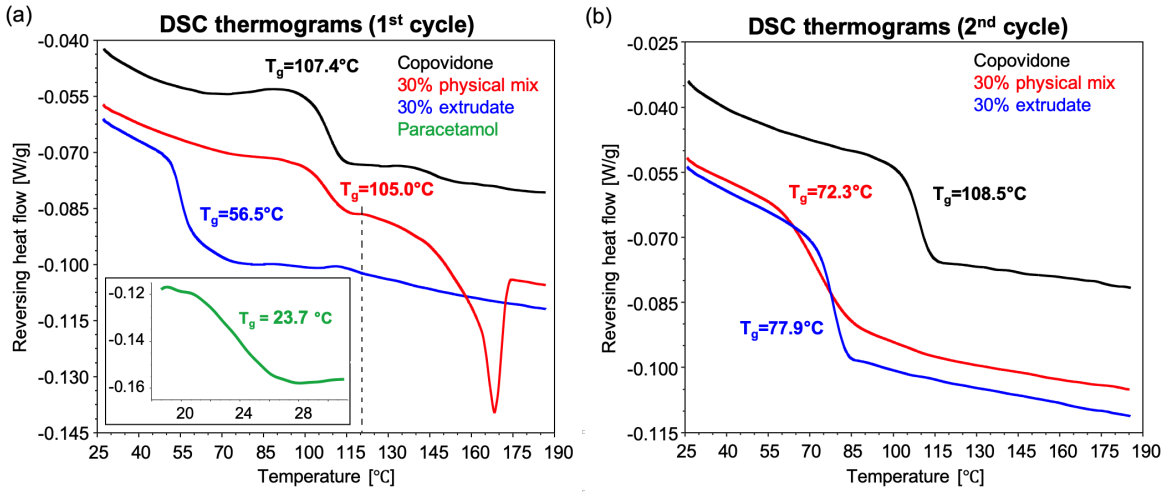

Fig. 4.7 DSC thermograms of copovidone (black), paracetamol/copovidone physical mixture (red) and extrudate (blue), and paracetamol (green) for the (a) first and (b) second heating cycles. The dashed vertical line in (a) indicates the depression of the onset of the melting point of crystalline paracetamol in the physical mixture.

The thermogram of the extrudate in Figure 4.7a displays no melting endothem (indicating that there is no crystalline paracetamol present in the sample) and a single glass transition (56.5°C) at a temperature that lies between the T_g's of copovidone and paracetamol. This is indicative of the successful formation of an ASD during the extrusion process, in agreement with the CP-MAS results presented in the previous section. However 56.5°C is not a representative value of the system's T_g because it was not vacuum dried prior to analysis; any water present would plasticise the sample, decreasing its apparent T_g [4, 32]. Water loss during the first heating cycle resulted in an increase in T_g of the extrudate and decrease

in T_g for the physical mixture, in the second heating ramp (Figure 4.7b), to 77.9°C and 72.3°C, respectively. The same is true for copovidone, which is why its T_g is taken from the second heating cycle, once water was removed from the sample (this was not the case for pure paracetamol, which contained no moisture as revealed by DSC and TGA). The disparity in T_g between the two 30% paracetamol/copovidone systems was not considered to be significant as it is likely a result of differences in composition. DSC sample sizes are very small, which can lead to inaccurate drug loading of the individual samples.

The Gordon-Taylor equation predicts glass transition temperatures of amorphous mixtures from the glass transition temperatures of the individual components [29]:

$$T_{g,mix} = \frac{w_1 \cdot T_{g,1} + K \cdot w_2 \cdot T_{g,2}}{w_1 + K \cdot w_2} \tag{4.2}$$

where $T_{g,1}$ and $T_{g,2}$ are the glass transition temperatures of the two components in the mixture and w_1 and w_2 are their weight fractions. K is a constant parameter that can be estimated from the Simha-Boyer rule [30]:

$$K = \frac{d_1 \cdot T_{g,1}}{d_2 \cdot T_{g,2}} \tag{4.3}$$

where d_1 and d_2 are the densities of the components. The density of amorphous paracetamol, was calculated from the specific volume curve for liquid paracetamol provided by Espeau *et al.*: $V[cm^3/g] = 0.671 + 0.000539 \times T[K]$ [198]. Extrapolating for room temperature ($T = 293\ K$): $V[cm^3/g] = 0.829$. Applying equations 4.2 and 4.3 to the 30% paracetamol/copovidone system and using the parameters from Table 4.2, the predicted glass transition temperature of the 30% paracetamol/copovidone system is 52.8°C.

Table 4.2 Parameters for the Gordon-Taylor and Simha-Boyer equations for T_g prediction.

	w [−]	$\mathbf{T_g}$ [°C]	**d** [$\mathbf{g/cm^3}$]
Paracetamol	0.3	23.7[a]	1.21[b]
Copovidone	0.7	108.5[a]	1.18[c]

[a] Experimental value from DSC. [b] Value calculated from [198]. [c] Value from [199].

The predicted T_g of the system (52.8°C) is well below the experimentally obtained ones (77.9°C and 72.3°C for the extrudate and physical mixture, respectively). A strong positive deviation from the Gordon-Taylor prediction indicates that paracetamol-copovidone interactions are strong (stronger than paracetamol-paracetamol or copovidone-copovidone interactions) [106]. Strong drug-polymer interactions are favourable, among other factors, because they stabilise the ASD formulation in the presence of moisture. As mentioned above, moisture physically affects the stability by lowering the T_g of the mixture, which increases molecular mobility and the potential for phase separation; it also chemically decreases stability

by lowering the solubility of API in the polymer, increasing the supersaturation degree and leading to crystallisation [32]. The fact that this data suggests drug-polymer interactions reinforces the conclusion that the Stokes-Einstein equation is not applicable to the system under study (chapter 3, section 3.3.4).

It should be noted that in the second heating cycle the physical mixture displays the same behaviour as the extrudate in that the thermogram lacks a melting endotherm and exhibits a single glass transition, which suggests the formation of an ASD. This result disagrees with the CP-MAS NMR data presented in the previous sections 4.3.2 and 4.3.3, in which a paracetamol/copovidone physical mixture that has been heated to 170°C shows some degree of phase separation. Consequently, its micro-structural features are different from those of an extruded sample. However, the very small sample size in DSC pans (few milligrams) increases the likelihood of mixing and decreases the chances of nucleation and recrystallisation.

4.4 Conclusion

CP-MAS ^{13}C high resolution spectral line width observations were used to show that paracetamol is in an amorphous state (rather than crystalline) in all the hot-melt extruded samples (20-40 wt% drug loading). Differences between the chemical shift of the carbonyl VP (copovidone) resonance and the phenol paracetamol peak in the 30 wt% physical mixture and extruded systems provide an insight into drug/polymer molecular interactions promoted by the intimate mixing of paracetamol and copovidone *via* the HME process. This observation was backed up by DSC: the T_g predicted by Gordon-Taylor's equation of the paracetamol/copovidone system is well below the experimental T_g, which is indicative of strong paracetamol/copovidone interactions. The evidence of molecular interactions supports the statement made in chapter 3 regarding the validity of the Stokes-Einstein diffusion prediction to the paracetamol/copovidone system. Specifically for the sample under investigation, H-bonding between copovidone's VP carbonyl and paracetamol's phenolic moiety was identified. This intermolecular association could be responsible for stabilising paracetamol/copovidone ASDs. Paracetamol/copovidone interactions will be studied in more detail in chapter 5.

^{1}H relaxometry data *via* ^{13}C acquisition revealed no phase separation or recystallisation in the 20%, 30% and 40% extrudate systems. There was, however, some degree of phase separation in the 30 wt% physical mixture that was heated to 170°C, in which the T_1 constants of paracetamol and copovidone were identical (within the associated error), but the $T_{1\rho}$ values were different. In this sample, drug-rich domains were estimated to be 4.8 nm to 57.7 nm in size and crystalline in nature (as evidenced from the very long T_1 constant obtained from the deconvoluted bi-exponential fit). This result is further evidence that a multi-phase system with paracetamol-rich domains was formed upon heating during measurement of the self-diffusion coefficients in the paracetamol/copovidone physical mixture systems, as was hypothesized in chapter 3.

Chapter 5

Application of 2D NMR techniques for molecular interaction studies

5.1 Introduction

The role of drug-polymer interactions in the performance of ASD formulations has recently become a topic of interest. Intermolecular associations between the API and the excipient have been revealed to influence two key mechanisms in ASDs: crystallisation and dissolution. The nucleation and crystallisation kinetics of an API in a supersaturated ASD formulation is hindered or inhibited by the presence of drug-polymer interactions [76]. The extent of inhibition has been correlated with the strength of the molecular association [33]. Mistry *et al.* observed a relationship between the strength of the interaction and the extent of crystallisation inhibition; and this is hypothesized to be linked to the decrease in molecular mobility [102]. Drug-polymer interactions also play a role in enhancing drug solubility. The improved dissolution profile is achieved in two ways: intermolecular associations maintain the physical stability in supersaturated ASDs and they have been observed to increase the solubility of the drug in water (both by preventing crystal growth and increasing the saturation concentration) [32, 53]. Furthermore, drug/polymer interactions are favourable for the HME process because they lead to depression of the drug's melting point (enabling extrusion at lower temperatures) and because they lead to lower chemical potentials of the systems, enhancing solubility and miscibility of the drug in the polymer [32].

Several techniques have been used in the elucidation of drug/polymer molecular interactions in ASDs. Fourier-transform infrared, Raman and NMR spectroscopy are among the most widely employed [4, 102]. Some studies have applied alternative methods such as X-ray photoelectron spectroscopy and molecular dynamic simulations [200]. In spectroscopy-based techniques, such as high resolution NMR, drug/polymer associations can be inferred from shifts in the frequency/wave number of those atoms involved in the interaction (as discussed in chapter 4). Additionally, the NMR toolbox has several 2D experiments aimed at under-

standing the associations (scalar or dipolar) between atoms both intra- and inter-molecularly, hetero- and homo-nuclear as well as through-space and through-bond. Some frequently used 2D correlation experiments include COSY, HETCOR, MQC and NOESY (see chapter 2, section 2.1.5, for detailed explanations of the relevant techniques) [76].

Tatton *et al.* observed intermolecular drug/polymer through-space coupling *via* solid-state heteronuclear (^{14}N-^{1}H) MQC in ASDs [112]. These were identified as hydrogen bonds (H-bonds) between the drug's hydroxyl group and the polymer's carbonyl. Pham *et al.* used solid-state ^{1}H-^{13}C HETCOR to identify drug/polymer interactions and ^{1}H-^{1}H MQC for additional structural information [111]. HETCOR spectra at increasing contact times displayed more intense drug/polymer cross-peaks, as proton spin diffusion covers larger length scales. This is proof that a large percentage of API molecules are in intimate contact with polymer chains (molecular-level interactions).

2D correlation NMR experiments have also been performed in solution-state drug-polymer systems. Fule *et al.* used the ^{1}H-^{1}H COSY sequence on a pharmaceutical system dissolved in DMSO [43]. Couplings were observed at several points in the correlation spectra that indicated strong molecular interactions between the drug and the polymer. Liu *et al.* assessed the impact on intermolecular association by substituting the hydrogen-bonding proton in the API by a fluorine when the system was dissolved in deuterated chloroform [106]. Apart from the characteristic chemical shift, NOESY experiments revealed H-bonding between the drug and the polymer's carbonyl group.

Hydrogen bonding is the most common type of drug/polymer interaction identified in ASDs. In H-bonds a hydrogen atom is in association with two (electronegative) atoms, typically O or N. 2D NMR techniques such as HETCOR, NOESY and MQC indirectly probe for H-bonds by detecting through-space nuclear proximity. By selecting shorter mixing or contact times, smaller length scale (stronger) interactions become evident. The nuclei on both sides of the H-bond are magnetically coupled *via* a scalar interaction, which is what allows their observation in COSY (through-bond) experiments [188]. This coupling occurs through the re-distribution of electron densities around the bridging proton, which also manifests itself in the chemical shift changes discussed in the previous chapter.

This chapter reports findings from traditional solid-state ^{13}C-^{1}H HETCOR, which provide insights into API-polymer molecular interactions in ASD formulations. Additional solid-state ^{1}H-^{1}H NOESY and ^{1}H-^{1}H MQC experiments were performed at high-field (850 MHz) and fast MAS (60 kHz). This set-up offers the opportunity to obtain resolved solid-state ^{1}H spectra, as otherwise no resolution is obtained from static solid samples. Furthermore, this chapter presents results from molten-state ^{1}H-^{1}H COSY, which, when compared to solid-state techniques, has greater proton spectral resolution and provides further insights into API-polymer associations. To the best of my knowledge, there are no accounts in the literature of 2D NMR COSY being performed in the molten state, without a solvent present and at high temperatures relevant to the HME processes.

5.2 Materials and methods

5.2.1 Materials and sample preparation

The same materials and sample preparation methods were followed as those outlined in chapter 3 (section 3.2.1). The samples used for the work presented in this chapter are as follows:

- Paracetamol and copovidone
- Extrudate: 30 wt% paracetamol/copovidone

5.2.2 2D high-field solid-state NMR

High-field solid-state NMR characterisation was performed in a Bruker Avance spectrometer (BrukerBiospin, Billerica, USA) operating at a frequency of 850.23 MHz and 213.79 MHz for the ^{1}H and ^{13}C nucleus, respectively, at the UK 850 MHz solid-state Facility (University of Warwick, Coventry, UK). ^{1}H-^{1}H experiments were conducted at 60 kHz MAS in 1.3 mm rotors for improved proton resolution, while ^{13}C-^{1}H HETCOR was performed at 15 kHz in 4 mm rotors. The signal-to-noise ratio (SNR) of ^{13}C spectra at 60 kHz was very low. This was a combined effect from the low natural abundance of ^{13}C and the small sample volume in the 1.3 mm rotors used for spinning at 60 kHz and the decreased CP efficiency at high MAS rates [130, 201].

^{13}C-^{1}H HETCOR

^{13}C-^{1}H HETCOR was performed on a 4 mm DB-MAS dual-resonance probe at a MAS rate of 15 kHz. The pulse sequence used was based on the ramped CP-MAS with FSLG and TPPM decoupling HETCOR (schematic of the pulse sequence is shown in Figure 2.11a). Samples were packed in 4 mm diameter Zirconia rotors with Kel-F caps. The CP contact time was varied between 1-4 ms for an 80 Watt power pulse. The length of the 90° pulse was 2.5 μs for ^{1}H and 3.5 μs for ^{13}C, the magic angle pulse length was 1.52 μs (refer to Figure 2.11a) and the recycle delay was 2 s. Contact and decoupling pulses were optimised with glycine and alanine (refer to Figures 5.1 and 5.2). The data was processed in TopSpin and plotted using MATLAB_R2017b.

^{1}H-^{1}H NOESY

^{1}H-^{1}H NOESY experiments were performed on a 1.3 mm triple-resonance probe operating in double-resonance mode at a MAS rate of 60 kHz, (schematic of the pulse sequence is shown in Figure 2.10). Samples were packed in 1.3 mm diameter Zirconia rotors with Vespel caps. The mixing time was varied between 0.3 and 100 ms for 80 Watt power level pulses. The length of the 90° pulse was 2.5 μs and the recycle delay was 4 s for copovidone and

the extrudate formulation and 120 s for crystalline paracetamol. The data was processed in TopSpin and plotted using MATLAB_R2017b. Chemical shifts are referenced with respect to TMS using β-AspAla as a secondary reference.

^{1}H-^{1}H MQC SQ/DQ BABA

^{1}H-^{1}H MQC SQ/DQ rotor-synchronised BABA MAS experiments were performed on a 1.3 mm triple-resonance probe at a MAS rate of 60 kHz, using two rotor periods of double quantum excitation and two rotor periods of reconversion (schematic of the pulse sequence is shown in Figure 2.12). Samples were packed in 1.3 mm diameter Zirconia rotors with Vespel caps. The variable delay d_0 was stepped-up in 1 ms increments. The length of the 90° pulse was 2.5 μs and the recycle delay was 4 s for copovidone and the extrudate formulation and 120 s for crystalline paracetamol. The data was processed in TopSpin and plotted using MATLAB_R2017b. Chemical shifts are referenced with respect to TMS using β-AspAla as a secondary reference.

5.2.3 2D molten-state NMR: ^{1}H-^{1}H COSY

^{1}H-^{1}H liquid-state COSY was conducted on a 7.07 T Bruker Biospin DMX 300 MHz spectrometer (BrukerBiospin, Billerica, USA) operating at a ^{1}H frequency of 300.23 MHz through the ParaVision 4.0 software. A Bruker Biospin DIFF-30 probe was equipped with an extended variable temperature range ^{1}H/^{19}F 5 mm i.d. r.f. coil. Experiments were performed with 8 μs 90° pulse, on 100 mg of sample and either at room temperature or at 170°C.

COSY experiments were performed using a pair of pulsed-field gradients of 0.6 T/m for coherence transfer pathway selection (schematics of the pulse programs are shown in Figure 2.9a). The recycle time was 2 s (longer delays were evaluated, but SNR did not improve significantly and experimental time increased sharply). A sweep width of 5 kHz was used for the high-resolution spectra (dissolved copovidone and molten paracetamol) and 50 kHz for the spectra with wider-linewidths (molten paracetamol/copovidone extrudate). 32 scans were acquired for the traditional COSY experiments (Figure 2.9a), 64 scans for the SE-COSY (Figure 2.9b) at d_{SE}=1 ms and 80 scans at d_{SE}=10 ms, resulting in an experimental time of 5 hours, 10 hours and 12.5 hours, respectively. The data was processed in TopSpin and plotted using MATLAB_R2017b. Prior to recording at high temperatures, the temperature performance of the probe was calibrated as outlined in section 3.3.1.

5.3 Results and discussion

5.3.1 2D high-field solid-state NMR

Calibration

Prior to conducting the high-field CP-MAS solid-state experiments, key pulse sequence parameters (^{1}H and ^{13}C 90° pulses, and cross-polarisation contact pulse power) were calibrated on reference sample glycine (GLY) - its structure is shown in Figure 5.1 as an inset. The CP pulse power was optimised for a pulse length of 2 μs (Figure 5.1) and it was determined as 80 W.

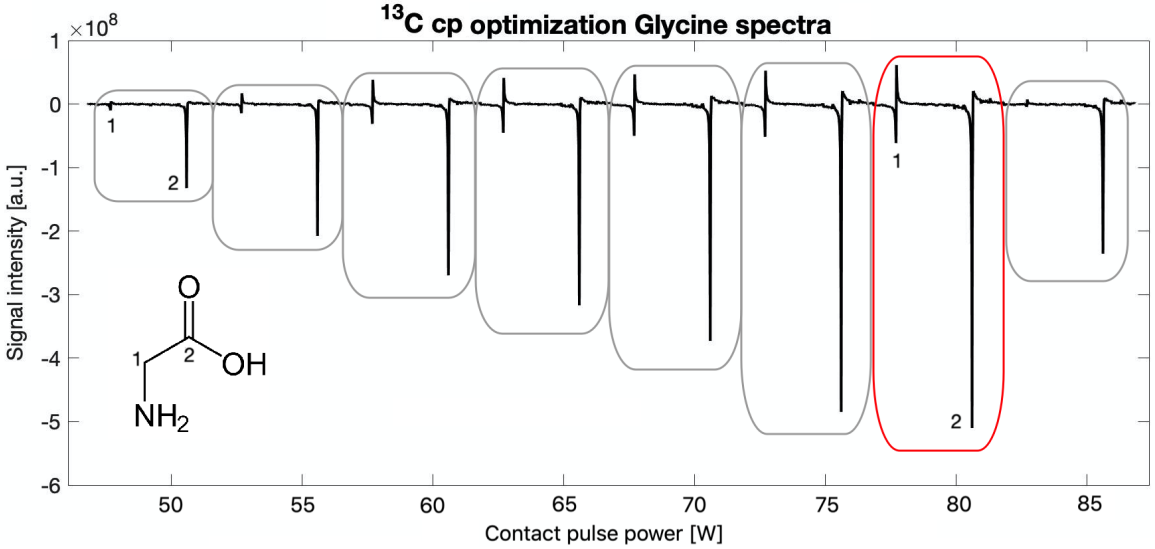

Fig. 5.1 ^{13}C CP optimisation spectra of GLY for different CP pulse power levels. The individual spectra within the optimisation experiment are marked in grey and the optimum spectrum is shown in red. The chemical structure of GLY is shown as an inset with carbon atoms labelled.

Alanine (ALA) is a simple amino acid very similar to GLY, but with a methyl group attached to the central carbon atom. The ionised form of ALA (chemical structure in Figure 5.2c) was used to select an appropriate HETCOR pulse sequence variant. As outlined in the methods sections, the sample was spun in a 4 mm rotor at 15 kHz and the contact time was 2 ms. Figure 5.2a shows the 2D HETCOR spectrum of ALA, with the ^{13}C projection along the top and the ^{1}H projection at the right of the plot. Carbons are labelled *1-3* and protons *a-c* with respect to the chemical structure in Figure 5.2c. The coloured horizontal lines in Figure 5.2a show the position of the individual rows plotted in Figure 5.2b. These correspond to the three peaks in the proton projection spectrum.

The 2D plot in Figure 5.2d was obtained from an identical HETCOR experiment to Figure 5.2a, but a FSLG pulse sequence was added for ^{1}H-^{1}H decoupling (d-HETCOR). This resulted in an improvement in proton linewidth resolution and for this reason the d-HETCOR

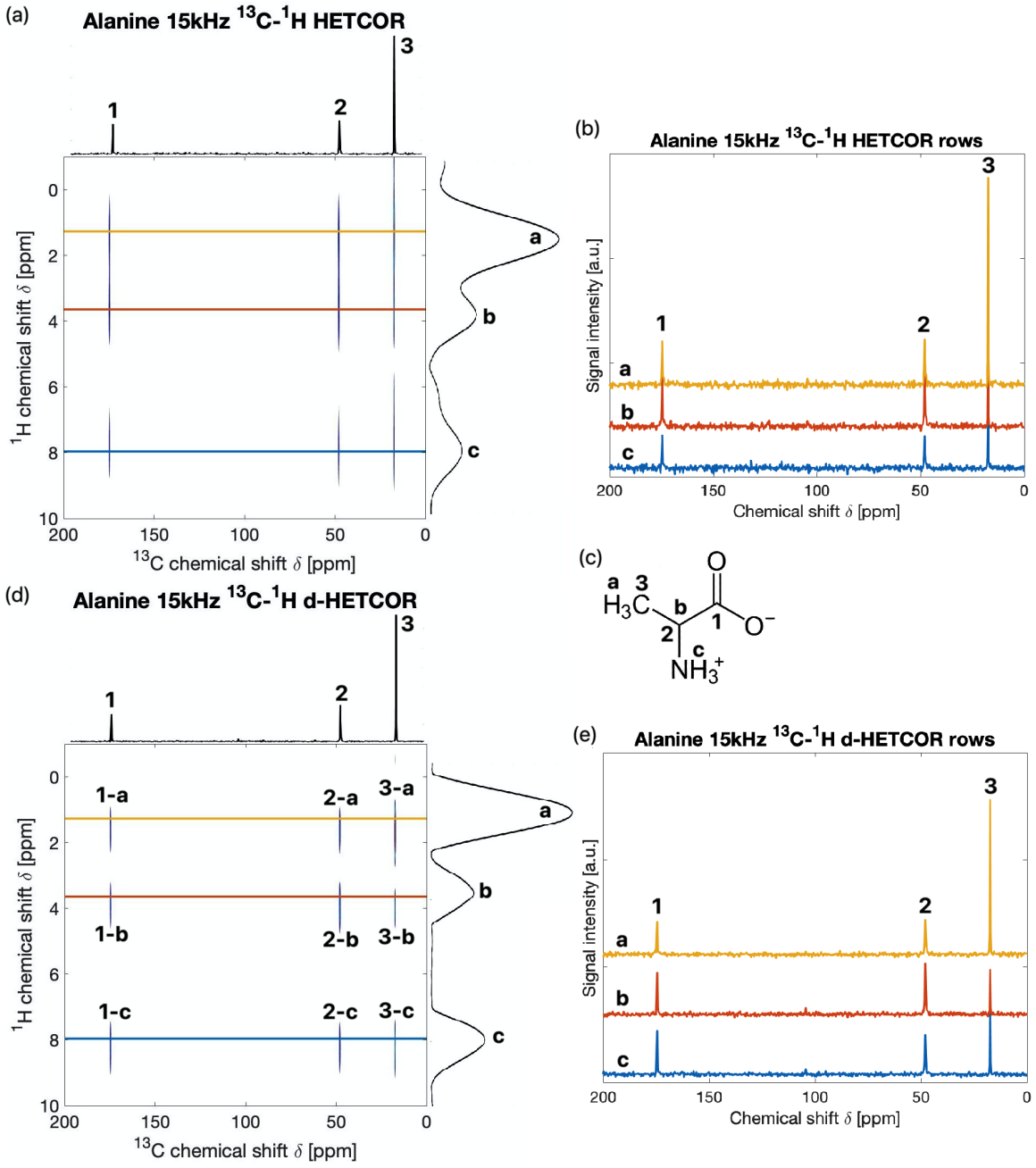

Fig. 5.2 ^{13}C-^{1}H CP-MAS (15 kHz) spectra of (a) HETCOR, (d) HETCOR with homonuclear FSLG decoupling (d-HETCOR) of calibration sample alanine with the carbon and proton spectra projections along the top and right axes, respectively. Carbon spectra extracted from proton rows in (b) HETCOR and (d) d-HETCOR experiments (resonance assignments refer to molecular structure (c)). (c) Chemical structure of alanine with protons (*a-c*) and carbons (*1-3*) labelled. Number-letter pairs in (d) refer to the carbon-proton interactions identified.

pulse program was employed with the paracetamol and copovidone samples. Figure 5.2e shows the ^{13}C spectra of three rows, each corresponding to one of the protons in ALA: the yellow for proton *a*, the red for *b* and the blue spectrum for proton *c*. These spectra indicate that the three protons are coupled with the three carbons, which is to be expected for a small molecule such as ALA at 2 ms contact time. Carbon-proton coupling is also indicated in the number-letter pairs in Figure 5.2d, next to each of the cross peaks. The way 2D NMR experiment results are presented in Figure 5.2 will be used throughout this chapter.

^{13}C-^{1}H HETCOR

The ^{13}C-^{1}H CP-MAS d-HETCOR of pure copovidone and crystalline paracetamol were acquired at 2 ms contact time and the results are shown in Figure 5.3. Assignment of paracetamol and copovidone ^{13}C and ^{1}H resonances (with reference to the labelling in Figures 5.3d and e) have been made by comparison with the literature [195, 157, 162, 164, 165, 163]. Note that carbon atoms are labeled with numbers and proton atoms with letters. The colour-bar in Figure 5.3b indicates the cross-peak signal intensity in 2D NMR plots, where higher intensity (red) is associated with a stronger coupling. This color-bar applies to all of the 2D plots presented in this chapter.

Figure 5.3a shows that every carbon in copovidone is coupled with both resolved proton environments. This is not surprising as, even though there are at least six proton environments discernible when dissolved in acetone (refer to chapter 3, Figure 3.3d), only two (and with a high degree of overlap) are observable in this solid-state experiment (as is observed in the proton spectrum projection), despite using the sequence with homonuclear decoupling. Cross-peaks involving *a* protons appear stronger than those involving *b* protons, but this is likely to be an effect from the stronger signal from the *a* protons rather than an indication of stronger coupling.

In Figure 5.3f there are three resolved paracetamol proton resonances: *c* corresponds to the methyl protons, *d* to the aromatic protons, and *e* to the OH– and NH– ones (the corresponding rows are shown in yellow, orange and blue, respectively, in Figure 5.3g). In this case, not all proton and carbon environments display cross-peaks. The signal arising at the chemical shift coordinates of peaks *16-c* reveal close interaction between the methyl carbon and methyl protons; and that at *11-c* is between the methyl protons and their neighbouring carbonyl carbon. Aromatic protons (orange trace in Figure 5.3g), as they are located in the middle of the molecule, display interactions with all carbons: methyl (*16-d*), carbonyl (*11-d*) and aromatic (*12,13,14,15-d*). Finally, a faint cross-peak is observable between the carbonyl carbon and, either the amine or hydroxyl protons (*11-e*), or even with both as will be described later in this chapter. These results agree with the observations by Zhou *et al.* [202].

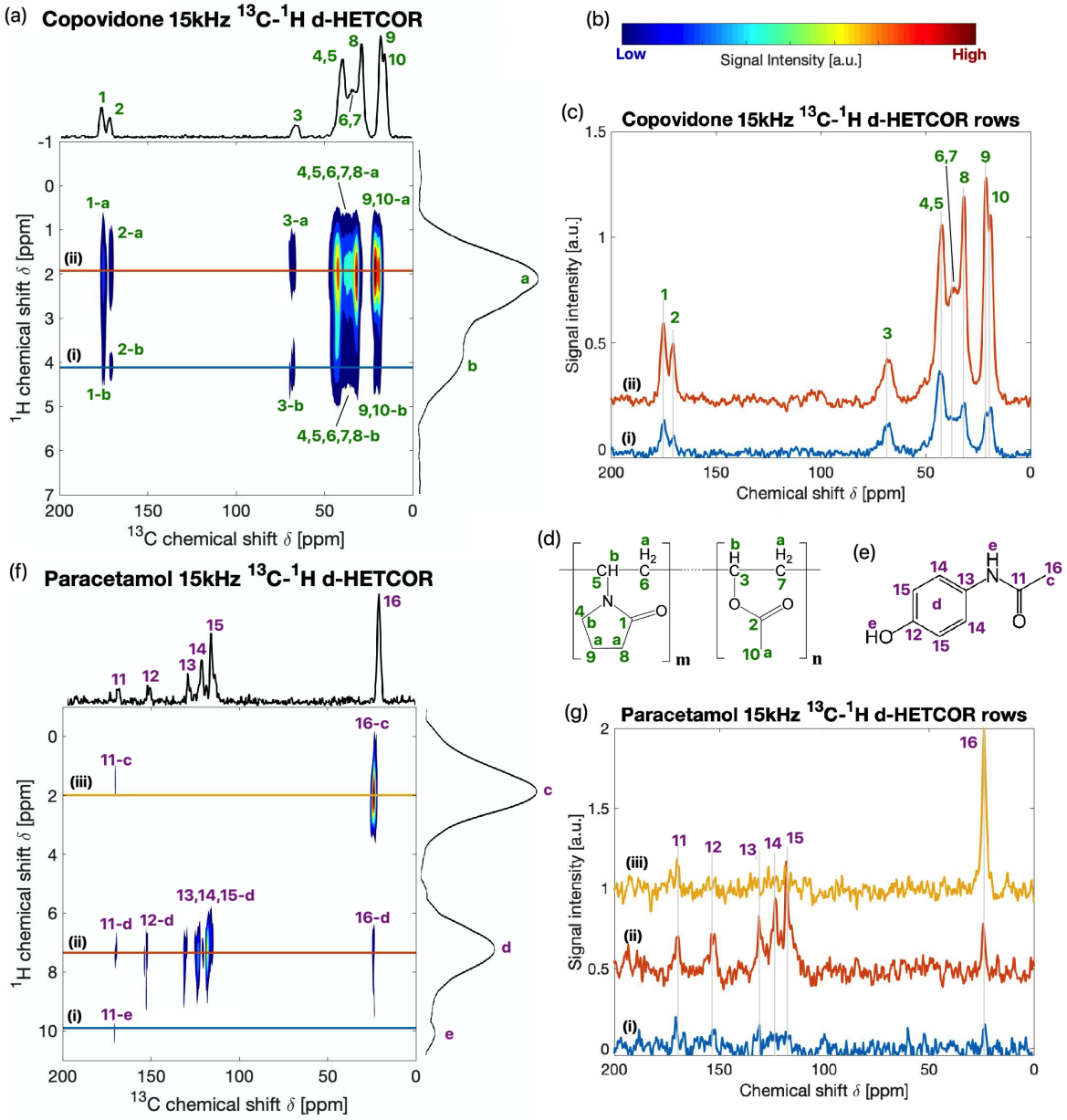

Fig. 5.3 ^{13}C-^{1}H CP-MAS (15 kHz) d-HETCOR of (a) copovidone and (f) paracetamol with the carbon and proton spectra projections along the top and right axes. Carbon spectra extracted from the proton rows of (c) copovidone and (g) paracetamol d-HETCOR (resonance assignments refer to molecular structures (d) and (e)). Chemical structure of (d) copovidone with protons (*a, b*) and carbons (*1-10*) labelled; and (e) paracetamol with protons (*c-e*) and carbons (*11-16*) labelled. (b) Colour bar used to plot all the 2D NMR spectra presented in this chapter. Number-letter pairs in (a) and (f) refer to the carbon-proton interactions identified.

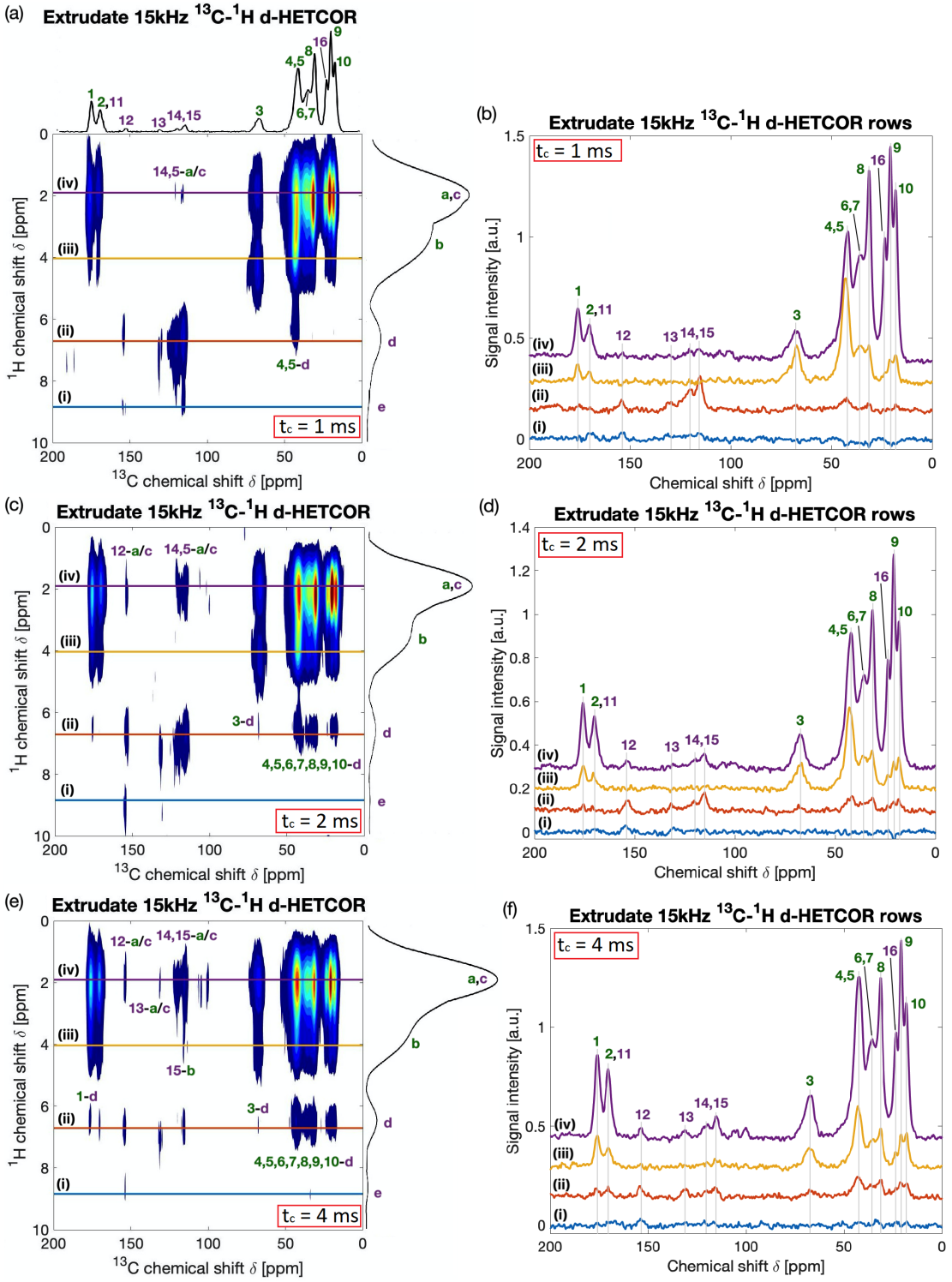

Fig. 5.4 ^{13}C-^{1}H CP-MAS (15 kHz) d-HETCOR of a 30 wt% paracetamol/copovidone extrudate for a contact time of (a) 1 ms, (c) 2 ms, and (e) 4 ms. The carbon and proton spectra projections are shown along the top and right axes. ^{13}C spectra extracted from the ^{1}H rows of the (b) 1 ms, (d) 2 ms, and (f) 4 ms contact time d-HETCOR experiments (resonance assignments refer to molecular structures shown in Figure 5.3d and e). Number-letter pairs in (a), (c) and (e) refer to the carbon-proton interactions identified in the extrudate sample that were not observed in the paracetamol or copovidone d-HETCOR experiments from Figure 5.3a and f (where green characters correspond to copovidone and the purple to paracetamol).

Figure 5.4 shows the ^{13}C-^{1}H HETCOR spectra of an amorphous dispersion prepared by HME with 30 wt% paracetamol and 70 wt% copovidone acquired at different cross-polarisation contact times (t_c): 1 ms, 2 ms and 4 ms. A number of cross-peaks are observable, but only those that were not detected for individual samples of paracetamol's and copovidone's HETCOR spectra (Figure 5.3) have been labelled.

At t_c=1 ms (Figure 5.4a and b), although faint, two sets of cross-peaks are highlighted. One of these corresponds to paracetamol's aromatic carbons with the 2 ppm ^{1}H resonance that pertains to both the methyl protons in paracetamol and copovidone (*14,15-a/c*). Although this signal was not observed in pure paracetamol (Figure 5.3f), it is not possible to assign it unequivocally to a drug-polymer interaction. The SNR of paracetamol's HETCOR spectrum was low and it could be that this cross-peak was hidden in the noise. The first unequivocal paracetamol/copovidone coupling detected was between part of copovidone's VP monomer carbons and paracetamol's aromatic protons (*4,5-d*). This agrees with the observations by Wen *et al.* that paracetamol's phenolic resonances formed Van der Waals coupling with PVP aliphatic groups [203].

At t_c=2 ms and 4 ms (Figure 5.4c, d, e and f), several additional cross-peaks are detected. Those that correspond to unambiguous paracetamol/copovidone correlations include *15-b*, paracetamol's aromatic carbons with copovidone's aliphatic protons. Additionally, copovidone's carbons *3, 4, 5, 6, 7, 8, 9* and *10* display cross-peaks with paracetamol's aromatic protons, which most likely arise from Van der Waals forces (copovidone's aliphatic with paracetamol's aromatic group) as well as H-bonding interactions (copovidone's PVP carbonyl with paracetamol's hydroxyl). Although, as previously mentioned, cross-peaks *12,13,14,15-a/c* cannot be unequivocally determined to be paracetamol-copovidone interactions, it would make sense if they were, as they correspond to paracetamol's aromatic carbons and copovidone's aliphatic protons and there has been other evidence of this interaction.

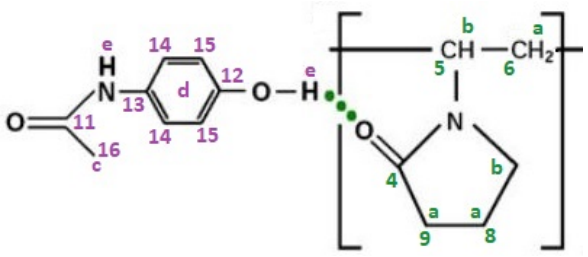

Fig. 5.5 Schematic of hydrogen bonding between paracetamol and the PVP monomer of copovidone (modified from [204]).

The number of cross-peaks detected as well as their intensity in Figures 5.4a, b and c increase at longer t_c. This occurs because CP is based on heteronuclear dipolar interactions and is sensitive to nuclear distances and mobility of the molecule or functional group to which the interacting nuclei belong [130]. As a consequence, longer contact times result in more cross-polarisation being transferred (from ^{1}H to ^{13}C) *via* dipolar couplings, as it is supplemented by spin diffusion effects [205]. However, the spin diffusion effect is limited to $0.3 - 0.5$ nm, which means that a large proportion of paracetamol molecules have to be in close contact with copovidone chains in order to produce the signals observed in Figure 5.4.

These conclusions were also drawn by Pham *et al.* for a 30 wt% paracetamol/PVP ASD system [111].

A summary of the results from the ^{13}C-^{1}H HETCOR experiments is found in Figure 5.6, where the circles denote the correlations identified between paracetamol and copovidone. Some of the cross-peaks in the red circle (*12,13,14,15-a/c*) cannot be unambiguously assigned to paracetamol-copovidone interactions because of the spectral overlap of methyl peaks from both species. The remaining highlighted signals provide evidence of drug-polymer molecular-level interactions in the paracetamol/copovidone HME ASD formulation, most likely through a mixture of Van der Waals and H-bond couplings [111, 106].

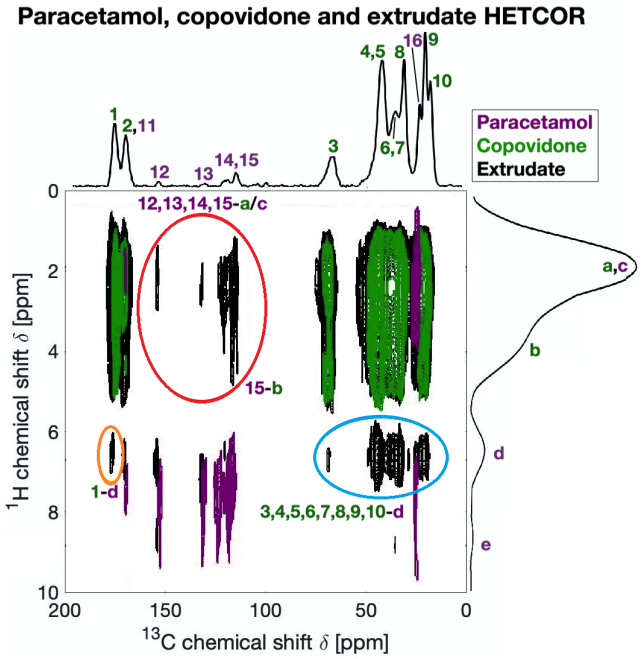

Fig. 5.6 Overlapped ^{13}C-^{1}H CP-MAS d-HETCOR of paracetamol (purple), copovidone (green) and a 30% extrudate (black) (the carbon and proton spectra projections of the extrudate are shown along the top and right axes, respectively). Number-letter pairs refer to the carbon-proton interactions identified in the extrudate sample that were not observed in the paracetamol or copovidone HETCOR spectra (resonance assignments refer to molecular structures shown in Figure 5.3d and e).

^{1}H-^{1}H NOESY

The 2D ssNMR ^{1}H-^{1}H experiments presented in this and the following sections were conducted at 60 kHz MAS. This resulted in improved proton spectral resolution, as can be observed by comparing the ^{1}H spectra at 60 kHz MAS of paracetamol, copovidone and a 30 wt% extrudate in Figure 5.7a with the 15 kHz MAS ^{1}H projections of the HETCOR experiments in Figures 5.3 and 5.4.

Figure 5.7 shows a comparison between the ^{1}H spectra of paracetamol (purple), copovidone (green) and a 30 wt% paracetamol/copovidone extrudate (black) obtained from solid-state samples at high-field 60 kHz MAS (Figure 5.7a) and from liquid-state samples (molten for paracetamol and extrudate and dissolved in deuterated acetone for copovidone, Figure 5.7b). As expected, the resolution is much higher for the liquid samples, as molecular tumbling averages out chemical shift anisotropy contributions. Other than that, the signals observed in both sets of spectra are very similar, with a few exceptions. Firstly, the methyl peak of crystalline (solid) paracetamol is centred around 1 ppm, while it appears at 2 ppm in the solid and molten extrudate formulation, as well as in the molten paracetamol. This suggests that the chemical shift of the methyl ^{1}H resonance for crystalline paracetamol is 1 ppm, whereas for amorphous paracetamol it is 2 ppm. Secondly, water peaks are visible in the extrudate and copovidone samples in the solid state in the $3.5 - 4$ ppm region because of copovidone's hygroscopicity. None is observed in the molten extrudate because it was at a temperature above water's boiling point. Finally, copovidone peaks between $3 - 5$ ppm, which are resolved in the extrudate and copovidone spectra in the liquid-state experiments, appear as a broad shoulder to the left of the methyl peak in the solid-state acquisitions due to the lower resolution.

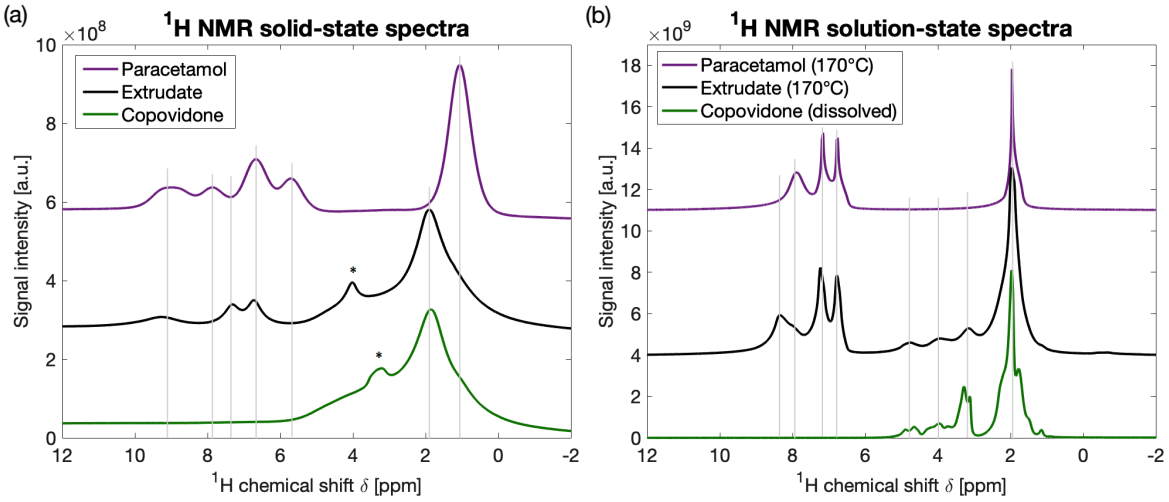

Fig. 5.7 Stacked (a) solid-state (MAS 60 kHz) and (b) liquid-state ^{1}H spectra of paracetamol, copovidone and a 30 wt% extrudate. The * indicates the presence of water

The ^{1}H-^{1}H NOESY spectra of copovidone and paracetamol were acquired with a mixing time (t_m) of 20 ms and the results are shown in Figure 5.8. Assignment of proton resonances was made with reference to the chemical structure labelling in Figure 5.8b and c. Figure 5.8a shows that due to the lack of resolution for copovidone, no meaningful information can be extracted from its ^{1}H-^{1}H NOESY spectrum other than that there is evidence of coupling between the a and b protons. However, a positive observation is that the water peak present in its ^{1}H spectrum (Figure 5.7a) does not appear in the NOESY plot.

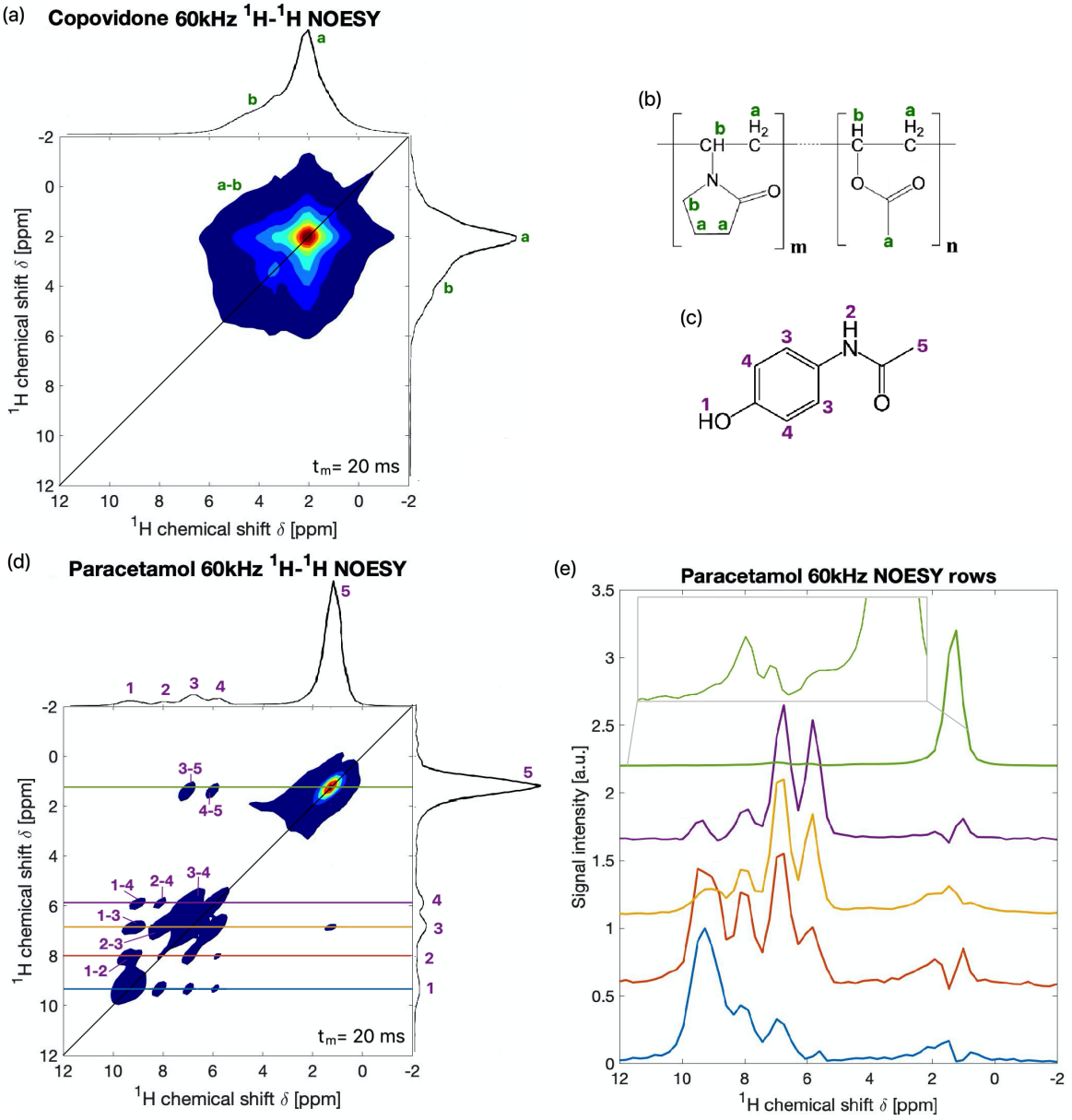

Fig. 5.8 ^{1}H-^{1}H MAS (60 kHz) NOESY of (a) copovidone and (d) paracetamol with the proton spectrum projection along the top and right axes. Chemical structure of (b) copovidone and (c) paracetamol with protons labelled (*a*, *b* for copovidone and *1-5* for paracetamol). (e) ^{1}H spectra rows extracted from the paracetamol 2D NOESY experiment. Letter-letter pairs in (a) and number-number pairs in (d) refer to the proton-proton interactions identified.

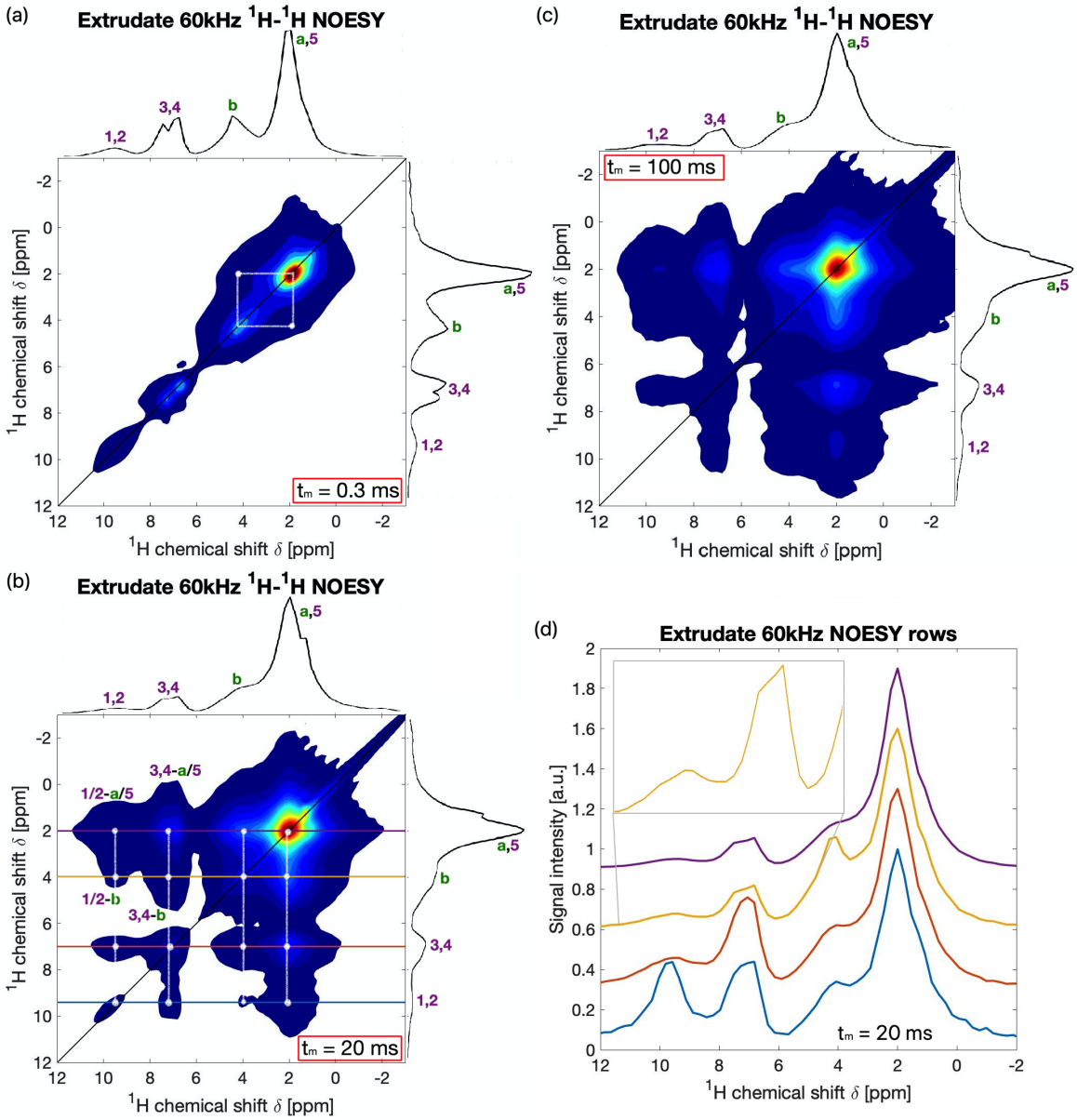

Fig. 5.9 ^{1}H-^{1}H MAS (60 kHz) NOESY of a 30 wt% paracetamol/copovidone extrudate for mixing times of (a) 0.3 ms, (b) 20 ms, and (c) 100 ms (resonance assignments refer to the molecular structures shown in Figure 5.8b and c). The proton spectrum projection for each experiment is shown along the top and right axes. (d) ^{1}H spectra rows extracted from the extrudate NOESY 2D spectra at 20 ms mixing time (b). Number-letter pairs in (b) and (d) refer to the proton-proton interactions identified in the extrudate sample that were not observed in the paracetamol and copovidone NOESY experiments from Figure 5.8a and d.

In Figure 5.8d there are five resolved paracetamol proton resonances: *1* corresponds to the hydroxyl protons, *2* to the amine, *3* and *4* to the aromatic protons and *5* to the methyl protons (the corresponding rows are shown in blue, orange, yellow, purple and green in Figure 5.8e) [202, 112]. Distinct cross-peaks are observed between most of the resolvable proton environments. This is not surprising, as paracetamol crystal structures are tightly packed, enabling through-space couplings, particularly at long mixing times.

Figure 5.9 shows the ^{1}H-^{1}H NOESY spectra of a 30 wt% paracetamol/copovidone ASD prepared by HME acquired at different t_m: 0.3 ms, 20 ms and 100 ms. Similarly as with the t_c in HETCOR, the number of cross-peaks detected and their intensity increase in the NOESY spectra at longer t_m. This happens because during t_m, the NOE effect affects spatially close nuclei, so for longer mixing times, the magnetisation reaches nuclei that are further away [206].

At t_m= 0.3 ms, the diagonal peaks are clearly visible, but the only cross-peaks detected are those between 2 ppm and 4 ppm (likely *a*-*b* proton intramolecular coupling in copovidone) and aromatic-aromatic proton intramolecular interactions in paracetamol (*3*-*4*).

At a mixing time of 20 ms several additional cross-peaks are observable, but only those that were not detected in paracetamol's and copovidone's NOESY spectra (Figure 5.8) have been labelled. Four proton environments were resolved: methyl group in paracetamol and methyl and methylene groups in copovidone (*a, 5*), other aliphatic protons in copovidone (*b*), paracetamol's aromatic protons (*3, 4*) and paracetamol OH– and NH– (*1, 2*). The corresponding rows are shown in blue, orange, yellow and purple in Figure 5.9d.

In the 4 ppm row (yellow), corresponding to copovidone's aliphatic protons, there are clear cross-peaks with the aromatic (*3,4*-*b*) and hydroxyl/amine (*1,2*-*b*) protons in paracetamol. These could result from Van der Waals forces between the aromatic ring in paracetamol molecules and copovidone's aliphatics and/or H-bonding between copovidone's carbonyl and paracetamol's hydroxyl protons. Further cross-peaks are observed along the 2 ppm row (purple), with the OH–/NH– resonances (*1,2*-*a/5*). Although it is not possible to definitively assign those as drug-polymer interactions, it is likely the case as the cross-peak was not observed in the paracetamol NOESY spectrum (Figure 5.8d). This interaction would probably be mediated through an H-bond between paracetamol and copovidone (refer to Figure 5.5 for a schematic). There is another cross-peak involving the aromatic protons (*3,4*-*a/5*), but this cannot be unambiguously assigned to paracetamol-copovidone interactions due to spectral overlap. At 100 ms t_m there was so much signal intensity that cross-peaks overlapped with each other and it was difficult to see fainter signals.

NOESY experiments have been used previously in the literature to explore intermolecular associations in pharmaceutical formulations. Liu *et al.* performed solution-state NOESY of a drug-polymer ASD and confirmed the existence of interaction between the drug (sorafenib) and the polymer (PVP) [106]. Due to the higher resolution achieved in liquid samples, it was possible to determine which specific protons were involved in the coupling and, combined with computational methods, it was determined that drug-polymer interactions occurred through H-bonds with the carbonyl group of PVP. Mann *et al.* conducted MAS ^{1}H-^{1}H NOESY on highly viscous pharmaceutical mixtures [207]. Specifically, intermolecular H-bonding was identified between ibuprofen and lidocaine.

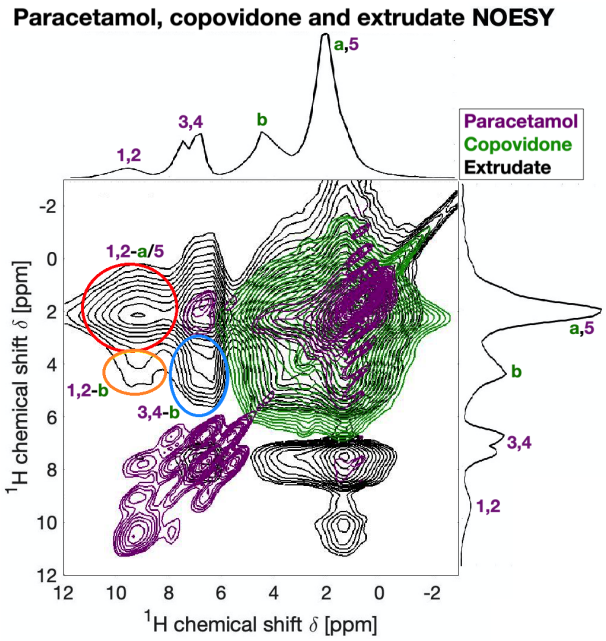

Fig. 5.10 Overlapping ^{1}H-^{1}H MAS NOESY of paracetamol (purple), copovidone (green) and a 30 wt% extrudate (black) (the proton spectrum projection of the extrudate is shown along the top and right axes). Number-letter pairs refer to the proton-proton interactions identified in the extrudate sample that were not observed in the paracetamol and copovidone 2D NOESY spectra (resonance assignments refer to molecular structures shown in Figure 5.8b and c).

A summary of the results from the ^{1}H-^{1}H NOESY experiments presented in this section is found in Figure 5.10, where the coloured circles denote the identified cross-peaks that suggest correlations between paracetamol and copovidone. Although the cross-peaks in the red circle (*1,2-a/5*) cannot be unambiguously assigned to paracetamol-copovidone interactions because of the spectral overlap of methyl peaks from both species at 2 ppm, this signal was not present in either of the pure component's NOESY spectra, suggesting that it could in fact result from drug-polymer interactions. The remaining highlighted signals (1,2,3,4-b) provide evidence of drug-polymer molecular-level interactions in the paracetamol/copovidone HME ASD formulation, most likely through a mixture of Van der Waals and H-bond couplings.

^{1}H-^{1}H MQC SQ/DQ BABA

In order to facilitate the interpretation of results from ^{1}H-^{1}H MQC experiments, it is useful to refer to the H-bonding pattern of paracetamol in its polymorph I crystal lattice structure shown in Figure 5.11.

The ^{1}H-^{1}H MQC BABA experiment, although similarly to NOESY in that it detects proton-proton through-space couplings, provides clearer observations as there is no interference from high-intensity diagonal components to conceal weak cross-peaks within the noise level. The MQC BABA spectra of copovidone and paracetamol are shown in Figure 5.12, where assignment of proton resonances is made with reference to the chemical structures labelled in Figure 5.12b and c. As for the NOESY experiment, due to the lack of proton spectral resolution for copovidone, no meaningful information can be extracted from its ^{1}H-^{1}H MQC BABA spectrum. There is some evidence suggesting coupling between the *a* and *b* protons in copovidone: at 6 ppm in the DQ dimension (blue line in Figure 5.12a) there is signal both at 2 ppm and 4 ppm in the SQ axis, but this could also be due to line broadening.

In Figure 5.12d the same five paracetamol resonances resolvable in the NOESY experiment are present in the MQC BABA spectrum. There are six cross-correlations (the corresponding row of each one of them is shown in Figure 5.12e) and one self-correlation present. The self-correlation corresponds to the only group in paracetamol that has several protons - the methyl (*5-5*), therefore this signal is positioned at the intersection of 1 ppm (SQ) and 2 ppm (DQ). The cross-correlations identified involved the following atom numbers:

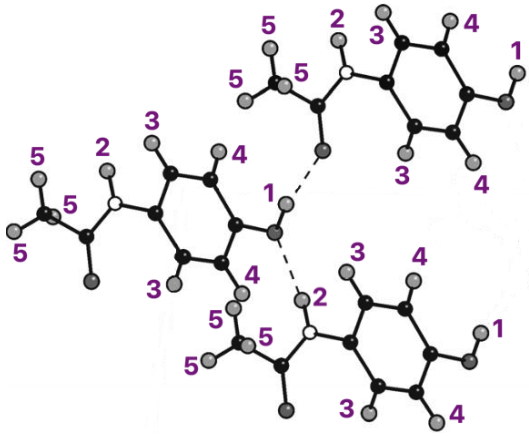

Fig. 5.11 Paracetamol polymorph I crystal lattice structure (modified from [208]).

5-4: corresponds to methyl and aromatic proton coupling at 1 and 6 ppm respectively. These are far apart in the paracetamol molecule, but when the molecules are assembled through H-bonds in the crystal lattice of polymorph I (refer to Figure 5.11), the protons in these groups are in close proximity, resulting in through-space intermolecular coupling being exhibited in the MQC BABA spectrum at 7 ppm in the DQ axis.

5-3: similar to the above, this corresponds to methyl protons with aromatic protons (the ones closer to the amine). As for *5-4*, this corresponds to intermolecular coupling because the H-bonds in the crystal lattice brings the protons involved in this interaction into close proximity.

5-1: this coupling involves the protons that are furthest apart in the paracetamol molecule - the methyl and the hydroxyl protons, at 1 and 9 ppm respectively. Again, looking at the arrangement of neighbouring molecules in the crystal structure (Figure 5.11), the methyl and hydroxyl protons become close in space (intermolecular coupling), giving rise to a cross-correlation at 10 ppm in the DQ dimension.

3-4: aromatic-aromatic coupling, likely arising from intramolecular interactions.

3-2: this corresponds to the intramolecular coupling between the aromatic protons closer to the amine and the amine protons themselves.

4-1: in an analogous way as the previously mentioned correlation, this one corresponds to the other aromatic protons (the ones closer to the hydroxyl group) and the hydroxyl resonances (intramolecular coupling).

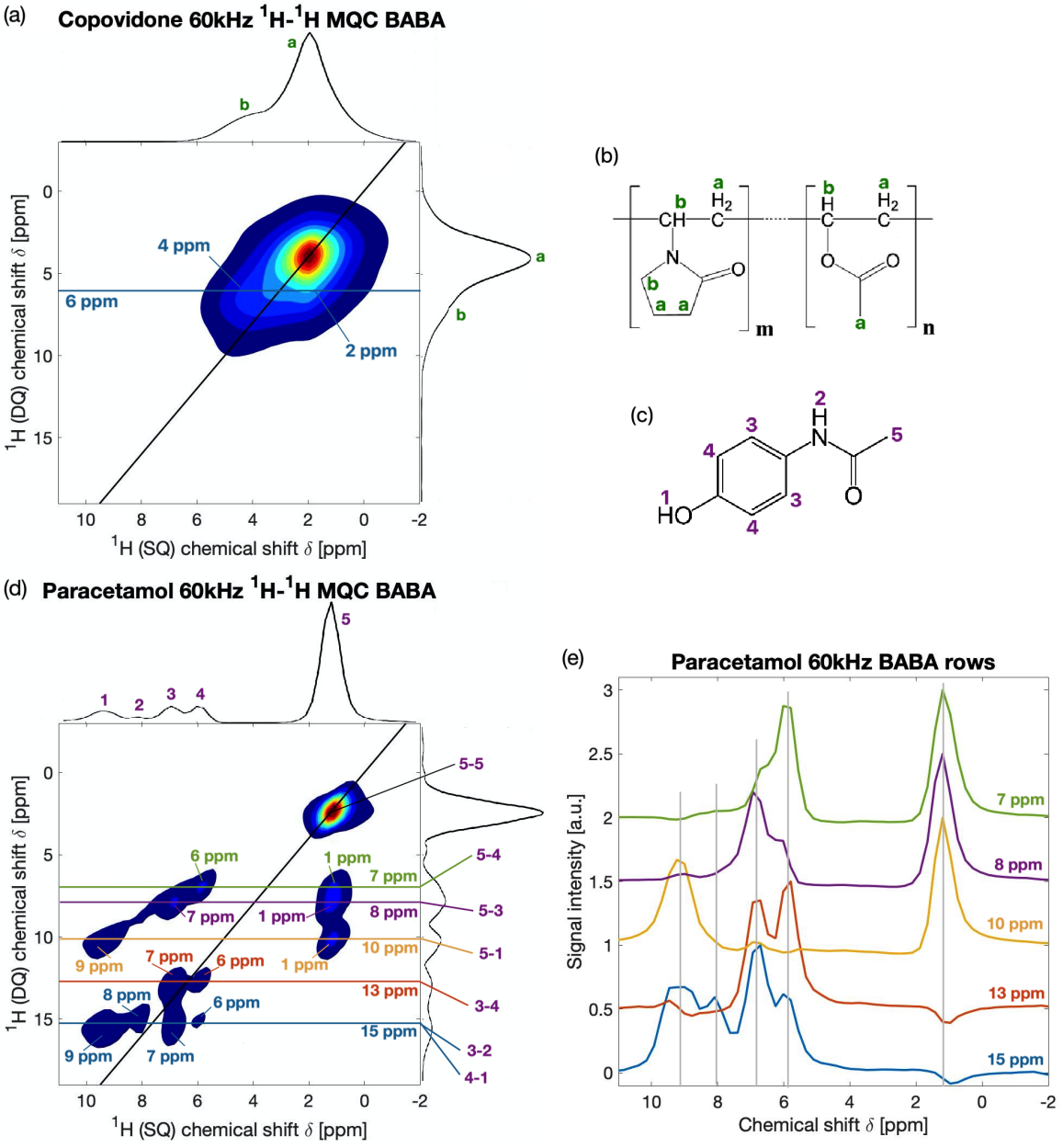

Fig. 5.12 ^{1}H-^{1}H MAS (60 kHz) MQC SQ/DQ BABA of (a) copovidone and (d) paracetamol, with the proton spectrum projection along the top and right axes. Chemical structure of (b) copovidone and (c) paracetamol with protons labelled (*a, b* for copovidone and *1-5* for paracetamol). (e) ^{1}H SQ spectra rows extracted from the paracetamol 2D BABA experiment. Number-number pairs in (d) refer to the proton-proton interactions identified.

Figure 5.13a shows the ^{1}H-^{1}H MQC BABA spectrum of a 30 wt% paracetamol/copovidone extrudate. Several rows of interest showing cross-peaks that were not observed in paracetamol's or copovidone's MQC BABA spectra (Figure 5.12) have been extracted for more detailed examination in Figure 5.13b, and the chemical shift position in the DQ axis they correspond to has been noted next to them.

Several correlations have been identified that could suggest drug-polymer interactions. In the green row at 9 ppm in the DQ axis, there is evidence of two correlations. One of them is a copovidone self-correlation between the *b* protons (*b*-*b*), located around 4.5 ppm in the SQ dimension. The other one is between paracetamol's aromatic protons (7 ppm) and a signal at 2 ppm. This coupling could be either with paracetamol's methyl (*5*) or with copovidone's *a* protons. There is evidence that paracetamol exists in an amorphous state in extrudates, meaning that the crystalline lattice has been disrupted by the polymer chains. Therefore the extent of paracetamol-paracetamol intermolecular interactions is expected to be significantly lower than for Figure 5.12d. The nature of this cross-correlation is intramolecular, but it is uncertain whether it corresponds to drug-polymer or drug-drug [111] .

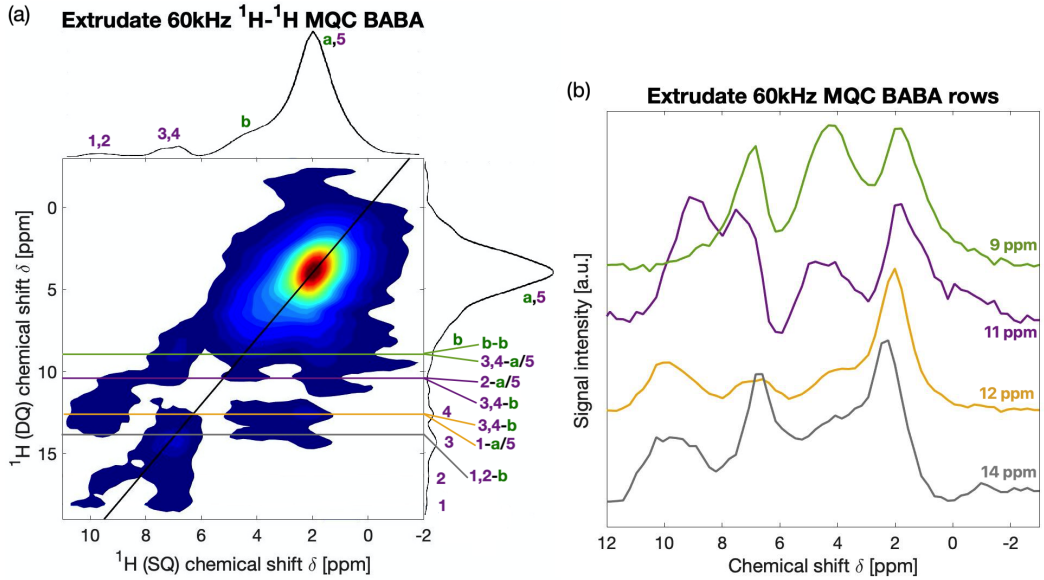

Fig. 5.13 (a) ^{1}H-^{1}H MAS (60 kHz) MQC SQ/DQ BABA of a 30 wt% paracetamol/copovidone extrudate, with the proton spectrum projection along the top and right axes (resonance assignments refer to the molecular structures shown in Figure 5.12b and c). (b) ^{1}H SQ spectra rows extracted from the 2D BABA experiment in (a). Number-letter pairs in (a) refer to the proton-proton interactions identified in the extrudate sample that were not observed in the paracetamol and copovidone BABA experiments from Figure 5.12a and d.

Along the purple row (11 ppm in the DQ axis) there is evidence of another two couplings. The first one (*2-a/5*) is between paracetamol's amine (9 ppm) and a signal at 2 ppm, which, following the same rationale as that in the previous paragraph, could be either from paracetamol or from copovidone's methyl protons and it is no possible to determine which.

The second one (*3,4-b*) involves paracetamol's aromatic protons (7 ppm) and copovidone's *b* resonances (4 ppm). This coupling unambiguously identifies a paracetamol-copovidone interaction, which could be a result from Van der Waals forces as was described in the previous section on the HETCOR experimental results [203].

On the yellow row (12 ppm in the DQ axis) there is evidence of two interactions, very similar to those described in the previous paragraph. One of them (*1-a/5*) involves paracetamol's hydroxyl (10 ppm) and protons at 2 ppm, either from paracetamol or copovidone, engaging in intermolecular couplings. The second one (*3,4-b*) entails paracetamol's aromatic groups (8 ppm) and copovidone's resonances at 4 ppm.

Finally, the grey row (14 ppm in the DQ axis) highlights the position of a cross-correlation (*1,2-b*) between paracetamol's OH– or NH– groups with copovidone's *b* protons. This unambiguous paracetamol-copovione coupling is likely to be the result of hydrogen bonding between paracetamol's hydroxyl and copovidone's carbonyl groups (although H-bonding is expected to occur at a greater extent with VP's carbonyl than VA's). H-bonding between paracetamol and PVP ASDs has already been reported by Tatton *et al.* (through ssNMR ^{14}N-^{1}H heteronuclear MQC) [112] and Liu *et al.* published evidence of H-bonding between other APIs with both PVP and copovidone (observed *via* solution-state ^{1}H-^{1}H NOESY) [106].

A summary of the results from the ^{1}H-^{1}H MQC BABA experiments presented in this section is found in Figure 5.14, where the coloured lines denote the rows in which the recorded signals suggest correlations between paracetamol and copovidone. As it was discussed, some of the cross-correlations (*1,2,3,4-a/5*) cannot be unambiguously assigned to paracetamol-copovidone interactions because of the spectral overlap of methyl peaks from both species at 2 ppm. The remaining highlighted signals (1,2,3,4-b) provide evidence of drug-polymer molecular-level interactions in the paracetamol/copovidone HME ASD formulation, most likely through a mixture of Van der Waals and H-bond couplings, which coincides with the findings from the HETCOR and NOESY experiments presented previously.

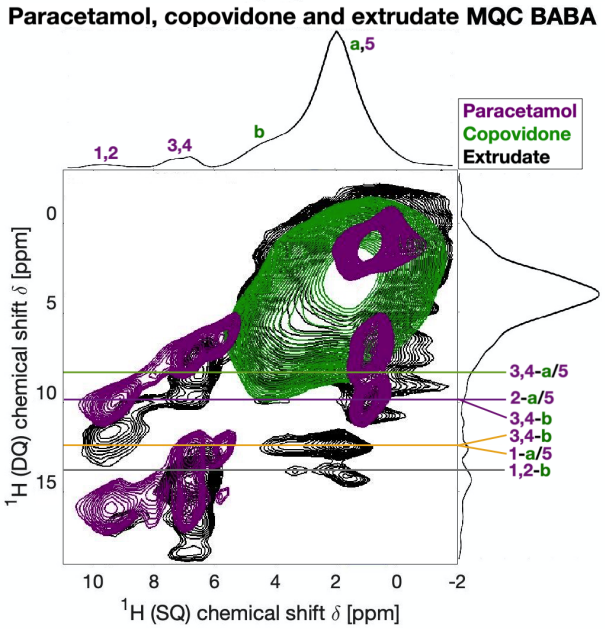

Fig. 5.14 Overlapping ^{1}H-^{1}H MAS MQC SQ/DQ BABA of paracetamol (purple), copovidone (green) and a 30 wt% extrudate (black) (the proton spectrum projection of the extrudate is shown along the top and right axes). Resonance assignments refer to molecular structures shown in Figure 5.12b and c.

5.3.2 2D liquid-state NMR: ^{1}H-^{1}H COSY

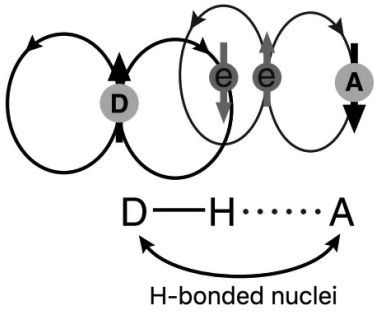

Fig. 5.15 Schematic of scalar coupling in hydrogen bonding (modified from [188]).

Due to the lack of resolution in the proton spectrum on the 2D ssNMR plots shown in the previous section, it is not possible to determine exactly which nuclei in the molecule are involved in the paracetamol-copovidone couplings. Liquid-state spectra display significant resolution improvement (as was shown in Figure 5.7) due to the averaging of chemical shift anisotropy contributions. Therefore this section explores the use of liquid-state (achieved through solubilisation or melting) 2D NMR techniques to gain better understanding on paracetamol/copovidone mixtures at temperatures relevant to HME. The experiment of choice was ^{1}H-^{1}H COSY, which identifies through-bond molecular couplings. COSY detects nuclei that are involved in scalar interactions. This means that the magnetic moment of one nuclei (D) disturbs the electron cloud of the another nuclei (A), which in turn induces a magnetic field that interacts with the magnetic moment of the second nuclei (Figure 5.15). This applies to covalent bonds, but also to H-bonds and Van der Waals forces as they follow the same electron-mediated interaction mechanism (Figure 5.15) [188, 209].

The ^{1}H-^{1}H COSY of copovidone dissolved in deuterated acetone (at room temperature) and molten paracetamol (no solvent, at 170°C) were acquired and the results are shown in Figure 5.16. Assignment of proton resonances was made with reference to the chemical structure labelling in Figure 5.16c and d. Figure 5.16a shows that there are five resolvable proton environments in solution-state copovidone (whereas there were only two in ssNMR, even at high-MAS rates), but there is still an overlap between protons *d, e, f* and *g*. Some rows have been extracted in Figure 5.16b for closer examination of the signals acquired. There are numerous cross-peaks detected, particularly involving those around the 2 ppm region, but it should be noted that all copovidone-copovidone couplings are observed in the chemical shift region from 1 to 5 ppm.

In Figure 5.16e there are four discernible proton environments in molten paracetamol (the corresponding rows are shown in Figure 5.16f) and distinct couplings between several of them have been labelled. One of these corresponds to aromatic-aromatic intramolecular interaction (*3-4*). Another coupling detected is OH– or NH– with methyl protons (*1/2-5*). Due to spectral overlap it is unclear which of the two resonances is displaying an interaction with the methyl group. It could be intramolecular correlation between the NH– and methyl or intermolecular coupling between the OH– and methyl (through the H-bond between neighbouring OH– and C=O groups, as was illustrated in Figure 5.11).

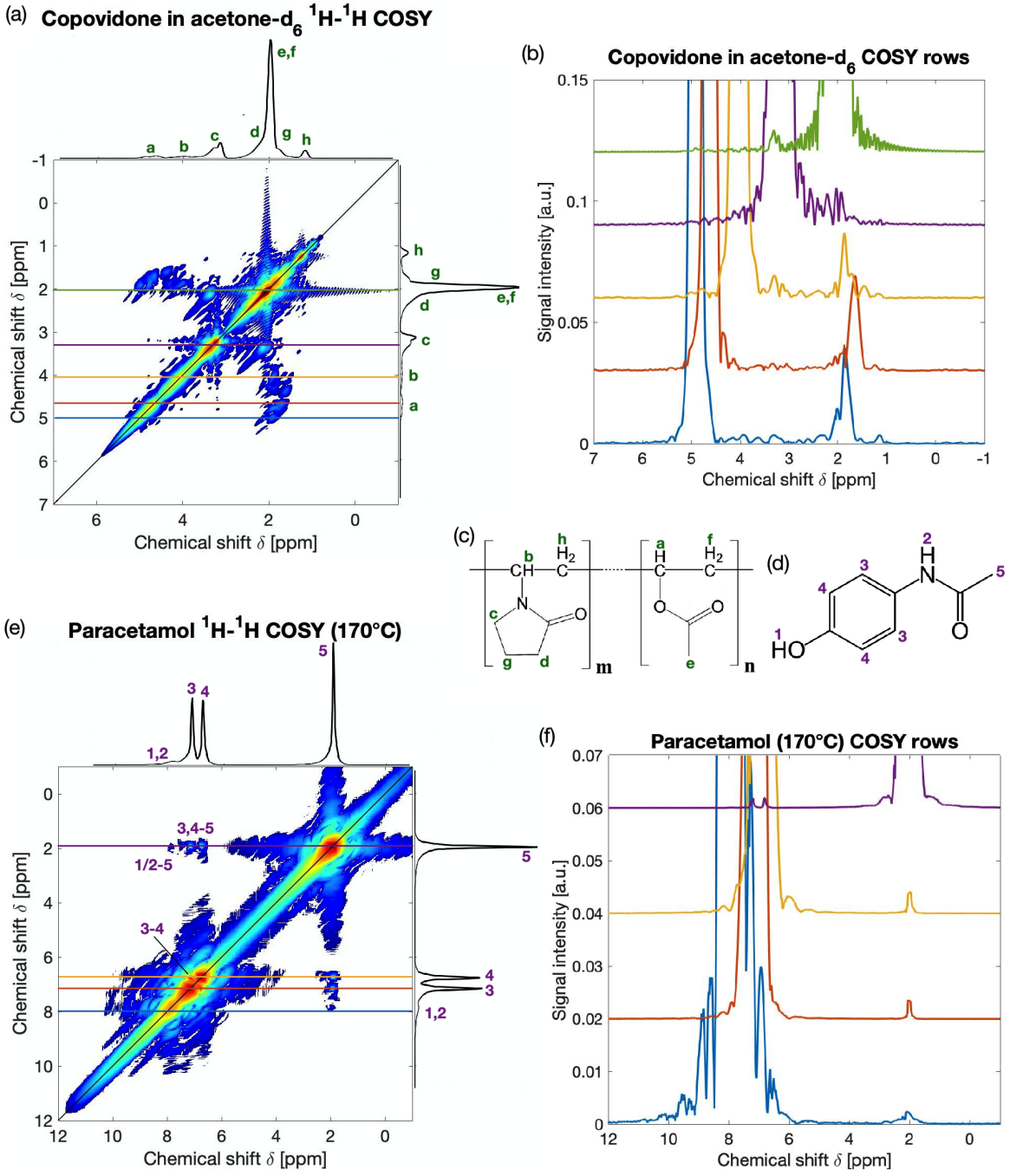

Fig. 5.16 ^{1}H-^{1}H COSY of (a) copovidone dissolved in deuterated acetone and (e) molten paracetamol (170°C), with the proton spectrum projection along the top and right axes. Chemical structure of (c) copovidone and (d) paracetamol with protons labelled (*a-h* for copovidone and *1-5* for paracetamol). ^{1}H spectra rows extracted from (b) copovidone and (f) paracetamol 2D COSY experiments. Number-number pairs in (e) refer to the proton-proton interactions identified.

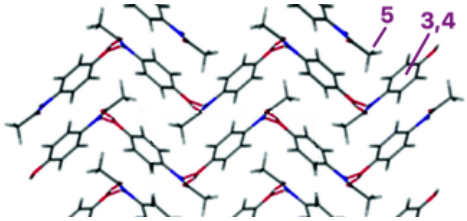

Fig. 5.17 Paracetamol polymorph I crystal lattice structure (modified from [210]).

Lastly, there is a cross-peak between the aromatic and the methyl protons (*3,4-5*). These nuclei are too far in the paracetamol structure to display intramolecular coupling in COSY experiments. However, there is evidence in the literature that the layers of H-bonded paracetamol molecules are secured to each other *via* Van der Waals forces [208]. A schematic of paracetamol's (polymorph I) crystal structure is shown Figure 5.17. Methyl groups are in close proximity to the aromatic rings of neighbouring molecules, so it could be possible that the Van der Waals interactions between paracetamol layers are responsible for the cross-peak observed in the COSY spectrum. As COSY is a through-bond technique, it does not detect the through-space couplings observed in NOESY and MQC BABA plots between neighbouring paracetamol molecules.

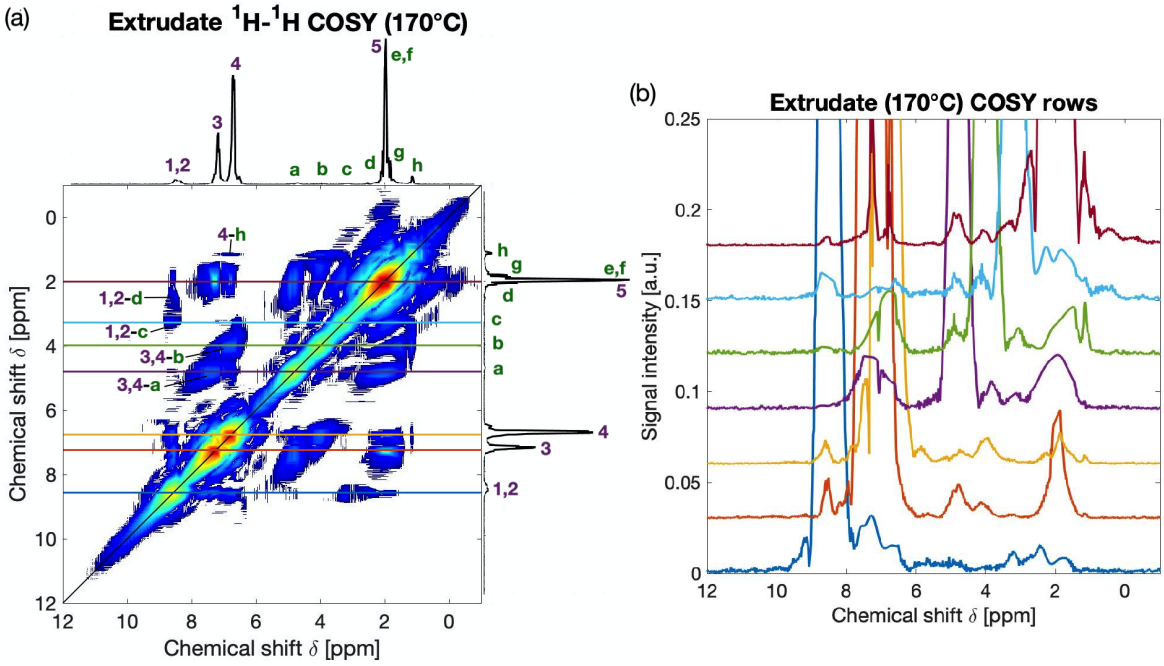

Fig. 5.18 (a) ^{1}H-^{1}H COSY of a molten 30 wt% paracetamol/copovidone extrudate (170°C), with the proton spectrum projection along the top and right axes (resonance assignments refer to the molecular structures shown in Figure 5.16c and d). (b) ^{1}H spectra rows extracted from the 2D COSY experiment in (a). Number-letter pairs in (a) refer to the proton-proton interactions identified in the extrudate sample that were not observed in the paracetamol and copovidone COSY experiments from Figure 5.16a and e.

Figure 5.18a shows the ^{1}H-^{1}H COSY spectrum of a 30 wt% paracetamol/copovidone extrudate. There are eight resolvable resonances: three from paracetamol (*1/2, 3* and *4*), four from copovidone (*a, b, c* and *h*) and one peak at 2 ppm resulting from the overlap of four copovidone (*d, e, f* and *g*) and one paracetamol (*5*) proton environments. Seven rows of

interest have been extracted for closer examination and these are plotted in Figure 5.18b. The six cross-peaks that were not observed in paracetamol's or copovidone's COSY spectra (Figure 5.16) have been labelled. The cross-correlations identified involved the following resonance pairs:

3,4-h: corresponds to copovidone's PVP methylene and paracetamol's aromatic protons coupling. This agrees with the previous ssNMR (HETCOR, NOESY and MQC BABA) observations and with literature sources that report drug-polymer Van der Waals interactions between paracetamol's aromatic ring and PVP aliphatic groups [203, 111].

1,2-c,d: this coupling involves the OH– or NH– protons in paracetamol and the closest protons to copovidone's PVP carbonyl. This corresponds with the evidence presented in the previous section on paracetamol-copovidone H-bonding, which has also been identified in the literature [112, 111], especifically between PVP's carbonyl and paracetamol's OH– group.

3,4-a,b: similarly to *3,4-h*, this correlation corresponds to copovidone's methine groups in the polymer backbone and paracetamol's aromatics. Therefore the same interpretation applies: Van der Waals interactions between the aromatic ring of paracetamol and the aliphatic resonances of copovidone are being detected in the COSY experiment.

A summary of the results from the ^{1}H-^{1}H COSY experiments presented is found in Figure 5.16, where the coloured circles denote the cross-peaks that suggest correlations between paracetamol and copovidone. In accordance with previous interpretation of results, *1,2-c,d* (blue circle) suggest H-bonding between paracetamol's hydroxyl and copovidone's PVP carbonyl. This does not mean that H-bonding is not taking place with copovidone's PVA carbonyl [211]. There is a cross-peak that could correspond to *1,2-e*, but since this overlaps in the 2 ppm region with paracetamol's methyl resonance, the interpretation is ambiguous. The other cross-peaks, *4-h* and *3,4-a,b* (red and orange circles), are consistent with Van der Waals interactions between the paracetamol aromatic ring and copovidone's aliphatic backbone chain.

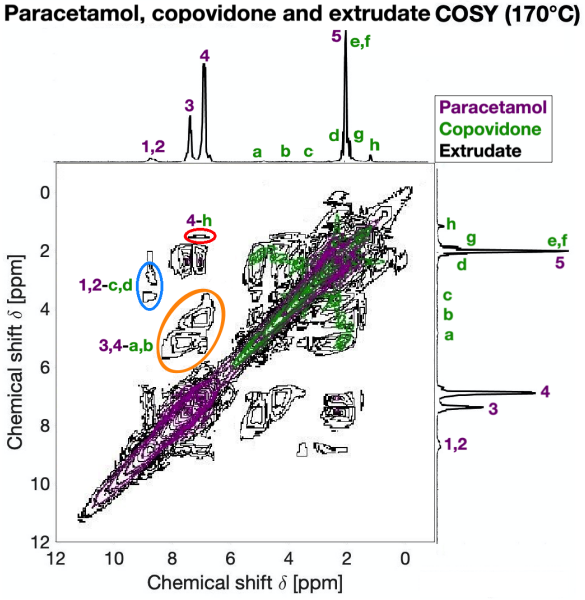

Fig. 5.19 Overlapping ^{1}H-^{1}H COSY of paracetamol (purple), copovidone (green) and a 30 wt% extrudate (black) (the proton spectrum projection of the extrudate is shown along the top and right axes). Number-letter pairs refer to the proton-proton interactions identified in the extrudate sample that were not observed in the paracetamol and copovidone COSY spectra. Resonance assignments refer to Figure 5.16c and d).

To further substantiate the idea that the cross-peaks identified are paracetamol-copovidone interactions were in fact so, spin-echo weighted COSY (SE-COSY) experiments were conducted. The rationale behind this is that, generally, slower molecular motions originating from large molecules, solid lattices or bound species are associated with a shorter T_2 constant (Figure 5.20) [32]. During the spin-echo delay, magnetisation dephases at a rate proportional to the T_2 value. Therefore protons that are bound (through H-bonding or Van der Waals forces) are expected to exhibit shorter T_2 and, at increasing spin-echo delays, these signals would reduce in intensity or vanish altogether.

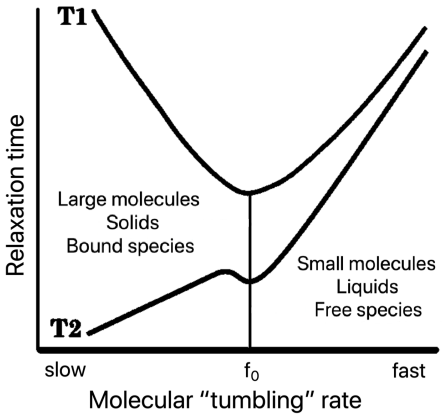

Fig. 5.20 Relationship between T_1 and T_2 values and molecular "tumbling" rate, where f_0 is the Larmor frequency (modified from http://mri-q.com).

Figure 5.21a-c shows the ^{1}H-^{1}H COSY and SE-COSY spectra of a 30 wt% paracetamol/copovidone extrudate at different spin-echo delays: (a) no delay, (b) 1 ms and (c) 10 ms. Figure 5.21a corresponds to Figure 5.18a, and so the same cross peaks are observed. When a 1 ms spin-echo delay is introduced, the COSY spectrum remains the same except for the *3,4-a,b* cross-peak (orange circle), which is not detected any more. This could be because the Van der Waals interactions between aromatic paracetamol protons and copovidone's aliphatic backbone is the most rigid and has the shortest T_2. It should be noted that the T_2 value of the OH/NH resonance in paracetamol is shorter than those of the aromatic protons (data not shown), so the fact that cross-correlations involving protons *3* and *4* were the first to disappear when spin-echo delay was lengthen is indicative that the reason for their decreased T_2 is associated with molecular interactions.

When the spin-echo delay is increased to 10 ms, all cross-peaks that had been associated with paracetamol-copovidone couplings are no longer present (both the ones pertaining to H-bonding, *1,2-c,d* and the one identified as Van der Waals interactions, *4-h*). The resulting spectrum does not display any cross-peaks other than those observed for the pure paracetamol and copovidone components (Figure 5.16), suggesting that all the cross-peaks identified as drug-polymer interactions were probably in fact so. This is clearly depicted in Figure 5.21, where the spectra of the SE-COSY experiments (at 0 ms, 1 ms and 10 ms delay) are overlapped. These results are not in disagreement with the literature, that have consistently shown that copovidone's carbonyl form H-bonds with drugs, strongly favouring the PVP monomer over the PVA one, and that specifically paracetamol engages both in H-bonding and Van der Waals interactions with PVP-based polymers such as copovidone.

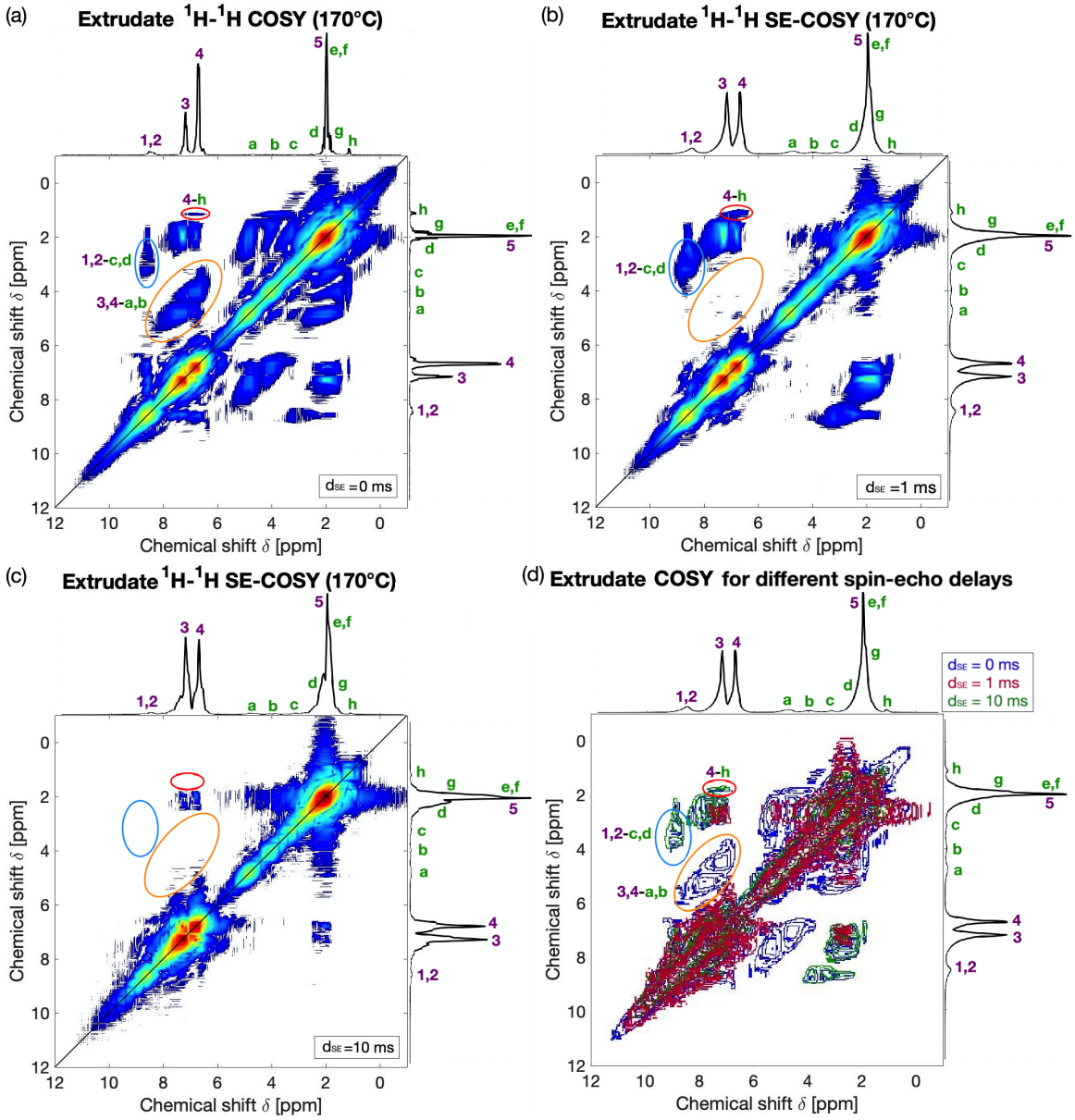

Fig. 5.21 ^{1}H-^{1}H COSY a 30 wt% paracetamol/copovidone extrudate for spin-echo times of (a) 0 ms, (b) 1 ms, and (c) 10 ms (resonance assignments refer to the molecular structures shown in Figure 5.16c and d). The proton spectrum projection for each experiment is shown along the top and right axes. (d) Overlapped ^{1}H-^{1}H COSY of a 30 wt% paracetamol/copovidone extrudate for spin-echo times of 0 ms (blue), 1 ms (red), and 10 ms (green) (the proton spectrum projection of the normal COSY experiment is shown along the top and right axes). Number-letter pairs refer to the proton-proton interactions identified in the extrudate sample that were not observed in the paracetamol and copovidone COSY experiments from Figure 5.16a and e, where green characters correspond to copovidone and the purple to paracetamol.

5.4 Conclusion

A range of solid-state and liquid-state 2D NMR techniques were used in this chapter to explore whether paracetamol-copovidone interactions were established as a result of the HME process, and if so, what the nature of these molecular interactions were. This is relevant because drug-polymer molecular associations are known to increase formulation stability and prevent drug recrystallisation upon storage.

High-field ^{13}C-^{1}H HETCOR spectra were acquired at a range of contact times. The unambiguous correlations observed involved paracetamol's aromatic protons and copovidone's aliphatic carbons. Some of these aliphatic carbons belonged to the backbone of the polymer chain, which, as suggested by the literature, was assigned to Van der Waals interactions, and the rest corresponded to those carbons closest to the carbonyl groups, which could be a result from H-bonding, as other experiments indicated. The increasing signal intensity and number of cross-peaks at longer contact times suggested the presence of intermolecular through-space interactions between a large proportion of paracetamol molecules and copovidone monomers.

^{1}H-^{1}H NOESY, and especially ^{1}H-^{1}H MQC BABA fast-MAS experiments, in agreement with HETCOR results, displayed paracetamol aromatic ring coupling (*via* Van de Waals forces) as well as paracetamol's hydroxyl proton resonances (through H-bonds) with copovidone aliphatic groups. However, all the solid-state experiments suffered from broad proton resonance bandwidths, even at high-field and fast-MAS rates, which prevented assignment of correlations to individual nuclei.

A key advantages of liquid-state spectroscopy is the increased resolution, which allows more precise identification of the nuclei involved in the couplings. Overall, the results from the ^{1}H-^{1}H molten COSY experiments agree with the conclusions drawn from ssNMR data. Cross-peaks between several individual copovidone's backbone protons and paracetamol's aromatic protons were observed. Also, a correlation was identified between paracetamol's hydroxyl and the two proton environments closest to copovidone's PVP monomer carbonyl. The introduction of a spin-echo delay in the COSY experiments resulted in the reduction of the number of cross-peaks detected, which was correlated with the length of the delay, indicating that the signals in question displayed a very short T_2 value. A likely explanation is that this occurred due to the establishment of paracetamol-copovidone interactions (in the form of Van der Waals forces and H-bonds) that reduced the mobility of the groups involved.

Chapter 6

Studies of alternative drug/polymer systems and the effect of processing variables

6.1 Introduction

The previous chapters have focused on paracetamol/copovidone systems to illustrate the use of high-temperature ^{1}H NMR spectroscopy (for material characterisation) and diffusometry (for drug/polymer mass transport analysis) and ^{13}C CP-MAS spectroscopy and relaxometry (as an insight into the microstructure of the formulation and drug-polymer interactions). To demonstrate the versatility of this NMR toolbox, the techniques have been applied to alternative drug/polymer systems. Traditional analytical DSC measurements were also conducted to aid in the characterisation of the compounds and act as a benchmark.

The first systems studied included mixtures of paracetamol with PVA (poly vinyl acetate) and PVP (poly vinyl pyrrolidone) polymers. These polymers are made up of the monomers that comprise copovidone (also known as PVPVA). Despite the similarities between these three polymers, they have contrasting properties with regards to their T_g, T_m and H-bonding abilities. The second system studied involved another API - nifedipine, and copovidone. Nifedipine is a small-molecule drug, but it is considerably larger than paracetamol, which should result in slower self-diffusion coefficient. Additionally, it has no H-bonding hydroxyl group.

Lastly, the experiments were conducted on several samples from a DoE (design of experiments) run, in which extrudates were produced at different drug loadings, temperatures, screw speeds and with two commercially available copovidone brands (Plasdone and Kollidon). The aim was to identify if any of these variables had significant impact on either the mass

transport coefficients of paracetamol in the melts (high-temperature diffusometry) or in the microstructure of the formulations (solid state relaxometry).

6.2 Materials and methods

6.2.1 Materials and sample preparation

The two APIs used in the studies presented in this chapter were paracetamol and nifedipine, provided by AstraZeneca. Paracetamol is a very common analgesic with a small molecular weight of 151.2 g/mol (T_m=170°C); whereas nifedipine is a calcium channel blocker to treat high blood pressure and has a higher molecular weight of 346.3 g/mol (T_m=173°C). Additionally, three polymers have been used. These were PVP, a polymer composed of vinyl pyrrolidone monomers, PVA, made up only of vinyl acetate monomers, and copovidone, a copolymer of VP and VA monomers in 6:4 mass ratio.

The samples from the DoE were paracetamol/copovidone extrudates. They differed in drug loading, processing temperature, screw speed and commercial brand of copovidone used - Plasdone (Ashland) or Kollidon (Basf). The composition and processing details for each sample can be found in Table 6.1.

Table 6.1 Composition and processing details of DoE extruded samples.

Sample	**Polymer**	**Paracetamol [wt%]**	**Temperature [°C]**	**Screw speed [rpm]**
1A	Plasdone	20	140	200
1B	Plasdone	20	140	300
1D	Plasdone	20	180	300
2A	Plasdone	30	140	200
2B	Plasdone	30	140	300
2D	Plasdone	30	180	300
7A	Kollidon	20	140	200
7B	Kollidon	20	140	300
7D	Kollidon	20	180	300
8A	Kollidon	30	140	200

Extrudates and physical mixtures were prepared following the same methods that were outlined in chapter 3 (section 3.2.1).

6.2.2 Solution-state NMR spectroscopy and diffusometry

The solution-state NMR spectroscopy and diffusometry experimental methods followed were identical as those outlined in chapter 3 (section 3.2.2).

6.2.3 Modulated differential scanning calorimetry

The modulated differential scanning calorimetry experimental methods followed were identical as those outlined in chapter 3 (section 3.2.3).

6.2.4 Solid-state NMR spectroscopy and relaxometry

The solid-state NMR spectroscopy and relaxometry experimental methods followed were identical as those outlined in chapter 4 (section 4.2.2).

6.3 Results and discussion

Section 6.3.1 will examine the behaviour of physical mixtures of paracetamol with three different polymers. Section 6.3.2 will consider both nifedipine/copovidone physical mixtures and extrudates and a discussion of the two will follow. Finally, section 6.3.3 will focus solely on paracetamol/copovidone extrudates.

6.3.1 Alternative drug/polymer systems: paracetamol in PVA and PVP physical mixtures

High-temperature characterisation *via* ^{1}H NMR and DSC

The chemical structures of PVA, copovidone and PVP, with protons labelled *a-g* are shown in Figure 6.1a-c. The variable-temperature ^{1}H spectra were acquired for each polymer (Figure 6.1e-g), and these highlight some of the differences between them (note that there was no solvent present in these samples, all polymer mobility was attained through thermal mobility).

Firstly, PVA's spectrum displays two resolved peaks at as low as 130°C, which indicates a lack of rigidity in the polymer chains. For copovidone, the spectra at 100°C and 120°C are likely from residual water tightly attached to the polymer chains *via* H-bonds, which then evaporates. From 140°C on, the single broad resonance increases in signal intensity, but resolution is still low due to lack of mobility. Finally, PVP shows a general lack of resolution and low signal intensity, which is a result of the broad resonance due to restricted mobility and the long T_1 constant (between $4.1 - 6.6$ s for the range of temperatures examined), leading to a certain degree of T_1-weighting, respectively. Interestingly for PVP, the highest signal intensity spectrum (Figure 6.1g, purple plot) is obtained at the lowest temperature (130°C), which suggests that this resonance is comprised of water protons to a large extent. It is not surprising that PVP has a higher adsorbed water concentration, as it has the strongest H-bonding ability [106]. Note that there is no T_2-weighting in these spectra, because they were obtained in pulse-and-acquire experiments. In agreement with the conclusions drawn from the high-temperature NMR spectrosopy and relaxometry, the DSC thermogram (Figure 6.1d) displays the markedly different glass transition temperatures (T_g) of the three polymers: PVA transitions to a rubbery state at 40.2°C, whereas copovidone remains glassy until 109.2°C and PVP has the highest T_g at 156.0°C. There are no other events in the thermograms because these polymers are amorphous in nature.

Figure 6.2a-c, shows the variable-temperature ^{1}H spectra of 30 wt% physical mixtures of paracetamol in PVA, copovidone and PVP. The trends observed are very similar to those

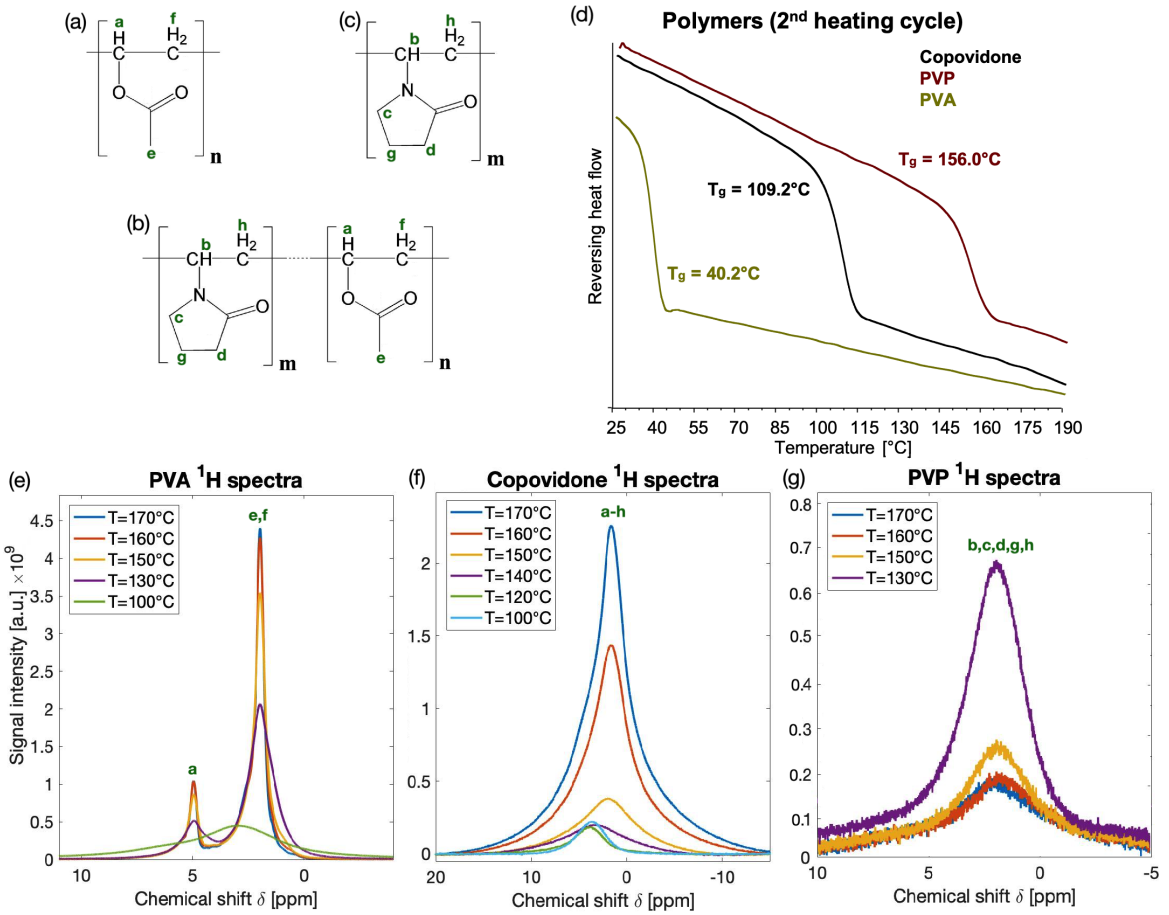

Fig. 6.1 Chemical structures of (a) PVA, (b) copovidone and (c) PVP with protons labelled *a*-*h*; (d) high temperature characterisation of PVA, copovidone and PVP using DSC thermogram - only the second heating ramp of two consecutive heat-cool cycles is shown. ^{1}H NMR spectra, at high temperatures between 100-170°C, of (e) PVA, (f) copovidone and (g) PVP (resonance assignments refer to the molecular structures).

from the polymer-only experiments. In the paracetamol/PVA mixture, even the spectrum at 120°C is clearly resolvable into several resonances: 2 ppm (paracetamol and PVA), 5 ppm (PVA) and 6-9 ppm (paracetamol). This is a combined effect from the low T_g of PVA and the plasticising ability of paracetamol (already pointed out in mixtures with copovidone in chapter 3), which dissolves between the polymer chains creating space that enhances mobility. The same two resonances (at 2 and 5 ppm) that were visible in the polymer-only spectra are identified in Figure 6.2a. In the case of copovidone with paracetamol, line-widths are very broad up to 160°C, when several resonances become evident. Once 170°C is reached, peaks become sharper and several copovidone resonances (at $3-5$ ppm) that had not been visible in the polymer-only spectra, are discernible. At 170°C paracetamol is fully molten, so it would act as a solvent for copovidone, producing a spectrum similar to that obtained in chapter 3 from copovidone in deuterated acetone. Finally, PVP is so stiff, that almost no

signal is recorded at 130°C and 140°C. From 150 – 170°C, paracetamol resonances become recognisable, although the spectral resolution is very poor. This is a result of increased polymer mobility through paracetamol plasticisation, although due to the very high T_g of PVP, spectral line-widths remain broad. An interesting observation from these spectra is that the paracetamol peaks are observed well below its T_m of 170°C, indicating that the presence of PVA, copovidone and PVP has lowered the melting temperature of paracetamol.

Figure 6.2d-f shows the DSC thermograms of the second heating cycle of 20, 30 and 40 wt% paracetamol physical mixtures in the three polymers of interest. Two trends that become apparent are: (i) mixtures of paracetamol in PVP have significantly higher T_g than mixtures in copovidone, which in turn display higher T_g than PVA systems; and (ii) for each polymer, T_g consistently decreases with increasing paracetamol content. The first finding agrees with the results from Figure 6.1d in that $T_{g,PVP} > T_{g,cop} > T_{g,PVA}$. The second observation is consistent with paracetamol acting as a plasticising agent.

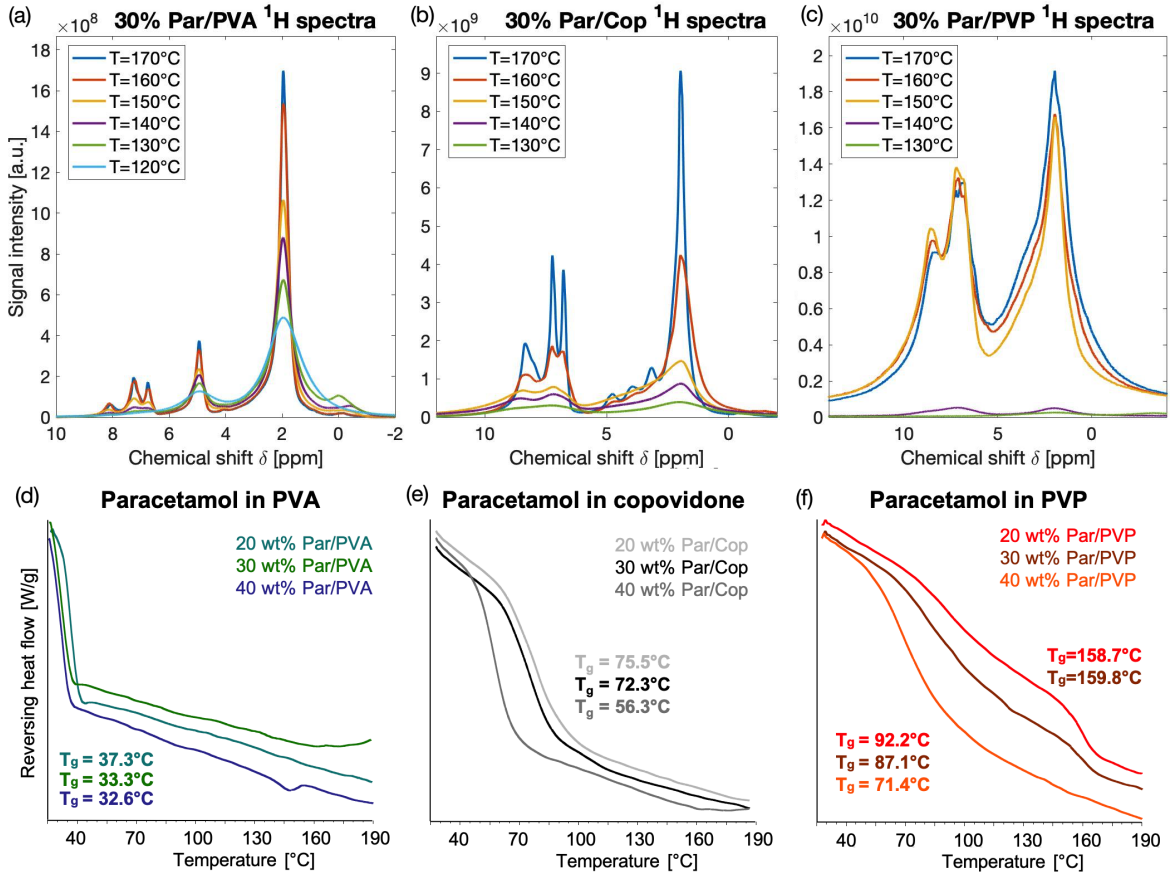

Fig. 6.2 ^{1}H spectra, at high temperatures between 120−170°C, of 30 wt% paracetamol physical mixture in (a) PVA, (b) copovidone and (c) PVP. (d) High temperature characterisation of 20, 30 and 40 wt% paracetamol physical mixtures in (d) PVA, (e) copovidone and (f) PVP using DSC thermograms - only the second heating ramps of two consecutive heat-cool cycles are shown.

Furthermore, there are other interesting observations. Firstly, there are no other thermal events in the thermograms shown, other than glass transitions, with the exception of a small melting endotherm at 148°C in Figure 6.2d, for the 40 wt% paracetamol/PVA system (dark blue). The relevance of this is that, after a heating cycle, paracetamol has become amorphous in the polymer mixtures. However, at the higher drug loading sample, and for the weak H-bonding polymer, PVA has failed to stabilise all of the paracetamol in an amorphous state, so a fraction of the drug recrystallises and melts again during the second heating cycle. This is consistent with the observations of Chan *et al.*: PVA systems resulted in a lower degree of amorphisation compared to PVP or copovidone [212].

Secondly, for the two lower drug loadings in PVP, the thermogram displays two T_g events (red and brown lines). The first one, at 92.2°C and 87.1°C for the 20 wt% and 30 wt% mixtures, respectively, correspond to the glass transition of the paracetamol/PVP mixture. The second one, at 158.8°C and 159.8°C, belongs to pure PVP. This occurs because PVP is so efficient at stabilising paracetamol (likely due to its strong H-bonding ability) that, at low drug loadings, there are PVP domains remaining after dissolution of paracetamol particles.

Thirdly, not all polymers display the same degree of plasticisation when mixed with paracetamol. The relative decrease in the T_g between the pure polymers and, for example, a mixture with 30 wt% paracetamol, is 17% for PVA, 34% for copovidone and 44% for PVP. This implies that paracetamol has a greater degree of dispersion in PVP and copovidone than PVA, creating space between the chains to allow for mobility and disrupting polymer-polymer interactions. The fact that PVP's carbonyl group has high H-bonding capabilities, results in strong drug-polymer interactions, that enhance the dissolution and dispersion of paracetamol.

Determination of the self-diffusion coefficient of paracetamol in polymer physical mixtures

As was explained in chapter 3, due to the spectral overlap of these three polymers with paracetamol in the 2 ppm (methyl) region, diffusion coefficients for paracetamol in polymer mixtures were calculated from the signal of the aromatic and NH–/OH– resonances ($6 - 10$ ppm). Table 6.2 summarises paracetamol's diffusion coefficients in 30 wt% physical mixtures at 150°C, 160°C and 170°C. Paracetamol's self-diffusivity (at 170°C) is included for comparison and the standard deviation errors from three measurements are quoted in parenthesis.

The results from Table 6.2, which are better visualised in Figure 6.3, show that the diffusion coefficient of paracetamol is significantly faster in PVA than in copovidone or PVP physical mixtures. This is likely due to the low viscosity of PVA at this temperature range, which is over 100°C degrees above its T_g, and possibly due to the lesser extent of drug-polymer interactions. Nevertheless, these values are still several-fold lower than in a pure molten state, suggesting that the diffusion of paracetamol is heavily influenced and restricted by PVA (viscosity effects and molecular interactions are likely to play a large role). Paracetamol

in PVP and copovidone exhibits slower diffusion coefficients, in agreement with previous observations on T_g and polymer mobility. All three systems display a small but statistically significant increase in diffusion coefficient over the 20°C range studied.

Table 6.2 Diffusion coefficients of paracetamol in PVA, copovidone and PVP 30 wt% physical mixtures. The self diffusion coefficient of paracetamol measured at 170°C (from chapter 3) is also included for comparison.

	$D \times 10^{-12} m^2/s$		
30 wt% paracetamol in	150 °C	160 °C	170 °C
PVA	28.5 (±0.21)	43.7 (±0.57)	55.7 (±0.64)
Copovidone	3.85 (±0.59)	5.04 (±0.71)	7.40 (±0.73)
PVP	3.05 (±0.25)[a]	3.85 (±0.01)	4.83 (±0.02)
Paracetamol	–	–	190.0 (±20.0)

[a] The numbers in parenthesis indicate the standard deviation of three repeat measurements.

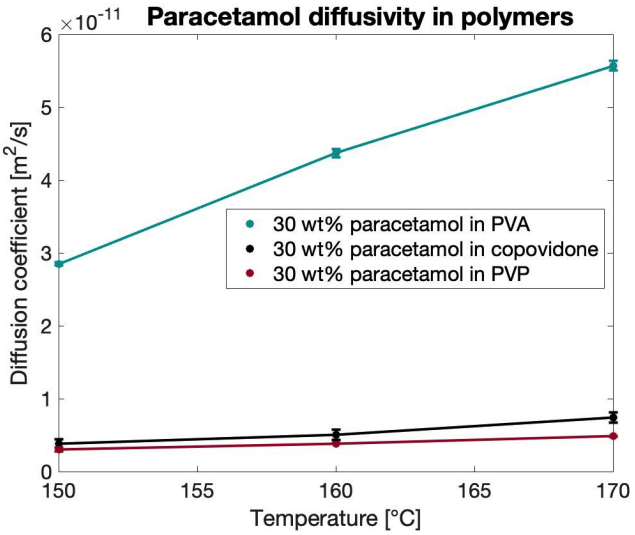

Fig. 6.3 Visual representation of the data in Table 6.2. Diffusion coefficients of paracetamol in 30 wt% physical mixtures with PVA, copovidone and PVP *vs* temperature (error bars represent the standard deviation of three measurements).

From the results presented in this section it can be concluded that there are both advantages and disadvantages to formulating a system with either PVP or PVA. A paracetamol/PVA formulation would be easy to extrude, as the T_g is low and a high degree of molecular dispersion is anticipated as the diffusion coefficient of paracetamol in this polymer is considerably high. The downside of a low T_g that is barely above room temperature ($T_g = 33.3°C$ at 30 wt% drug loading) is that phase separation is more likely to occur during storage due to high molecular mobility. Furthermore, the lack of H-bonding abilities of PVA fail to provide physical stability and the solubility of paracetamol is low, such that only low drug loading ASDs can be achieved. On the other hand, the T_g of PVP is so high (156°C) that extrusion would have to be performed at temperatures on or above paracetamol's

melting point, which could result in thermal degradation. Additionally, the strong H-bonding capability of PVP, facilitates the dissolution and stabilisation of much higher concentrations of paracetamol, but it also means that it is very hygroscopic and high water content is associated with phase separation and recrystallisation. Rask, *et al.* determined that solubility of a model drug (celecoxib) in a co-polymer of PVP and PVA increased with increasing relative VP content until 60 wt% [213]. Above this limit the solubility reached a plateau, which was attributed to paracetamol molecules in association with PVP monomers preventing other drug molecules from binding to neighbouring chain units. Therefore having a mixture of PVP and PVA monomers is a good compromise on polymer characteristics, T_g, H-bonding capabilities, hygroscopicity, physical stability and drug solubility, which is why copovidone (co-polymer of PVP and PVA at 60:40 mass ratio) is considered the best choice.

6.3.2 Alternative drug/polymer systems: nifedipine in copovidone physical mixtures and extrudates

High-temperature characterisation *via* ^{1}H NMR and DSC

The ^{1}H spectra of nifedipine (molten, 175°C) and copovidone (dissolved in deuterated acetone) are shown in Figure 6.4c. The proton resonances of nifedipine (chemical structure and nuclei labelling in Figure 6.4a) were assigned by comparison with the literature [214, 215]. The molten nifedipine spectrum is well resolved and all seven proton environments can be identified. The inset in Figure 6.4c shows the variable-temperature spectra (150-170°C) of the $6-8$ ppm region of nifedipine, which reveals the temperature dependence of peak *4* (NH group).

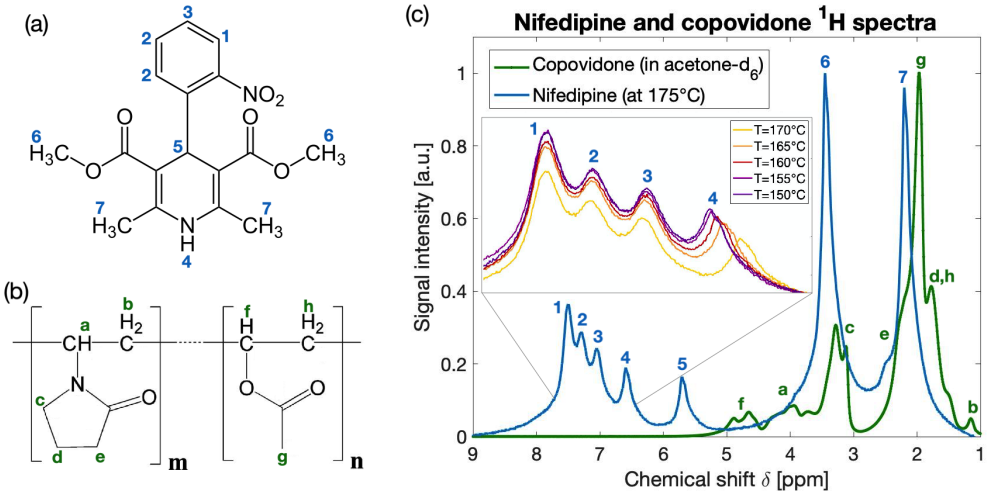

Fig. 6.4 Chemical structures of (a) nifedipine and (b) copovidone with protons labelled (*1-7* for nifedipine and *a-g* for copovidone). (c) Overlaid ^{1}H spectra of molten nifedipine at 175°C and copovidone dissolved in deuterated acetone.

To better characterise the high temperature behaviour of nifedipine, a DSC experiment where the sample was subjected to two consecutive heat-cool cycles between room temperature and 200°C was performed. In the first heating ramp (Figure 6.5, blue trace) nifedipine exhibits a melting endotherm at 173.1°C. There was no cystallisation observed in the first cooling cycle (Figure 6.5, green trace), indicating that nifedipine had remained in an amorphous glassy state. Upon the second heating ramp, three events are clearly defined: the glass transition at 41.9°C, a crystallisation exotherm at 101.9°C and a melt event at 171.4°C. This type of thermal behaviour classifies nifedipine as a class II drug, the same as paracetamol.

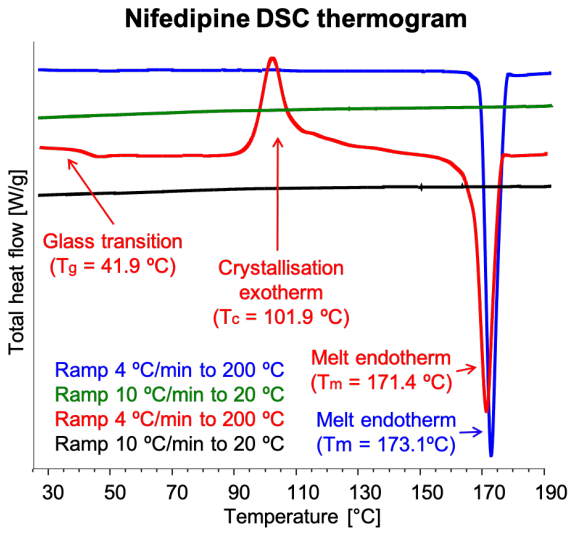

Fig. 6.5 DSC high temperature characterisation thermogram of crystalline nifedipine consisting of two consecutive heat-cool cycles. Key thermal transitions have been annotated.

Determination of the self-diffusion coefficient of nifedipine and nifedipine/copovidone physical mixtures

Figure 6.6a shows the average Stejskal-Tanner plot from three PGSTE experiments for nifedipine at 175°C. The gradient of the line of best fit yields the molecular self-diffusivity of molten nifedipine as $4.3{\cdot}10^{-11}(\pm 0.1{\cdot}10^{-11})$ m^2/s. This is four times slower than paracetamol at its respective melting point. Nifedipine's slower diffusion is likely a consequence of its significantly larger molecular radius and weight.

Table 6.3 Diffusion coefficients of 40 wt% nifedipine in copovidone physical mixtures. The self diffusion coefficient of nifedipine measured at 175°C is also included for comparison.

	$D \times 10^{-12} m^2/s$			
Nifedipine content	150 °C	155 °C	170 °C	175 °C
40% physical mix	0.45 (±0.03)[a]	0.54 (±0.04)	1.06 (±0.02)	–
Nifedipine	–	–	–	42.9 (±1.4)

[a] The numbers in parenthesis indicate the standard deviation of three repeat measurements.

Table 6.3 summarises nifedipine's diffusion coefficients in a 40 wt% physical mixture with copovidone, at three different temperatures. Nifedipine's self-diffusivity at 175°C is included for comparison. Consistently with the diffusometry results from paracetamol in copovidone, PVP and PVA, the diffusion of nifedipine was over 40 times slower in mixtures with copovidone than in its pure molten state. This is even greater than the difference

between paracetamol and paracetamol/copovidone mixtures and it is a consequence of the polymer hindering drug mobility through viscosity effects and the larger molecular size of nifedipine. The data also show that there was a positive correlation between diffusivity and temperature (Figure 6.6b).

It should be noted that results are only presented on a 40% drug loading system because the diffusion coefficients obtained were at the limit of the measurable value with the available equipment (maximum magnetic field gradient strength was 1,200 G/cm). A 30 wt% nifedipine/copovidone physical mixture was also examined, but the SNR of the diffusion-weighted spectra was too low to obtain sufficiently accurate diffusion coefficients to be presented in this thesis.

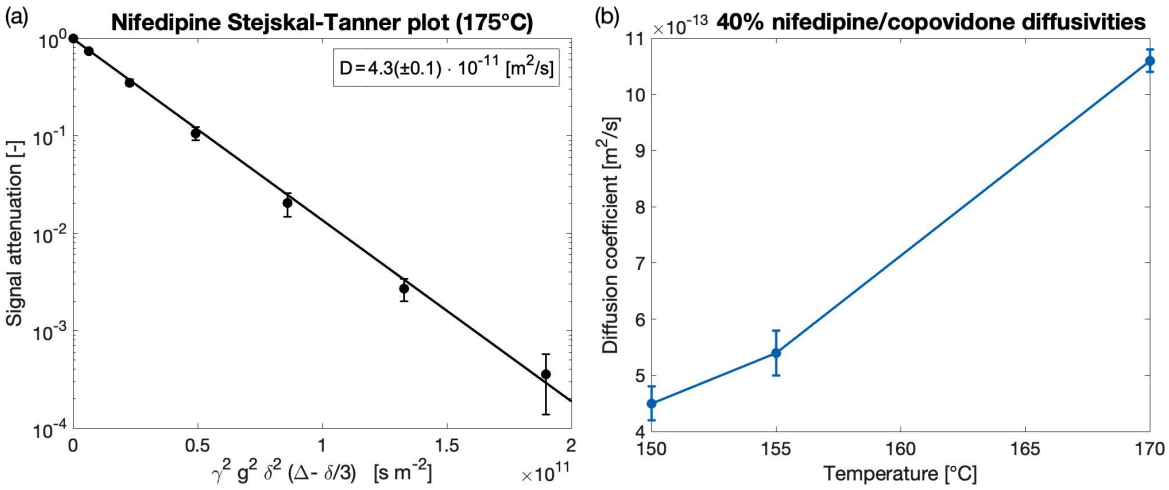

Fig. 6.6 (a) Diffusion signal attenuation plot of molten nifedipine (175°C) fitted to the Stejskal-Tanner equation. (b) Diffusion coefficients of nifedipine in a 40 wt% drug loaded extrudate with copovidone plotted against temperature. Error bars represent the standard deviation of three measurements.

Comparison between physical mixtures and extrudates *via* DSC

The normalised reversing heat flow thermograms for 20, 30 and 40 wt% nifedipine/copovidone physical mixtures (Figure 6.7a and b) and extrudates (Figure 6.7c and d) have been acquired for two consecutive heat-cool cycles. The three physical mixtures display a glass transition that corresponds to the copovidone in the system, $T_{g,copov}$=108.5°C (page 78, chapter 3), and a melt endotherm from crystalline nifedipine ($T_{m,nif}$=173.1°C) in the first heating ramp. The size of the melt peak is proportional to the amount of nifedipine in the sample. On the second heating cycle there is no melt event observed (no crystalline nifedipine present), indicative that nifedipine and copovidone are a miscible system at 20-40% drug loading. The only event is a glass transition at a temperature between copovidone's and nifedipine's ($T_{g,nif}$=41.9°C). The temperature at which the glass transition occurs is correlated with nifedipine content, such that the higher the drug loading, the lower the T_g: 103.6°C, 99.5°C

and 86.3°C for 20, 30 and 40 wt% nifedipine, respectively. This is consistent with nifedipine acting as a plasticiser for copovidone, as paracetamol does.

Unlike for the physical mixtures, there is no melting endotherm in the first heating cycle of the extrudates, which is indicative of an amorphous dispersion being achieved *via* HME. The thermogram of the second heating ramp looks very similar as the first, but the glass transition temperatures are slightly higher. This is likely due to the presence of water plasticising the extrudate in the first heating. As it was observed for the physical mixtures, the T_g of the extrudates (both in the first and second cycle) are correlated with nifedipine content. There is some disparity between the T_g of the physical mixtures and the extrudates, but this is likely a result of slight differences in composition.

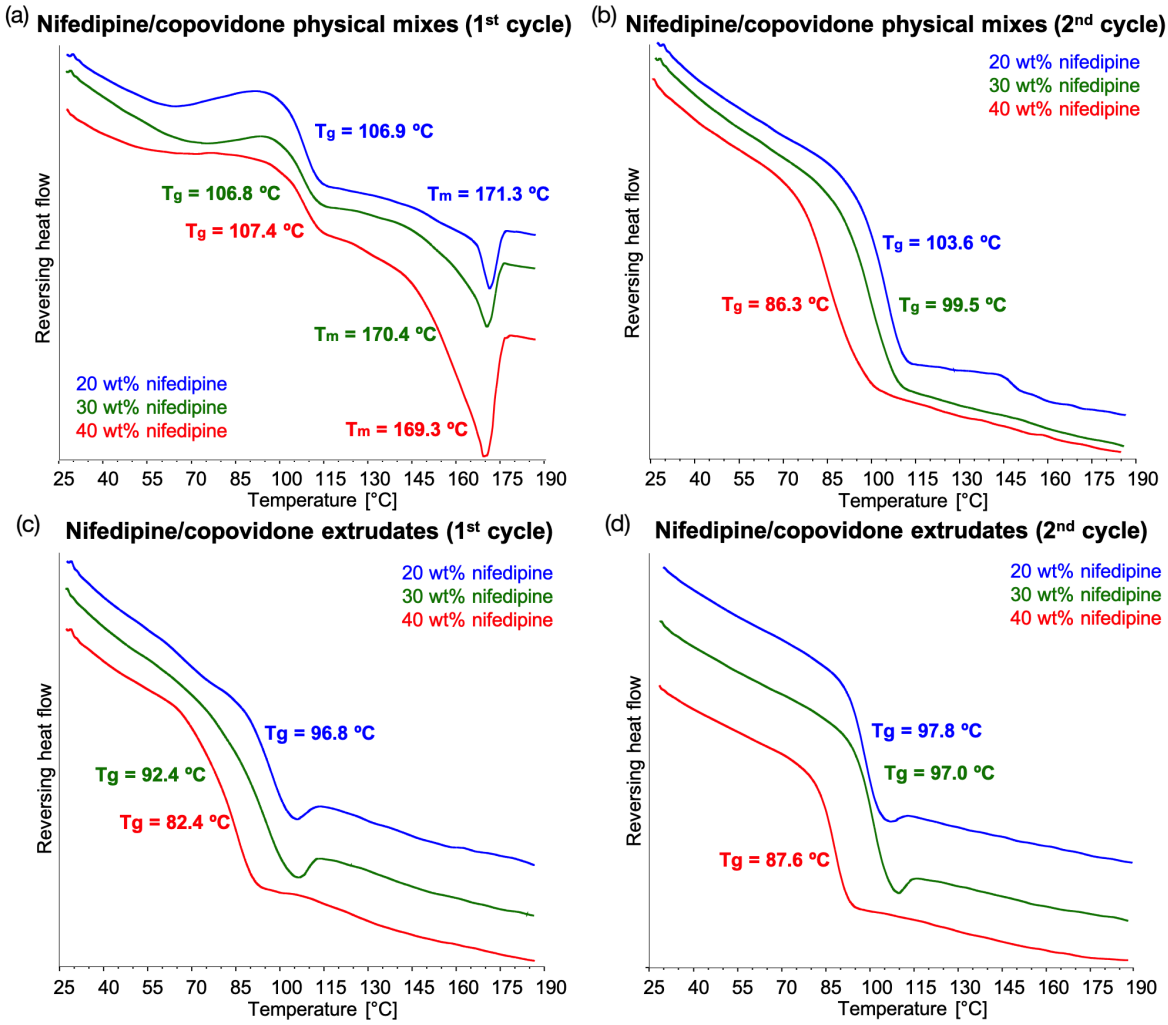

Fig. 6.7 High temperature characterisation through DSC of 20, 30 and 40 wt% nifedipine/copovidone (a), (b) physical mixtures and (c), (d) extrudates. Each thermogram consists of two consecutive heat-cool cycles, the first heating ramp in shown in (a) and (c) and the second heating ramp in (b) and (d).

Solid-state NMR studies of phase separation in nifedipine/copovidone extrudates

The ^{13}C CP-MAS spectra of pure copovidone and crystalline nifedipine were acquired and are shown in Figure 6.8c. Assignment of nifedipine ^{13}C resonances (with reference to Figure 6.8a) have been made by comparison with the literature [214, 99]. As expected, nifedipine's line-widths are narrow, because the sample was crystalline, and copovidone's are wider due to its amorphous nature.

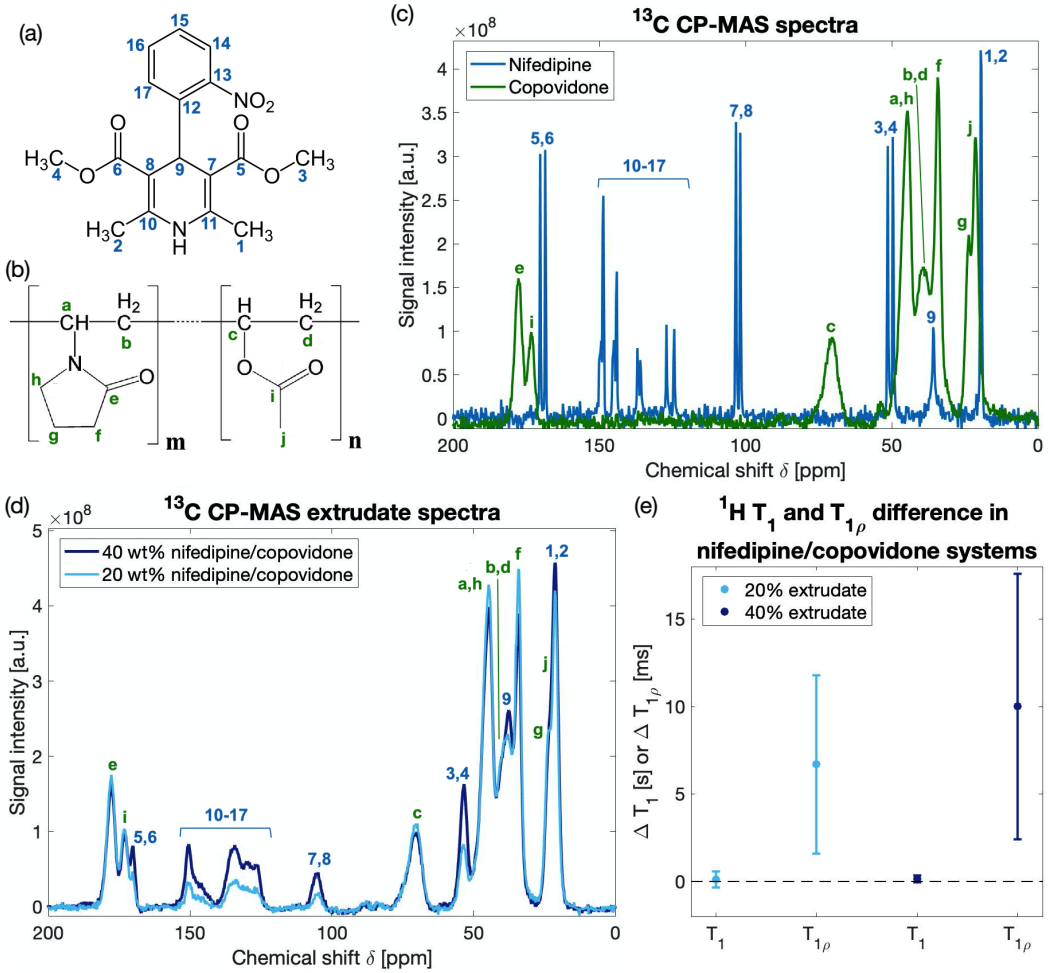

Fig. 6.8 Chemical structures of (a) nifedipine and (b) copovidone with carbon atoms labelled (*1-17* for nifedipine and *a-j* for copovidone). Overlaid ^{13}C CP-MAS spectra of (c) solid-state pure nifedipine and pure copovidone and (d) 20 and 40 wt% nifedipine/copovidone extrudates. (e) ^{1}H T_1 and $T_{1\rho}$ difference between average nifedipine and copovidone relaxation values obtained *via* ^{13}C resolved resonances for the 20 and 40 wt% nifedipine/copovidone extrudates.

The ^{13}C CP-MAS spectra of two extruded samples at 20 and 40 wt% drug loading are displayed in Figure 6.8d. In contrast to Figure 6.8c, all nifedipine resonances appear broad, indicating that it has become amorphous through the HME process (in agreement with DSC

results). Closer examination of Figure 6.8d reveals that the intensities of the resonances that correspond to nifedipine (*1-17*) increase with drug loading and the intensities of copovidone peaks slightly decrease at higher drug loadings, as expected. This, however, was not the case for the paracetamol/copovidone system analysed in chapter 4 (page 76), in which both paracetamol and copovidone signal intensity increased with drug loading. The hypothesis presented was that, as the two components were in such close contact (molecular-level dispersion) the CP efficiency from the ^{1}H in paracetamol to the ^{13}C in copovidone had increased with drug loading, as more paracetamol molecules were in intimate contact with the polymer chains. In contrast, nifedipine/copovidone extrudates do not display an increased CP efficiency for copovidone resonances at increased drug loading, suggesting that perhaps nifedipine is not as well dispersed. This hypothesis is supported by the ssNMR T_1 and $T_{1\rho}$ relaxometry experiments in the next paragraph.

Further characterisation of the solid-state microstructure of the nifedipine/copovidone extrudates was achieved through CP-MAS ^{1}H relaxometry measurements of T_1 and $T_{1\rho}$ *via* ^{13}C detection. The ^{13}C resonances used for nifedipine ^{1}H T_1 and $T_{1\rho}$ calculations were the ones resolvable in the 90-160 ppm region, as there is no copovidone signal in that frequency range (Figure 6.8c). Four copovidone-specific resonances centred at 177 ppm, 70 ppm, 44 ppm and 34 ppm were selected for calculating copovidone's relaxation constants.

Following the same approach as was detailed in chapter 4, a ^{1}H T_1 and $T_{1\rho}$ value was calculated for nifedipine and copovidone, from the average of the individual peaks. The absolute difference between nifedipine's and copovidone's T_1 and $T_{1\rho}$ constants are shown for a 20 and a 40 wt% nifedipine/copovidone extrudate in Figure 6.8e. Error bars represent the standard deviation of the relaxation values for each species. The dashed line at zero represents the position at which the T_1 or $T_{1\rho}$ is identical for nifedipine and copovidone. The results show conclusively that for both systems under consideration the T_1 of nifedipine and copovidone is identical, but there is a significant difference in their $T_{1\rho}$. Consequently, the domain sizes for nifedipine in these systems can be approximated (using equation 4.1, chapter 4) to be smaller than 35 nm, but larger than 5 nm for the 20 wt% extrudate and smaller than 40 nm, but larger than 5 nm for the 40 wt% system. The small degree of phase separation in the nifedipine/copovidone extrudates was not observed in the paracetamol/copovidone systems (all extrudates displayed approximate domain sizes smaller than 4 nm). This could be due to several factors, such as poorer miscibility between nifedipine and copovidone or weaker drug-polymer interactions failing to stabilise the molecular amorphous dispersion. Furthermore, this would explain why the enhanced CP-effect wasn't observed for the nifedipine/copovidone extrudates.

6.3.3 Effects of processing variables

Internal research performed by AstraZeneca was aimed at better understanding the effects of processing parameters on the behaviour and characteristics of the resulting formulation. A DoE matrix was built to account for four variable parameters: drug loading, processing temperature, screw speed and copovidone commercial brand. Table 6.1 shows the samples from the DoE that were provided and these included extrudates from two commercial brands of copovidone (Plasdone and Kollidon), two drug loadings (20 wt% and 30 wt%), two processing temperatures (140°C and 180°C) and two screw speeds (200 and 300 rpm).

The first tests conducted were aimed at ensuring that the two polymer brands used were not significantly different. Figure 6.9a shows the ^{13}C CP-MAS solid-state spectra of Plasdone and Kollidon and their resonances are so similar that they are virtually indistinguishable. High temperature characterisation was performed with two consecutive heat-cool DSC cycles and the resulting normalised reversing heat flow thermogram (of the second heating ramp) can be found in Figure 6.9b. The glass transition event occurs at roughly the same temperature for both copovidone brands ($T_{g,Kollidon}$=108.6°C and $T_{g,Plasdone}$=109.0°C). In conclusion, in terms of solid-state microstructure and thermal behaviour, both copovidone brands seem to be identical.

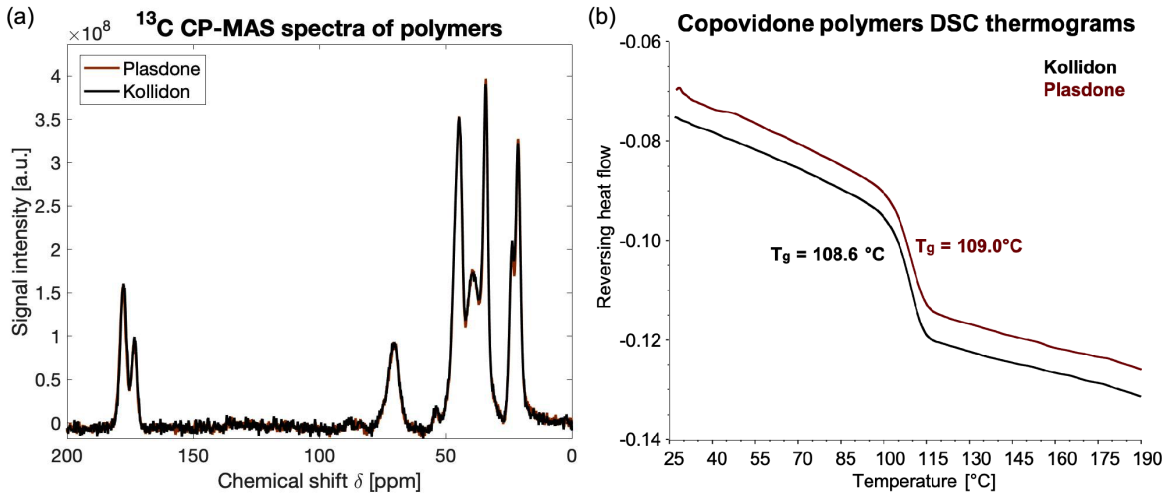

Fig. 6.9 (a) ^{13}C CP-MAS spectroscopy and (b) DSC thermograms of two copovidone commercial brands (Plasdone and Kollidon). In the thermograms only the second heating ramp of two consecutive heat-cool cycles is shown.

The second set of experiments performed on the DoE samples consisted on measuring the diffusion coefficients of paracetamol in several of the formulations (1B, 2A, 2B, 7A and 8A). The APG-STE sequence was employed and measurements were performed at 150°C, 160°C and 170°C. Figure 6.10 shows the temperature dependence of the diffusion coefficients of paracetamol in the Plasdone and Kollidon extrudates (error bars indicate the standard deviation from three measurements). No significant differences were observed between the formulations containing Plasdone or Kollidon, nor between the extrudates processed at 200 or 300 rpm. The only statistically significant trend revealed by Figure 6.10 was the positive correlation between diffusivity and drug loading, which was previously observed in chapter 3. The samples containing 30 wt% drug loading displayed diffusivities significantly higher than the ones with 20 wt% paracetamol. The diffusion coefficient data is consistent with the previous measurements in chapter 3.

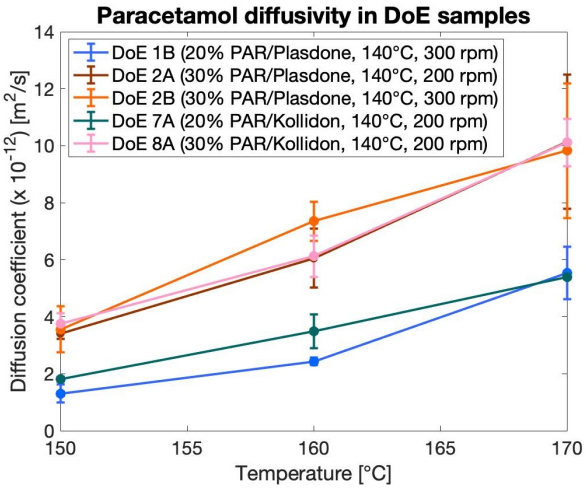

Fig. 6.10 Diffusion coefficients of DoE 20 and 30 wt% paracetamol extrudates in Plasdone and Kollidon *vs* temperature (error bars represent the standard deviation of three measurements).

Thermal characterisation was also performed on all ten DoE samples *via* two consecutive heat-cool cycles and the resulting thermograms are shown in Figure 6.11. During the first heating ramp (Figure 6.11a), the glass transitions occur at very low temperatures between 35°C and 45°C. Such a low T_g is a result of plasticisation from water, as these polymers absorb moisture easily. Compared with the 30 wt% paracetamol/copovidone extrudate presented in chapter 4 (page 80, Figure 4.7, T_g=56.5°C) the range of T_g measured for DoE samples is considerably lower, likely because of higher water moisture. A broad "bump" centred about 105°C is also observed for all samples. Given its position, it is likely caused by the evaporation of water. In the second heating ramp the range of T_g's observed rose to $70-85$°C, which is more representative of the paracetamol/copovidone systems than the T_g's from the first heating ramp, since there was no water present any more, and agreed with results from chapter 4.

There is no significant difference in the glass transition behaviour between samples processed at different temperatures or screw speeds, nor between the two polymer brands. As was the case in the diffusometry experiments, the only trend identified was a negative correlation between T_g and drug loading: the higher the drug loading the lower the T_g. The reason for this is that paracetamol molecules plasticise copovidone by dispersing in between the polymer chains and reducing polymer-polymer interactions. Interestingly, there

is no melting endotherm in the first heating cycle for any of the samples. This means that, according to DSC, paracetamol has successfully been rendered amorphous *via* HME, even for the samples at higher drug loading (30 wt%) that were processed at 140°C (2A, 2B and 8A). This supports the hypothesis presented in chapter 3, that the viscosity at 140°C would be low enough for 30% paracetamol/copovidone mixtures to be processed successfully.

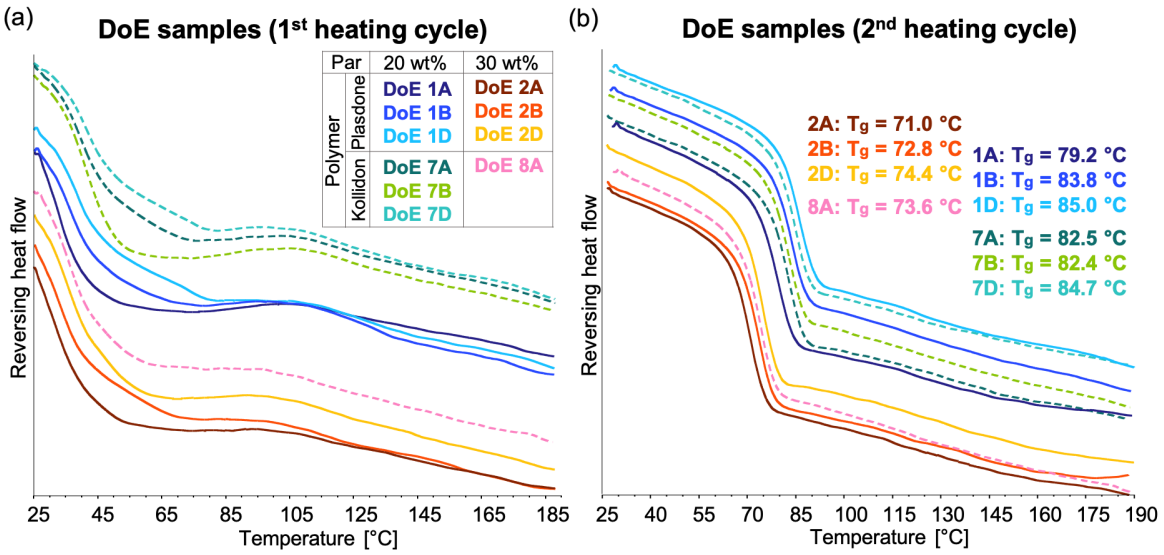

Fig. 6.11 High temperature characterisation through DSC (two consecutive heat-cool cycles) of DoE 20 and 30 wt% paracetamol extrudates in Plasdone and Kollidon, where (a) shows the first heating ramp and (b) the second heating ramp.

The fourth and final experimental approach employed to analyse the DoE sample was high resolution ^{13}C CP-MAS spectroscopy and relaxometry. In agreement with DSC results, the solid-state ^{13}C spectra of extrudates 1B, 2B, 2D, 7A, 7B, 7D and 8A (Figure 6.12a) are all virtually identical and display broad resonances indicative of paracetamol having been transformed to an amorphous state. No sharp (crystalline) resonances were recorded, even for the extrudates processed at 140°C (30°C below paracetamol's T_m).

CP-MAS ^{1}H T_1 and $T_{1\rho}$ relaxometry measurements *via* ^{13}C detection was performed on a subset of the DoE samples to determine whether there was any degree of phase separation present in the extrudates. In the same way as in chapter 4, four peaks in the 105-165 ppm region were used for paracetamol's constant calculation and for copovidone, the resonances centred at 34 ppm, 45 ppm, 70 ppm and 178 ppm were considered. From these, a ^{1}H T_1 and $T_{1\rho}$ value was calculated for paracetamol and copovidone and the absolute difference between the two is plotted in Figure 6.12b. The error bars represent the standard deviation of the relaxation value for each species and the dashed line at zero the position at which the T_1 or $T_{1\rho}$ is identical for drug and polymer. Figure 6.12b shows that there is no statistical difference between the T_1 or $T_{1\rho}$ of paracetamol and copovidone in any of the extrudates from the DoE. This indicates that there is no phase separation since (using equation 4.1) domain

sizes are estimated to be smaller than 4 nm. In agreement with DSC methods, the results from this DoE sample characterisation conclude that processing at 140°C yields amorphous solid dispersions that are identical to those processed at 180°C in terms of their thermal behaviour (DSC) and homogeneity (ssNMR T_1 and $T_{1\rho}$).

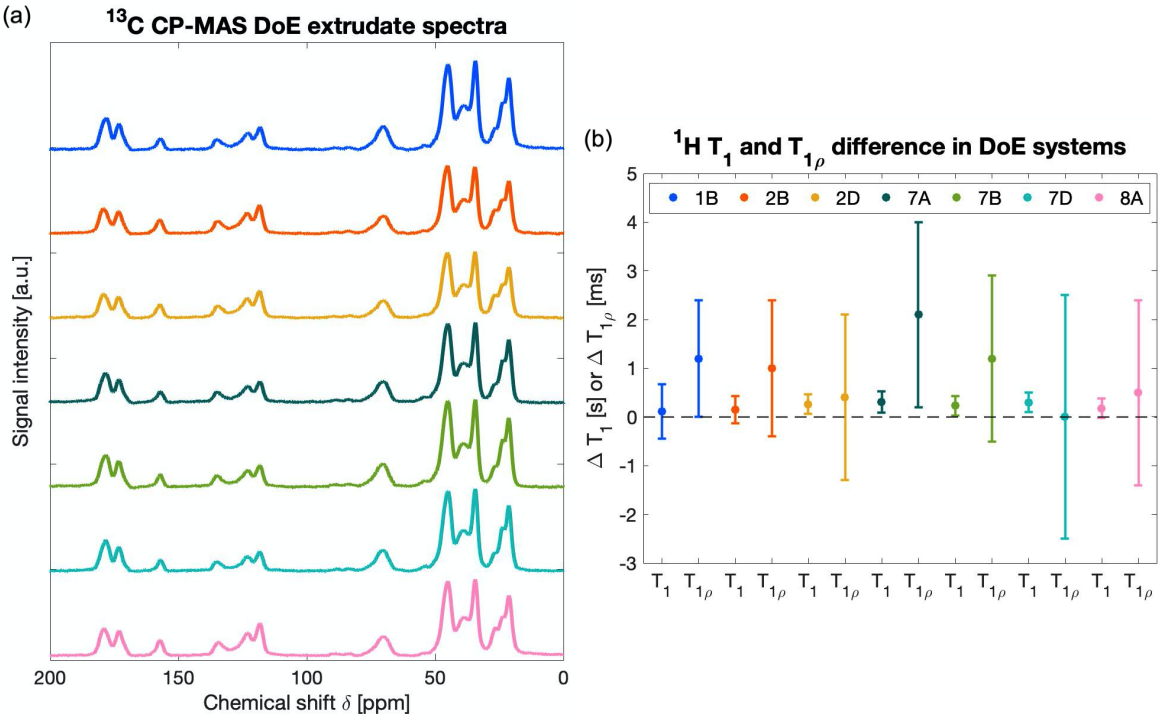

Fig. 6.12 (a) Stacked ^{13}C CP-MAS spectra and (b) ^{1}H T_1 and $T_{1\rho}$ difference between average paracetamol and copovidone relaxation values obtained *via* ^{13}C of DoE 20 and 30 wt% paracetamol extrudates in Plasdone and Kollidon.

6.4 Conclusion

In this chapter, the techniques employed on a model paracetamol/copovidone pharmaceutical system (in chapters 3 and 4) were applied for the characterisation of alternative formulations. In particular, diffusion coefficients of API in polymer melts were measured *via* high-temperature ^{1}H diffusometry, thermal performance was characterised with DSC and structural analysis to understand sample homogeneity was conducted through ssNMR ^{13}C spectroscopy and ^{1}H relaxometry.

In the first section, copovidone was compared with PVP and PVA in physical mixtures with paracetamol. The DSC and high-temperature (100−170°C) NMR experiments performed on the polymers revealed that PVA has a much lower T_g (40.2°C) and PVP a significantly higher one (156.0°C) that copovidone (109.2°C). The higher chain mobility of PVA at temperatures higher than 100°C was revealed in the variable temperature NMR spectra as

sharp, resolved resonances, whereas copovidone and PVA displayed only one broad peak in the same temperature range. When these polymers were in physical mixtures with paracetamol, a depression in its melting point was observed (as low as 130°C). Additionally, DSC thermograms exhibited the plasticising effect of paracetamol in all three polymers, resulting in lower T_g's at the higher drug loadings. PVP experienced the highest relative change in its T_g compared to when in paracetamol mixtures, possibly due to its strong H-bonding capabilities and thus enhanced solubilisation of paracetamol. Finally, the lower T_g of PVA was reflected in the significantly faster diffusion coefficient of paracetamol in paracetamol/PVA mixtures. The diffusion of paracetamol in PVP was an order of magnitude slower, which could be a combined effect of the higher T_g of the mixture (higher viscosity) and the increased and stronger drug-polymer molecular interactions.

The second system examined was nifedipine/copovidone. Nifedipine, although also considered a small molecule drug, is twice the molecular weight of paracetamol. This was evidenced in the self-diffusion coefficient in the molten state. Nifedipine's diffusivity at its T_m was four times slower than paracetamol's (at its respective T_m). PFG NMR diffusometry experiments at high temperature for nifedipine/copovidone samples could only be conducted on 40 wt% drug loading systems, because the diffusivities measured were at the limit of detection of the equipment available, as was the temperature at which the measurements were performed. With a stronger gradient set it would have been possible to determine the slower diffusion coefficients of nifedipine in lower drug loaded samples. However, these experiments on nifedipine/copovidone systems showed that the high-temperature PFG NMR technique reported in this thesis is not only applicable to a model system (paracetamol/copovidone), but also to a sample that is more representative of an industrially relevant compound for extrusion. Through high resolution CP-MAS ^{13}C spectroscopy, it was determined that nifedipine was in an amorphous state in the 20 and 40 wt% drug loaded extrudates and this was corroborated using DSC. However, ^{1}H T_1 and $T_{1\rho}$ *via* ^{13}C measurements revealed that there was a small degree of phase separation, with domain sizes estimated to be smaller than 40 nm and larger than 4 nm. This is probably due to a number of reasons, such as weak drug-polymer interactions or poor miscibility.

Finally, a number of extruded paracetamol/copovidone samples formulated with different processing parameters were analysed. From the PFG NMR diffusion coefficient measurements, it was observed that in the 20 wt% drug loaded extrudates the diffusion coefficient of paracetamol was significantly slower than in the 30 wt% ones, but none of the other parameters (copovidone brand and extrusion screw speed) resulted in visible differences in the diffusion coefficient of paracetamol. ^{13}C NMR spectroscopy and DSC revealed that in all the DoE samples paracetamol was in an amorphous state and ssNMR relaxometry that the drug domain sizes were smaller than 4 nm, irrespective of drug loading, copovidone brand, screw speed or processing temperature. This applies even for the extrudates formulated at 140°C (30°C below paracetamol's T_m). In chapter 3, it was hypothesised that 170°C was too high

for 30% paracetamol/copovidone extrusion, because the viscosity of the system was below the optimal range, the material would be free flowing and would not provide a good mixing medium; and thus lowering the temperature below 144°C would be advantageous. This chapter has demonstrated that extruding a 30 wt% paracetamol/copovidone system at 140°C results in satisfactory products, with fully amorphisised drug and no phase separation.

Chapter 7

Predicting and modelling drug solubility in polymer mixtures

7.1 Introduction

The previous chapters have shown that NMR experimental techniques can provide valuable information on a range of features of drug/polymer systems and ASD formulations such as diffusion coefficients of components in the molten mixture, intermolecular associations and homogeneity of an extruded sample. However, before preparing an extruded formulation and conducting time and resource heavy analysis on a particular system, it would be desirable to be able to predict some key properties of the system. These could be the solubility of the drug in the polymer at a certain temperature condition, which would limit the drug loading; or the time to dissolution, which would dictate how long a sample should be processed for to yield an ASD. For an in-depth review on the application of modelling to the formation and stability of ASDs, refer to DeBoyance *et al.* [216].

Determining the drug solubility in a polymer has been the focus of numerous publications and a summary of qualitative and quantitative methods was presented in chapter 1 (section 1.2.5, page 11). One of the reasons why it has attracted so much attention is that it is a parameter that underpins other important mechanisms such as dissolution rate or diffusivity, however, drug solubility in a polymer at high temperature cannot be measured directly through experimentation. Indirect experimental measurements of solubility have been proposed, among others, by Yang *et al.* [155]. They determined the solubility of paracetamol in PEO (polyethylene oxide) employing three different empirical approaches: rheology, thermal (DSC) and microscopy (hot-stage microscopy). Although results from the three approaches were consistent, the results had significant error bars and the experimentation involved was time consuming, as samples of different compositions had to be analysed at several temperatures. More recently, Bordos *et al.* introduced THz-Raman spectroscopy to determine the saturation solubility of a crystalline API in polymer matrices during HME in

real time by observation of the solid state spectrum of the drug [75]. As the drug dissolved in the polymer, the intensity of the spectral characteristics associated with crystalline API decreased.

Experimental approaches to estimate drug solubility, however, are not prevalent in the literature because they are time consuming and do not provide a sufficient level of accuracy. Instead an approach that combines experimental data with theoretical calculations is by far the most frequently used. This is based on the Flory-Huggins (FH) lattice theory, which was initially developed for polymer-solvent systems to take molecular size into account and is still considered an appropriate starting point to understand polymer thermodynamics. If the amorphous drug is considered to behave similar to a solvent, the FH model can be applied to describe the thermodynamics of drug-polymer systems [113]. Refer to [44, 39, 35] for more information on FH theory and its application to drug-polymer systems.

FH lattice theory defines an interaction parameter, χ, that describes the thermodynamics of mixing through the interaction of the polymer chains with the drug molecules. χ quantifies the relative strength of cohesive and adhesive interactions (such as Van der Waals, H-bonding and ionic interactions) and is dependent on composition and temperature. A negative or smaller than 0.5 value for the interaction parameter is indicative of miscibility [217]. χ can be evaluated in two different ways:

(i) The difference in solubility parameters (δ) between the drug and polymer as a function of the volume of the lattice site (V_{site}), as defined by the FH theory:

$$\chi = \frac{V_{site}}{RT}(\delta_{drug} - \delta_{polymer})^2 \tag{7.1}$$

(ii) Experimentally *via* melting point (T_m) depression method.

$$\left(\frac{1}{T_m^{mix}} - \frac{1}{T_m^{pure}}\right) = \frac{-R}{\Delta H_{fus}}\left[ln\phi_{drug} + \left(1 - \frac{1}{m}\right)\phi_{poly} + \chi\phi_{poly}^2\right] \tag{7.2}$$

The interaction parameter can be computed in a number of ways. Among the most popular approach is the solubility parameter group contribution method by Hansen (Equation 7.1) [42, 218]. The solubility parameter δ for the drug and the polymer is calculated from the contribution of dispersion, hydrogen bonding and polar forces. These values have been tabulated for many chemical groups, polymers and drugs [219].

The interaction parameter can also be calculated experimentally through the melting point depression of the drug. If a drug and polymer are miscible, a significant melting point depression, correlated with the composition of the system, is observed due to the exothermic mixing, ΔH_{fus} (Equation 7.2) [113]. By measuring the melting temperature of the drug in polymer system at several drug loadings (ϕ_{drug}), equation 7.2 can be fitted to obtain a value for χ.

The most common way to represent the results from the interaction parameter calculations is in the form of a phase diagram, where the solubility, miscibility and glass transition are plotted at different composition and temperature coordinates. Miscibility and solubility curve estimations are based on the value of χ (the mathematical expressions will be presented in section 7.4.1). One key advantage is that a phase diagram not only indicates the saturation concentration at a range of temperatures, but also displays the regions at which a formulation is stable, metastable and unstable. Drug-polymer phase diagrams have been employed in numerous articles, for some examples refer to [75, 39, 35, 104, 220, 36, 199, 37, 38].

Accurate prediction of dissolution kinetics and solubility and thus the formation of stable ASDs has been attempted through computational modelling and simulations. Molecular descriptors and molecular modelling have been used to account for molecular kinetics factors, such that the greatly reduced molecular mobility in the solid state that can prevent phase separation even if the formulation solubility limit has been exceeded [216]. However, there are a lack of accurate models that take into account the features of HME, such as screw speed and architecture, degree of fill or residence time distribution. One model, proposed by Derksen *et al.*, simulates the dissolution of spherical particles in laminar shear flow [117]. The laminar shear is a simplification of the complex shear field exerted by the rotating screws on the drug/polymer melt. A detailed explanation of this model will be presented in section 7.2.2. Another model was proposed more recently by Schittny *et al.* [118]. They were the first to explore the links between the formation of ASDs and HME process parameters by combining calculations of time to dissolution of solid drug particles in a molten polymer with a model of mean residence time.

This chapter will present two models for the simulation of the dissolution of a solid drug particle in a polymer melt. One of them will be simple, as dissolution is simulated to occur in a static medium (based upon the Berkeley Madonna mathematical modelling software), and the second more complex model will simulate dissolution under laminar shear [117]. The modelling predictions will be compared to experimentally obtained data on time to dissolution of a paracetamol particle in a copovidone melt. Finally, a phase diagram for the paracetamol/copovidone model system will be constructed by calculating the solubility and miscibility curves and measuring its T_g.

7.2 Development of numerical methods

7.2.1 Static particle dissolution model (based on the Berkeley Madonna model)

One of the simplest approaches to model the dissolution of a drug crystal in a polymer melt is presented by the Berkeley Madonna modelling software package (https://berkeley-madonna.myshopify.com). This model considers a spherical drug particle of radius r suspended in a dissolution medium in which the only mode of mass transport is diffusion. This would result in concentric shells of uniform solute concentration, that decreases with distance from the particle (refer to Figure 7.1). Applying Fick's first law [221] to this system and considering only the flux (F) across the plane perpendicular to the x axis:

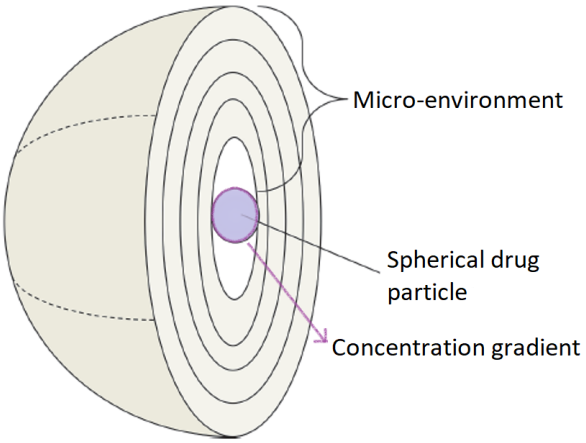

Fig. 7.1 Schematic of the dissolution of a spherical particle.

$$F = -D \cdot A \cdot \frac{dc}{dx} \tag{7.3}$$

where D is the diffusion coefficient and c is the concentration.

The surface area (A) of each of the shells depicted in Figure 7.1 is defined by:

$$A = 4 \cdot \pi x^2 \tag{7.4}$$

where x is the distance from the surface of the spherical particle.

Combining equations (7.3) and (7.4), the concentration gradient at a distance x from the particle surface is:

$$\frac{dc}{dx} = -\frac{F}{4 \cdot \pi \cdot x^2 \cdot D} \tag{7.5}$$

which can be integrated to:

$$c = \frac{F}{4 \cdot \pi \cdot x \cdot D} + k \tag{7.6}$$

Considering as the boundary condition that a perfect sink exists after the outermost shell (positioned at r_{out}), then $c = 0$ at this point and the constant of integration (k) is given by:

$$k = -\frac{F}{4 \cdot \pi \cdot r_{out} \cdot D} \tag{7.7}$$

Using the definition of k shown in equation (7.7), the concentration at any position x is given by equation (7.6) as:

$$c = \frac{F}{4 \cdot \pi \cdot D} \left(\frac{1}{x} - \frac{1}{r_{out}} \right) \tag{7.8}$$

The concentration at the surface of the particle (where $x = r_0$) is assumed to be the equilibrium solubility (c_0):

$$c_0 = \frac{F}{4 \cdot \pi \cdot D} \left(\frac{1}{r_0} - \frac{1}{r_{out}} \right) \tag{7.9}$$

Following from equation (7.7), the total flux through each layer is given by:

$$F = 4 \cdot \pi \cdot D \cdot c_0 \left(\frac{r_{out} \cdot r_0}{r_{out} - r_0} \right) \tag{7.10}$$

If $r_{out} >> r_0$, then equation (7.8) can be simplified to:

$$F = 4 \cdot \pi \cdot D \cdot c_0 \cdot r_0 \tag{7.11}$$

In a non-infinite system holding several spherical drug particles, the rate of increase of drug mass in solution ($m_s(t)$) can be related to the radius of the drug particle ($R(t)$), by taking into account the definition for flux in equation (7.11) and the difference between the drug solubility (S) and the concentration of drug in solution:

$$\frac{dm_s(t)}{dt} = n_{part} \cdot 4 \cdot \pi \cdot D \cdot R(t) \cdot \left(S - \frac{m_s(t)}{V} \right) \tag{7.12}$$

The total number of drug particles in the system (n_{part}) can be calculated as:

$$n_{part} = \frac{3 \cdot m_0}{4 \cdot \pi \cdot R_0^3 \cdot \rho_d} \tag{7.13}$$

where m_0 is the total solid drug mass (before dissolution commences), R_0 is the initial radius of the spherical drug particles, and ρ_d is the density of the crystalline drug.

Another equation was required to describe the rate of decrease of the drug particle radius as the dissolution process advanced. According to the Berkeley Madonna dissolution model, this is proportional to the difference between the saturation concentration and the

concentration of drug in solution:

$$\frac{dR(t)}{dt} = -\frac{D}{\rho_d \cdot R(t)} \cdot \left(S - \frac{m_s(t)}{V}\right) \tag{7.14}$$

The system of differential equations formed by (7.12) and (7.14) were solved simultaneously using the *ode23* ordinary differential equation solver in MATLAB_R2017b to obtain a dissolution rate plot. The initial conditions imposed for the two variables were that the initial drug particle radius was R_0 ($R(0) = R_0$) and that at the initial time there was no drug in solution ($m_s(0) = 0$).

7.2.2 Shear flow particle dissolution model

A key outcome of HME is to achieve homogeneous products. To ensure this, one could process the mixture for an extended period of time, but in doing so, thermal degradation is risked. It is therefore highly relevant to be able to predict the dissolution time of a drug/polymer system at conditions similar to those within the extrusion barrel. In the context of HME drug particle dissolution modelling in a polymer melt, Derksen *et al.* published an article in which laminar shear flow was taken into account [117]. This is relevant because in HME, solid polymer and drug particles are fed into an extruder, inside of which the rotation of screws exerts shearing forces on the drug/polymer mixture. Derksen *et al.* performed numerical simulations for the dissolution of spherical drug particles to model this process.

The approach they followed was to solve the convection-diffusion equation, setting the saturation concentration as a boundary condition at the surface of the particle. The model coupled the solid (drug particles) and liquid (molten polymer) phases so that the liquid flow translated and rotated particles (no slip boundary condition was imposed at interface between phases) using the lattice-Boltzmann method. As the simulation evolved drug particle size decreased as a result of solid-to-liquid mass transfer at the particle's surface, and in turn, the liquid phase contained an increasing concentration of dissolved solute, which underwent diffusion and convection by the liquid flow. Additionally, the mixture underwent simple laminar shear, simulated by two rectangular plates moving in opposite directions. The outcome of the simulations were plots of the decay of the solids volume fraction with respect to time, as a function of process and material conditions such as: initial solids volume fraction, diffusion coefficient, solubility and shearing rate. Final dissolution time was determined as the time at which 95% of the initial solid fraction had dissolved in order to remove the uncertainty from the last few undissolved fragments.

There are five key dimensionless parameters that govern the flow dynamics of the simulation:

- Initial Reynolds number: $Re_0 \equiv \frac{\dot{\gamma} a_0^2}{\nu}$, where $\dot{\gamma}$ is the shear rate, ν is the kinematic viscosity and a_0 the initial particle radius.

- Initial solids volume fraction: $\phi_0 \equiv \frac{4\pi N a_0^3}{3HLW}$, where N is the total number of particles and H, L and W is the distance between the shearing plates, their length and width, respectively.
- Initial solid over liquid density ratio: $\frac{\rho_s}{\rho}$
- Peclet number: $Pe \equiv \frac{\dot{\gamma} a_0^2}{\Gamma}$, where Γ is the diffusion coefficient of the solute.
- Schmidt number: $Sc \equiv \frac{\nu}{\Gamma}$, where ν is the kinematic viscosity and Γ is the diffusion coefficient of the solute. The Schmidt number is also the ratio of the Peclet number to the Reynolds number.

Several assumptions and simplifications were made. Firstly, it is considered that the polymer first melts and reaches the simulated temperature and only then begins the dissolution of the drug, however in reality, the melting point of the drug could be depressed by the presence of the polymer (as it occurred for the paracetamol/copovidone system) and in this case drug dissolution could commence as the polymer is heating up above its glass transition temperature, but before the processing temperature has been reached. Secondly, the liquid phase (polymer melt) is assumed to be Newtonian (even though in chapter 3, section 3.3.4, it was shown that copovidone's viscosity did vary at different angular frequencies). Thirdly, the particles are assumed to be spherical and remain spherical during dissolution; however, microscopy experiments in section 7.4.4 showed that the shape was irregular and Moseson *et al.* observed under polarized light microscopy that the dissolution patterns of drug crystals in molten polymers were highly irregular and involved the formation of channels, holes and fragmentation [151]. Also, the liquid's viscosity and density are considered uniform, independent of local solute concentration, but in chapter 3 section 3.3.4 it was shown that viscosity varies greatly with drug loading, particularly as, in the case of paracetamol/copovidone, the drug has a strong plasticising effect on the polymer. Finally, the initial Reynolds number for the parameters used by Derksen *et al.* ($\dot{\gamma}$=10 s^{-1}, ν=0.2 m^2/s, a_0=100 μm) was $Re_0 = 5 \cdot 10^{-7}$. This is a very low number that would either require a very high viscosity, which would limit the accuracy of the model, or a very low plate velocity, which would make the simulations very lengthy. Since the Reynolds number was significantly smaller than 1, it was assumed that the dynamics of the flow were independent of it, and so Re_0 was set to a more practical value of 0.05. Table 7.1 shows the input parameters used by Derksen *et al.* for the dissolution simulations.

The main conclusions drawn from the simulation runs are as follows:

- Higher initial solids volume fraction (ϕ_0) leads to slower dissolution. That is because higher solute concentration in the liquid reduces the concentration gradient between the particles' surfaces and the bulk liquid and thus reduces the driving force for solid-liquid mass transfer.

- Increasing Peclet number (Pe) (effectively decreasing diffusion coefficient, Γ) results in slower dissolution because the mass flux at the solids' surfaces is reduced.
- Dissolution curves exhibit a fast initial decay as the solute penetrates the liquid around the solid with high concentration gradients and then tail off as the solute concentration in the bulk liquid increases.
- Reducing the drug/polymer solubility parameter (S) significantly increases dissolution time.
- Plotting dissolution time as a function of Peclet number indicates that dissolution time is highly sensitive to diffusion coefficient but, that increasing shear rate within the range considered, does not reduce dissolution time.

Table 7.1 Parameter values used by Derksen *et al.* for dissolution simulations

Parameter	**Value**	**Description**
ϕ_0	$0.2 - 0.4$	Initial solids volume fraction
$\frac{\rho_s}{\rho}$	1.25	Solid over liquid density ratio
Re_0	$5 \times 10^{-7} \rightarrow 0.05$	Initial Reynolds number based on a_0 and $\dot{\gamma}$
Pe_0	$20 - 800$	Initial Peclet number
Sc	300	Schmidt number
Γ	$10^{-9} - 10^{-8}\ m^2/s$	Diffusion coefficient of solute
S	$0.4 - 0.6$ wt%	Solubility in $180 - 200$°C range
a_0	$100\ \mu m$	Initial particle radius
ν	$0.2\ m^2/s$	Liquid kinematic viscosity
$\dot{\gamma}$	$1 - 100\ s^{-1}$	Shear rate

7.3 Materials and methods

7.3.1 Materials and sample preparation

The API/polymer model system for the work presented in this chapter was: paracetamol/copovidone. Paracetamol (mean particle diameter $\sim 300\ \mu$m, Mallinckrodt) and copovidone (Kollidon VA 64®, M_w=45,000-70,000, BASF), were supplied by AstraZeneca.

Paracetamol/copovidone discs were required for experiments on the Rheoscope (rheometer coupled with a microscopy camera module, see section 7.3.2). When copovidone is heated, bubbles are formed from moisture evaporation and compression of the powder. These air bubbles interfere with imaging approaches, so the MeltPrep equipment was used to make bubble-free discs. The Meltprep is able to produce bubble-free discs by creating a vacuum

within the vacuum compression molding (VCM) insert, inside of which the sample that will be converted into a disc is contained, while being heated (refer to Figure 7.2a).

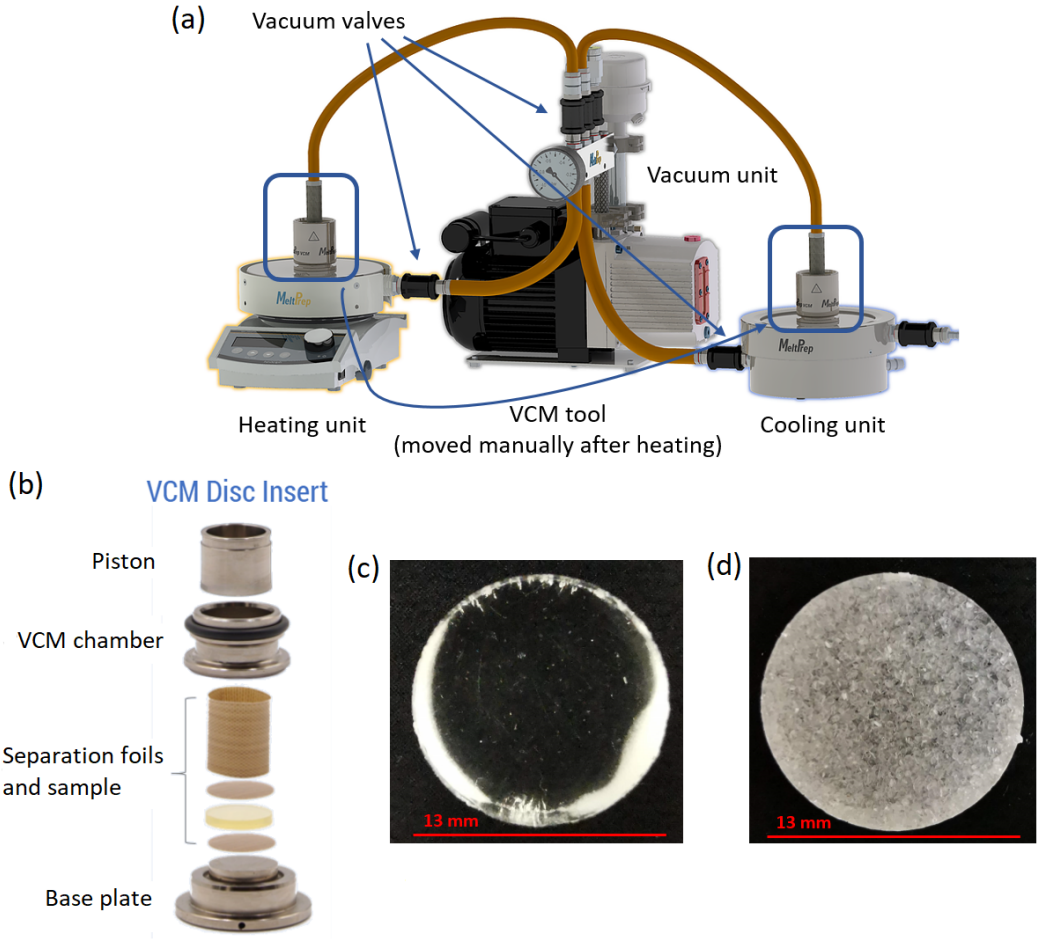

Fig. 7.2 (a) Schematic of the MeltPrep equipment, where the different parts of the apparatus are labelled; and (b) magnified view of the VCM (vacuum compression molding) insert (modified from https://www.meltprep.com/). Photographs of bubble-free 13 mm (c) copovidone and (d) 30 wt% paracetamol/copovidone discs prepared with the MeltPrep.

Discs of 13 mm in diameter and approximately 2.8 mm thick were prepared from copovidone and 5%, 20%, 30%, 40% and 60% paracetamol/copovidone physical mixtures. 440 mg of material was introduced in the VCM chamber, in between the non-stick separation foils, as is shown in Figure 7.2b. The VCM insert was then attached to the vacuum unit and to the heating unit, which was set to 130°C. After 30 min the VCM insert was carefully moved to the cooling unit for 20 min and then the sample disc was extracted from the VCM insert and placed in a sealed plastic bag prior to analysis. The VCM disc insert was secured to the heating and cooling units via vacuum to ensure good thermal contact. Figure 7.2c shows a copovidone disc prepared in the MeltPrep, displaying a uniform glassy appearance with no bubbles (the brighter edges are a shadow effect from the photo). Figure 7.2d displays a 30

wt% paracetamol/copovidone disc, in which paracetamol crystals are suspended in the glassy polymer.

7.3.2 Dissolution studies under static and shearing conditions

A Haake MARS rheometer equipped with a MARS III controller and an integrated microscopy camera module fitted with a x5 objective, known as a Rheoscope was used for observational dissolution studies under static and shearing conditions. Zero gap calibration was performed at the test temperature and the sample disc prepared in the MeltPrep was loaded between the 29 mm parallel polished plates. The bottom plate had a glass opening to accommodate the microscopy objective and light source, and the polished top plate ensured that light was reflected so it could be detected by the microscopy camera module. The plates were brought together until the sample filled the entire plates' surfaces (usually resulting in a 0.7 mm gap).

The temperature, shearing rate, experiment length and imaging rate were controlled with the Haake Rheo Win Job Manager software. The shearing rates studied were 0.1 s^{-1} and 1 s^{-1}, as any higher resulted in blurry images. Imaging rate was set to one frame per 10 s and temperature to 140°C. As well as images, viscosity values were obtained at every sampled time point. The cross-polarised light (aligned on a single plane) setting was used for ease of data analysis, as paracetamol crystals (anisotropic) would split the light beam into orthogonal components that are later reunited, while amorphous material (isotropic) would just let the light through. Consequently, crystals are captured as high intensity pixels and amorphous components as low intensity. By increasing image contrast, white pixels were associated with crystals and black pixels with molten/amorphous species. DSC was performed on fragments of the discs to ensure paracetamol was still crystalline after processing in the MeltPrep. Image analysis and plots were generated on MATLAB_2017b.

7.3.3 DSC: melting point depression, glass transition temperature and heat capacity calculations

Thermal analysis was conducted with a Q2000 (TA Instruments, New Castle, DE, USA) differential scanning calorimeter. The data was processed using TRIOS software (TA Instruments).

Standard DSC for T_m measurements

Approximately 3-7 mg of sample was sealed in a standard aluminium pan and heated from 20°C to 200°C at a rate of 1°C/min and cooled back to 20°C at 20°C/min. Two controlled sequential heat-cool cycles were performed on all samples under a nitrogen stream of 50 mL/min. Melting temperatures were determined as the inflection point of the endotherms in the normalised total heat flow plots.

Modulated DSC for T_g measurements

Approximately 3-7 mg of sample was sealed in a standard aluminium pan and heated from 20°C to 200°C at a rate of 4°C/min, with a modulation amplitude of ±1°C and period of 60 s, and cooled back to 20°C at 10°C/min. Two controlled sequential heat-cool cycles were performed on all samples under a nitrogen stream of 50 mL/min. Glass transition temperatures were assigned to the stationary point of the normalised reversing heat flow data.

Modulated DSC for C_p measurements

Approximately 3-7 mg of sample was sealed in a Tzero aluminium pan (in which the base is almost perfectly flat for improved thermal contact with the heated discs) and heated from 0°C to 200°C in 10°C steps where they were held quasi-isothermally, with a modulation amplitude of ±0.5°C and period of 60 s. A quasi-isothermal mode is required because it is not possible to measure C_p data at a constant temperature, as is apparent from the relationship between heat flow and C_p:

$$\frac{dH}{dt} = C_p \frac{dT}{dt} + f(T,t) \tag{7.15}$$

where $\frac{dH}{dt}$ is the heat flow, $\frac{dT}{dt}$ is the heating rate and $f(T,t)$ is the kinetic component of the heat flow (which is a function of temperature and time).

Two controlled quasi-isothermal sequential heat cycles were performed on all samples under a nitrogen stream of 50 mL/min. The heat capacity data data was extracted using TRIOS software (TA Instruments).

7.3.4 TGA for sample stability

Thermogravimetric analysis was conducted with a Discovery TGA (TA Instruments, New Castle, DE, USA) instrument. Approximately 5-10 mg of sample was weighed into a tared platinum pan. Isothermal tests at 140°C, 150°C, 160°C and 170°C were conducted for $3 - 12$ hours. Temperature ramps were performed at a heating rate of 5 °C/min from room temperature to 170°C. All tests were conducted under nitrogen to avoid sample oxidation. The data was visualized using TRIOS software (TA Instruments).

7.4 Results and discussion

7.4.1 Paracetamol/copovidone solubility and miscibility

The calculation of the interaction parameter for the paracetamol/copovidone system is presented in this section. The interaction parameter is used to compute the miscibility and

solubility curves, which will be plotted on a phase diagram, where the stable, metastable and unstable temperature-composition regions will be shown and discussed. Meng *et al.* defined drug-polymer miscibility as the tendency of the amorphous or molten drug to disperse in the polymer matrix, while solubility refers to the ability of the polymer to act as a solvent and dissolve the crystalline drug [40].

Interaction parameter

The first step to calculate the solubility and miscibility curves is determining a value for the interaction parameter. χ is temperature and composition dependent, but in polymer systems the effects of composition are negligible compared to temperature [222]:

$$\chi = A + \frac{B}{T} \tag{7.16}$$

where A and B are fitting parameters. In order to obtain the temperature-dependent value of χ, it was evaluated at the melting point of the drug and at room temperature and then extrapolated using equation 7.16.

The value of χ at the melting temperature of paracetamol ($T_m = 169.8°C$) was obtained through the experimental melting point depression method. This is based on the fact that the presence of polymer reduces the melting temperature of the drug when the two are miscible; the extent of the depression is related to the miscibility of the components [101]. This method is best suited for systems in which the T_g of the polymer is significantly lower than the T_m of the drug, because the polymer needs to be rubbery to interact with the drug [154].

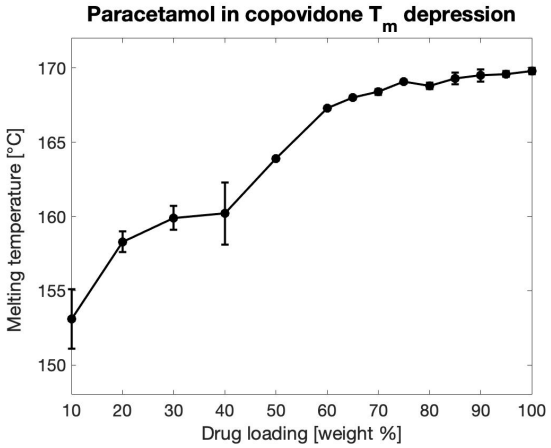

Fig. 7.3 Melting point depression of paracetamol in copovidone at several concentrations, obtained from DSC thermograms. Error bars indicate the standard deviation from three independent measurements.

Results from DSC experiments on the melting point depression of paracetamol are shown in Figure 7.3. Equation 7.2 can be rearranged as:

$$\left(\frac{1}{T_m^{mix}} - \frac{1}{T_m^{pure}}\right) \cdot \frac{\Delta H_{fus}}{-R} - ln\phi_{drug} - \left(1 - \frac{1}{m}\right)\phi_{poly} = \chi\phi_{poly}^2 \tag{7.17}$$

The values in Table 7.2 and 7.3 were substituted in Equation 7.17 to obtain the value of χ. ϕ_{poly} and ϕ_{drug}, the volume fractions of polymer and drug, respectively, were calculated

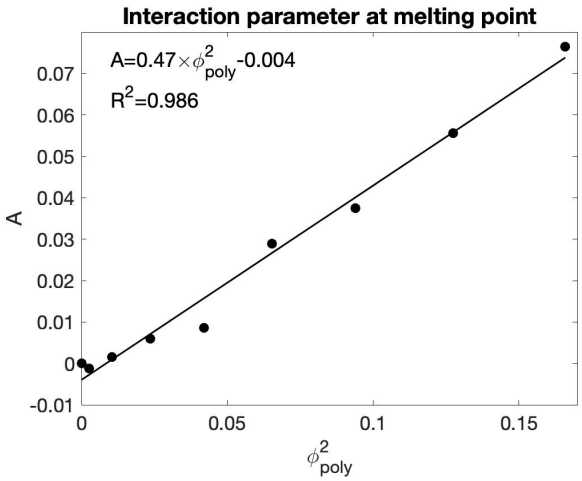

Fig. 7.4 Melting point depression experimental data fitted to a first order polynomial to obtain a value for χ, the interaction parameter, at 169.8°C for a paracetamol/copovidone system.

from the mass fractions and the density values quoted in Table 7.3. Figure 7.4 is a plot of $\left(\frac{1}{T_m^{mix}} - \frac{1}{T_m^{pure}}\right) \cdot \frac{\Delta H_{fus}}{-R} - ln\phi_{drug} - \left(1 - \frac{1}{m}\right)\phi_{poly}$, defined as A, *versus* ϕ^2_{poly}, fit to a first degree polynomial such that the gradient corresponds to the interaction parameter.

Negative or values of χ smaller than 0.5 suggest that the adhesive forces of drug-polymer interactions are stronger than the cohesive forces of drug-drug or polymer-polymer associations [217, 32]. The value obtained for χ at the melting point of paracetamol was 0.47, which is indicative of miscibility between the components in the system at this temperature.

The next step was to calculate χ at room temperature. This was done using the solubility parameter approach, for which Equation 7.1 was adapted by Hansen to account for the effects of dispersive, polar and hydrogen bond forces on the solubility parameters. For systems where dispersion forces dominate over polar and hydrogen bonding ones the equation to determine χ is [42]:

$$\chi = \frac{V_{site}}{RT}\left[(\delta_{drug,d} - \delta_{poly,d})^2 + 0.25\,(\delta_{drug,p} - \delta_{poly,p})^2 + 0.25\,(\delta_{drug,h} - \delta_{poly,h})^2\right] \quad (7.18)$$

where V_{site} is the lattice site volume from the FH theory, which in this scenario corresponds to the molar volume of the drug (ν_{drug}). The values in Table 7.4 were substituted in Equation 7.18 to obtain an interaction parameter at room temperature of 1.14.

Coefficients A and B from Equation 7.16 can be calculated with the two values of χ obtained: $\chi(T = 298.15\ K) = 1.14$ and $\chi(T = 442.95\ K) = 0.47$. The temperature dependent behaviour of χ is displayed in Figure 7.5 and it will be used in the following sections for the calculation of the solubility and miscibility curves: $\chi = -0.903 + \frac{607.9}{T}$

Table 7.2 Parameter values used to calculate the interaction parameter at the melting point for the paracetamol/copovidone system following the melting point depression approach

Parameter	Value	Description
T_m^{pure}	169.8 $[°C] = 442.95$ $[K]$ [a]	Melting point of pure paracetamol
R	8.314 $[\frac{J}{K \cdot mol}]$	Gas constant
ΔH_{fus}	175.5 $[\frac{J}{g}]$ [a]	Heat of fusion of paracetamol
ϕ_{drug}	$\phi_{drug} = \frac{mass\ fraction}{\rho_{drug}}$	Volume fraction of paracetamol
m	$\frac{\frac{M_{w,poly}}{\rho_{poly}}}{\frac{M_{w,drug}}{\rho_{drug}}}$	Ratio of molecular volumes
$M_{w,poly}$	$55,000$ $[g/mol]$ [b]	Molecular weight of copovidone
ρ_{poly}	1.15 $[g/cm^3]$ [b]	Density of copovidone
$M_{w,drug}$	151 $[g/mol]$ [c]	Molecular weight of paracetamol
ρ_{drug}	1.35 $[g/cm^3]$ [d]	Density of paracetamol

[a] Experimental value from DSC; [b] Value from [199]; [c] Value from the PubChem Compound Databse (CID=1983); [d] Value from [208]

Table 7.3 Melting point depression of paracetamol in copovidone at several concentrations, obtained from DSC thermograms.

Paracetamol [wt%]	$\mathbf{T_m^{mix}}$ $[°C]$	Paracetamol [wt%]	$\mathbf{T_m^{mix}}$ $[°C]$
95	169.6	60	167.3
90	169.5	50	163.9
85	169.3	40	160.2
80	168.8	30	159.9
75	169.1	20	158.3
70	168.4	10	153.1
65	168.0		

Solubility curve

Solubility is defined as the drug loading of saturated drug-polymer solid solution without the tendency of re-crystallisation [32]. Therefore the solubility curve defines the stable regions of the phase diagram. As proposed by Marsac *et al.*, the solubility of a crystalline material in a solvent can be described by [113]:

$$ln(\gamma_{drug} \cdot x_{drug}) = -\frac{\Delta H_{fus}}{RT}\left[1 - \frac{1}{T_m}\right] - \frac{1}{RT}\int_{T_m}^{T} \Delta C_p dT + \frac{1}{R}\int_{T_m}^{T} \frac{\Delta C_p}{T} dT \tag{7.19}$$

where it is assumed that the polymer can take the role of a solvent.

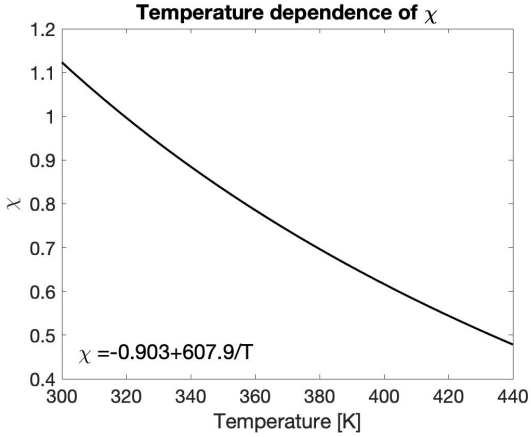

Fig. 7.5 Temperature dependence of the interaction parameter, χ, for the paracetamol/copovidone system.

Table 7.4 Parameter values used to calculate interaction parameter at room temperature for paracetamol/copovidone system by the solubility parameter approach

Parameter	**Value**	**Description**
ν_{drug}	$\frac{M_w}{\rho_{drug}} = 124.2\ [cm^3/mol]$	Molar volume of the drug
R	8.314 $[\frac{J}{K \cdot mol}]$	Gas constant
T	25 $[°C] = 298.15\ [K]$	Room temperature
$\delta_{drug,d}$	20.66 [a]	Paracetamol dispersion forces
$\delta_{drug,p}$	11.50 [a]	Paracetamol polar forces
$\delta_{drug,h}$	12.78 [a]	Paracetamol H-bond forces
$\delta_{poly,d}$	18.0 [b]	Copovidone dispersion forces
$\delta_{poly,p}$	7.8 [b]	Copovidone polar forces
$\delta_{poly,h}$	5.8 [b]	Copovidone H-bond forces
M_w	151 $[g/mol]$ [c]	Molecular weight of paracetamol
ρ_{drug}	1.35 $[g/cm^3]$ [d]	Density of paracetamol

[a] Value from [223]; [b] Value from [49] and [224]; [c] Value from the PubChem Compound Databse (CID=1983); [d] Value from [208]

The activity coefficient (γ) is a factor that accounts for deviations from ideality in mixing processes. Applying FH lattice theory, the activity coefficient of the drug can be defined by [40]:

$$ln\gamma_{drug} = ln\frac{\phi_{drug}}{x_{drug}} + \left(1 - \frac{1}{m}\right)\phi_{poly} + \chi\phi_{poly}^2 \tag{7.20}$$

All of the parameters in Equations 7.19 and 7.20 have been previously calculated or measured, except for ΔC_p. Heat capacity (C_p) is a physical property of matter, defined as the amount of thermal energy that produces a unit change in its temperature. ΔC_p is known as the configurational heat capacity, which is defined as the difference between the heat capacity in the amorphous state and the crystalline form. It was measured *via* DSC, following the method presented in section **??**. Figure 7.6 shows the heat capacity of paracetamol measured by DSC on two consecutive heating cycles. The first heating ramp (red trace) represents the C_p of the crystalline state, until 170°C, when paracetamol melts and a jump in the C_p value is observed. For the second heating cycle (blue trace), the data points (0-60°C) correspond to paracetamol in an amorphous-glassy state. At 60°C there is a sharp decrease in the C_p, which corresponds to a crystallisation process. The difference in C_p between the data point at 50°C and 70°C were used to calculate the configurational heat capacity: $\Delta C_p = 0.51\ \frac{J}{g \cdot °C}$ (arrow in Figure 7.6). Since paracetamol crystallises during heating, it was not possible to measure the ΔC_p for the whole temperature range and it was assumed to be constant [225].

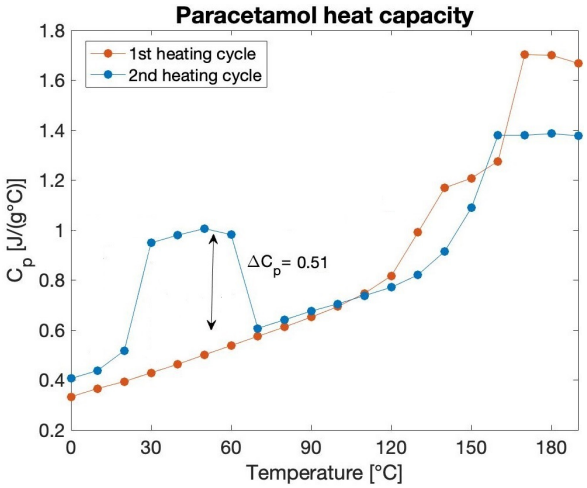

Fig. 7.6 Heat capacity of paracetamol measured by DSC on two consecutive heating cycles.

Equation 7.19 can be rearranged as:

$$0 = -\frac{\Delta H_{fus}}{RT}\left[1 - \frac{1}{T_m}\right] - \frac{1}{RT}\int_{T_m}^{T} \Delta C_p dT + \frac{1}{R}\int_{T_m}^{T} \frac{\Delta C_p}{T} dT - ln\gamma_{drug} - lnx_{drug} \tag{7.21}$$

By substituting the definition of $ln\gamma_{drug}$ from Equation 7.20 into Equation 7.21:

$$\begin{aligned} 0 = -\frac{\Delta H_{fus}}{RT}\left[1 - \frac{1}{T_m}\right] - \frac{1}{RT}\int_{T_m}^{T} \Delta C_p dT + \frac{1}{R}\int_{T_m}^{T} \frac{\Delta C_p}{T} dT - ln\frac{\phi_{drug}}{x_{drug}} + \\ \left(1 - \frac{1}{m}\right)\phi_{poly} + \chi\phi_{poly}^2 - lnx_{drug} \end{aligned} \tag{7.22}$$

Equation 7.22 was solved using Microsoft Excel's *Solver* add-in by finding the value of x_{drug} (molar fraction) that would minimise the value of the equation, for the parameters shown in Table 7.5. The constraint imposed was that: $0.0000001 < x_{drug} < 0.999999$. The results are shown in Figure 7.7 as the weight fraction of paracetamol that is soluble in copovidone at a temperature range between 25°C and 170°C. Yang *et al.* experimentally estimated the solubility of paracetamol in PEO (a different polymer) to be 14% at 80°C and 41% at 140°C [155]. In Figure 7.7 the solubility of paracetamol at 80°C is 9.2% and 37.6% at 140°C. The results are similar in value, and there are reasons for solubility in PEO to be higher at those temperatures, such as the very low glass transition temperature of PEO, -55°C.

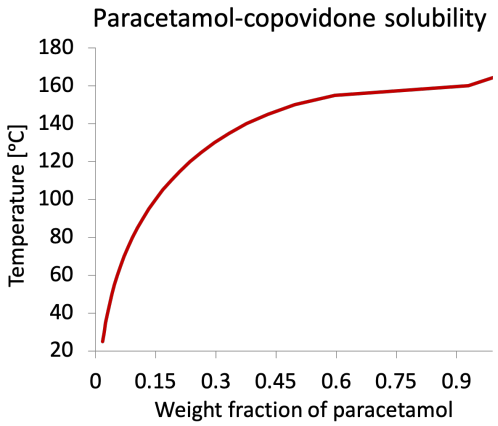

Fig. 7.7 Temperature-composition solubility curve of paracetamol in copovidone.

Table 7.5 Parameter values used to calculate the solubility curve for the paracetamol/copovidone system

Parameter	**Value**	**Description**
ΔH_{fus}	175.5 $[\frac{J}{g}]$	Heat of fusion of paracetamol
R	8.314 $[\frac{J}{K \cdot mol}]$	Gas constant
T	$25 \sim 170\ [°C] = 298 \sim 443\ [K]$	Temperature range for which miscibility was calculated
T_m	169.8 $[°C] = 442.95\ [K]$ [a]	Melting temperature of paracetamol
ΔC_p	0.51 $[\frac{J}{g \cdot °C}]$ [a]	Configurational heat capacity (0-180°C)
ϕ_{drug}	$\phi_{drug} = \frac{mass\ fraction}{\rho_{drug}}$	Volume fraction of paracetamol
x_{drug}	$x_{drug} = \frac{mass\ fraction}{M_w}$	Mole fraction of paracetamol
m	$\frac{\frac{M_{w,poly}}{\rho_{poly}}}{\frac{M_{w,drug}}{\rho_{drug}}}$	Ratio of molecular volumes
χ	$\chi = -0.903 + \frac{607.9}{T}$	Interaction parameter
$M_{w,poly}$	$55,000\ [g/mol]$ [b]	Molecular weight of copovidone
ρ_{poly}	1.15 $[g/cm^3]$ [b]	Density of copovidone
$M_{w,drug}$	151 $[g/mol]$ [c]	Molecular weight of paracetamol
ρ_{drug}	1.35 $[g/cm^3]$ [d]	Density of paracetamol

[a] Value from DSC; [b] Value from [199]; [c] Value from the PubChem Compound Database (CID=1983); [d] Value from [208]

Miscibility curve

The degree of miscibility is important for the formation of physically stable ASDs [40]. The miscibility curve defines the metastable and unstable regions of the phase diagram. Compositions in the metastable regions are relatively stable to small molecular fluctuations [4].

To calculate the miscibility of a drug-polymer system, the equation for the free energy of mixing, ΔG_{mix}, is considered [226]:

$$\Delta G_{mix} = \Delta H_{mix} - T \cdot \Delta S_{mix} \tag{7.23}$$

where ΔH_{mix} and ΔS_{mix} are the enthalpy and entropy of mixing, respectively.

Applying FH lattice theory, Equation 7.23 can be reformulated as [4]:

$$\Delta G_{mix} = RT \left[\phi_{drug} ln \phi_{drug} + \frac{\phi_{poly}}{m} ln \phi_{poly} + \chi \phi_{drug} \phi_{poly} \right] \tag{7.24}$$

where $\left[\phi_{drug} ln \phi_{drug} + \frac{\phi_{poly}}{m} ln \phi_{poly} \right]$ is the entropy term and $[\chi \phi_{drug} \phi_{poly}]$ the enthalpy term. Applying Equation 7.24 to drug-polymer systems enables the evaluation of the relative contributions of entropy and enthalpy to the free energy of mixing. A plot of ΔG_{mix} against ϕ_{drug} would result in a concave (negative free energy of mixing) or convex (positive free energy of mixing) for which $\Delta G_{mix} = 0$ at $\phi_{drug} = 0$ and $\phi_{drug} = 1$.

The maximum drug-polymer miscibility is determined by calculating the inflection point of Equation 7.24 [35]:

$$\begin{aligned} G_{mix} &= RT \left[\phi_{drug} ln \phi_{drug} + \frac{1 - \phi_{drug}}{m} ln(1 - \phi_{drug}) + \chi \phi_{drug} (1 - \phi_{drug}) \right] \\ \frac{\partial G_{mix}}{\partial \phi_{drug}} &= RT \left[ln \phi_{drug} + 1 - \frac{1}{m} (ln(1 - \phi_{drug}) + 1) + \chi - 2\chi \phi_{drug} \right] \\ \frac{\partial^2 G_{mix}}{\partial \phi_{drug}^2} &= RT \left[\frac{1}{\phi_{drug}} + \frac{1}{m(1 - \phi_{drug})} - 2\chi \phi_{drug} \right] = 0 \end{aligned} \tag{7.25}$$

Equation 7.25 was solved using Microsoft Excel's *Solver* add-in by finding the value of ϕ_{drug} (volume fraction) that would zero the value of the equation, for the parameters shown in Table 7.6. The constraint imposed was: $0.02 < \phi_{drug} < 0.95$. The results are shown in Figure 7.8 as the weight fraction of paracetamol that is miscible in copovidone at a temperature range between 25°C and 170°C.

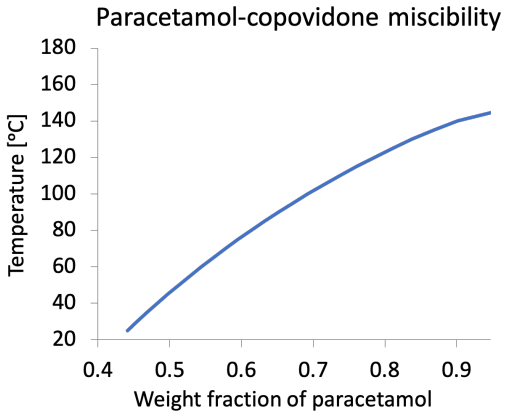

Fig. 7.8 Temperature-composition miscibility curve of paracetamol in copovidone.

Table 7.6 Parameter values used to calculate the miscibility curve for the paracetamol/copovidone system

Parameter	Value	Description
ϕ_{drug}	$\phi_{drug} = \frac{mass\ fraction}{\rho_{drug}}$	Volume fraction of paracetamol
m	$\frac{\frac{M_{w,poly}}{\rho_{poly}}}{\frac{M_{w,drug}}{\rho_{drug}}}$	Ratio of molecular volumes
χ	$\chi = -0.903 + \frac{607.9}{T}$	Paracetamol-copovidone interaction parameter
$M_{w,poly}$	$55,000\ [g/mol]$ [a]	Molecular weight of copovidone
ρ_{poly}	$1.15\ [g/cm^3]$ [a]	Density of copovidone
$M_{w,drug}$	$151\ [g/mol]$ [b]	Molecular weight of paracetamol
ρ_{drug}	$1.35\ [g/cm^3]$ [c]	Density of paracetamol

[a] Value from [199]; [b] Value from the PubChem Compound Databse (CID=1983); [c] Value from [208]

Phase diagram

In the previous sections, the solubility and miscibility curves for the paracetamol/copovidone system were calculated. To complete the characterisation of the system and build a phase diagram, the glass transition temperature of systems at drug loadings between 0% and 95% were measured with DSC. Additionally, the theoretical T_g, as predicted by the Gordon-Taylor equation (refer to chapter 4, section 4.3.4, page 81), was also calculated for comparison.

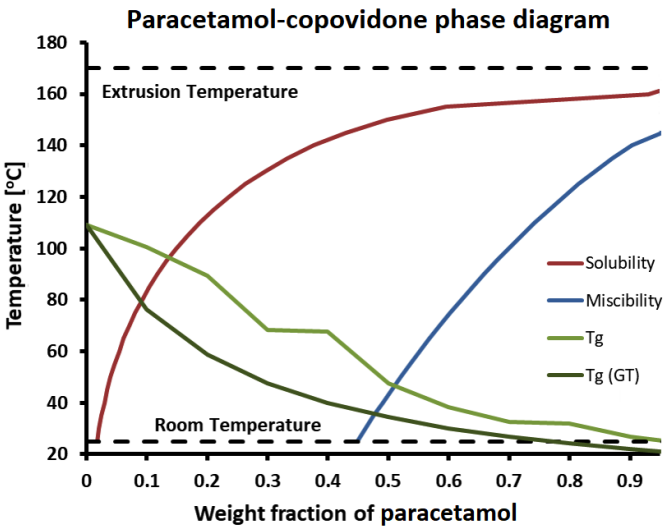

Fig. 7.9 Temperature-composition phase diagram of paracetamol-copovidone systems.

Figure 7.9 shows the phase diagram for paracetamol/copovidone systems in the $25-170°C$ and $0-100\%$ drug loading ranges. It is composed of four curves: solubility (red), miscibility (blue) and glass transition temperature (dark and light green for predicted and measured, respectively).

Firstly, the T_g curve decreases with increasing drug loading because paracetamol is acting as a plasticiser. This effect is caused by the increase in free volume around polymer chains created by the drug molecules, which reduces polymer-polymer interaction and friction [227]. Furthermore, there is a consistent positive deviation throughout the composition range in the measured T_g from the predicted value. This is indicative of strong drug-polymer interactions, which result in poorer chain mobility [32, 31]. T_g depicts the transition from the glassy to the rubbery state and, although the it does not mark a thermodynamic phase transition, it indicates a drastic change in mobility and viscosity. Consequently, it plays an important role in the rate of crystallization and/or phase separation and kinetic stabilisation of ASDs (even at thermodynamically metastable conditions) [37].

Secondly, the miscibility curve, also known as the spinodal curve marks the boundary between the metastable and the unstable formulations. That is because it was calculated from the free energy of mixing, which provides information on the spontaneity of two components mixing, or on the other hand, phase separating. Li *et al.*, however, identified that for a system extruded between the miscibility and solubility curves (metastable region), the lack of thermodynamic forces to achieve complete drug amorphisation could be compensated for by increasing the extrusion screw speed, as this increased the system's entropy [71].

Finally, the solubility (or liquid-solid transition) curve, indicates the temperature-composition region in which an ASD is thermodynamically stable [37]. Bordos *et al.* used THz-Raman spectroscopy to construct an empirical solubility curve of paracetamol/copovidone in the temperature range $110-170°C$ [75]. Experiments were conducted in-line during the extrusion process, at the end of the barrel, before extrudate ejection through the die. For this reason, the lowest temperature studied was 110°C, which is just above copovidone's T_g. The resulting solubility curve is shown in Figure 7.10, where "*Cc*" denotes the critical concentration up to which no crystallinity was found at 110°C (the minimum temperature in this study). Interestingly, Figure 7.10 shows that at 145°C the saturated concentration ranges between 45-60 wt%, this "plateau effect"

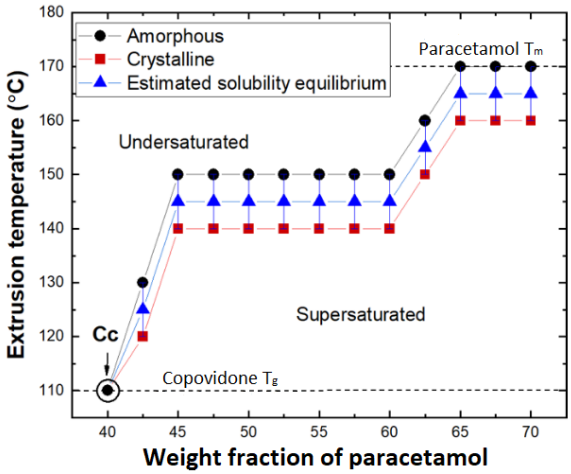

Fig. 7.10 Temperature-composition solubility curve of paracetamol/copovidone systems determined experimentally *via* THz-Raman spectroscopy (modified from [75]).

was hypothesised to be related to temperature-dependent structural changes of copovidone. It has been described that PVP polymers can adopt helical conformation [228], which could unwind to accommodate additional drug molecules.

According to Bordos *et al.* the solubility of paracetamol in copovidone at 140°C is 44 wt%. This value is slightly higher than the one obtained in this chapter (37.6 wt%). Although these values are similar, there are two reasons why the one measured by Bordos *et al.* could be higher than the value calculated here. Firstly, Bordos *et al.* conducted experiments in temperature steps of 10°C, so their solubility estimations are associated with an error of at least ±5°C. Secondly, there could be small residual crystalline particles that fall under the limit of detection or paracetamol-rich amorphous domains that are undetected in the THz-Raman spectra.

7.4.2 Static particle dissolution model

The system of differential equations formed by Equations 7.12 and 7.14 were solved simultaneously using the parameter values shown in Table 7.7. The outcome from the dissolution simulation model is displayed in a plot of the decrease in particle radius [μm] as a function of time [min]. Figure 7.11 summarises the dissolution rate results for a range of values of the diffusion coefficient (D), initial particle radius (R_0) and solubility (S).

Table 7.7 Parameter values used for solving the static particle dissolution model system of differential equations

Parameter	**Value**	**Description**
D	$2 \cdot 10^{-12} \sim 4 \cdot 10^{-12}\ m^2/s$ [a]	Diffusion coefficient of paracetamol
ρ_d	$1300\ kg/m^3$ [b]	Crystalline paracetamol density
S	$350 \sim 500\ kg/m^3$ [c]	Paracetamol solubility concentration
V	$3.7 \cdot 10^{-7}\ m^3$ [d]	Total volume
m_0	$1.3 \cdot 10^{-4}\ kg$ [d]	Initial solid paracetamol mass
R_0	$3 \cdot 10^{-5} \sim 8 \cdot 10^{-5}\ m$ [e]	Initial paracetamol particle radius

[a] Value from experiments in chapter 3, section 3.3.3. [b] Value from [198]. [c] Value from phase diagram in section 7.4.1. [d] Value for paracetamol/copovidone Rheoscope discs, refer to section 7.3.1. [e] This value corresponds to particle sizes (diameters) of $60 - 160\ \mu m$

The parameters chosen for this model correspond to a scenario where the paracetamol particles are suspended in a copovidone melt at 140°C, to be consistent with the results presented in sections 7.4.1 and 7.4.4. Figure 7.11a-c shows the dissolution rate curves for three diffusion coefficients: $2{\cdot}10^{-12}$ m^2/s, $3{\cdot}10^{-12}$ m^2/s and $4{\cdot}10^{-12}$ m^2/s, and in each graph there is a curve that corresponds to one of four initial particle sizes considered: 30 μm, 40 μm, 50 μm and 80 μm. All dissolution curves have the same shape, and there is a positive

correlation between dissolution time and particle radius and a negative correlation with diffusion coefficient. This correlation is stronger for particle size, as a two-fold increase in drug crystal radius results in, roughly, four-fold increase in dissolution time, whereas a two-fold increase in diffusion coefficient leads to a two-fold decrease in dissolution time.

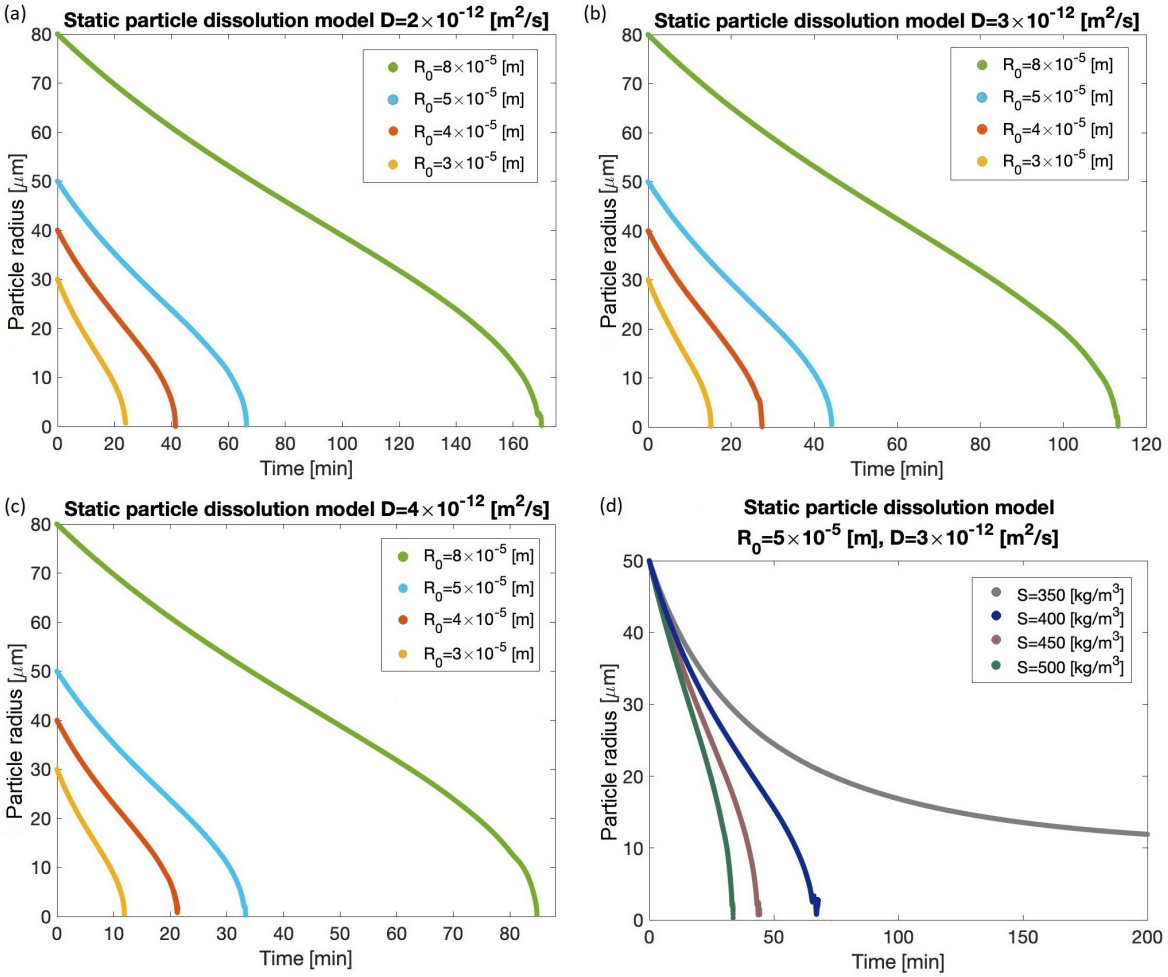

Fig. 7.11 Static particle dissolution model results: decay of particle radius (R) as a function of time. Diffusion coefficients of (a) $2{\cdot}10^{-12}$ m^2/s, (b) $3{\cdot}10^{-12}$ m^2/s and (c) $4{\cdot}10^{-12}$ m^2/s are evaluated for initial particle radii of 30, 40, 50 and 80 μm, and a solubility of 447 kg/m^3. (d) Solubilities of 350, 400, 450 and 500 kg/m^3 for 50 μm initial particle size and $3{\cdot}10^{-12}$ m^2/s diffusion coefficient.

The effect of the solubility value on dissolution time is depicted in Figure 7.11d. Four solubilities were modelled: 350, 400, 450 and 500 kg/m^3 for an initial particle radius of 50 μm and a diffusion coefficient of $3{\cdot}10^{-12}$ m^2/s. The results indicate, as expected, that for lower solubilities, time to dissolution increases. The grey trace ($S = 350\ kg/m^3$) illustrates the case in which the solubility is lower than the total drug loading of the system, in which case complete dissolution will not be achieved.

As will be shown in section 7.4.4, the static dissolution of a paracetamol crystal particle (of approximately 70 μm in radius), although in the same order of magnitude, was observed to be faster than the predicted one. This could be due to several reasons. Firstly, the solubility of paracetamol in copovidone was calculated theoretically (section 7.4.1) and not substantiated experimentally, so the actual value could be higher than the estimated. Among other simplifications in the model, it was assumed that the drug particle is a perfect sphere, but in reality the shape is irregular, leading to a higher exposed surface area for dissolution, which would result in a faster rate. Another explanation would be that, as it has been repeatedly shown in this thesis (chapter 3, section 3.3.3 and chapter 6, section 6.3.3), the diffusion coefficient is strongly dependent on drug loading. Considering the static particle dissolution model schematic presented in Figure 7.1, it follows that the the shells closest to the particle will have a high drug loading (in the inner-most cell, this concentration would be the saturation concentration). Figure 7.11a has shown that the diffusion coefficient makes a large effect on dissolution rate. Diffusivity is likely underestimated in the inner shells, resulting in slower predicted dissolution rates.

7.4.3 Shear flow particle dissolution model

A collaborator from AstraZeneca (Gavin Reynolds, Pharmaceutical Development), who was one of the authors of the publication described in section 7.2.2 regarding the simulations of the dissolution of spherical particles in shear flow [117], attempted to use the parameters measured and calculated in this thesis as inputs to the model used in the article. Table 7.8 summarises the key simulation input parameters for the paracetamol/copovidone system studied in this work.

Table 7.8 Parameter values from paracetamol/copovidone system for dissolution simulation model proposed by Derksen *et al.* (2015)

Parameter	**Value**	**Description**
ϕ_0	0.29	Initial solids volume fraction
Γ	$4 \cdot 10^{-12}\ m^2/s$	Diffusion coefficient of solute
S	447 kg/m^3	Solubility at 140°C
a_0	100 μm	Initial particle radius
$\dot{\gamma}$	1 s^{-1}	Shear rate
Pe_0	2500	Initial Peclet number
Sc	$2.5 \cdot 10^{10}$	Schmidt number
ν	0.1 m^2/s	Liquid kinematic viscosity

To match the experimental set-up of the 30 wt% paracetamol/copovidone disc (13 mm in diameter and 2.8 mm thick) used for the Rheoscope (section 7.3.2), the initial solids volume fraction (ϕ_0) was 0.29. This was calculated from the number of particles in the disc, which was $2.59{\cdot}10^4$ for 100 μm particle radius and 1200 kg/m^3 density; and the total volume of the disc ($3.7{\cdot}10^{-7}$ m^3). The diffusion coefficient was selected from Table 3.2, from the 30% drug loaded system at 150°C as $4{\cdot}10^{-12}$ m^2/s. A solubility of 38 wt% (447 kg/m^3) was calculated from the phase diagram in section 7.4.1 for paracetamol in copovidone at 140°C. Shear rates greater than 1 s^{-1} could not be used in the Rheoscope set-up, as otherwise the images captured were too blurry for analysis. Kinematic viscosity is the dynamic viscosity of a material divided by its density. The kinematic viscosity of copovidone was calculated from the dynamic viscosity plot (Figure 3.8a, section 3.3.4), divided by its density ($1.18{\cdot}10^3$ kg/m^3).

The initial Peclet number for a 1 s^{-1} shearing rate, 100 μm initial particle radius and $4{\cdot}10^{-12}$ m^2/s diffusion coefficient was calculated as 2,500. This is higher than the range considered by Derksen *et al.*: $10 \leq Pe_0 \leq 2000$. The low diffusion coefficient that resulted in the high Peclet number, also greatly increased the simulation time. As the time steps in the simulation where fixed by the shear rate, a very large number of time steps were required to observe the effects in the concentration fields for such small diffusion coefficients. This resulted in numerical noise dominating the solution, since the change in the state of the system between time steps was so small. Similarly as with the Peclet number, the Schmidt number obtained from the parameter values in Table 7.8 is $2.5{\cdot}10^{10}$, which is much higher than the Sc number the model by Derksen was benchmarked for ($Sc = 300$). These could be some of the reasons why the simulations repeatedly failed to run until particle dissolution was achieved.

One way the model could be adapted to cope with very low diffusion coefficients would be to decrease the grid size of the simulation to be able to capture smaller changes in concentration fields. The downside of this is that computational requirements would steeply increase. However, it should be considered whether such a detailed model as the one presented by Derksen *et al.* is over-complicated, knowing that the system is so diffusion-limited.

7.4.4 Dissolution studies under static and shearing conditions

In order to corroborate the predictions from the mathematical models of particle dissolution, experimental analysis on paracetamol/copovidone discs was conducted on the Rheoscope both under static and shearing conditions (refer to section 7.3.1 and 7.3.2 for sample preparation and experimental setup). Imaging was performed under polarised light and high contrast in order to ease analysis. Figure 7.12 shows a field of view from a 30 wt% paracetamol/copovidone disc at room temperature, which was used for calibration of the camera settings. These settings were saved and used for subsequent imaging.

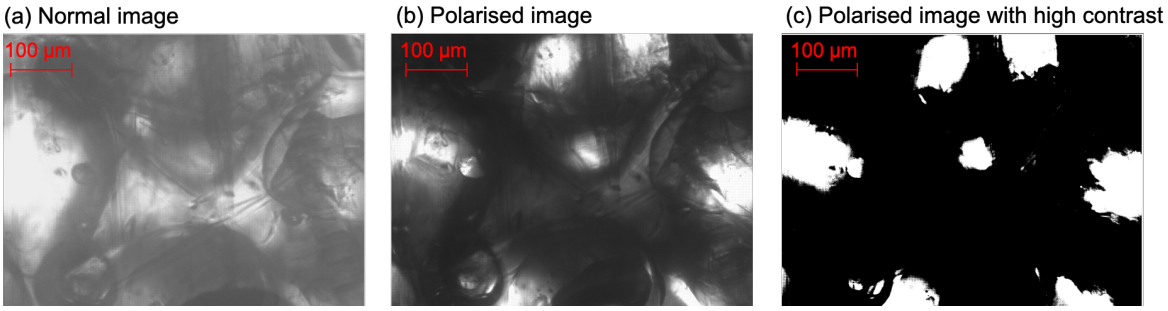

Fig. 7.12 Rheoscope calibration images under (a) normal light, (b) polarised light and (c) polarised light and high contrast.

Figure 7.13a shows a Rheoscope image for an isolated paracetamol crystal at 140°C. It wasn't trivial obtaining a good field of view, as some bubbles would appear due to copovidone melting and obscure the images and often paracetamol particles would move within the plasticised copovidone and disappear from the field of view, making it impossible to follow the dissolution of a single crystal. In this case, however, the single crystal remained within the field of view and it was possible to follow its dissolution in the polymer. The signal intensity of each frame (acquired every 10 s) was measured as the number of white pixels. Then the signal intensity evolution was plotted against time to determine the time elapsed until full dissolution. The initial instability in the image intensity observed in Figure 7.13b between $0 - 500$ s, is due to the crystal moving up and down in the field of view, which made it appear smaller and larger.

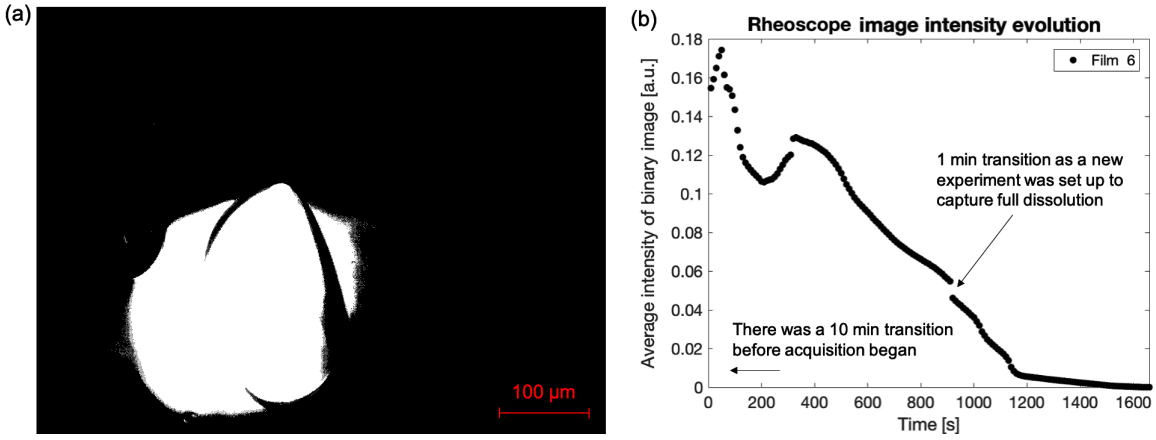

Fig. 7.13 Rheoscope (a) image and (b) image intensity evolution data for the dissolution of a paracetamol crystal under static conditions at 140°C.

The last white pixel was detected in frame 157 out of the 160 acquired. Taking into account that there was a one-minute lapse (between frames 90 and 91) as a new experiment was set up because the crystal had still not dissolved in the 15 min of the first experiment, and that there was about a 10 min initial transition before the image acquisition was started to

allow for temperature stabilisation and choice of a satisfactory field of view (one in which the paracetamol particle remained static), the total time to dissolution was about 37 min. This is of the same order of magnitude, but still significantly shorter than what was predicted by the static particle dissolution model presented above. A few reasons why this could be have already been presented in section 7.4.2. Additionally, it is possible that the micro-environment of the paracetamol particle imaged had a lower concentration of paracetamol than 30 wt%, which would result in faster dissolution due to lower concentration of paracetamol in the bulk solution and thus a higher concentration gradient between the particle's surface and the bulk. Another factor that might enhance dissolution time in the Rheoscope experiments is that molten copovidone tends to bubble and these bubbles would be disrupting the concentration gradient layer and carrying paracetamol away from the dissolving particle. This forced convection mass transport would be much faster than the microscopic self-diffusion.

Over 20 discs were analysed under shearing conditions in the Rheoscope, ranging from $0 - 60$ wt% drug loading under shearing conditions of 0.1 s^{-1} or 1 s^{-1}. The Rheoscope was set to 140°C because higher temperatures resulted in severe leakage of the sample from the Rheoscope plates due to its low viscosity. Viscosity values were measured throughout the experiments and these plots were compared with the image intensity graphs resulting from the analysis of the Rheoscope microscopy images that were acquired every 10 s.

Figure 7.14 shows the viscosity and image intensity plots for 0%, 5%, 20%, 40% and 60% paracetamol/copovidone discs at 0.1 s^{-1} shear. Copovidone-only discs were used as a baseline to compare the other results against. Three trends are observed in the viscosity of copovidone (Figure 7.14a, black trace):

i. There is first an increase in viscosity, which corresponds to the sample spreading out to cover the entire surface of the plates. A higher area for shear results in an increase in the measured viscosity as there is stronger resistance to the plate's motion.

ii. Then viscosity decreases as a result of copovidone chains disentangling and aligning with the direction of shear.

iii. Finally, there is an increase in the viscosity caused by leakage of the sample from between the plates. As copovidone leaks, it covers the edges and outer surface of the plates, imposing higher resistance. The viscosity measured in chapter 3, section 3.3.4, for copovidone at 140°C was $2{\cdot}10^4$ Pa·s, which is similar to that observed in the Rheoscope.

The image analysis of the copovidone disc (most clearly seen in Figure 7.14d, black data points) shows that the number of white pixels is very low, particularly when compared to the data from the higher drug loaded paracetamol/copovidone discs (Figure 7.14c). There is, however, some signal being detected that does not correspond to amorphous polymer, and this is probably caused by sample or instrument contamination with small fibres.

The 5 wt% paracetamol/copovidone disc displays a considerably lower viscosity than for copovidone alone (Figure 7.14a, grey trace). This is a result of the strong plasticisation effect that paracetamol has on copovidone, even at such low drug loadings. Accordingly, Figure 7.14d shows that there is an initial surge in the image intensity data above noise level, meaning that several paracetamol crystals were captured in the field of view. However, this quickly decreases to noise level as paracetamol dissolves in copovidone and is no longer crystalline.

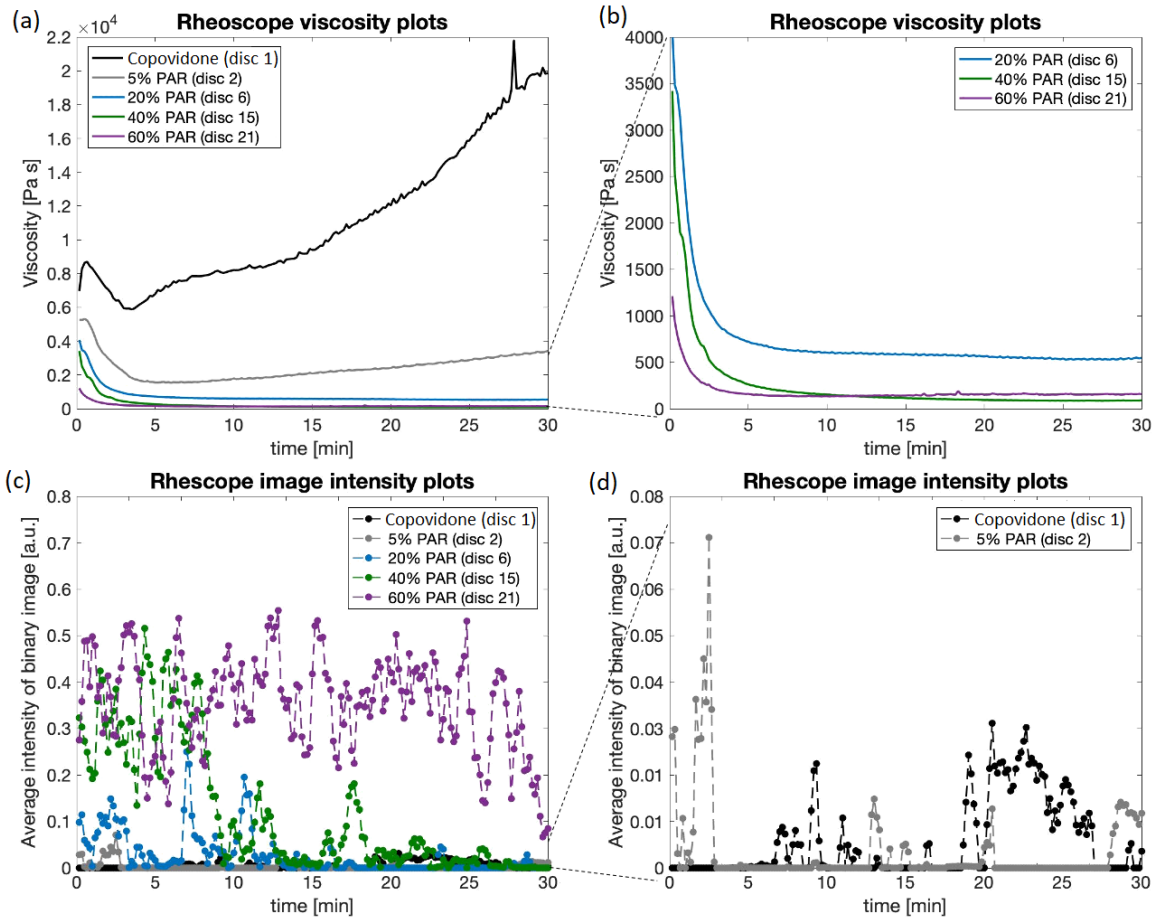

Fig. 7.14 Rheoscope (a), (b) viscosity plot and (c), (d) image intensity evolution data for the dissolution of paracetamol crystals in a 0, 5, 20, 40 and 60 wt% paracetamol/copovidone discs under shearing conditions (0.1 s^{-1}) at 140°C. (b) and (d) show an amplified view of (a) and (c), respectively.

The viscosities of the samples at 20, 40 and 60% drug loading are shown in an amplified plot in Figure 7.14b. The shape of these plots is very similar to that of the 5% paracetamol/copovidone disc, but begin at a lower viscosity value. This is because there is some paracetamol dissolution during the setting up of the experiment (approximately 4 min elapsed on average between the disc being introduced in the Rheoscope and data acquisition

commencing) that has already plasticised copovidone by the time the first data point for viscosity is measured. Also, the rate of viscosity decrease is faster at higher drug loadings during the first few minutes of the experiments. Higher drug loaded samples contain more dispersed paracetamol particles, which plasticise the polymer more efficiently.

The 20 wt% paracetamol/copovidone disc (Figure 7.14b, blue trace) stabilises at a viscosity value considerably lower than the 5 wt% disc, but higher than the 40% and 60% paracetamol content samples. All paracetamol crystals are expected to dissolve during this experiment, since 20% is well below the saturation concentration for paracetamol in copovidone at 140°C (refer to section 7.4.1). This is supported by the image analysis data (Figure 7.14c, blue trace) which captured a few crystalline paracetamol particles during the first 12 min of the experiment, and afterwards the image intensity fell within noise level, indicating that dissolution was complete.

Similarly to the 20% disc, the 40% paracetamol/copovidone disc (Figure 7.14b, green trace) tails off at a viscosity below those samples at lower drug loading due to the increased plasticisation. 40% is just above the solubility limit of paracetamol in copovidone at the experimental temperature, 140°C, (according to the calculation from section 7.4.1). Image analysis shows a large amount of paracetamol crystals being captured in the first 10 min. This decreased until after 20 min (from the start of the experiment), when image intensity dropped and only very small particles were detected, which reveals that almost all paracetamol had solubilised.

Lastly, the 60 wt% paracetamol/copovidone sample followed a similar behaviour as the 20% and 40% ones. The key difference is that this concentration was well above the solubility limit. Consequently, although some decrease in the average image intensity was observed (Figure 7.14c, purple trace), by the end of the experiment, there was clear evidence of paracetamol crystals remaining in the sample. For the viscosity plot, it meant that the starting point was lower and the decay was faster than at the lower paracetamol concentrations (Figure 7.14b, purple trace). However, the viscosity stabilised at a higher value than for the 40 wt% paracetamol/copovidone disc. This is in agreement with the image intensity results and is caused by the undissolved solid paracetamol crystals increasing the viscosity of the sample. Aho *et al.* made the same observation: paracetamol plasticised copovidone up to the saturation concentration, after which the remaining solid fraction resulted in an increase in viscosity expressed by the Krieger-Dougherty equation - undissolved drug acts as an insoluble filler [174, 72].

It should be taken into consideration that the melting of paracetamol would also result in the reduction of crystals observed in Rheoscope images as well as a decrease in the viscosity. However, Figure 7.3 shows that the depression in the melting point experienced by paracetamol when in contact with copovidone is not below the experimental temperature (140°C) in the Rheoscope experiments. The melting point for a 20 wt% paracetamol/copovidone mixture is 158°C, for 40 wt% it is 160°C, and for 60 wt% it is 167°C.

No significant differences were observed when the samples were sheared at 1 s^{-1}, which is consistent with the conclusions drawn by Derksen *et al.* that increasing shear rate had no significant effect in reducing dissolution time [117]. It should be noted, however, that not enough experiments were conducted to obtain an accurate dissolution plot by the averaging of individual experiments.

Although the Rheoscope was highly valuable in order to visualise the dissolution of crystal particles, providing an insight that is difficult to acquire through another technique, one of the main disadvantages is that the imaging field of view is very small compared to the sample size. This results in uneven sampling and noisy data, which makes results difficult to reproduce.

TGA

TGA testing was performed on paracetamol and paracetamol/copovidone physical mixtures to ensure there were no signs of sample degradation at the temperatures and time-scales relevant for the Rheoscope experiments. Medeiros *et al.* conducted dynamic TGA on paracetamol and identified two degradation stages, the first with an onset at 188°C and the second one at 325°C [229]. The degradation temperature of copovidone reported by the literature is 270°C [152].

The thermal analysis performed for this thesis considers temperatures up to 170°C. Figure 7.15a shows the TGA plot of paracetamol that was held isothermally at 150°C for 3 h, at 160°C for 3 h and at 170°C for 6h. The mass of paracetamol decreased at an increasing but constant rate (k) for the three temperatures considered, down to approximately 10% of the original sample mass. These rates were $k_{150°C} = -0.0006\ wt\%/s$, $k_{160°C} = -0.0013\ wt\%/s$ and $k_{170°C} = -0.0031\ wt\%/s$ (all with a goodness-of-fit R^2 value greater than 0.998). The fact that the decrease in mass was gradual, instead of rapid, indicates that it is not due to degradation. Degradation of paracetamol was observed as a decrease from 100% to 3% weight in under 10 minutes in TGA experiments [230]. An explanation was found in an article by Leyk *et al.*, that visualized the sublimation of paracetamol with hot-stage microscopy at 150°C [220]. It should be noted that these sublimation rates would be significantly lower in NMR experiments since the sample size was large (∼100 mg) and only a small surface (5 mm diameter tube) was available for sublimation, unlike in the large surface-to-volume ratio available in open TGA pans.

A 50 wt% paracetamol/copovidone physical mix was subjected to a very similar thermal cycle (Figure 7.15b) and the resulting thermogram exhibited characteristics analogous to that of paracetamol. In the same way, mass loss constant rates were obtained: $k_{140°C} = -0.0002\ wt\%/s$, $k_{150°C} = -0.0005\ wt\%/s$, $k_{160°C} = -0.0008\ wt\%/s$ and $k_{170°C} = -0.0010\ wt\%/s$ (all with a R^2 value greater than 0.996), but this time the rate constants and the extent of the mass loss were not as large. This is because paracetamol is subliming, but

copovidone, which accounts for 50% of the sample mass, is not. Furthermore, sublimation would be hindered by paracetamol/copovidone interactions, implied by the positive shifts in T_g compared to the predicted values observed in DSC experiments (Figure 7.9 section 7.4.1).

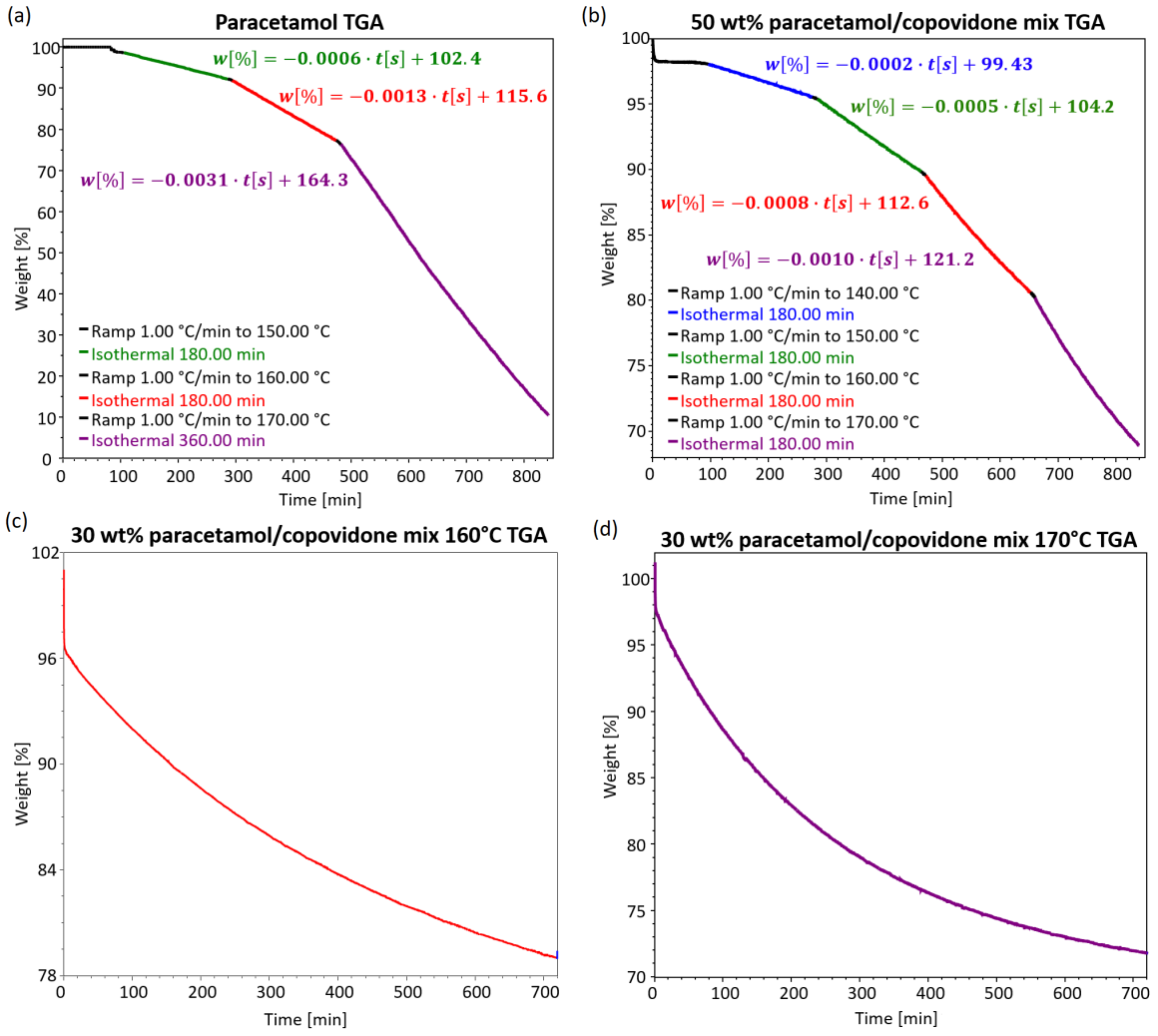

Fig. 7.15 High temperature characterisation of paracetamol using TGA on (a) a paracetamol sample held isothermally at 150°C and 160°C for 180 min and at 170°C for 360 min; (b) a 50 wt% physical mix held isothermally at 140°C, 150°C, 160°C and 170°C for 180 min; and a 30 wt% physical mix held isothermally at c) 160°C for 720 min and (d) 170°C for 720 min.

Figure 7.15c and d are isothermal TGA plots of 30 wt% paracetamol/copovidone physical mixtures held for 12 h at 160°C and 170°C, respectively. At such long experimental times, the mass loss gradient was no longer constant. This is because towards the end of the experiment, there is almost no paracetamol left, as most has sublimed and the left over paracetamol molecules are the ones attached strongest to copovidone. The fast mass decrease of about 4% at the onset of both experiments is due to the moisture in copovidone evaporating, which is why it is also observable in Figure 7.15b, but not in Figure 7.15a. The key findings are

that there is no indication of degradation in any of the samples even when subjected for 12 h at 170°C; and that no significant loss of paracetamol is expected under the test conditions (due to the relatively large sample size and small exposed surface areas).

7.5 Conclusion

This chapter has explored different methods and models to predict drug/polymer behaviour relevant to the formation of ASDs. In the first section, drug solubility and miscibility was calculated using Flory-Huggins lattice theory, following the melting point depression approach and solubility parameters to determine the interaction parameter χ. As a result, a temperature-composition phase diagram was constructed with three curves: solubility, miscibility and T_g, outlining the boundaries of the stable, metastable and unstable regions of drug/polymer composition as a function of temperature, respectively. It should be noted that this simple model does not account for all the complexities of a system. Paudel *et al.* noticed that that the FH thermodynamic model does not take into account the effect of polymer chain length on interaction and miscibility and that the solid solubility of drug in polymer is affected by parameters other than temperature, such as moisture content [231]. Nevertheless, the results from this chapter were in agreement with an experimentally obtained solubility curve of paracetamol in copovidone. Therefore phase diagrams are a fast and easy method to better understand drug/polymer stable and metastable compositions and they can be employed to make informed hypotheses of successful ASD systems and processing temperatures.

Additionally, a simple model was presented for the simulation of the dissolution of a solid drug particle in a polymer melt in a static medium. The parameters obtained in this and previous chapters were used as inputs to the model and a number of simulations were ran at varying, diffusion coefficients, initial drug particle radius and solubility. As expected, a positive correlation was observed between time to complete dissolution and particle radius; and there was an inverse correlation with diffusion coefficient and solubility. More importantly, the results were in the same order of magnitude as the experimental dissolution studies. The predicted time to dissolution was longer than the empirical one and several reasons were presented as to why this might be: (i) inaccuracy of the calculated solubility value; (ii) irregular shape of the real drug particle rather than spherical, resulting in larger surface area available for dissolution; and (iii) concentration dependence of the diffusion coefficient.

Innovative experimental dissolution studies, both under static and shearing conditions were conducted on a rheometer with an integrated microscopy module that permitted the visualisation of particles as they underwent dissolution. To facilitate analysis, images were acquired under polarised light and high contrast, and viscosity measurements were recorded simultaneously. Samples at drug loadings between $0 - 60$ wt% were examined under shearing stresses at 140°C. Interesting observations included that: (i) the initial sample viscosity

dropped as paracetamol dissolved in and plasticised copovidone; and (ii) the steady state viscosity value decreased with increasing paracetamol content for the 0, 5 20 and 40% drug loadings, but slightly increased at 60% as undissolved particles acted as a filler. Reassuringly, these findings correlated with the observations from image analysis plots. Additionally, no significant differences were observed for examples conducted at 0.1 s^{-1} and 1 s^{-1}, consistent with findings from [117].

Chapter 8

Summary of conclusions and proposed future work

The conclusions drawn from the experimental and numerical work performed for this thesis are presented in a chapter by chapter basis. This section will summarise and discuss those conclusions and explore the scope for future work.

Chapter 3 reported the first direct, non-invasive measurements of API diffusion in paracetamol/copovidone polymer melts at temperatures relevant to HME processes (150-170°C). The diffusivity results for hot melt extruded paracetamol/copovidone samples indicate, for a fixed temperature, that the diffusion of paracetamol is greatly influenced by the copovidone polymer and that increasing the amount of drug up to 30 wt% caused only a minor increase in drug diffusivity due to increased plasticisation of the polymer by the API. However, a sudden increase in the drug diffusivity was observed when the concentration of API in polymer approached the solubility limit (*c.a.* 40 wt%) indicating the presence of small drug-rich, phase-separated domains exhibiting faster diffusion coefficients. The novelty of measuring the diffusion coefficients of drug molecules in polymer melts in the absence of a liquid solvent is a critical advancement in the understanding of HME systems. The diffusion coefficient is a molecular parameter that underpins highly relevant processes such as mass transport and dissolution. This chapter explored the diffusivity of paracetamol, which is a very small molecule. It would be of interest to reproduce these experiments with more realistic and complex API/polymer systems. In this case, there are two possible issues that should be considered:

(i) Larger molecules will possibly exhibit lower diffusion coefficients than the ones measured in this work. However, the diffusivities measured were close to the limit of detection for the equipment used (capable of producing 1,200 G/cm magnetic field gradient). Therefore, stronger gradient sets should be in place for the characterisation of larger molecules.

(ii) More sophisticated drugs and polymers could result in ambiguous NMR spectra, where there are no peaks that can be unequivocally assigned to the drug and the spectrum is too complex to deconvolute. In this case, it might be useful to consider the use of multinuclear NMR. Fluorine, for example, is a nucleus common in drug molecules, but not in polymers.

Chapter 3 also examined the relationship between diffusion coefficient and viscosity. It was shown that the Stokes-Einstein model was not applicable to the variable (high) temperature PFG-NMR diffusivity data because of the smaller size of the solute (paracetamol molecule) than the solvent (copovidone polymer chain) and because of the large solute volume fraction and drug-polymer interactions, which hinder Brownian diffusion. Alternatively, good correlation was found with the Arrhenius model. The activation energy (and hence barrier to hop diffusion) extracted from the temperature dependence of the diffusion data can be interpreted as the energy needed to overcome drug-drug and drug-polymer interactions to allow diffusion. Future steps would investigate whether a straightforward measurement of the diffusion coefficient at a range of temperatures could be exploited through the Arrhenius model and become a novel approach to probe the strength of drug-polymer interactions at high temperature.

In **Chapter 4**, CP-MAS ^{13}C spectra of paracetamol/copovidone physical mixtures and extrudates were analysed by looking at two characteristics:

(i) The line-width of the paracetamol peaks were indicative of whether it was in a crystalline (sharp resonances) or amorphous (broad resonances) state. All HME formulations (20, 30 and 40 wt% drug loading) revealed the presence of amorphous paracetamol.

(ii) Changes in the chemical shift of peaks in the extrudate sample when compared to the physical mixture provided an insight into the intermolecular associations between the drug and the polymer promoted by the HME process. In this case, and as was observed in Chapter 5 as well as in the literature, the carbonyl in the VP monomer of copovidone was identified as having engaged in a hydrogen bond with the phenol in paracetamol.

The presence of drug-polymer interactions was also corroborated by DSC experiments, as the predicted T_g (by the Gordon-Taylor equation) was below the experimentally obtained values. The rationale behind this is that drug molecules attached to the polymer chains increase the effective molecular weight and volume and thus hinder mobility. The existence of these interactions further supports the findings in chapter 3 regarding the invalidity of the Stokes-Einstein diffusion prediction applied to the paracetamol/copovidone system.

^{1}H relaxometry data obtained *via* ^{13}C revealed no phase separation in any of the extrudates analysed, which, together with the evidence of amorphisation discussed in the previous paragraph, confirms that a successful ASD was formed upon processing *via* HME. This was

not the case, however, for the physical mixture that was exposed to 170°C (same as the HME processing temperature). This sample exhibited both some degree of phase separation and the presence of crystalline as well as amorphous paracetamol. This is indicative of recrystallisation, likely as there was no active mixing to promote drug dispersion and enough of drug-polymer interactions to stabilise the formulation. It is not surprising that active mixing is required to yield a homogeneous preparation, since the passive mass transport rate (diffusion coefficient) of paracetamol in copovidone melts measured in Chapter 3 is very slow. This conclusion is of particular importance because it highlights the requirement for HME processing to obtain ASDs, as just processing at high temperatures is not enough to produce adequate pharmaceutical products.

The work presented in this chapter could have been extended by characterising extrudates containing drug loadings higher than 40 wt% and at a range of processing temperatures. This could have provided further understanding on the solubility of paracetamol in copovidone at different temperatures as well as the stability of the formulation once it was cooled and stored at room temperature. It would serve as a benchmark for the solubility and miscibility predictions and the phase diagram discussed in Chapter 7.

Chapter 5 examined intermolecular associations in paracetamol/copovidone HME formulations employing a range of solid-state and molten-state 2D NMR techniques. Drug-polymer interactions are of interest because they have been determined to play an important role in the physical stabilisation of ASD products by preventing phase separation, recrystallisation and enhancing dissolution rate as well as solubility. ^{13}C-^{1}H HETCOR (heteronuclear correlation) solid-state experiments were performed in the UK 850 MHz Facility (University of Warwick, Coventry). Using the 850 MHz magnet made it possible to obtain enough resolution in the ^{1}H spectrum to identify three proton environments for paracetamol and two for copovidone. In the widely available 400 MHz magnets, only one proton resonance is resolved for either of the species. Results from the HETCOR acquisitions at a range of contact times revealed unambiguous correlations between paracetamol's aromatic ring protons and copovidone's aliphatic chain carbons. In agreement with the literature, these were assigned to Van der Waals interactions. Furthermore the increasing signal intensity and number of cross-peaks at longer contact times were evidence of the presence of intermolecular through-space interactions between a high proportion of paracetamol and copovidone molecules.

^{1}H-^{1}H solid-state experiments (NOESY and MQC BABA), were not only performed at high field (850 MHz), but also at fast spinning rates (60 kHz), which resulted in further enhancement in the ^{1}H resolution such that five paracetamol peaks were resolvable. These advanced experimental conditions allowed the assignment of cross-peaks to specific paracetamol protons. In agreement with HETCOR results, paracetamol aromatic and copovidone aliphatic chain proton coupling *via* Van der Waals interactions were identified. Additionally paracetamol's hydroxyl proton displayed a cross-peak with copovidone aliphatic groups. These were most

likely a result of H-bonding, but lack of resolution in copovidone's ^{1}H spectrum, prevented from making unambiguous assignments.

In this chapter molten-state 2D NMR ^{1}H-^{1}H COSY experiments were, to the extent of my knowledge, performed for the first time. The main advantage of molten-state NMR is that the spectral resolution is significantly increased due to averaging out of anisotropic contributions. In this case, the ^{1}H spectrum of copovidone was enhanced from two distinct resonances in the high-field fast-MAS solid-state to five resolvable peaks in the molten-state. Results from the COSY experiments corroborated the observations from solid-state HETCOR, NOESY and MQC BABA in regards to the presence of Van der Waals interaction and H-bonds between paracetamol and copovidone. However, in the molten-state it was possible to assign the H-bond to paracetamol's hydroxyl proton and copovidone's PVP monomer carbonyl oxygen. To ensure that the cross-peaks in the COSY spectra were in fact so, and not noise or artifacts, several spin-echo delays were introduced. The longer the delay, the more attenuated the cross-peaks identified as paracetamol-copovidone interactions appeared. The explanation for this is that rigid bonds (reduced mobility) lower the T_2 relaxation constant of the protons involved, such that their signal is lost at longer spin-echo delays.

Paracetamol/copovidone has been a good model system with which to develop the NMR techniques presented in this chapter. However, to validate them further, it would be of interest to apply them to more industrially relevant compounds, such as the nifedipine/copovidone system used in Chapter 6.

In **Chapter 6**, alternative formulations to paracetamol/copovidone were characterised employing the analytical techniques presented in Chapters 3 and 4. These alternative formulations included two different polymers (PVP and PVA), a more industrially relevant drug for HME (nifedipine) and ten samples from a paracetamol/copovidone design of experiments run to study the effect of processing parameters (temperature, screw speed, drug loading and copovidone commercial brand).

Copovidone, PVP and PVA were compared and the results indicated that:

(i) Due to PVA's low T_g, paracetamol/PVA formulations would be easy to extrude and it would be likely that processing below paracetamol's melting point should be viable, reducing risk of thermal degradation and lowering costs. However a very low T_g, that is barely above room temperature, is not an advantageous characteristic, since above the glass transition molecular mobility significantly increases. This, combined with the lack of H-bonding capabilities of PVA, greatly reduces physical stabilisation and prevention of drug recrystallisation.

(ii) On the other hand, PVP has a high T_g, but strong H-bonding capability. PVP would perform better in physically stabilising the amorphous drug, but it is also highly

hygroscopic. Increased moisture content is associated with increased likelihood of phase separation and recrystallisation.

(iii) Copovidone, which is made up of a mixture of the monomers that constitute PVA and PVP, presents a good compromise on polymer characteristics in terms of T_g, H-bonding capabilities, hygroscopicity, physical stability and drug solubility.

Nifedipine is a more industrially relevant compound for HME because it suffers from low water solubility. It is also a larger and more complex molecule than paracetamol. The NMR and complementary techniques developed in Chapters 3 and 4 were used on nifedipine/copovidone systems. Due to its larger molecular volume and higher molecular weight than paracetamol, the diffusion coefficients measured in the polymer melt were almost an order of magnitude slower. The slow diffusion restricted the quality of the measurements, particularly at lower drug loadings. Future work should consider using stronger magnetic field gradients to determine the diffusivity at a range of drug loadings and temperatures, as well as for alternative drug candidates for HME processing. Solid-state ^{13}C spectroscopy of nifedipine/copovidone extrudates determined that nifedipine was amorphous in 20 wt% and 40 wt% samples, however relaxometry experiments revealed a small degree of phase separation. This was probably due to weaker drug-polymer interactions and perhaps lack of miscibility. For scenarios like this one, the modelling and predictions presented in Chapter 7 are valuable to assess whether the API and polymer combination selected for processing are likely to produce ASDs.

In **Chapter 6**, paracetamol/copovidone extruded samples from a design of experiments (DOE) run were studied. They were prepared at different conditions to analyse the effect of process parameters on several formulation characteristics. The variables considered included polymer commercial brand, processing temperature and screw speed, and drug loading. Key findings were:

(i) In diffusometry experiments, only the drug loading variable resulted in a perceptible difference in the measured diffusion coefficient of paracetamol. The 20 wt% formulation exhibited slower diffusivities than the 30 wt% ones, consistent with the observations from chapter 3.

(ii) ^{13}C spectroscopy and DSC revealed that paracetamol was in an amorphous state in all samples. Interestingly, this included the 20 wt% and 30 wt% samples processed at 140°C, well below the melting point.

(iii) Similarly as in (ii), solid-state ^{1}H relaxometry indicated that there was no phase separation in any of the samples.

These results are relevant because in chapter 3, it was suggested that extrusion at temperatures lower than the melting point would be advantageous with regards to the

viscosity of the system. However, the question stood whether lower temperatures would yield amorphous and homogeneous products. The experiments presented in chapter 6 show that at processing temperatures as low as 140°C, satisfactory extrudates were obtained for 20 and 30% drug loaded systems. Future work could be conducted to expand on the DOE study, particularly to produce extruded samples at higher drug loadings and lower temperatures, and use solid-state NMR spectroscopy and relaxometry to determine where the temperature-composition limits of the system are and validate the phase diagram presented in chapter 7. The DOE study could also be extended to include a more relevant drug candidate for HME processing. The key advantages of processing at lower temperatures are the lower heating costs and the reduced risk of thermal degradation.

In **Chapter 7** paracetamol solubility and miscibility in copovidone were calculated using the Flory-Huggins lattice theory. A phase diagram was presented, which outlined the boundaries of the stable, metastable and unstable temperature-composition formulations. Although calculations for the phase diagram represent a simplified view of the system, it is a valuable resource to determine whether a specific system is likely to produce desirable extruded products. The work presented in this section could have been extended to experimentally validate the phase diagram for the paracetamol/copovidone system. This would have been done by extruding at different temperature and composition combinations, particularly those close to the curves in the phase diagram. Scope for future work could also involve the construction of a phase diagram for a more relevant HME system, such as nifedipine/copovidone, as was presented in Chapter 6.

Chapter 7 also explored mathematical models for prediction and simulation of drug/polymer system behaviour relevant to the formation of ASDs. A simple static dissolution model for a spherical drug particle in a polymer melt was presented. The model was populated with the measured and calculated values obtained in this and previous chapters for the diffusion coefficient and solubility. Interestingly, the results were of the same order of magnitude as the dissolution studies performed on the Rheoscope. The predicted time to dissolution was longer than the empirical one and this may be due to:

(i) Inaccuracies in the calculated solubility value of paracetamol in copovidone.

(ii) The irregular shape of the paracetamol crystal rather than the spherical modelled one, resulting in a larger available area for dissolution.

(iii) The solute concentration dependence of the diffusion coefficient.

Furthermore, the experiments conducted on the Rheoscope to visualise dissolution and measure viscosity revealed that:

(i) The initial drop in the viscosity of the sample correlated with paracetamol crystals dissolving in and plasticising copovidone

(ii) The steady state viscosity value decreased with paracetamol content for the 0−40 wt% drug loadings, but slightly increased for the 60 wt% sample, as undissolved particles acted as a filler. This agreed with the phase diagram presented in this chapter in that 60 wt% is above the solubility limit for the paracetamol/copovidone system at 140°C.

(iii) No significant differences were observed for the two considered shear rates: 0.1 s^{-1} and 1 s^{-1}.

This work did not consider shear rates larger than 1 s^{-1}, because the images captured were too blurry for analysis. Future work could study whether higher shear rates have an effect on the dissolution rate employing strobe illumination to yield sharp images. Strobe illumination consists on pulsing the light source for a short period of time, which results in the "freezing" of a fast moving object for image capturing purposes.

Several attempts were made at running the simulations proposed by Derksen, *et al.* using the parameters calculated in this thesis [117]. Unfortunately they failed to complete and there were several reasons for this:

(i) The Peclet and Schmidt numbers that resulted from the parameter values proposed in this thesis fell outside the benchmarked range in Derksen's work.

(ii) The low diffusion coefficient meant that the change in the state of the system between time steps was so small that numerical noise was prominent, which caused the simulations to fail.

(iii) The system appears to be highly diffusion-limited, which questions whether applying such a detailed model as the one presented by Derksen is reasonable.

A more recent model proposed by Schittny *et al.* is based on two large-scale variables: time to dissolution and the average residence time of the material in the extruder [118]. Schittny *et al.* took into account specific process parameters for HME such as extruder sections (powder transport, melt transport and pressurised flow) and screw geometry. Schittny's model assumes that drug dissolution is mainly diffusion-controlled due to the low diffusion coefficients and high viscosity of the polymer melt; however, in their publication, diffusion coefficients were estimated by molecular dynamics, which is a complex and computationally intensive method. There is scope to extend the simulation work presented in chapter 7 of this thesis to consider a model similar to Schittny's, which is less detailed than the one discussed in chapter 7 (by Derksen), together with the experimentally obtained values for diffusion coefficient and time to dissolution as an approach to simulate the hot-melt extrusion process.

References

[1] Li Di, Edward H Kerns, and Guy T Carter. Drug-like property concepts in pharmaceutical design. *Current Pharmaceutical Design*, 15(19):2184–94, 2009.

[2] Christian Leuner and Jennifer Dressman. Improving drug solubility for oral delivery using solid dispersions. *European Journal of Pharmaceutics and Biopharmaceutics*, 50(1):47–60, 2000.

[3] Ketan T. Savjani, Anuradha K. Gajjar, and Jignasa K. Savjani. Drug solubility: Importance and enhancement techniques. *ISRN Pharmaceutics*, 2012:1–10, 2012.

[4] H. D. Williams, N. L. Trevaskis, S. A. Charman, R. M. Shanker, W. N. Charman, C. W. Pouton, and C. J. H. Porter. Strategies to address low drug solubility in discovery and development. *Pharmacological Reviews*, 65(1):315–499, 2013.

[5] Abu T.M. Serajuddin. Solid dispersion of poorly water-soluble drugs: Early promises, subsequent problems, and recent breakthroughs. *Journal of Pharmaceutical Sciences*, 88(10):1058–1066, oct 1999.

[6] Teófilo Vasconcelos, Bruno Sarmento, and Paulo Costa. Solid dispersions as strategy to improve oral bioavailability of poor water soluble drugs. *Drug Discovery Today*, 12:1068–1075, dec 2007.

[7] Feng Qian, Jun Huang, and Munir A. Hussain. Drug–polymer solubility and miscibility: Stability consideration and practical challenges in amorphous solid dispersion development. *Journal of Pharmaceutical Sciences*, 99(7):2941–2947, jul 2010.

[8] Duncan Q.M M Craig. The mechanisms of drug release from solid dispersions in water-soluble polymers. *International Journal of Pharmaceutics*, 231(2):131–144, 2002.

[9] S.B. Murdande, M.J. Pikal, R.M. Shanker, and R.H. Bogner. Solubility advantage of amorphous pharmaceuticals: I. A thermodynamic analysis. *Journal of Pharmaceutical Sciences*, 99(3):1254–1264, 2010.

[10] Gordon L. Amidon, Hans Lennernäs, Vinod P. Shah, and John R. Crison. A theoretical basis for a biopharmaceutic drug classification: The correlation of in vitro drug product dissolution and in vivo bioavailability. *Pharmaceutical Research: An Official Journal of the American Association of Pharmaceutical Scientists*, 12(3):413–420, 1995.

[11] Mark G Papich and Marilyn N Martinez. Applying biopharmaceutical classification system (BCS) criteria to predict oral absorption of drugs in dogs: Challenges and pitfalls. *Americal Association of Pharmaceutical Scientists*, 17(4):948–964, 2015.

[12] Council of Europe. European pharmacopoeia - Dissolution test for solid dosage forms. In *European Pharmacopoeia*, chapter 2.9.3, pages 228–230. EDQM, 5th edition, 2005.

[13] Keiji Sekiguchi and Noboru Obi. Studies on absorption of eutectic mixture. I. A comparison of the behavior of eutectic mixture of sulfathiazole and that of ordinary sulfathiazole in man. *Chemical Pharmaceutical Bulletin*, 9:866–872, 1961.

[14] Win Loung Chiou and Sidney Riegelman. Preparation and dissolution characteristics of several fast-release solid dispersions of Griseofulvin. *Journal of Pharmaceutical Sciences*, 58(12):1505–1510, dec 1969.

[15] Eman A. Ashour, Soumyajit Majumdar, Abdulla Alsheteli, Sultan Alshehri, Bader Alsulays, Xin Feng, Andreas Gryczke, Karl Kolter, Nigel Langley, and Michael A. Repka. Hot melt extrusion as an approach to improve solubility, permeability and oral absorption of a psychoactive natural product, piperine. *Journal of Pharmacy and Pharmacology*, 68:989–998, 2016.

[16] Nicole Wyttenbach and Martin Kuentz. Glass-forming ability of compounds in marketed amorphous drug products. *European Journal of Pharmaceutics and Biopharmaceutics*, 112:204–208, 2017.

[17] Arthur A. Noyes and Willis R Whitney. The rate of solution of solid substances in their own solutions. *Journal of the American Chemical Society*, 19(12):930–934, 1897.

[18] Aristides Dokoumetzidis and Panos Macheras. A century of dissolution research: From Noyes and Whitney to the Biopharmaceutics Classification System. *International Journal of Pharmaceutics*, 321(1-2):1–11, 2006.

[19] Boris Shekunov and Eda Ross Montgomery. Theoretical analysis of drug dissolution: I. Solubility and intrinsic dissolution rate. *Journal of Pharmaceutical Sciences*, 105(9):2685–2697, 2016.

[20] VG Levich. Physicochemical hydrodynamics. *Prentice-Hall*, (Englewood Cliffs, NY), 1962.

[21] Hemlata Patil, Roshan V. Tiwari, and Michael A. Repka. Hot-melt extrusion: From theory to application in pharmaceutical formulation. *AAPS PharmSciTech*, 17(1):20–42, 2016.

[22] Abhishek Singh and Guy Van den Mooter. Spray drying formulation of amorphous solid dispersions. *Advanced Drug Delivery Reviews*, 100:27–50, 2015.

[23] Bhavesh B. Patel, Jayvadan K. Patel, Subhashis Chakraborty, and Dali Shukla. Revealing facts behind spray dried solid dispersion technology used for solubility enhancement. *Saudi Pharmaceutical Journal*, 23(4):352–365, 2015.

[24] Catherine Potter, Yiwei Tian, Gavin Walker, Colin McCoy, Peter Hornsby, Conor Donnelly, David S. Jones, and Gavin P. Andrews. Novel supercritical carbon dioxide impregnation technique for the production of amorphous solid drug dispersions: A comparison to hot melt extrusion. *Molecular Pharmaceutics*, 12(5):1377–1390, 2015.

[25] Osama Mahmah, Rami Tabbakh, Adrian Kelly, and Anant Paradkar. A comparative study of the effect of spray drying and hot-melt extrusion on the properties of amorphous solid dispersions containing felodipine. *Journal of Pharmacy and Pharmacology*, 66(2):275–284, 2014.

[26] Michal Beneš, Tomáš Pekárek, Josef Beránek, Jaroslav Havlíček, Lukáš Krejčík, Michal Šimek, Marcela Tkadlecová, and Pavel Doležal. Methods for the preparation of amorphous solid dispersions - A comparative study. *Journal of Drug Delivery Science and Technology*, 38:125–134, 2017.

[27] Sanjay Verma and Varma S. Rudraraju. A systematic approach to design and prepare solid dispersions of poorly water-soluble drug. *AAPS PharmSciTech*, 15(3):641–657, 2014.

[28] Shrawan Baghel, Helen Cathcart, and Niall J. O'Reilly. Polymeric amorphous solid dispersions: A review of amorphization, cystallization, stabilization, solid-state characterization, and aqueous solubilization of biopharmaceutical classification system Class II drugs. *Journal of Pharmaceutical Sciences*, 105(9):2527–2544, 2016.

[29] Manfred Gordon and James S. Taylor. Ideal copolymers and the second-order transitions of synthetic rubbers. i. Non-crystalline copolymers. *Journal of Applied Chemistry*, 2(9):493–500, may 1952.

[30] Robert Simha and R. F. Boyer. On a general relation involving the glass temperature and coefficients of expansion of polymers. *The Journal of Chemical Physics*, 37(5):1003–1007, 1962.

[31] Ioannis M. Kalogeras. A novel approach for analyzing glass-transition temperature vs. composition patterns: Application to pharmaceutical compound + polymer systems. *European Journal of Pharmaceutical Sciences*, 42(5):470–483, 2011.

[32] Yongcheng Li, Huishi Pang, Zhefei Guo, Ling Lin, Yixuan Dong, Ge Li, Ming Lu, and Chuangbin Wu. Interactions between drugs and polymers influencing hot melt extrusion. *Journal of Pharmacy and Pharmacology*, 66(2):148–166, 2014.

[33] Khushboo Kothari, Vishard Ragoonanan, and Raj Suryanarayanan. The role of drug–polymer hydrogen bonding interactions on the molecular mobility and physical stability of nifedipine solid dispersions. *Molecular Pharmaceutics*, 12(1):162–170, jan 2015.

[34] Jared A. Baird, Bernard Van Eerdenbrugh, and Lynne S. Taylor. A classification system to assess the crystallization tendency of organic molecules from undercooled melts. *Journal of Pharmaceutical Sciences*, 99(9):3787–3806, 2010.

[35] Krishna Bansal, Uttam Singh Baghel, and Seema Thakral. Construction and validation of binary phase diagram for amorphous solid dispersion using Flory–Huggins theory. *AAPS PharmSciTech*, 17(2):318–327, 2016.

[36] Esther S. Bochmann, Dirk Neumann, Andreas Gryczke, and Karl G. Wagner. Microscale prediction method for API-solubility in polymeric matrices and process model for forming amorphous solid dispersion by hot-melt extrusion. *European Journal of Pharmaceutics and Biopharmaceutics*, 107:40–48, 2016.

[37] Christian Luebbert, Fabian Huxoll, Gabriele Sadowski, Guy Van Den Mooter, and Holger Grohganz. Amorphous-amorphous phase separation in API/polymer formulations. *Molecules*, 22(296):1–17, 2017.

[38] Malte Bille Rask, Matthias Manne Knopp, Niels Erik Olesen, René Holm, and Thomas Rades. Comparison of two DSC-based methods to predict drug-polymer solubility. *International Journal of Pharmaceutics*, 540(1-2):98–105, 2018.

[39] Yiwei Tian, Jonathan Booth, Elizabeth Meehan, David S. Jones, Shu Li, and Gavin P. Andrews. Construction of drug-polymer thermodynamic phase diagrams using flory-huggins interaction theory: Identifying the relevance of temperature and drug weight fraction to phase separation within solid dispersions. *Molecular Pharmaceutics*, 10(1):236–248, 2013.

[40] Fan Meng, Vivek Dave, and Harsh Chauhan. Qualitative and quantitative methods to determine miscibility in amorphous drug-polymer systems. *European Journal of Pharmaceutical Sciences*, 77:106–111, 2015.

[41] M. K. Cheung, J. Wang, S. Zheng, and Y. Mi. Miscibility of poly(epichlorohydrin)/poly(vinyl acetate) blends investigated with high-resolution solid-state 13C NMR. *Polymer*, 41(4):1469–1474, 2000.

[42] Charles M Hansen. The three dimensional solubility parameter and solvent diffusion coefficient. Their importance in surface coating formulation. *J. Paint Technology*, page 104, 1967.

[43] Ritesh Fule, Vivek Paithankar, and Purnima Amin. Hot melt extrusion based solid solution approach: Exploring polymer comparison, physicochemical characterization and in-vivo evaluation. *International Journal of Pharmaceutics*, 499(1-2):280–294, 2016.

[44] Paul J. Flory. Thermodynamics of high polymer solutions. *The Journal of Chemical Physics*, 9:660–661, aug 1941.

[45] Maurice L. Huggins. Solutions of long chain compounds. *The Journal of Chemical Physics*, 9:440, 1941.

[46] A. Newman, D. Engers, S. Bates, I. Ivanisevic, R. C. Kelly, and G. Zografi. Characterization of amorphous API:polymer mixtures using X-ray powder diffraction. *Journal of Pharmaceutical Sciences*, 97(11):4840–4856, 2008.

[47] X Yuan, D Sperger, and E J Munson. Investigating miscibility and molecular mobility of nifedipine-PVP amorphous solid dispersions using solid-state NMR spectroscopy. *Molecular Pharmaceutics*, 11:329–337, 2014.

[48] Julie L. Calahan, Stephanie C. Azali, Eric J. Munson, and Karthik Nagapudi. Investigation of phase mixing in amorphous solid dispersions of AMG 517 in HPMC-AS using DSC, solid-state NMR, and solution calorimetry. *Molecular Pharmaceutics*, 12(11):4115–4123, 2015.

[49] M. Maniruzzaman, M. M. Rana, J. S. Boateng, J. C. Mitchell, and D. Douroumis. Dissolution enhancement of poorly water-soluble APIs processed by hot-melt extrusion using hydrophilic polymers. *Drug Development and Industrial Pharmacy*, 2012:1–10, 2012.

[50] Dana E. Moseson, Naila A. Mugheirbi, Andrew A. Stewart, and Lynne S. Taylor. Nanometer-Scale Residual Crystals in a Hot Melt Extruded Amorphous Solid Dispersion: Characterization by Transmission Electron Microscopy. *Crystal Growth and Design*, 18(12):7633–7640, 2018.

[51] Yuejun Song, Lianyan Wang, Ping Yang, Robert M. Wenslow, Bo Tan, Hailu Zhang, and Zongwu Deng. Physicochemical characterization of Felodipine-Kollidon VA64 amorphous solid dispersions prepared by hot-melt extrusion. *Journal of Pharmaceutical Sciences*, 102(6):1915–1923, 2013.

[52] Francesco Tres, Steven R Coombes, Andrew R Phillips, Leslie P Hughes, Stephen A C Wren, Jonathan W Aylott, and Jonathan C Burley. Investigating the dissolution performance of amorphous solid dispersions using magnetic resonance imaging and proton NMR. *Molecules*, 20:16404–16418, 2015.

[53] Shrawan Baghel, Helen Cathcart, and Niall J. O'Reilly. Understanding the generation and maintenance of supersaturation during the dissolution of amorphous solid dispersions using modulated DSC and 1H NMR. *International Journal of Pharmaceutics*, 536(1):414–425, jan 2018.

[54] J. S. Papanu, D. S. Soane (Soong), A. T. Bell, and D. W. Hess. Transport models for swelling and dissolution of thin polymer films. *Journal of Applied Polymer Science*, 38(5):859–885, 1989.

[55] Nikolaos A. Peppas, J. C. Wu, and Ernst D. von Meerwall. Mathematical modeling and experimental characterization of polymer dissolution. *Macromolecules*, 27(20):5626–5638, 1994.

[56] I. Devotta, V. D. Ambeskar, A. B. Mandhare, and R. A. Mashelkar. The life time of a dissolving polymeric particle. *Chemical Engineering Science*, 49(5):645–654, 1994.

[57] A. C. Ouano and J. A. Carothers. Dissolution dynamics of some polymers: Solvent-polymer boundaries. *Polymer Engineering and Science*, 20(2):160–166, jan 1980.

[58] P. D. Krasicky, R. J. Groele, and F. Rodriguez. Measuring and modelling the transition layer during the dissolution of glassy polymer films. *Journal of Applied Polymer Science*, 35(3):641–651, feb 1988.

[59] I. Devotta, M. V. Badiger, P. R. Rajamohanan, S. Ganapathy, and R. A. Mashelkar. Unusual retardation and enhancement in polymer dissolution: Role of disengagement dynamics. *Chemical Engineering Science*, 50(16):2557–2569, aug 1995.

[60] Ö Pekcan, Ş Uğur, and Y. Yilmaz. Real-time monitoring of swelling and dissolution of poly(methyl methacrylate) discs using fluorescence probes. *Polymer*, 38(9):2183–2189, 1997.

[61] Denise Wade Rafferty and Jack L. Koenig. FTIR imaging for the characterization of controlled-release drug delivery applications. *Journal of Controlled Release*, 83(1):29–39, sep 2002.

[62] Beth A. Miller-Chou and Jack L. Koenig. A review of polymer dissolution. *Progress in Polymer Science*, 28(8):1223–1270, 2003.

[63] Dajun D. Sun and Ping I. Lee. Probing the mechanisms of drug release from amorphous solid dispersions in medium-soluble and medium-insoluble carriers. *Journal of Controlled Release*, 211:85–93, 2015.

[64] M. A. El-Egakey, M. Soliva, and P. Speiser. Hot extruded dosage forms. I. Technology and dissolution kinetics of polymeric matrices. *Pharmaceutica Acta Helvetiae*, 46(1):31–52, jan 1971.

[65] Mohammed Maniruzzaman, Joshua S Boateng, Martin J Snowden, and Dennis Douroumis. A review of hot-melt extrusion: Process technology to pharmaceutical products. *ISRN Pharmaceutics*, 2012:1–9, 2012.

[66] Maria Fátima Pina, Min Zhao, João F. Pinto, João J. Sousa, and Duncan Q M Craig. The influence of drug physical state on the dissolution enhancement of solid dispersions prepared via hot-melt extrusion: A case study using olanzapine. *Journal of Pharmaceutical Sciences*, 103(4):1214–1223, 2014.

[67] Seema Thakral, Maxwell W. Terban, Naveen K. Thakral, and Raj Suryanarayanan. Recent advances in the characterization of amorphous pharmaceuticals by X-ray diffractometry. *Advanced Drug Delivery Reviews*, 100:183–193, may 2016.

[68] Geert Verreck, Karel Six, Guy Van den Mooter, Lieven Baert, Jef Peeters, and Marcus E. Brewster. Characterization of solid dispersions of itraconazole and hydroxypropylmethylcellulose prepared by melt extrusion - Part II. *International Journal of Pharmaceutics*, 251(1-2):165–174, 2003.

[69] Sheng Qi, Peter Belton, Kathrin Nollenberger, Nigel Clayden, Mike Reading, and Duncan Q M Craig. Characterisation and prediction of phase separation in hot-melt extruded solid dispersions: A thermal, microscopic and NMR relaxometry study. *Pharmaceutical Research*, 27(9):1869–1883, 2010.

[70] Ashish L. Sarode, Harpreet Sandhu, Navnit Shah, Waseem Malick, and Hossein Zia. Hot melt extrusion for amorphous solid dispersions: Temperature and moisture activated drug-polymer interactions for enhanced stability. *Molecular Pharmaceutics*, 10:3665–3675, 2013.

[71] Shu Li, Yiwei Tian, David S. Jones, and Gavin P. Andrews. Optimising drug solubilisation in amorphous polymer dispersions: Rational selection of hot-melt extrusion processing parameters. *AAPS PharmSciTech*, 17(1):200–213, 2016.

[72] Jeroen Van Renterghem, Chris Vervaet, and Thomas De Beer. Rheological characterization of molten polymer-drug dispersions as a predictive tool for pharmaceutical hot-melt extrusion processability. *Pharmaceutical Research*, 34(11):2312–2321, 2017.

[73] Lien Saerens, Chris Vervaet, Jean Paul Remon, and Thomas De Beer. Visualization and process understanding of material behavior in the extrusion barrel during a hot-melt extrusion process using raman spectroscopy. *Analytical Chemistry*, 85(11):5420–5429, 2013.

[74] Jeroen Van Renterghem, Ashish Kumar, Chris Vervaet, Jean Paul Remon, Ingmar Nopens, Yvan Vander Heyden, and Thomas De Beer. Elucidation and visualization of solid-state transformation and mixing in a pharmaceutical mini hot melt extrusion process using in-line Raman spectroscopy. *International Journal of Pharmaceutics*, 517:119–127, 2017.

[75] Ecaterina Bordos, Muhammad T. Islam, Alastair J. Florence, Gavin W. Halbert, and John Robertson. Use of Terahertz-Raman spectroscopy to determine solubility of the crystalline active pharmaceutical ingredient in polymeric matrices during hot melt extrusion. *Molecular Pharmaceutics*, 16(10):4361–4371, 2019.

[76] Amrit Paudel, Marco Geppi, and Guy Van den Mooter. Structural and dynamic properties of amorphous solid dispersions: The role of solid-state nuclear magnetic resonance spectroscopy and relaxometry. *Journal of Pharmaceutical Sciences*, 103:2635–2662, 2014.

[77] J. Craig Richardson, Richard W. Bowtell, Karsten Mäder, and Colin D. Melia. Pharmaceutical applications of magnetic resonance imaging (MRI). *Advanced Drug Delivery Reviews*, 57(8):1191–1209, 2005.

[78] R. Bowtell, J. C. Sharp, A. Peters, P. Mansfield, A. R. Rajabi-Siahboomi, M. C. Davies, and C. D. Melia. NMR microscopy of hydrating hydrophilic matrix pharmaceutical tablets. *Magnetic Resonance Imaging*, 12(2):361–364, 1994.

[79] G Tomer, M D Mantle, L F Gladden, and J M Newton. Measuring water distribution in extrudates using magnetic resonance imaging (MRI). *International Journal of Pharmaceutics*, 189:19–28, 1999.

[80] C A Fyfe and A I Blazek. Investigation of hydrogel formation from hydroxypropylmethylcellulose (HPMC) by NMR spectroscopy and NMR imaging techniques. *Macromolecules*, 30(97):6230–6237, 1997.

[81] B. Narasimhan, J. E. M. Snaar, R. W. Bowtell, S. Morgan, C. D. Melia, and N. A. Peppas. Magnetic resonance imaging analysis of molecular mobility during dissolution of poly(vinyl alcohol) in water. *Macromolecules*, 32:704–710, 1999.

[82] Muhammad Ashraf, Virginia L. Iuorno, David Coffin-Beach, C. Anderson Evans, and Larry L. Augsburger. A novel nuclear magnetic resonance (NMR) imaging method for measuring the water front penetration rate in hydrophilic polymer matrix capsule plugs and its role in drug release. *Pharmaceutical Research*, 11(5):733–737, 1994.

[83] Thomas M. Hyde and Lynn F. Gladden. Simultaneous measurement of water and polymer concentration profiles during swelling of poly(ethylene oxide) using magnetic resonance imaging. *Polymer*, 39(4):811–819, 1998.

[84] Y.Y. Chen, L.P. Hughes, L.F. Gladden, and M.D. Mantle. Quantitave ultra-fast MRI of HPMC swelling and dissolution. *Journal of Pharmaceutical Sciences*, 99(8):3462–3472, 2010.

[85] S R Coombes, L P Hughes, A R Phillips, and S A Wren. Proton NMR: A new tool for understanding dissolution. *Analytical Chemistry*, 86(5):2474–2480, 2014.

[86] E. L. Cussler. *Diffusion: mass transfer in fluid systems*. Cambridge University Press, 3rd edition, 2009.

[87] Errol V. Mathias, Julia Aponte, Julia A. Kornfield, and Yong Ba. Properties of small molecular drug loading and diffusion in a fluorinated PEG hydrogel studied by 1H molecular diffusion NMR and 19F spin diffusion NMR. *Colloid and Polymer Science*, 288(18):1655–1663, 2010.

[88] J. E. M. Snaar, R. Bowtell, C. D. Melia, S. Morgan, B. Narasimhan, and N. A. Peppas. Self-diffusion and molecular mobility in PVA-based dissolution-controlled systems for drug delivery. *Magnetic Resonance Imaging*, 16(5-6):691–694, 1998.

[89] L A Weisenberger and J L Koenig. NMR Imaging of diffusion processes in polymers: Measurement of the spatial dependence of solvent mobility in partially swollen PMMA rods. *Macromolecules*, 23:2445–2453, 1990.

[90] Ali R. Rajabi-Siahboomi, Richard W. Bowtell, Peter Mansfield, Martyn C. Davies, and Colin D. Melia. Structure and behavior in hydrophilic matrix sustained release dosage forms: 4. Studies of water mobility and diffusion coefficients in the gel layer of HPMC tablets using NMR imaging. *Pharmaceutical Research*, 13(3):376–380, 1996.

[91] M. Kojima, S. Ando, K. Kataoka, T. Hirota, K. Aoyagi, and H. Kakagami. Magnetic resonance imaging (MRI) study of swelling and water mobility in micronized low-substituted hydroxypropylcellulose matrix tablets. *Chemical & Pharmaceutical Bulletin*, 46(2):324–328, 1998.

[92] B. Madhu, J. Hjartstam, and B. Soussi. Studies of the internal flow process in polymers by 1H NMR microscopy at 500 MHz. *Journal of Controlled Release*, 56:95–104, 1998.

[93] M. Kojima and H. Nakagami. Investigation of water mobility and diffusivity in hydrating micronized low-substituted hydroxypropyl cellulose, hydroxypropylmethyl cellulose, and hydroxypropyl cellulose matrix tablets by magnetic resonance imaging (MRI). *Chemical & Pharmaceutical Bulletin*, 50(12):1621–1624, 2002.

[94] Saša Baumgartner, Gojmir Lahajnar, Ana Sepe, and Julijana Kristl. Quantitative evaluation of polymer concentration profile during swelling of hydrophilic matrix tablets using 1H NMR and MRI methods. *European Journal of Pharmaceutics and Biopharmaceutics*, 59(2):299–306, 2005.

[95] Turner Alfrey, E. F. Gurnee, and W. G. Lloyd. Diffusion in glassy polymers. *Journal of Polymer Science Part C: Polymer Symposia*, 12(1):249–261, mar 1966.

[96] Jadwiga Tritt-goc and Narcyz Pislewski. Magnetic resonance imaging study of the swelling kinetics of hydroxypropylmethylcellulose (HPMC) in water. *Journal of Controlled Release*, 80:79–86, 2002.

[97] Jelena Obradovic, James H P Collins, Ole Hirsch, Michael D. Mantle, Michael L. Johns, and Lynn F. Gladden. The use of THz time-domain reflection measurements to investigate solvent diffusion in polymers. *Polymer*, 48(12):3494–3503, 2007.

[98] Marco Geppi, Giulia Mollica, Silvia Borsacchi, Carlo Alberto Veracini, Marco Geppi, Giulia Mollica, Silvia Borsacchi, and Carlo Alberto Veracini. Solid-state NMR studies of pharmaceutical systems. *Applied Spectroscopy Reviews*, 43(3):202–302, 2008.

[99] David C. Apperley, Angus H. Forster, Romain Fournier, Robin K. Harris, Paul Hodgkinson, Robert W. Lancaster, and Thomas Rades. Characterisation of indomethacin and nifedipine using variable-temperature solid-state NMR. *Magnetic Resonance in Chemistry*, 43(11):881–892, 2005.

[100] Yukio Aso, Sumie Yoshioka, Tamaki Miyazaki, Tohru Kawanishi, Kazuyuki Tanaka, Satoshi Kitamura, Asako Takakura, Takashi Hayashi, and Noriyuki Muranushi. Miscibility of nifedipine and hydrophilic polymers as measured by 1H-NMR spin-lattice relaxation. *Chemical & Pharmaceutical Bulletin*, 55(8):1227–1231, 2007.

[101] Jinglin Yin, Chengbin Huang, Hanxi Guan, Zhenfeng Pang, Yongchao Su, and Xueqian Kong. In situ solid-state NMR characterization of pharmaceutical materials: An example of drug-polymer thermal mixing. *Magnetic Resonance in Chemistry*, (December):1–6, 2019.

[102] Pinal Mistry, Sarat Mohapatra, Tata Gopinath, Frederick G. Vogt, and Raj Suryanarayanan. Role of the strength of drug-polymer interactions on the molecular mobility and crystallization inhibition in ketoconazole solid dispersions. *Molecular Pharmaceutics*, 12(9):3339–3350, 2015.

[103] Tomoyuki Watanabe, Susumu Hasegawa, and Naoki Wakiyama. Comparison between polyvinylpyrrolidone and silica nanoparticles as carriers for indomethacin in a solid state dispersion. *International journal of pharmaceutics*, 250:283–286, 2003.

[104] M Maniruzzaman, D Morgan, A Mendham, J Pang, M Snowden, and D Douroumis. Drug-polymer intermolecular interactions in hot-melt extruded solid dispersions. *International Journal of Pharmaceutics*, 443:199–208, 2013.

[105] Xiaoda Yuan, Tian Xiang Xiang, Bradley D. Anderson, and Eric J. Munson. Hydrogen bonding interactions in amorphous indomethacin and its amorphous solid dispersions with poly(vinylpyrrolidone) and poly(vinylpyrrolidone-co-vinyl acetate) studied using 13C solid-state NMR. *Molecular Pharmaceutics*, 12:4518–4528, 2015.

[106] Chengyu Liu, Cong-Qiao Xu, Junguang Yu, Yipshu Pui, Huijun Chen, Shan Wang, Alan (Donghua) Zhu, Jun Li, and Feng Qian. Impact of a single hydrogen substitution by fluorine on the molecular interaction and miscibility between sorafenib and polymers. *Molecular Pharmaceutics*, 16:318–326, 2019.

[107] B. J. Van Rossum, H. Förster, and H. J.M. De Groot. High-field and high-speed CP-MAS 13C NMR heteronuclear dipolar-correlation spectroscopy of solids with frequency-switched Lee-Goldburg homonuclear decoupling. *Journal of Magnetic Resonance*, 124(2):516–519, 1997.

[108] W P Aue, E Bartholdi, and R R Ernst. Two-dimensional spectroscopy. Application to nuclear magnetic resonance. *Journal of Chemical Physics*, 64(5):2229–2246, 1976.

[109] Steven P. Brown, Marta Pérez-Torralba, Dionísia Sanz, Rosa María Claramunt, and Lyndon Emsley. The direct detection of a hydrogen bond in the solid state by NMR through the observation of a hydrogen-bond mediated 15N-15N J coupling. *Journal of the American Chemical Society*, 124(7):1152–1153, 2002.

[110] S. P. Brown, M. Pérez-Torralba, D. Sanz, R. M. Claramunt, and L. Emsley. Determining hydrogen-bond strengths in the solid state by NMR: The quantitative measurement of homonuclear J couplings. *Chemical Communications*, 8(17):1852–1853, 2002.

[111] Tran N Pham, Simon A Watson, Andrew J Edwards, Manisha Chavda, Jacalyn S Clawson, Mark Strohmeier, and Frederick G Vogt. Analysis of amorphous solid dispersions using 2D solid-state NMR and 1H T1 relaxation measurements. *Molecular Pharmaceutics*, 7(5):1667–1691, 2010.

[112] Andrew S. Tatton, Tran N. Pham, Frederick G. Vogt, Dinu Iuga, Andrew J. Edwards, and Steven P. Brown. Probing hydrogen bonding in cocrystals and amorphous dispersions using 14N-1H HMQC solid-state NMR. *Molecular Pharmaceutics*, 10(3):999–1007, 2013.

[113] Patrick J. Marsac, Sheri L. Shamblin, and Lynne S. Taylor. Theoretical and practical approaches for prediction of drug-polymer miscibility and solubility. *Pharmaceutical Research*, 23(10):2417–2426, 2006.

[114] Jonathan Grimard, Laurent Dewasme, and Alain Vande Wouwer. A review of dynamic models of hot-melt extrusion. *Processes*, 4(2):19, 2016.

[115] Andreas Eitzlmayr, Johannes Khinast, Gudrun Hörl, Gerold Koscher, Gavin Reynolds, Zhenyu Huang, Jonathan Booth, and Philip Shering. Experimental characterization and modeling of twin-screw extruder elements for pharmaceutical hot melt extrusion. *American Institue of Chemical Engineers*, 59(11):4440–4450, nov 2013.

[116] Andreas Eitzlmayr, Gerold Koscher, Gavin Reynolds, Zhenyu Huang, Jonathan Booth, Philip Shering, and Johannes Khinast. Mechanistic modeling of modular co-rotating twin-screw extruders. *International Journal of Pharmaceutics*, 474(1-2):157–176, 2014.

[117] Jos J. Derksen, Gavin Reynolds, Alex Crampton, Zhenyu Huang, and Jonathan Booth. Simulations of dissolution of spherical particles in laminar shear flow. *Chemical Engineering Research and Design*, 93:66–78, 2015.

[118] A. Schittny, H. Ogawa, J. Huwyler, and M. Puchkov. A combined mathematical model linking the formation of amorphous solid dispersions with hot-melt-extrusion process parameters. *European Journal of Pharmaceutics and Biopharmaceutics*, 132:127–145, 2018.

[119] I.I. Rabi, J.M.B. Kellogg, and J.R. Zacharias. The magnetic moment of the proton. *Physical Review*, 46(3):157–163, 1934.

[120] F. Bloch. Nuclear induction. *Physical Review*, 70(7-8):460–474, 1946.

[121] E. M. Purcell, H.C. Torrey, and R.V. Pound. Resonance absorption by nuclear magnetic moments in a solid. *Physical Review*, 69(681):37–38, 1946.

[122] Malcolm H. Levitt. *Spin dynamics: Basics of nuclear magnetic resonance*. 2001.

[123] James. Keeler. *Understanding NMR spectroscopy*. John Wiley and Sons, 2002.

[124] R. L. Vold, J. S. Waugh, M. P. Klein, and D. E. Phelps. Measurement of spin relaxation in complex systems. *The Journal of Chemical Physics*, 48(8):3831–3832, 1968.

[125] S. Meiboom and D. Gill. Modified spin-echo method for measuring nuclear relaxation times. *Review of Scientific Instruments*, 29(8):688–691, 1958.

[126] E O Stejskal and J E Tanner. Spin diffusion measurements: Spin echoes in the presence of a time-dependant field gradient. *The Journal of Chemical Physics*, 42:288–292, 1965.

[127] J. E. Tanner. Use of the stimulated echo in NMR diffusion studies. *Journal of Chemical Physics*, 52(5):2523–2526, 1970.

[128] R. M Cotts, M. J. R Hoch, T. Sun, and J. T. Markert. Pulsed field gradient stimulated echo methods for improved NMR diffusion measurements in heterogeneous systems. *Journal of Magnetic Resonance*, 83(2):252–266, 1989.

[129] P. Mansfield and P. K. Grannell. NMR 'diffraction' in solids? *Journal of Physics C: Solid State Physics*, 6:422–426, 1973.

[130] Waclaw Kolodziejski and Jacek Klinowski. Kinetics of cross-polarization in solid-state NMR: A guide for chemists. *Chemical Society Reviews*, 102:613–628, 2002.

[131] E.R. Andrew, A. Bradbury, and R.G. Eades. Nuclear magnetic resonance spectra from a crystal rotated at high speed. *Nature*, 182:1659, 1958.

[132] I. J. Lowe. Free induction decays of rotating solids. *Physical Review Letters*, 2(7):285–287, 1959.

[133] D.P. Raleigh, M.H. Levitt, and R.G. Griffin. Rotational resonance in solid state NMR. *Chemical Physics Letters*, 146(1):71–76, 1988.

[134] B. M. Fung, A. K. Khitrin, and K. Ermolaev. An improved broadband decoupling sequence for liquid crystals and solids. *Journal of Magnetic Resonance*, 142(1):97–101, 2000.

[135] Thomas Bräuniger, Philip Wormald, and Paul Hodgkinson. Improved proton decoupling in NMR spectroscopy of crystalline solids using the SPINAL-64 sequence. *Monatshefte fur Chemie*, 133(12):1549–1554, 2002.

[136] S. R. Hartmann and E. L. Hahn. Nuclear double resonance in the rotating frame. *Physical Review*, 128(5):2042–2053, 1962.

[137] Günter Metz, Xiaoling Wu, and Steven O. Smith. Ramped-amplitude cross polarization in magic-angle-spinning NMR. *Journal of Magnetic Resonance*, 110:219–227, 1994.

[138] K. V. Lingam, P. G. Nair, and B. Venkataraman. Spin-lattice relaxation studies on semiquinone ions. *Proceedings of the Indian Academy of Sciences - Section A*, 76(5):207–220, 1972.

[139] W. Sommer, J. Gottwald, D. E. Demco, and H. W. Spiess. Dipolar heteronuclear multiple-quantum NMR spectroscopy in rotating solids. *Journal of Magnetic Resonance, Series A*, 113:131–134, 1995.

[140] M. Feike, D. E. Demco, R. Graf, J. Gottwald, S. Hafner, and H. W. Spiess. Broadband multiple-quantum NMR spectroscopy. *Journal of Magnetic Resonance - Series A*, 122(2):214–221, 1996.

[141] Rongchun Zhang, Manoj Kumar Pandey, Yusuke Nishiyama, and Ayyalusamy Ramamoorthy. A novel high-resolution and sensitivity-enhanced three-dimensional solid-state NMR experiment under ultrafast magic angle spinning conditions. *Scientific Reports*, 5(May):1–9, 2015.

[142] M. J. O'Neill. The analysis of a temperature-controlled scanning calorimeter. *Analytical Chemistry*, 36(7):1238–1245, 1964.

[143] Tim Osswald and Natalie Rudolph. *Polymer rheology. From molecular structure to polymer process.* Carl Hanser Verlag, Munich, 2013.

[144] Christopher A. Grabowski and Ashis Mukhopadhyay. Size effect of nanoparticle diffusion in a polymer melt. *Macromolecules*, 47(20):7238–7242, 2014.

[145] W Liu, D G Ray, Peter L Rinaldi, and T Zens. High-temperature pulsed-field-gradient multidimensional NMR of polymers. *Journal of Magnetic Resonance*, 140(2):482–486, 1999.

[146] Janez Stepišnik, Gojmir Lahajnar, Ivan Zupančič, and Aleš Mohorič. Study of translational dynamics in molten polymer by variation of gradient pulse-width of PGSE. *Journal of Magnetic Resonance*, 236(November 2016):41–46, 2013.

[147] U. Matenaar, J. Richter, and M.D. Zeidler. High-temperature–high-pressure NMR probe for self-diffusion measurements in molten salts. *Journal of Magnetic Resonance, Series A*, 122:72–75, 1996.

[148] Adolf Feinauer and Günter Majer. Diffusion of 23Na and 39K in the eutectic melt Na(0.32)K(0.68). *Physical Review B*, 64(13):134302, 2001.

[149] Anne Laure Rollet, Vincent Sarou-Kanian, and Catherine Bessada. Self-diffusion coefficient measurements at high temperature by PFG NMR. *Comptes Rendus Chimie*, 13(4):399–404, 2010.

[150] Takahiro Ohkubo, Mallory Gobet, Vincent Sarou-Kanian, Catherine Bessada, Muneharu Nozawa, and Yasuhiko Iwadate. Self-diffusion coefficient of lithium in molten xLi2O-(1-X)B2O3 system using high-temperature PFG NMR. *Chemical Physics Letters*, 530:61–63, 2012.

[151] Dana E. Moseson, Andrew S. Parker, Christopher J. Gilpin, Andrew A. Stewart, Stephen P. Beaudoin, and Lynne S. Taylor. Dissolution of indomethacin crystals into a polymer melt: Role of diffusion and fragmentation. *Crystal Growth and Design*, 19(6):3315–3328, 2019.

[152] Simerdeep Singh Gupta, Anuprabha K. Meena, Tapan Parikh, and Abu T. M. Serajuddin. Investigation of thermal and viscoelastic properties of polymers relevant to hot melt extrusion - I: Polyvinylpyrrolidone and related polymers. *Journal of Excipients and Food Chemicals*, 5(1):32–45, 2014.

[153] Simerdeep Singh Gupta, Nayan Solanki, and Abu T. M. Serajuddin. Investigation of thermal and viscoelastic properties of polymers relevant to hot melt extrusion, IV: Affinisol HPMC HME polymers. *AAPS PharmSciTech*, 17(1):148–157, 2016.

[154] Patrick J. Marsac, Tonglei Li, and Lynne S. Taylor. Estimation of drug-polymer miscibility and solubility in amorphous solid dispersions using experimentally determined interaction parameters. *Pharmaceutical Research*, 26(1):139–151, 2009.

[155] Min Yang, Peng Wang, Herman Suwardie, and Costas Gogos. Determination of acetaminophen's solubility in poly(ethylene oxide) by rheological, thermal and microscopic methods. *International Journal of Pharmaceutics*, 403(1-2):83–89, 2011.

[156] Fengyuan Yang, Yongchao Su, Lei Zhu, Chad D Brown, Lawrence A Rosen, and Kenneth J Rosenberg. Rheological and solid-state NMR assessments of copovidone/clotrimazole model solid dispersions. *International Journal of Pharmaceutics*, 500:20–31, 2016.

[157] Fengyuan Yang, Yongchao Su, Jingtao Zhang, James Dinunzio, Anthony Leone, Chengbin Huang, and Chad D. Brown. Rheology guided rational selection of processing temperature to prepare copovidone-nifedipine amorphous solid dispersions via hot melt extrusion (HME). *Molecular Pharmaceutics*, 13(10):3494–3505, 2016.

[158] R S Chaudhary, C Patel, V Sevak, and M Chan. Effect of Kollidon VA64 particle size and morphology as directly compressible excipient on tablet compression properties. *Drug Development and Industrial Pharmacy*, 44(1):19–29, jan 2018.

[159] M L Kaplan, F A Bovey, and H N Cheng. Simplified method of calibrating thermometric nuclear magnetic resonance standards. *Analytical Chemistry*, 47(9):1703–1705, 1975.

[160] Claude Ammann, Pierre Meier, and AndréE Merbach. A simple multinuclear NMR thermometer. *Journal of Magnetic Resonance*, 46(2):319–321, 1982.

[161] Torgny Rundlof, Marie Mathiasson, Somer Bekiroglu, Birgit Hakkarainen, Tim Bowden, and Torbj??rn Arvidsson. Survey and qualification of internal standards for quantification by 1H NMR spectroscopy. *Journal of Pharmaceutical and Biomedical Analysis*, 52(5):645–651, 2010.

[162] Maiara Da S. Santos and Luiz Alberto Colnago. Validação de método quantitativo por RMN de 1H para análises de formulações farmacêuticas. *Quimica Nova*, 36(2):324–330, 2013.

[163] Paola Roscigno, Fioretta Asaro, Giorgio Pellizer, Ornella Ortona, and Luigi Paduano. Complex formation between poly(vinylpyrrolidone) and sodium decyl sulfate studied through NMR. *Langmuir*, 19(23):9638–9644, 2003.

[164] Yuxia Luan, Aixin Song, and Guiying Xu. Location of probe molecule in double-chain surfactant aggregates in absence and presence of water-soluble polymer by NMR. *Soft Matter*, 5(13):2587–2595, 2009.

[165] Vijay Kumar Patel, Niraj Kumar Vishwakarma, Avnish Kumar Mishra, Chandra Sekhar Biswas, and Biswajit Ray. (S)-2-(ethyl propionate)-(O-ethyl xanthate)- and (S)-2-(Ethyl isobutyrate)-(O-ethyl xanthate)-mediated RAFT polymerization of vinyl acetate. *Journal of Applied Polymer Science*, 125(4):2946–2955, 2012.

[166] Bradford P. Cross and Thomas Schleich. Temperature dependence of the chemical shift of commonly employed proton NMR reference compounds. *Organic Magnetic Resonance*, 10:82–85, 1997.

[167] Elena V. Boldyreva, V. A. Drebushchak, I. E. Paukov, Yulia A. Kovalevskaya, and Tatiana N. Drebushchak. DSC and adiabatic calorimetry study of the polymorphs of paracetamol: An old problem revisited. *Journal of Thermal Analysis and Calorimetry*, 77(2):607–623, 2004.

[168] Jonathan C. Burley, Melinda J. Duer, Robin S. Stein, and Ranko M. Vrcelj. Enforcing Ostwald's rule of stages: Isolation of paracetamol forms III and II. *European Journal of Pharmaceutical Sciences*, 31(5):271–276, 2007.

[169] Amjad Alhalaweh, Ahmad Alzghoul, Denny Mahlin, and Christel A.S. Bergström. Physical stability of drugs after storage above and below the glass transition temperature: Relationship to glass-forming ability. *International Journal of Pharmaceutics*, 495(1):312–317, 2015.

[170] Ana C.F. Ribeiro, Marisa C.F. Barros, Luís M.P. Veríssimo, Cecilia I.A.V. Santos, Ana M.T.D.P.V. Cabral, Gualter D. Gaspar, and Miguel A. Esteso. Diffusion coefficients of paracetamol in aqueous solutions. *Journal of Chemical Thermodynamics*, 54:97–99, 2012.

[171] Albert Einstein. On the motion of small particles suspended in a stationary liquid, as required by the molecular kinetic theory of heat. *Annalen der Physik*, 322:549–560, 1905.

[172] John R. Wagner, Eldridge M. Mount, and Harold F. Giles. *Extrusion: The Definitive Processing Guide and Handbook*. Elsevier Inc., 2nd edition, 2013.

[173] Klemens. Kohlgruber. *Co-rotating twin-screw extruder: Fundamentals, technology, and applications*. Carl Hanser Verlag GmbH & Co, 2007.

[174] Johanna Aho, Magnus Edinger, Johan Botker, Stefania Baldursdottir, and Jukka Rantanen. Oscillatory shear rheology in examining the drug-polymer interactions relevant in hot melt extrusion. *Journal of Pharmaceutical Sciences*, 105(1):160–167, 2016.

[175] Irvin M. Krieger and Thomas J. Dougherty. A mechanism for non-Newtonian flow in suspensions of rigid spheres. *Transactions of the Society of Rheology*, 3(1):137–152, 1959.

[176] J. K. Morse. The structure and dimensions of the benzene ring. *Proceedings of the National Academy of Sciences*, 13(12):789–793, 1927.

[177] I. Avramov. Relationship between diffusion, self-diffusion and viscosity. *Journal of Non-Crystalline Solids*, 355(10-12):745–747, 2009.

[178] Jun Liu, Dapeng Cao, and Liqun Zhang. Molecular dynamics study on nanoparticle diffusion in polymer melts: A test of the Stokes-Einstein law. *Journal of Physical Chemistry C*, 112(17):6653–6661, 2008.

[179] John T. Edward. Molecular volumes and the Stokes-Einstein equation. *Journal of Chemical Education*, 47(4):261–270, 1970.

[180] M. Pilar Tarazona and Enrique Saiz. Combination of SEC/MALS experimental procedures and theoretical analysis for studying the solution properties of macromolecules. *Journal of Biochemical and Biophysical Methods*, 56(1-3):95–116, 2003.

[181] Patrick Knappe, Ralf Bienert, Steffen Weidner, and Andreas F. Thünemann. Characterization of poly(N-vinyl-2-pyrrolidone)s with broad size distributions. *Polymer*, 51(8):1723–1727, 2010.

[182] Vincent A. Martinez, Jana Schwarz-Linek, Mathias Reufer, Laurence G. Wilson, Alexander N. Morozov, and Wilson C K Poon. Flagellated bacterial motility in polymer solutions. *Proceedings of the National Academy of Sciences of the United States of America*, 111(50):17771–17776, 2014.

[183] Teng Ian Chan and Defang Ouyang. Investigating the molecular dissolution process of binary solid dispersions by molecular dynamics simulations. *Asian Journal of Pharmaceutical Sciences*, 13(3):248–254, 2018.

[184] Svante Arrhenius. Über die Dissociationswärme und den Einfluss der Temperatur auf den Dissociationsgrad der Elektrolyte. *Zeitschrift für Physikalische Chemie*, 4U(1):96–116, 1889.

[185] N. F.A. Van Der Vegt. Temperature dependence of gas transport in polymer melts: Molecular dynamics simulations of CO2 in polyethylene. *Macromolecules*, 33(8):3153–3160, 2000.

[186] Carmine D'Agostino, Mick D. Mantle, Claire L. Mullan, Christopher Hardacre, and Lynn F. Gladden. Diffusion, ion pairing and aggregation in 1-ethyl-3-methylimidazolium-based ionic liquids studied by 1H and 19F PFG NMR: Effect of temperature, anion and glucose dissolution. *ChemPhysChem*, 19(9):1081–1088, 2018.

[187] Armando Lucero-Acuña, Cindy Alejandra Gutiérrez-Valenzuela, Reynaldo Esquivel, and Roberto Guzmán-Zamudio. Mathematical modeling and parametrical analysis of the temperature dependency of control drug release from biodegradable nanoparticles. *RSC Advances*, 9(16):8728–8739, 2019.

[188] Andrew J. Dingley, Florence Cordier, and Stephan Grzesiek. An introduction to hydrogen bond scalar couplings. *Concepts in Magnetic Resonance*, 13(2):103–127, 2001.

[189] Yi-Qiao Song. Magnetic Resonance of Porous Media (MRPM): A perspective. *Journal of Magnetic Resonance*, 229:12–24, apr 2013.

[190] Kieran J. Crowley and George Zografi. Water vapor absorption into amorphous hydrophobic drug/poly(vinylpyrrolidone) dispersions. *Journal of Pharmaceutical Sciences*, 91(10):2150–2165, 2002.

[191] Kassibla Elodie Dempah, Joseph W. Lubach, and Eric J. Munson. Characterization of the particle size and polydispersity of dicumarol using solid-state NMR spectroscopy. *Molecular Pharmaceutics*, 14(3):856–865, 2017.

[192] Matthias Ernst and Beat H. Meier. *Spin Diffusion in Solids*. Elsevier, 1998.

[193] R. E. Taylor. Setting up 13C CP/MAS experiments. *Concepts in Magnetic Resonance Part A*, 22A(1):1–32, 2004.

[194] Corey R Morcombe and Kurt W Zilm. Chemical shift referencing in MAS solid state NMR. *Journal of Magnetic Resonance*, (162):479–486, 2003.

[195] Xiaochuan Yang, Ta Chung Ong, Vladimir K. Michaelis, Scott Heng, Robert G. Griffin, and Allan S. Myerson. Formation of organic molecular nanocrystals under soft confinement. *CrystEngComm*, 17(31):6044–6052, 2015.

[196] Tapan Parikh, Simerdeep Singh Gupta, Anuprabha K. Meena, Imre Vitez, Nidhi Mahajan, and Abu T.M. Serajuddin. Application of Film-Casting Technique to Investigate Drug-Polymer Miscibility in Solid Dispersion and Hot-Melt Extrudate. *Journal of Pharmaceutical Sciences*, 104(7):2142–2152, 2015.

[197] Juraj Sibik, Korbinian Löbmann, Thomas Rades, and J. Axel Zeitler. Predicting crystallization of amorphous drugs with terahertz spectroscopy. *Molecular Pharmaceutics*, 12(8):3062–3068, 2015.

[198] Philippe Espeau, René Céolin, Josep Lluis Tamarit, Marc Antoine Perrin, Jean Pierre Gauchi, and Franck Leveiller. Polymorphism of paracetamol: Relative stabilities of the monoclinic and orthorhombic phases inferred from topological pressure-temperature and temperature-volume phase diagrams. *Journal of Pharmaceutical Sciences*, 94(3):524–539, 2005.

[199] Dana E. Moseson and Lynne S. Taylor. The application of temperature-composition phase diagrams for hot melt extrusion processing of amorphous solid dispersions to prevent residual crystallinity. *International Journal of Pharmaceutics*, 553:454–466, dec 2018.

[200] M. Maniruzzaman, Martin J. Snowden, Mike S. Bradely, and D. Douroumis. Studies of intermolecular interactions in solid dispersions using advanced surface chemical analysis. *Royal Society of Chemistry Adv.*, 5(91):74212–74219, 2015.

[201] Karl J. Dria, Joseph R. Sachleben, and Patrick G. Hatcher. Solid-state Carbon-13 nuclear magnetic resonance of humic acids at high magnetic field strengths. *Journal of Environment Quality*, 31(2):393, 2002.

[202] Donghua H. Zhou and Chad M. Rienstra. Rapid analysis of organic compounds by proton-detected heteronuclear correlation NMR spectroscopy with 40 kHz magic-angle spinning. *Angewandte Chemie - International Edition*, 47(38):7328–7331, 2008.

[203] Hong Wen, Kenneth R. Morris, and Kinam Park. Study on the interactions between polyvinylpyrrolidone (PVP) and acetaminophen crystals: Partial dissolution pattern change. *Journal of Pharmaceutical Sciences*, 94(10):2166–2174, 2005.

[204] Deng Guang Yu, Christopher Branford-White, Kenneth White, Xue Lian Li, and Li Min Zhu. Dissolution improvement of electrospun nanofiber-based solid dispersions for acetaminophen. *AAPS PharmSciTech*, 11(2):809–817, 2010.

[205] Joanna Kolmas and Waclaw Kolodziejski. Inverse 31P → 1H NMR cross-polarization in hydrated nanocrystalline calcium hydroxyapatite. *Chemical Physics Letters*, 554:128–132, 2012.

[206] Kurt Wüthrich. NMR studies of structure and function of biological macromolecules (Nobel Lecture). *Angewandte Chemie - International Edition*, 42(29):3340–3363, 2003.

[207] Sarah K. Mann, Tran N. Pham, Lisa L. McQueen, Józef R. Lewandowski, and Steven P. Brown. Revealing intermolecular hydrogen Bbonding structure and dynamics in a deep eutectic pharmaceutical by magic-angle spinning NMR spectroscopy. *Molecular Pharmaceutics*, 17:622–631, 2020.

[208] D. A. Druzhbin, T. N. Drebushchak, V. S. Min'kov, and E. V. Boldyreva. Crystal structure of two paracetamol polymorphs at 20 K: A search for the "structure-property" relationship. *Journal of Structural Chemistry*, 56(2):317–323, 2015.

[209] M. P. Ledbetter, G. Saielli, A. Bagno, N. Tran, and M. V. Romalis. Observation of scalar nuclear spin-spin coupling in van der Waals complexes. *Proceedings of the National Academy of Sciences*, 109(31):12393–12397, jul 2012.

[210] Majda Srabovic, Melita Huremovic, Benjamin Catovic, and Samra Muratovic. Design synthesis and crystallization of acetaminophen. *Journal of Chemical , Biological and Physical Sciences*, 7(January):218–230, 2017.

[211] Mei Wen Huang, Shiao Wei Kuo, Hew Der Wu, Feng Chih Chang, and Su Yun Fang. Miscibility and hydrogen bonding in blends of poly(vinyl acetate) with phenolic resin. *Polymer*, 43(8):2479–2487, 2002.

[212] Siok Yee Chan, Yin Ying Chung, Xin Zi Cheah, Eryn Yen Ling Tan, and Joan Quah. The characterization and dissolution performances of spray dried solid dispersion of ketoprofen in hydrophilic carriers. *Asian Journal of Pharmaceutical Sciences*, 10(5):372–385, 2015.

[213] Malte Bille Rask, Matthias Manne Knopp, Niels Erik Olesen, René Holm, and Thomas Rades. lnfluence of PVP/VA copolymer composition on drug-polymer solubility. *European Journal of Pharmaceutical Sciences*, 85:10–17, 2016.

[214] V.S. Grechishkin, R.V. Grechishkina, G.S. Kuprianova, J.N. Latosinska, and B. Nogaj. High-Resolution NMR Studies of Nifedipine. *Applied Magnetic Resonance*, 17:113–118, 1999.

[215] Tarun Handa, Saranjit Singh, and Inder Pal. Characterization of a new degradation product of nifedipine formed on catalysis by atenolol : A typical case of alteration of degradation pathway of one drug by another. *Journal of Pharmaceutical and Biomedical Analysis*, 89:6–17, 2014.

[216] Kevin DeBoyace and Peter L.D. Wildfong. The application of modeling and prediction to the formation and stability of amorphous solid dispersions. *Journal of Pharmaceutical Sciences*, 107(1):57–74, 2018.

[217] Elisabetta Princi and Silvia Vicini. Evaluation of the interaction parameter for poly(e-caprolactone)/poly(styrene-co-acrylonitrile) blends. *Journal of Polymer Science*, 48:2129–2139, 2010.

[218] D.W. Van Krevelen. *Properties of polymers: Their correlation with chemical structure, their numerical estimation and prediction from additive group contributions*. Elsevier, Amsterdam, 3rd edition, 1990.

[219] Thomas Lindvig, Michael L Michelsen, and Georgios M Kontogeorgis. A Flory–Huggins model based on the Hansen solubility parameters. *Fluid Phase Equilibria*, 203:247–260, 2002.

[220] Edyta Leyk and Marek Wesolowski. Interactions between paracetamol and hypromellose in the solid state. *Frontiers in Pharmacology*, 9(JAN):1–11, 2019.

[221] Adolph Fick. On liquid diffusion. *Journal of Membrane Science*, 100:33–38, 1995.

[222] Michael Rubinstein and Ralph H Colby. *Polymer Physics*. 2003.

[223] Jerome Barra, Francois Lescure, Eric Doelker, and Pilar Bustamante. The Expanded Hansen Approach to Solubility Parameters. Paracetamol and Citric Acid in Individual Solvents. *Journal of Pharmacy and Pharmacology*, 49:644–651, 1997.

[224] Teja Kitak, Aleksandra Dumičič, Odon Planinšek, Rok Šibanc, Stanko Srčič, Thomas Rades, Holger Grohganz, and Korbinian Löbmann. Determination of solubility parameters of ibuprofen and ibuprofen lysinate. *Molecules*, 20(12):21549–21568, 2015.

[225] Patrick J. Marsac, Hajime Konno, and Lynne S. Taylor. A comparison of the physical stability of amorphous felodipine and nifedipine systems. *Pharmaceutical Research*, 23(10):2306–2316, 2006.

[226] D J W Grant, M Mehdizadeh, Ah-l Chow, and J E Fairbrother. Non-linear van't Hoff solubility-temperature plots and their pharmaceutical interpretation. *International Journal of Pharmaceutics*, 18:25–38, 1984.

[227] Esther S. Bochmann, Elgin E. Üstüner, Andreas Gryczke, and Karl G. Wagner. Predicting melt rheology for hot-melt extrusion by means of a simple Tg-measurement. *European Journal of Pharmaceutics and Biopharmaceutics*, 119:47–55, 2017.

[228] Qing Du, David R. Harding, and Hong Yang. Helical peanut-shaped poly(vinyl pyrrolidone) ribbons generated by electrospinning. *Polymer*, 54(25):6752–6759, 2013.

[229] Antonil F D Medeiros, Ana Flávia O Santos, F S De Souza, J V V Procópio, Márcia Ferraz Pinto, and R O Mac. Thermal stability of paracetamol and its pre-formulates obtained by spray drying. *Journal of Thermal Analysis and Calorimetry*, 88(2):377–382, 2007.

[230] G. G.G. de Oliveira, A. Feitosa, K. Loureiro, A. R. Fernandes, E. B. Souto, and P. Severino. Compatibility study of paracetamol, chlorpheniramine maleate and phenylephrine hydrochloride in physical mixtures. *Saudi Pharmaceutical Journal*, 25(1):99–103, 2016.

[231] Amrit Paudel, Jan Van Humbeeck, and Guy Van Den Mooter. Theoretical and Experimental Investigation on the Solid Solubility and Miscibility of Naproxen in Poly(vinylpyrrolidone). *Molecular Pharmaceutics*, 7(4):1133–1148, 2010.

Appendix A

High temperature characterisation of materials

A.1 T_1 and T_2 temperature dependence of samples

Table A.1 T_1 and T_2 temperature dependence of paracetamol, copovidone and a 30 wt% physical mix acquired with the inversion recovery and CPMG sequences, respectively (Figure 2.3 and 2.4). The paracetamol signal at 130°C and 140°C from the inversion recovery experiments was too low for T_1 measurement.

	Paracetamol	**Copovidone**	**30 wt% physical mix**
		T_1 [s]	
130°C	–	4.9±0.1	2.6±0.2
140°C	–	5.1±0.3	2.0±0.2
150°C	0.3±0.1	4.7±0.1	2.0±0.3
160°C	0.6±0.1	3.4±0.1	1.7±0.3
170°C	1.2±0.1	3.0±0.1	1.0±0.1
		T_2 [ms]	
130°C	17±1.4	1.5±0.2	3.6±0.5
140°C	43±1.1	0.4±0.1	11±0.6
150°C	97±1.5	0.3±0.1	37±0.5
160°C	177±34.1	0.6±0.1	59±0.5
170°C	435±36.1	1.4±0.2	43±0.2